UNIVERSITÀ DEGLI STUDI DI BARI

DIPARTIMENTO INTERUNIVERSITARIO DI FISICA

"Michelangelo Merlin"

Dottorato di ricerca in Fisica - Ciclo XXXVIII
Settore scientifico-disciplinare FIS/02

Probing Fundamental Physics with Core-Collapse Supernovae: Insights from a Multimessenger Perspective

Dottorando: Dott. Alessandro Lella

Coordinatore: Ch.mo Prof. Vincenzo Luigi Spagnolo

Supervisore: Ch.mo Prof. Alessandro Mirizzi

ESAME FINALE 2026

Università degli Studi di Bari Aldo Moro, Piazza Umberto I, 1 - 70121 BARI
C.F. 80002170720 | p.i. 01086760723 | www.uniba.it

Foreword

My research activity as a PhD student develops at the interface of Particle Physics and Astrophysics. I studied the role of axions and other feebly-interacting particles (FIPs) in extreme astrophysical environments, such as Core-Collapse Supernovae (CC SNe) and Neutron Stars (NS), both characterizing possible indirect signatures arising from their impact on stellar evolution, and direct signatures connected to observable fluxes at Earth. These studies rely on a synergistic approach combining theoretical predictions and experimental searches conducted through various cosmic messengers. Through the development of these projects, I have acquired significant expertise in advanced quantum field theory techniques in dense plasmas, the implementation of complex numerical codes, and multimessenger astrophysics methods that integrate gamma-ray, neutrino, and gravitational-wave signatures. The results discussed in this Thesis are based on the publications (P1)-(P4), (P6)-(P8) and (P11)-(P12) shown in the list below.

List of Publications

(P1) A. Lella, P. Carenza, G. Lucente, M. Giannotti, A. Mirizzi, "Protoneutron stars as cosmic factories for massive axionlike particles", Phys.Rev.D **107** (2023) no.10, 103017 [arXiv:2211.13760 [hep-ph]].

(P2) A. Lella, G. Co', P. Carenza, G. Lucente, M. Giannotti, A. Mirizzi, T. Rauscher, "Getting the most on supernova axions", Phys.Rev.D **109** (2024) no.2, 023001 [arXiv:2306.01048 [hep-ph]].

(P3) P. Carenza, G. Co', M. Giannotti, A. Lella, A. Mirizzi, T. Rauscher, "Cross section for supernova axion observation in neutrino water Čherenkov detectors", Phys.Rev.C **109** (2024) no.1, 015501 [arXiv:2306.17055 [hep-ph]].

(P4) A. Lella, E. Ravensburg, P. Carenza, M.C.D. Marsh, "Supernova limits on QCD axionlike particles", Phys.Rev.D **110** (2024) no.4, 043019 [arXiv:2405.00153 [hep-ph]].

(P5) A. Lella, F. Calore, P. Carenza, A. Mirizzi, "Constraining gravitational-wave backgrounds from conversions into photons in the Galactic magnetic field", Phys.Rev.D **110** (2024) no.8, 083042 [arXiv:2406.17853 [hep-ph]].

(P6) A. Lella, F. Calore, P. Carenza, C. Eckner, M. Giannotti, G. Lucente, A. Mirizzi, "Probing protoneutron stars with gamma-ray axionscopes", JCAP **11** (2024) 009 [arXiv:2405.02395 [hep-ph]].

(P7) S. Balaji, P. Carenza, P. De la Torre Luque, A. Lella, L. Mastrototaro, "In-flight positron annihilation as a probe of feebly interacting particles", Phys.Rev.D **111** (2025) no.8, 083053 [arXiv:2501.07725 [hep-ph]].

(P8) P. Carenza, J. A. Garcia Pascual, M. Giannotti, I. G. Irastorza, M. Kaltschmidt, A. Lella, A. Lindner, G. Lucente, A. Mirizzi, M. J. Puyuelo, "Detecting Supernova Axions with IAXO", JCAP **07** (2025) 075 [arXiv:2502.19476 [hep-ph]].

(P9) F. Lecce, A. Lella, G. Lucente, V. Vijayan, A. Bauswein, M. Giannotti, A. Mirizzi, "Probing axion-like particles with multimessenger observations of neutron star mergers", Phys.Rev.D **112** (2025) no.2, 023001 [arXiv:2504.02032 [hep-ph]].

(P10) F. R. Candòn, S. Ganguly, M. Giannotti, T. Kumar, A. Lella, F. Mescia, "A Fresh Look at the Diffuse ALP Background from Supernova", Phys. Rev. D **112** no.1, 015006 [arXiv:2505.05567 [hep-ph]].

(P11) D. F. G. Fiorillo, A. Lella, C. A. J. O'Hare, E. Vitagliano, "Leading bounds on micro- to picometer fifth forces from neutron star cooling", Phys. Rev. Lett. 135 **2025** no.21, 21 2506.19906 [arXiv:2506.19906 [hep-ph]].

(P12) F. Lecce, A. Lella, G. Lucente, M. Giannotti, A. Mirizzi, "Detecting light axions from supernovae in nearby galaxies" [arXiv:2512.04185 [hep-ph]], submitted to Phys. Rev. Lett.

Articles in preparation

(P14) S. Mittal, T. Siegert, F. Calore, P. Carenza, L. Eisenberger, M. Giannotti, A. Lella, A. Mirizzi, D. Tsatsis, H. Yoneda, "Search for Axion-Like Particles from Nearby Pre-Supernova Stars", submitted to A&A Journal.

(P15) A. Lella, G. Lucente, D. Kresse, R. Glas, H.T. Janka, A. Mirizzi, "An analysis of the gravitational wave signals from three-dimensional supernova models", in preparation.

Contents

Introduction

Core-collapse supernovae (CC SNe) are among the most dramatic and complex phenomena known in astrophysics. Such catastrophic events have been recognized long ago as powerful cosmic engines involving many aspects of fundamental physics, ranging from particle interactions and nuclear equation of state to general relativity and hydrodynamics of dense plasmas. SN events mark the endpoint of the evolution of massive stars (with masses $M \gtrsim 8\,M_{\odot}$), happening when their iron can no longer support itself against the gravitational collapse (Burrows and Goshy, 1993; Janka et al., 2007; Janka, 2012; Burrows and Vartanyan, 2021). As the star's inner core undergoes progressive contraction, it may eventually reach the density threshold at which nuclear matter becomes incompressible. Then, the subsequent bounce of the core originates a powerful shock-wave which reverts the implosion into an explosion, ejecting the whole stellar mantle in the interstellar medium. Alongside, the core of the star cools down by emitting the 99% of its energy ($E \sim 10^{53}$ erg) through the release of a tremendous neutrino burst lasting in ~ 10 s, making a SN explosion a real cosmic neutrino factory.

Neutrinos from CC SNe have been observed only once to date, in occasion of the explosion of SN 1987A, which occurred in the Large Magellanic Cloud on the 23$^{\text{rd}}$ February 1987. The detection of the neutrino burst emitted from such an event deserves to be regarded as one of the milestones in particle astrophysics. The most relevant observations of the event come from three different neutrino detectors, namely Kamiokande II (KII) (Hirata et al., 1987; Hirata et al., 1988), which recorded 11 neutrino events, the Irvine-Michigan-Brookhaven (IMB) (Bionta et al., 1987; Bratton et al., 1988), which detected 8, and the Baksan Scintillator Telescope (BUST) (Alekseev et al., 1987), which observed 5 events. Despite the sparseness of data and the correlated large uncertainties, this detection permitted to test many relevant aspects

of the standard SN explosion mechanism, showing good agreement between theoretical predictions and observational evidences (see Fiorillo, Heinlein, et al., 2023 for a recent analysis). In parallel, observations of the SN 1987A neutrino burst have been largely employed to probe the existence of a large variety of exotic feebly-interacting particles emerging in extensions of the Standard Model (SM) of particle physics. Indeed, since the emission of these novel degrees of freedom might be copiously enhanced by the extreme conditions of temperature and density observed in the SN core, they could open an additional cooling channel, shortening the observed duration of the SN 1987A neutrino burst (Raffelt, 1996). This argument has been applied to constrain many Beyond Standard Model (BSM) particles, such as sterile neutrinos (Shi et al., 1994; Raffelt and Zhou, 2011; Carenza, Lucente, et al., 2024), muonic bosons (Caputo et al., 2022a), dark photons (DeRocco et al., 2019), Kaluza-Klein gravitons (Hannestad and Raffelt, 2001), unparticles (Hannestad et al., 2007) and scalars mixed with the Higgs boson (Hardy, Sokolov, et al., 2025).

As it will be extensively discussed in this Thesis, one of the most studied BSM candidates is the elusive axion. The QCD axion is a pseudoscalar particle introduced as a solution of the strong Charge-Parity (CP) problem of Quantum ChromoDynamics (QCD), related to the absence of CP violation in the strong sector of the SM (Peccei and Quinn, 1977b; Peccei and Quinn, 1977a; Weinberg, 1978; Wilczek, 1978). Moreover, the behavior of the axion field under the QCD phase transition makes it a well-motivated candidate for Dark Matter (DM). Besides the QCD axion, different kinds of axion-like particles are predicted in many SM extensions and share similar properties to the QCD axion (Anselm, 1988; Kachru et al., 2003; Conlon, 2006b; Conlon, 2006a; Choi, Kim, and Kim, 2007; Arvanitaki, Dimopoulos, Dubovsky, et al., 2010; Cicoli et al., 2012; Jaeckel and Ringwald, 2010). Nowadays, a wide experimental program is ongoing to probe the existence of these pseudoscalars (Irastorza et al., 2018).

Indirect axion searches through astrophysical probes complement the regions of the axion parameter space investigated by laboratories. In this regard, the analysis of signatures of axions emitted during SN explosions play a crucial role in constraining properties of axions coupled to nucleons. In recent years, the evaluation of axion production in the nuclear medium of the PNS has been the focus of different studies (Carenza et al., 2019; Carenza et al., 2021; Choi et al., 2022; Ho et al., 2023; Springmann et al., 2025), relating the

emission of a potential SN axion burst to various observable signatures. In this context, agreement between observations of SN 1987A neutrinos and the standard picture of SN cooling phase allows one to set stringent constraints on the axion parameter space (Caputo and Raffelt, 2024; Carenza, Giannotti, et al., 2025). Furthermore, if axions are also provided with couplings to photon or leptons, they could give rise to a large variety of gamma-ray signatures. In particular, light axions produced in the SN core can escape the stellar volume unimpeded and then convert in astrophysical magnetic fields (Brockway et al., 1996; Grifols, Masso, and Toldra, 1996; Payez et al., 2015; Hoof et al., 2023). Conversely, heavy axions may efficiently decay in photon or lepton pairs giving rise to time-delayed axion-induced gamma-ray bursts (Jaeckel et al., 2018; Müller et al., 2023b) or affecting the 511 keV annihilation line (Calore et al., 2022b). In this regard, multiwavelength observations of CC SNe across the electromagnetic spectrum serve as valuable tools to investigate axion phenomenology (see, e.g., Müller et al., 2023a; Benabou, Manzari, et al., 2025 for recent works).

The potential of CC SN in constraining non-standard physics is, however, tightly bound to our complete understanding of the complex physical phenomena occurring within the SN interior. In this context, gravitational waves (GWs) emerge as a crucial probe of the dynamics of the stellar interior, offering a complementary window into the SN core to what probed by neutrinos (Kuroda, Kotake, et al., 2017). Indeed, CC SNe are expected to be powerful sources of GWs generated by the anisotropic emission of neutrinos and non-radial flows of matter. In this context, the development of a large variety of multidimensional CC SN simulations extended till few seconds after the core bounce allows a precise characterization of the expected GW signal, relating peculiar features observable in the GW burst to the physical phenomena determining the dynamics of the stellar interior, such as the rising of convective overturns in post-shock layers, the development of Standing Accretion Shock Instabilities (SASI) and the occurrence of PNS oscillations (see, e.g., Vartanyan, Burrows, et al., 2023; Choi, Burrows, et al., 2024 for some recent studies based on a vast catalog of 3D SN simulations). Remarkably, the low-frequency component of the GW spectrum turns out to be detectable by future deci-Hertz interferometers for SN events occurring at extragalactic distances (Mukhopadhyay, Lin, et al., 2022). At the same time, the full GW spectrum is expected to fall well within the sensitivity range of

next-generation GW detectors for Galactic SN events (Choi, Burrows, et al., 2024), opening up the exciting prospect for a multimessenger observation of such events.

In this Thesis work, we explore the potential of CC SNe as laboratories for fundamental physics, focusing on the cosmic messengers described above: axions and GWs. This perspective aims to highlight how the adoption of a multimessenger approach may open new avenues for studying both standard and exotic phenomena taking place in one of the most extreme astrophysical environments known to date.

In Chapter 1 we present a general overview of the main aspects characterizing the physics of CC SNe, focusing on the SN explosion mechanism, the development of SN simulations and analyzing the signals related to the different cosmic messengers released during such powerful events. This Chapter sets the stage for the study of the standard and non-standard physical phenomena explored in following Chapters. In Chapter 2, we introduce the axion as one of the main BSM candidate. We outline the theoretical frameworks in which the axion emerges and present an overview of current bounds in the axion parameter space. In Chapters 3, 4 and 5 we study possible signatures of axions emitted during CC SN events by means of their couplings to nucleons. Specifically, Chapter 3 is devoted to an analysis of the possible impact over the SN neutrino burst, considering both cases of free-streaming axions and axions trapped in the interior of the SN core. Here, we show that observations of the SN cooling phase via neutrino emission places one of the most stringent constraints on the QCD axion mass. In Chapter 4 we discuss signatures triggered by SN axions interacting in ground-based detectors. We focus on the scenario in which axions coupled to nucleons produce signals in water Čherenkov detectors due to their interactions with oxygen nuclei, as well as on the detection prospects for the IAXO experiment in case of axions provided with an additional photon coupling and produced in a future nearby SN. In Chapter 5 we discuss direct and indirect gamma-ray signatures sourced by SN axions. We consider the case of heavy axions ($m_a \gtrsim 1$ MeV), which may decay in photon or leptons pairs leading to various gamma-ray probes, as well as the case of light axions ($m_a \lesssim 10^{-9}$ eV) freely escaping the SN core before being converted in gamma-rays in the Galactic magnetic field. We argue that the possible detection by means of *Fermi*-LAT experiment may shed light on different controversial aspects in relation to the

physics of the PNS. In Chapter 6 we provide a comprehensive analysis of GW signals extracted from two state-of-the-art three dimensional SN simulations produced by `GARCHING` group, never analyzed before. Chapter 7 serves as a counter-example highlighting how CC SNe are not always the best astrophysical environment to constrain some kinds of BSM candidates, showing how cold isolated neutron stars introduce the most stringent astrophysical bound on the parameter space of light scalars with masses $m_\phi \lesssim 1$ MeV. Finally, in Chapter 8 we summarize our results and conclude. The last Chapter is then followed by several appendices dedicated to some technical aspects involved in our work. In particular, in Appendix A we provide explicit expressions for SN axion emission rates via NN bremsstrahlung and pionic processes and describe the axion absorption processes in the trapping regime. In Appendix B we detail the computation for the axion-oxygen cross section for axions interacting in water Čherenkov detectors. In Appendix C we study the interplay between the QCD axion and ALPs coupled the content of the strong sector of the SM. Finally, in Appendix D we report parameters for the fitting expressions of axion emission spectra introduced in Chapter 5.

Chapter 1

Cosmic messengers from core-collapse Supernovae

In this Chapter we present an overview of the main physical aspects characterizing core-collapse supernovae (CC SNe), necessary to set the framework for the investigation of standard and exotic signals released in such powerful events. In particular, Sec. 1.1 briefly outlines the main stages of stellar evolution with a particular focus on the case of massive stars ($\mathcal{M} \gtrsim 8$ M$_\odot$). Phases of stellar evolution are described until reaching the onset of the gravitational collapse, leading to a supernova explosion, which is described in details in Sec. 1.2. Sec. 1.3 traces the development of supernova simulations, starting from pioneering works based on one-dimensional simulations to the state-of-the-art three-dimensional simulations. Sec. 1.4 is dedicated to a description of the main observable signals from supernova events. Specifically, Sec. 1.4.1 focuses on the SN neutrino burst with an insight on the groundbreaking detection of the SN 1987A neutrinos in Sec. 1.4.2. Furthermore, Sec. 1.4.3 describes the main characteristics of the predicted CC SN gravitation-wave signal. Finally, in Sec. 1.4.4 we discuss the possible emission of exotic light feebly-interacting particles (with mass $\lesssim 1$ MeV) from core-collapse supernovae.

1.1 Life and Death of massive stars

Stars are formed from hot and dense clouds of gas bound together by gravity. The system would loose energy via photons produced in collisions between electrons and protons. As energy is lost, the cloud becomes more tightly bound and the temperature increases towards values which could trigger hydrogen ignition. Hydrogen burning leads to the release of 26.73 MeV of energy, partially carried away by neutrino emission, and leaves helium as final product. This injection of energy counterbalances attractive gravitational pressure, resulting in a final stable configuration. Star masses could span a wide range of values between $0.08 - 100$ $M_\odot$ (Raffelt, 1996). Lower-mass clouds never reach temperatures high enough to trigger the nuclear fusion, giving rise to clump of gases similar to gaseous planets, commonly known as brown dwarfs.

Life and death of stars is determined, in first approximation, by a single parameter: their initial mass. The majority of them spends almost all of their life in the *main sequence* (MS) phase, burning hydrogen into helium in the stellar core. Typically, a 1 $M_\odot$ star lives about 10 Gyr on the main sequence. Since the luminosity of a star of mass $\mathcal{M}$ goes roughly as $\mathcal{L} \sim \mathcal{M}^3$, heavier stars burn brighter and their life is shorter. Thus, given the age of the Universe, stars with masses $\mathcal{M} \lesssim 0.7 - 0.8$ $M_\odot$ formed soon after the Big Bang have not completed the MS phase yet, while heavier stars show more advanced evolutionary stages.

As long as hydrogen is burnt, helium ashes start to accumulate in the hot and dense stellar core. When hydrogen is completely depleted in the center, the system reaches a new stable configuration composed by a denser helium core surrounded by a shell of burning hydrogen. In this phase, the envelope of the star expands and the surface temperature decreases as established by the Stefan-Boltzmann law, thus the star becomes a red giant (RG). Meanwhile, more and more helium is accumulated in the core, and when density increases enough electrons become degenerate. Then, the degenerate helium core shrinks and the electron degeneracy pressure is increased, as well as the gravitation potential at the edge of the helium core. Therefore the hydrogen burning shell becomes hotter and the star more luminous.

While remaining in the *red giant branch* (RGB), the helium core accretes its mass till temperature becomes high enough to ignite helium via an almost

explosive process, commonly known as "helium flash". Energy released in the helium flash rapidly expands the core reducing the overall luminosity of the star. On the contrary, the envelope shrinks and the star appears bluer. The final configuration, consisting of a helium burning core surrounded by a hydrogen burning shell, is called *horizontal branch* star since it evolves at constant luminosity. When also helium is exhausted, we observe the formation of a degenerate carbon-oxygen (CO) core surrounded by shells of burning helium and hydrogen. Similarly to the RG phase, the envelope inflates and the star enters the *asymptotic-giant branch* (AGB).

The following evolutionary stages strictly depend on the star mass. In low mass stars ($\mathcal{M} \lesssim 2-3$ M$_\odot$) carbon and oxygen never ignite, thus they progressively eject their mantle leaving a carbon-oxygen White Dwarf (WD), a remnant of typical density $\rho \sim 10^6$ g cm^{-3} cooling via neutrino emission. On the contrary, massive stars ($\mathcal{M} \gtrsim 6-8$ M$_\odot$) can reach temperatures high enough to trigger carbon and oxygen burning. This is possible since, despite all possible losses, high-mass stars are left with CO cores massive enough to grow close to their Chandrasekhar limit, namely the maximum mass that can be supported by electron degeneracy pressure, where densities are so high to induce carbon ignition. After that, ashes of carbon burning, namely oxygen, neon, magnesium and silicon, accumulate in a degenerate core, which subsequently ignites neon burning, and so forth. Finally, silicon burning, which lasts just for a few days, produces a degenerate iron core. This core is surrounded by an onion-like structure made up of burning shells of lighter elements formed during previous evolutionary stages, as shown in Fig. 1.1. Since the synthesis of iron and heavier elements would produce a negative energetic feedback on the system, the central core cannot be further burnt. The temperature is at $T \simeq 0.8 \times 10^{10}$ K$= 0.7$ MeV, the density at $\rho \simeq 3 \times 10^9$ g cm^{-3}, and there are about $Y_e = 0.42$ electrons per baryon. At this stage, the only effect which can counterbalance gravitational contraction is electron degeneracy pressure. Nevertheless, electron captures on nuclei reduce the electron fraction and the electron Fermi momentum, lowering the Pauli pressure. In parallel, the contraction of the core enhances photodissociation of iron, which subtracts further energy from the center. The iron core is able to accrete mass till reaching its Chandrasekhar limit at $\mathcal{M} \sim 1.44$ M$_\odot$. Then, electron degeneracy pressure cannot counterbalance gravity anymore, resulting in the onset of the gravitational collapse, which is the first step

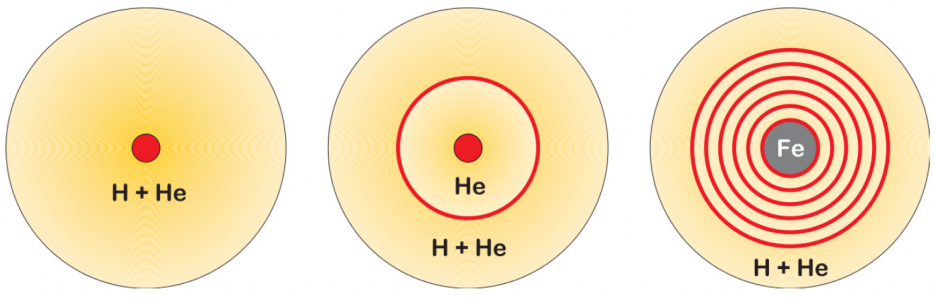

Figure 1.1: Stages of the stellar evolution. *Left*: hydrogen fusion in the stellar core. *Center*: helium-burning phase with a hydrogen burning shell. *Right*: onion-like shell structure of a massive star with an iron core and shells of lighter elements formed during the different evolutionary stages.

towards a *core-collapse* (CC) *supernova* (SN) explosion.

1.2 The supernova explosion mechanism

Core-collapse SNe are the terminal phase of massive stars, which develop electron-degenerate iron cores at the end of their life. Shells of burning elements tend to accrete the iron core mass till electron degeneracy pressure is not able to contrast gravitational pressure anymore, giving rise to the onset of the gravitational collapse. The contraction of the core proceeds until protons and neutrons in the iron core become degenerate themselves. Then, when the inner core reaches the nuclear saturation density at $\rho \sim 10^{14}$ g cm^{-3}, nuclear matter becomes incompressible and the core bounces back, generating a shock-wave which converts the implosion into an explosion. The sound pressure carried by the shock wave ejects the stellar mantle, causing the release of elements as oxygen, carbon, magnesium, silicon, calcium, sulphur and nichel in the interstellar medium. A successful SN explosion event leaves as a remnant a young and hot neutron star (NS), cooling via the emission of neutrinos. Typical values for the NS radius and mass are $r \sim 10$ km and a mass $\mathcal{M} \sim 1-2$ M$_\odot$, depending on the stiffness of the equation of state (EoS) describing nuclear matter.

Hardly the physical description of any other astrophysical event can be considered as complex as the one required for CC SNe. Notably, dynamics of

plasmas in a strong gravitational field gives birth to the event and set the stage for the occurrence of a successful explosion, weak interactions govern the transport of the huge amount of neutrinos emitted, electromagnetic and strong interactions determine the thermodynamics of the nuclear medium, and nuclear and weak interactions change the composition of the stellar plasma. Nowadays, the physical processes involved in the SN explosion mechanism can be tracked by employing complex large-scale numerical simulations taking into account the hydrodynamics of stellar plasmas, the nuclear EoS, neutrino transport equations and progenitor conditions. Despite the outcomes of a SN simulation directly depend on input conditions and some of the details of the explosion mechanism are still under investigation, experts agree that six main phases can be recognized (Janka et al., 2007). These are schematically depicted in Fig. 1.2 and described in details below.

- *Initial phase of collapse* (post-bounce time $t_{\rm pb} \sim 0$). The initial phases of collapse are sensitive to the entropy and to the electron fraction Y_e (Bethe, Brown, Applegate, et al., 1979). In particular, in the early stages, Y_e is rapidly decreased due to electron captures ($e^- + p \rightarrow n + \nu_e$) on nuclei (Fe peak), which are energetically favorable for degenerate electrons with Fermi momentum of few MeV. This phenomenon reduces electron degeneracy pressure and favors the neutronization of nuclear matter. Then, neutron-rich nuclei are subject to efficient β-decays which release additional energy. In addition, temperatures in the core are high enough to allow for the photodisintegration of the iron group to α particles ($\gamma + {}^{56}\mathrm{Fe} \rightarrow 13\alpha + 4n$). All of these processes take part in subtracting energy from the core and decreasing the electron fraction, thus accelerating the gravitational collapse.

- *Neutrino trapping* ($t_{\rm pb} \sim 0.1$ s). When the nuclear density reaches $\rho \approx 10^{12}\,\mathrm{g\,cm^{-3}}$, an important change in the physics of the collapse occurs. Indeed, due to coherent scattering on nuclei, the neutrino diffusion time becomes longer than the collapse time, trapping neutrinos in the densest region of the core (Bethe, 1990). Thus, the electron fraction Y_e is nearly conserved at the value reached at the time of trapping. Under these conditions, β-decays create a sea of degenerate electron neutrinos ν_e. In this phase, due to the lower compressibility of nuclear matter, the collapse of the inner region of the core with $R_{\rm hc} \approx 100$ km

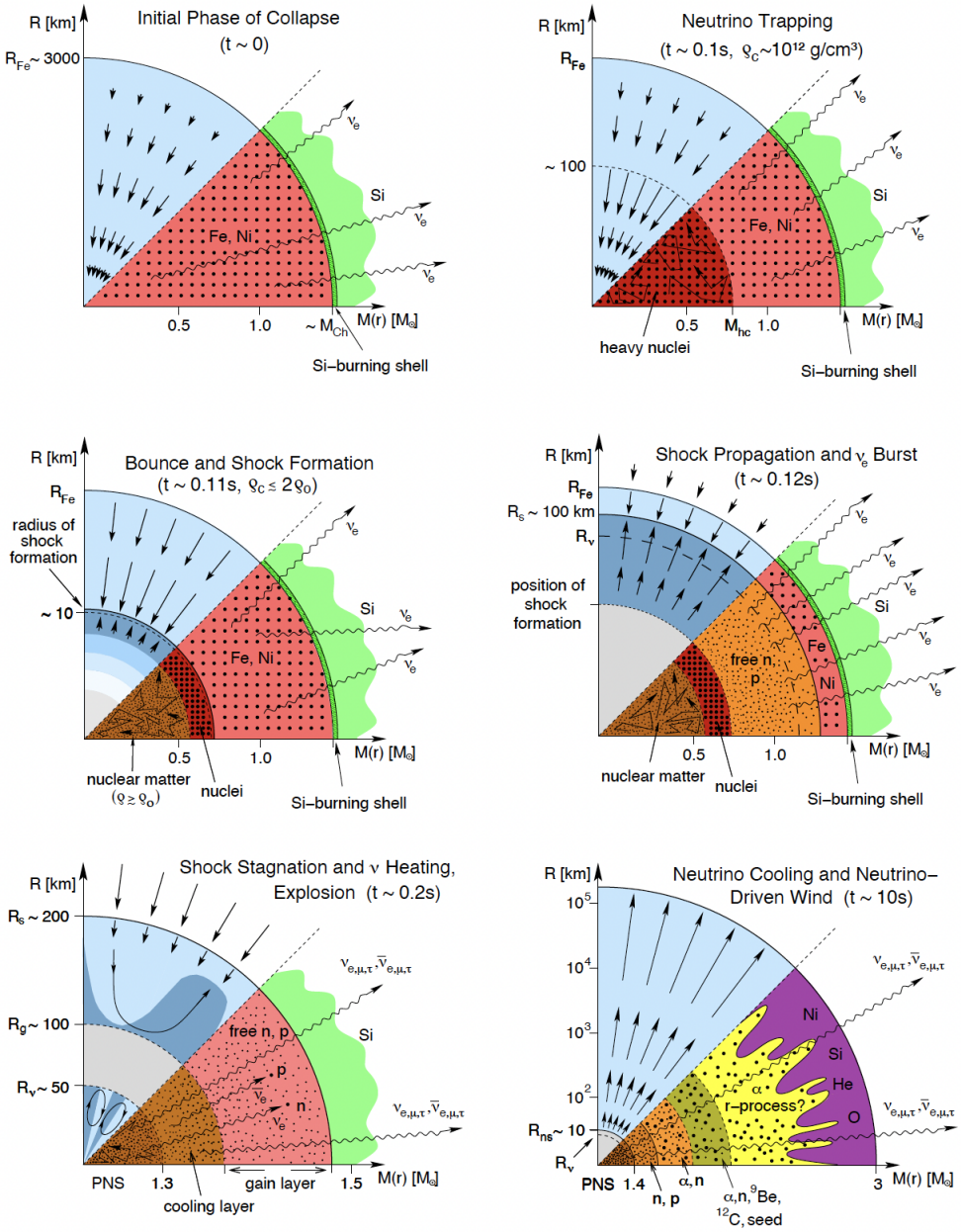

Figure 1.2: Schematic representation of the six different stages characterizing stellar core collapse. The upper half of the panels displays the dynamical conditions, with arrows representing velocity vectors. The nuclear composition and the nuclear and weak processes involved are indicated in the lower half of each panel. Figure taken from Janka et al., 2007.

proceeds "homologously" at subsonic velocity (Goldreich et al., 1980), while the outer layers keep collapsing at supersonic speed.

- *Bounce and shock formation* ($t_{\rm pb} \sim 0.11$ s). The collapse of the homologous core continues until nuclear saturation density is reached $\rho \approx 10^{14}$ g cm^{-3}. Then matter becomes highly incompressible and the collapse decelerate until it stops. Meanwhile, outer layers keep falling inwards, so that the homologous core bounces in response to the increased nuclear matter pressure. This bounce generates a shock wave which starts propagating into the outer core, converting the gravitational collapse into an explosion.

- *Shock propagation and neutronization* ($t_{\rm pb} \sim 0.12$ s). Along its propagation in the outer core, the shock wave loses almost all of its energy by dissociating heavy nuclei. In this regard, all SN simulations agree that the simple core bounce is not able to store enough energy in the shock wave to allow for the ejection of the outer burning shells of the star. This rules out the *prompt explosion* mechanism (Colgate and Johnson, 1960), in which the shock-wave ejection of the mantle takes place in a single step. Layers crossed by the shock front are then characterized by an increased fraction of free protons, leading to a strong enhancement of electron captures. These processes induce further neutronization of nuclear matter and produce a huge amount of electron neutrinos. Since they are produced from regions just behind the shock front, where neutrinos are not trapped, they can quiclky leave the star unimpeded in the so-called "prompt ν_e burst", releasing about 10^{51} erg of energy.

- *Shock stagnation and ν heating* ($t_{\rm pb} \sim 0.2$ s). Along its path in the outer core, the shock wave is significantly weakened by heavy-nuclei dissociation and, eventually, it stalls at a distance $100 - 200$ km from the SN core. While the shock wave is stalled, matter keeps falling inwards from the outer layers and accretes on the compact object at the center of the star. During this phase, infalling matter powers the emission of neutrinos of all species. The nascent compact object at the center is usually called proto-neutron star (PNS), since it is the progenitor of the remnant left by the explosion event. In particular, this remnant would consist in a NS if the shock will resume its motion and the progenitor

star is lighter than ~ 25 $M_\odot$, or a black hole otherwise. Indeed, without any mechanism revitalizing the shock-wave motion, the SN would eventually recollapse into itself. At this stage, neutrinos emitted from the PNS play a crucial role. Indeed, despite being trapped in the inner regions of the PNS, their emission can occur from a last-scattering surface dubbed *neutrino-sphere*. Neutrino emission is the major cooling channel for CC SNe, releasing $\sim 99\%$ of the energy set free by the gravitational collapse of the stellar core, about $\sim 10^{53}$ erg (Burrows, 1990). Part of this energy can be deposited behind the shock front, via processes as $n + \nu_e \to p + e^-$ and $p + \bar{\nu}_e \to n + e^+$. The neutrino heating increases the pressure behind the shock and the heated layers begin to expand, creating a zone of low density and high temperature between the PNS and the shock-wave front, the so-called "hot bubble" (Colgate, 1989). The high pressure revitalizes the shock wave, eventually leading to a SN explosion. This is the so-called "delayed explosion scenario" (Bethe and Wilson, 1985; Wilson et al., 1986). Moreover, the neutrino heating is more effective at ~ 100 km around the gain layer, defined as the surface where the neutrino heating rate equals the neutrino cooling rate. This generates a negative entropy gradient (Colgate, Herant, et al., 1993; Janka, 2025), which induces the development of violent convective overturns. Convective instabilities may eventually cause dynamical deformations of the shock front, known as standing accretion shock instability (SASI) (Blondin, Mezzacappa, et al., 2003). All of this kind of hydrodynamical instabilities favor neutrino energy deposition behind the shock front, helping the shock wave to resume its motion.

- *Neutrino cooling and neutrino-driven wind* ($t_{\rm pb} \sim 10$ s). After the neutrino shock revival, the shock wave ejects the outer layers of the star in the so-called "neutrino driven wind". Then, after about $0.5 - 1$ s the PNS has a radius $R \approx 20$ km and behaves as a black-body which cools via the emission of (anti)neutrino of all flavors. After $5 - 10$ s the star has lost essentially all of its energy. This is the so-called "Kelvin-Helmotz cooling phase".

1.3 From one- to three-dimensional simulations

The exceptional complexity of a quantitative description of the SN explosion mechanism lies in a self-consistent treatment of all the various physical aspects involved. Hydrostatic equilibrium of the stellar structure, a detailed treatment of nuclear physics, changing in the chemical compositions of the stellar gas, neutrino transport and hydrodynamics of dense plasmas are all crucial ingredients to properly account for in order to achieve a complete description of a CC SN event. The subtle interplay between these aspects impose the development of sophisticated numerical codes to simulate the sequence of events that can eventually lead to a successful SN explosion (see, e.g., Fischer, Whitehouse, et al., 2009; Fischer et al., 2010; Hudepohl et al., 2010). The first attempts to apply the theory developed for the delayed-explosion scenario to consistent one-dimensional (1D) (i.e., spherically-symmetric) numerical simulations have been performed during the early 1980s by the Livermore group (see, e.g., Wilson, 1974; Tubbs et al., 1979; Bethe, Brown, Cooperstein, et al., 1983; Bethe and Wilson, 1985; Wilson et al., 1986; Mayle, Wilson, and Schramm, 1986 and Bethe, 1990 for a review of pioneering works). These models have been recognized to be too simplistic, concerning the hydrodynamics scheme or resolution, the limited treatment of the neutrino transport, and the lack of relevant neutrino energy transport processes. Significant improvements were subsequently achieved, including general-relativistic effects, a more complete set of neutrino scattering interactions and refined hydrodynamics and neutrino-transport codes. However, even after these improvements, self-consistent explosions were obtained only for low-mass SN progenitors with mass $\mathcal{M} \lesssim 10\ \mathrm{M}_\odot$ (see Fischer et al., 2010; Hudepohl et al., 2010). For massive progenitors with mass $\mathcal{M} \gtrsim 10\ \mathrm{M}_\odot$, explosions had to be artificially triggered by enhancing the neutrino energy deposition behind the shock wave.

A further breakthrough was achieved with the advent of first multidimensional (multi-D) SN simulations taking into account Rayleigh-Taylor instability, i.e. the mixing of fluids at difference densities at the interfaces of shells. Initially, these simulations were mostly constrained to two spatial dimensions [2D, i.e., axisymmetric (Chevalier et al., 1978; Kane et al., 1997; Ebisuzaki et al., 1989; Benz et al., 1990; Fryxell, Mueller, et al., 1991; Müller, Fryxell, et al., 1991; Herant et al., 1991; Herant et al., 1992)]. It soon became clear that

a multi-D treatment of the core of the collapsed star was necessary to trigger a self-consistent explosion. Indeed, 2D hydrodynamic simulations demonstrated the development of strong convective overturns in the gain layer, between the shock front and and the gain radius, where neutrino absorption dominates neutrino cooling. The related efficient energy transfer generates a negative entropy gradient (Janka, 2025), which triggers non-radial mass motions. In this regard, the inclusion of postshock convection was shown to lower the critical neutrino luminosity required to resume the motion of the stalled shock compared to the case of 1D simulations. In particular, material heated by neutrinos close to the gain layer could rise in buoyant plumes, pushing the stagnant shock to larger radii. In parallel, convection in the gain layer gives rise to downflows of matter carrying low-entropy matter close to the gain radius, where it can be subsequently heated by neutrinos. Furthermore, highly time-dependent postshock flows have a direct impact on the shock evolution through the imprint of SASI (Blondin, Mezzacappa, et al., 2003; Foglizzo, Galletti, et al., 2007a). It is a global, non-radial instability of the stalled accretion shock whose effects could be amplified when favorable growth conditions are met. SASI activity could trigger secondary post-shock convection, which could support shock expansion and neutrino energy transport. Moreover, the employment of multi-D simulations showed that ejecta are characterized by a clearly asymmetric configuration, matching the observations of material surrounding SN remnants.

The last 30 years have seen increasing effort of the astrophysics community in developing sophisticated multi-D SN simulations, bridging the gap between the two- and the three-dimensional (3D) treatment, which is far more computationally expensive. Nowadays, SN simulations employ an elaborate neutrino transport treatment, tracking Boltzman neutrino hydrodynamic equations completely in 3D starting from progenitor structures shortly earlier than the pre-collapse stage, following the collapse of degenerate cores, and lasting deep in the SN cooling phase (see Janka, 2025; Burrows and Vartanyan, 2021 for recent reviews on long-term simulations). These simulations include the state-of-the-art microphysics, i.e. accurate neutrino reaction rates, EoS of the stellar plasma and a treatment for the changing nuclear composition of the core. In this regard, the impressive progresses achieved in this area have begun to link physics of stellar progenitors and their explosion by employing multi-D modeling on both sides. As an exemplary case,

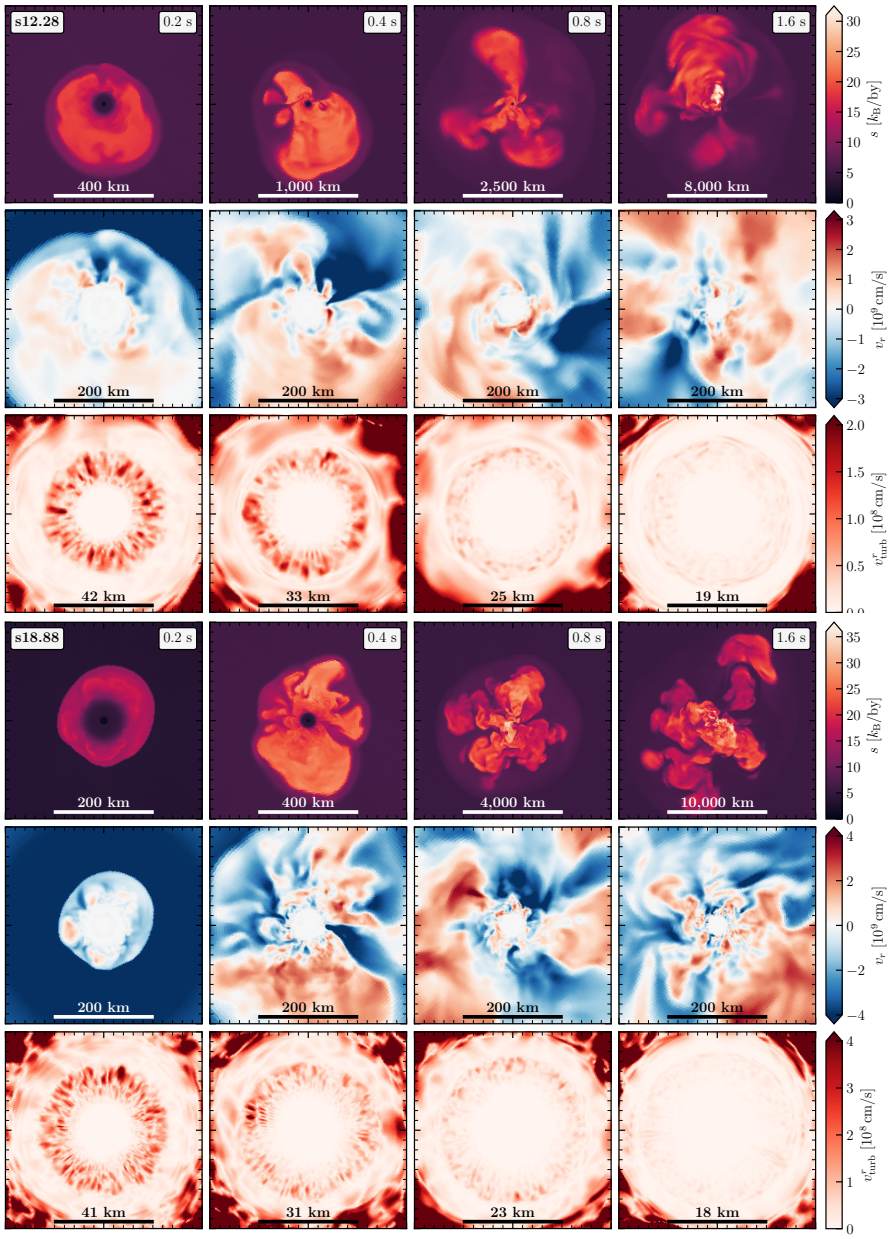

Figure 1.3: Cross-sectional renderings at different post-bounce snapshots of some of the hydrodynamics properties of the two 3D SN models produced by `Garching` group and employed in this Thesis work (see Janka, 2025, for a review). In particular, isocontours of specific entropy (*top*), radial fluid velocity (*middle*) and turbulent radial velocity inside the PNS (*bottom*) are shown. Figures courtesy of Daniel Kresse.

in Fig. 1.3 we report cross-sectional cuts of 3D renderings of some hydrodynamical properties referring to the two 3D SN models developed by GARCHING group and employed in this Thesis work. For these models, the Newtonian hydrodynamics equations are solved by the PROMETHEUS hydrodynamics module (Fryxell, Müller, et al., 1989; Kifonidis et al., 2003) and the energy and velocity dependent three-flavor neutrino transport is solved by the VERTEX transport module (Rampp et al., 2002). Moreover both models employ a post-Newtonian treatment of gravity. The s12.28 simulation, already used in Janka and Kresse, 2024, was launched from a 12.28 $M_{\odot}$ (Sukhbold et al., 2018; Yadav, 2023) progenitor and it was evolved with the EoS of Lattimer and Swesty (Lattimer et al., 1991). On the other hand, the s18.88 simulation is evolved from a 18.88 $M_{\odot}$ progenitor and the SFHo EoS (Hempel, Fischer, et al., 2012; Steiner et al., 2013) was used, leading to the results reported in (Bollig, Yadav, et al., 2021; Janka and Kresse, 2024). For both the models, asymmetric initial conditions of the density, velocity field, and chemical composition were self-consistently generated by simulating in 3D the final evolution period before the core-collapse (seven minutes for s18.88 and one hour for s12.28) (Yadav et al., 2019).

Furthermore, most recent simulations extend till ~ 10 s after the core bounce, which has been out of reach of self-consistent multi-D simulations until recently (Burrows and Vartanyan, 2021; Janka, 2025). Remarkably, these allow one to follow the evolution of the stellar explosion until nucleosynthesis from nuclear statistical equilibrium and nuclear burning is completed, defining some of the birth properties of compact remnants of the SN explosion. This makes possible a direct comparison between simulation outcomes and observational evidences of SN events and their remnants.

1.4 Signals from supernovae

Multi-D simulations not only progressively improved the description of the neutrino-driven mechanism, but they have also improved predictions for other signals originating from CC SNe. In the following, we review the main signals expected from a future SN event, namely the neutrino burst, gravitational waves (GWs) and, eventually, flows of exotic feebly interacting particles (FIPs). For illustrative purposes, a schematic representation of multi-

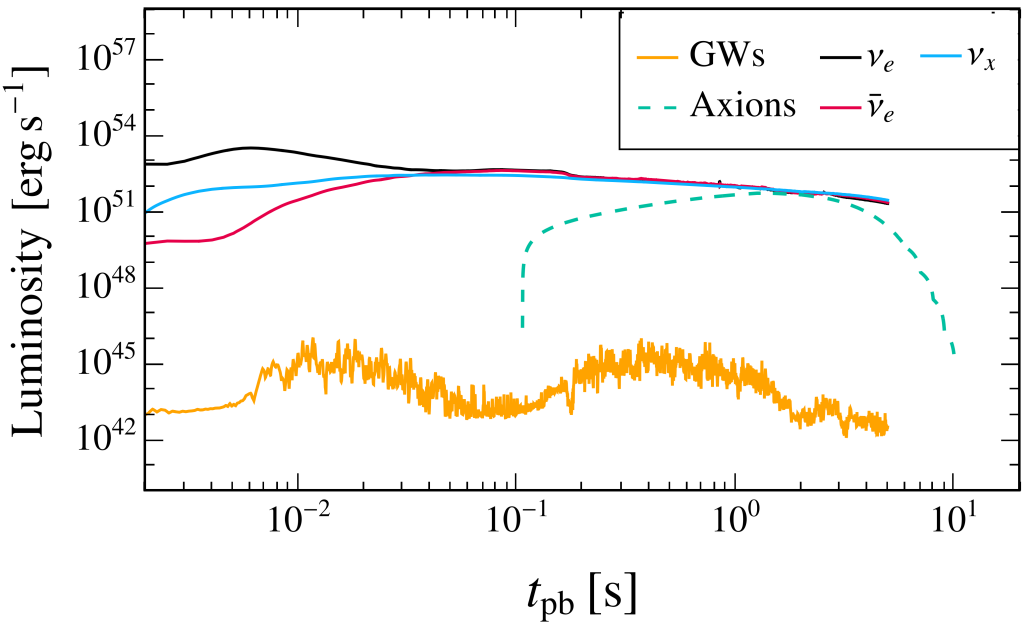

Figure 1.4: Energy per unit time (in erg s^{-1}) emitted in different messengers from a CC SNe. Spherically averaged neutrino signals and the GW signal are derived from the 3D s12.28 `GARCHING` group SN model (Janka, 2025). As an exemplary scenario for FIP emission, we consider the SN axion flux, which is computed by employing the unperturbed 1D SFHo-s18.8 `GARCHING` group SN profile (*Garching core-collapse supernova research archive* n.d.).

messenger signals from CC SNe, based on SN simulations employed in this Thesis work, is provided in Fig. 1.4. These results suggest that a SN is an exceptional laboratory to develop multi-messenger astrophysics, combining the different signals produced during such catastrophic events.

1.4.1 The supernova neutrino signal

Neutrinos are the most relevant messenger from CC SN events. The $\sim 99\%$ of the total gravitational binding energy $E_{\rm B}$ stored in the PNS is emitted in a neutrino burst lasting ~ 10 s. The details of the evolution of the SN neutrino signal are deduced directly from simulations. Nevertheless, some of the main features can be inferred on the basis of simple physical arguments (Raffelt, 1996). Assuming the PNS to be approximated by a sphere, the binding

energy is given by (Burrows, 1990; Raffelt, 1996)

$$E_{\rm B} \approx \frac{3}{5}\frac{G_N\,\mathcal{M}^2}{R} \approx 3\times 10^{53}\,{\rm erg}\left(\frac{\mathcal{M}}{1.4\ {\rm M}_\odot}\right)^2\left(\frac{10\,{\rm km}}{R}\right)\,. \tag{1.1}$$

Therefore, if one assumes equipartition of energy among the six different neutrino flavors, we end up with a neutrino luminosity $L_\nu \sim 10^{52}$ erg s^{-1} for each neutrino species. As discussed in Sec. 1.2, neutrinos are trapped in the interior of the PNS. Therefore, during the cooling phase their emission occurs from a last-scattering surface commonly dubbed *neutrino-sphere* at radius $R_\nu \approx 15$ km. Since the neutrino emission from the neutrino-sphere is a (quasi-)thermal process, the ν spectrum can be approximated by a blackbody spectrum with average energy $\langle E_\nu\rangle$ set by the temperature of the neutrino sphere T_ν. Once again, the average neutrino energy can be estimated through simple physical principles. Indeed, neutrinos produced in nucleon scattering carry away the average nucleon kinetic energy, which can be evaluated by employing the virial theorem. In particular, a nucleon in thermal equilibrium on the neutrino-sphere surface is provided with a kinetic energy which is half of its gravitational binding energy $2\,\langle E_{\rm kin}\rangle \approx G_N\mathcal{M}m_N/R_\nu$, where m_N is the nucleon mass and G_N is the Newton's gravitational constant. Thus, with a typical NS mass $\mathcal{M} = 1.4$ M$_\odot$, one finds $\langle E_{\rm kin}\rangle \approx 25$ MeV and a neutrino-sphere temperature $T_\nu \approx 17$ MeV. Analogously, the duration of the neutrino burst is expected to be a multiple of the neutrino diffusion time-scale $t_{\rm diff}$ within the PNS

$$t_{\rm diff} \approx \frac{R^2}{\lambda_\nu}\,, \tag{1.2}$$

where λ_ν is the neutrino mean free path in the nuclear medium of the SN core. Given the typical neutrino scattering cross section over non-relativistic nucleons $\sigma \simeq 10^{-42}$ cm$^2\,(E_\nu/10$ MeV$)^2$ and the typical specific density of baryons in the PNS $n_B \sim 10^{38}$ cm^{-3}, one obtains a neutrino mean free path $\lambda_\nu \approx (n_B\,\sigma)^{-1} \sim 10$ m. This value corresponds to a typical diffusion time-scale $t_{\rm diff} \sim \mathcal{O}(10)$ s, which is a good estimation of the duration of the burst. These rough estimations can be compared to the outcomes of SN simulations. In this Thesis work, we adopt as benchmark model the 1D spherically-symmetric `GARCHING` group's SN model SFHo-s18.8 provided in Ref. *Garching core-collapse supernova research archive* n.d. and based on the neutrino-hydrodynamics code `PROMETHEUS-VERTEX` (Rampp et al., 2002). The code takes into account all neutrino reactions identified as relevant for core-collapse

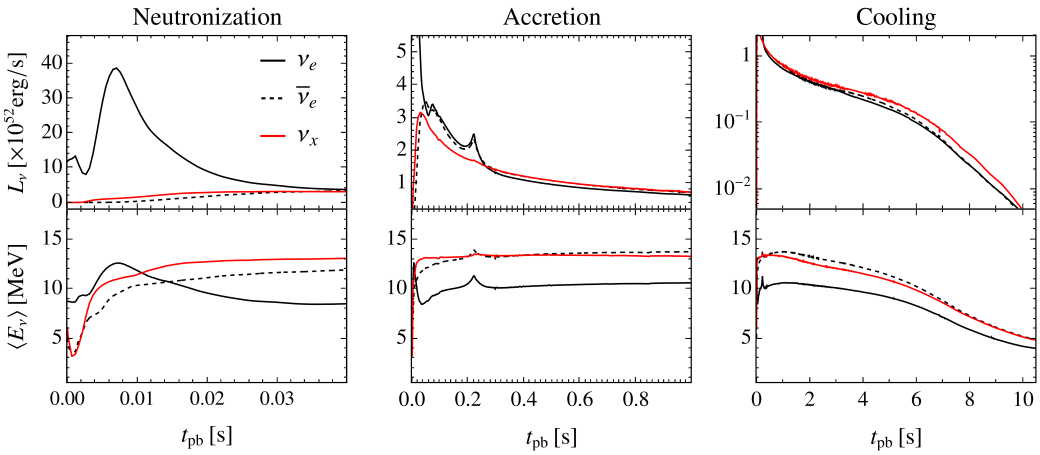

Figure 1.5: Different stages of neutrino emission. Data refers to the 1D spherically-symmetric `GARCHING` group's SN model SFHo-s18.8 provided in the *Garching core-collapse supernova research archive* n.d.

SNe (Buras et al., 2006; Janka, 2012; Bollig, Janka, et al., 2017) and includes a 1D treatment of PNS convection via mixing-length theory, convective fluxes (Mirizzi et al., 2016) and muonic physics (Bollig, Janka, et al., 2017). The simulation employs the SFHo EoS (Hempel and Schaffner-Bielich, 2010; Steiner et al., 2013) and is launched from a stellar progenitor with mass 18.8 $M_\odot$ (Sukhbold et al., 2018), leading to NS with baryonic mass 1.35 $M_\odot$. We recall that in this simulation the explosion is triggered artificially. Fig. 1.5 shows the SN neutrino signal obtained from this model. In general, details of the neutrino light curves depends on many different inputs, as nuclear physics, the EoS employed in the simulation and the final NS mass (see Lucente, Heinlein, et al., 2024 for simple fitting expressions for cooling neutrino light curves from a vast ensemble of SN models). However, the SN neutrino burst from all simulations always shows three main phases of emission, that we discuss below.

- *Neutronization burst* ($t_{\rm pb} \sim 0 - 40\,$ms, left panel). As discussed in Section 1.2 the stellar collapse is triggered by a prompt reduction of the electron degeneracy pressure, induced by electron captures on protons in heavy nuclei $e^- + p \to n + \nu_e$, resulting into a strong neutronization of nuclear matter. This process produces a strong enhancement in the ν_e luminosity and mean energy, as shown in the left panel of Fig. 1.5.

As matter becomes more compressed due to the ongoing gravitational collapse, this process becomes more efficient. During this phase, lasting in only $\sim 20\,\mathrm{ms}$, an amount of energy of about $10^{51}\,\mathrm{erg}$ is taken away by electron neutrinos. This phase of emission is largely independent of the progenitor mass and EoS and it continues until density becomes so high that neutrinos are not able to escape the SN core anymore.

- *Accretion phase* ($t_{\mathrm{pb}} \sim 50 - 300\,\mathrm{ms}$, left panel). This phase is characterized by the the stall of the shock wave which has lost most of its energy and it stalls at a distance $100 - 200$ km from the center of the star. While the shock wave is stalled, neutrino fluxes are powered by plumes of matter falling onto the core. This process enhances charged currents reactions $n + e^+ \rightarrow \bar{\nu}_e + p$ and $p + e^- \rightarrow \nu_e + n$. Other species production is confined in the inner regions of the PNS, where the density is high enough to allow an efficient pair production, as $e^+ + e^- \rightarrow \nu + \bar{\nu}$. During the accretion phase, electron-neutrino mean energy $\langle E_{\nu_e} \rangle$ is typically lower than the one observed for other electron antineutrinos $\langle E_{\bar{\nu}_e} \rangle$ and for other species $\langle E_{\nu_x} \rangle$ ($x = \mu, \tau$), due to the different processes experienced when interacting with matter. Indeed, while electron (anti-)neutrinos can interact with the thermal bath via neutral and charged current processes as $\nu_e + n \rightarrow p + e^-$ and $\overline{\nu}_e + p \rightarrow n + e^+$, these scattering channels are less efficient for muon and tauon (anti-)neutrinos because of the mass of muons and tauons. Therefore, they are able to decouple in inner regions of the star, where temperature, and thus the average neutrino energy, is higher. Analogously, also the average energy of electron antineutrinos is higher than electron neutrinos, since they menage to decouple from nuclear matter at inner regions of the PNS due to the lower abundance of protons compared to neutrons. This phase strongly depends on the progenitor mass and the EoS employed, because mass accretion flows and the chemical composition of the core play a crucial role.

- *Cooling phase* ($t_{\mathrm{pb}} \sim 0.5 - 10\,\mathrm{s}$, left panel). Once the shock wave is revitalized by neutrino heating process and hydrodynamical instabilities (see Section 1.2) and has resumed its motion, the PNS cools via neutrino emission. Starting from $0.5 - 1$ s the PNS enters the Kelvin-Helmotz cooling phase, where the the stellar-core energy is released via

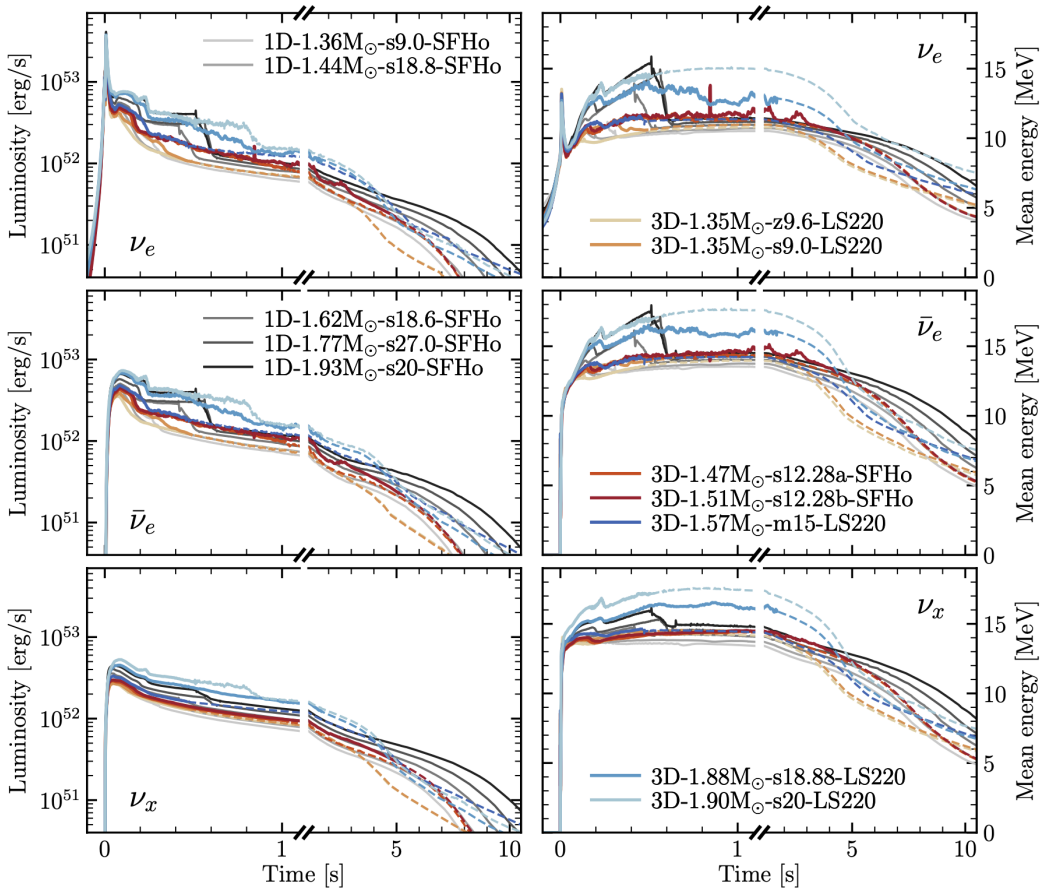

Figure 1.6: Time evolution of laboratory frame luminosities (*left panel*) and mean energies (*right panels*) for different neutrino species. Different colors depict outcomes from a wide set of 1D and 3D SN simulations by `GARCHING` group, differing for the progenitor mass, the final baryonic NS mass and the EoS employed. Figure taken from Janka, 2025.

neutrinos of all flavors with typical luminosities $L_\nu \sim 10^{52}$ erg s^{-1}. As the PNS cools down, also neutrino mean energies are decreased.

Neutrino signals in 3D simulations

Passing from 1D to 3D models, neutrino luminosities and mean energies show a clear angular dependence. The neutrino signal during the accretion phase is characterized by strong anisotropy. Indeed, non-radial flows of matter induce a dynamical deformation of the shock front and seed anisotropies

in accretion rates onto the PNS, naturally affecting the corresponding neutrino emission rate. Moreover, at given observation angle, convection and SASI modes can impose a peculiar imprint on the time evolution of the neutrino signal. In particular, while convection leads to small-amplitude, high-frequency ($\gtrsim 100\,\mathrm{Hz}$) fluctuations in neutrino mean energies and luminosities, SASI sloshing and spiral modes create a quasi-periodic modulation with bigger amplitudes (up to 10-20% of neutrino luminosities) but at lower frequencies $\lesssim 100\,\mathrm{Hz}$, since expansion and contraction phases in SASI phenomena imply time-dependent variations in the mass accretion flows towards the PNS (Tamborra, Hanke, et al., 2013; Tamborra, Raffelt, et al., 2014). Fig. 1.6 compares neutrino light-curves derived from various 1D and 3D `GARCHING` group SN simulations. In particular, neutrino signals and mean energies from 3D models are obtained by averaging over the solid angle in the simulation reference frame. We observe that 3D models show time modulation in neutrino signals due to imprints of accretion instabilities at $t_{\mathrm{pb}} < 1$ s. Interestingly, the measurements of neutrino events from a future Galactic SN by large underground neutrino detectors, like IceCube (Aartsen et al., 2017) and the planned Hyper-Kamiokande (Abe et al., 2018), will well be able to point out the presence of these modulations, providing a significant test of our purely-theoretical picture of shock dynamics (Lund, Marek, et al., 2010; Lund, Wongwathanarat, et al., 2012; Tamborra, Hanke, et al., 2013; Tamborra, Raffelt, et al., 2014). Furthermore, Fig. 1.6 illustrates that when the phase of massive PNS accretion before and after the onset of the explosion is over, properties of neutrino signal from 1D models asymptotically mimic the ones obtained from 3D models (Janka, 2025). On the other hand, major differences are visible at the end of the accretion phase. Indeed, in 1D simulations accretion ends quite abruptly when the explosion is artificially triggered and neutrino luminosities decline sharply from the accretion plateau. Conversely, in 3D simulations traces of mass accretion can still be present for several seconds after the shock expansion. Therefore, neutrino luminosities and mean energies decrease less steeply than in the 1D case.

1.4.2 Neutrino signal from SN 1987A: data and interpretations

CC SNe are rare events. The expected event rate is about one per second in the entire Universe, and just few per century within the Milky Way (Li et al., 2011; Rozwadowska et al., 2021). In particular, the average distance from Earth for Galactic SN events is in the order of ~ 10 kpc as indicated by the Galactic distribution of NSs (Lorimer, 2004; Yusifov et al., 2004; Mirizzi et al., 2006; Adams et al., 2013). Due to the rareness of SN events sufficiently close to the Earth, the only SN neutrino signal collected so far is the one associated to SN 1987A. This represents a milestone event for particle astrophysics, allowing for the first detection of astrophysical neutrinos, after solar neutrinos. SN 1987A was located in the Large Magellanic Cloud, a small satellite of the Milky-Way at a distance of 51.4 kpc. The SN 1987A progenitor was a ~ 20 $M_\odot$ blue supergiant called Sanduleak$-69°202$. On the 23rd February 1987 different detectors have observed neutrinos from such an event, followed by the subsequent optical signal ~ 3 hours later. The most relevant observations were achieved by the Kamiokande II (KII) (Hirata et al., 1987; Hirata et al., 1988) and the Irvine-Michigan-Brookhaven (IMB) (Bionta et al., 1987; Bratton et al., 1988) water-Cherenkov detectors, while two other smaller scintillator detectors, the Baksan Scintillator Telescope (BUST) (Alekseev et al., 1987) and the the Mont Blanc Liquid Scintillator Detector (LSD) (Dadykin et al., 1987) also reported a few events[1]. The detection channel for SN 1987A neutrinos consisted in inverse-beta decay (IBD) $\overline{\nu}_e + p \rightarrow n + e^+$, with the subsequent detection of Cherenkov light from the emitted positron. As shown in Fig. 1.7, IMB (*top panel*) detected 8 neutrino events with average energy of 31.9 MeV spread over a time window of 6 s, KII (*middle-top panel*) observed 11 neutrino events with mean energy of 15.4 MeV in a 12 s burst while BUST (*middle-bottom panel*) detected 5 neutrino events with mean energy of 18.1 MeV in 9 s.

This restricted sample of events has been studied in a wide number of works (see, e.g., Jegerlehner et al., 1996; Loredo et al., 2002; Pagliaroli et al., 2009; Yuksel et al., 2007; Ianni et al., 2009; Li et al., 2023; Fiorillo, Heinlein, et al., 2023). From these studies one infers that the observations of this burst

[1]We point out that LSD neutrino burst detection is still controversial, since neutrino events were recorded five hours before than the others.

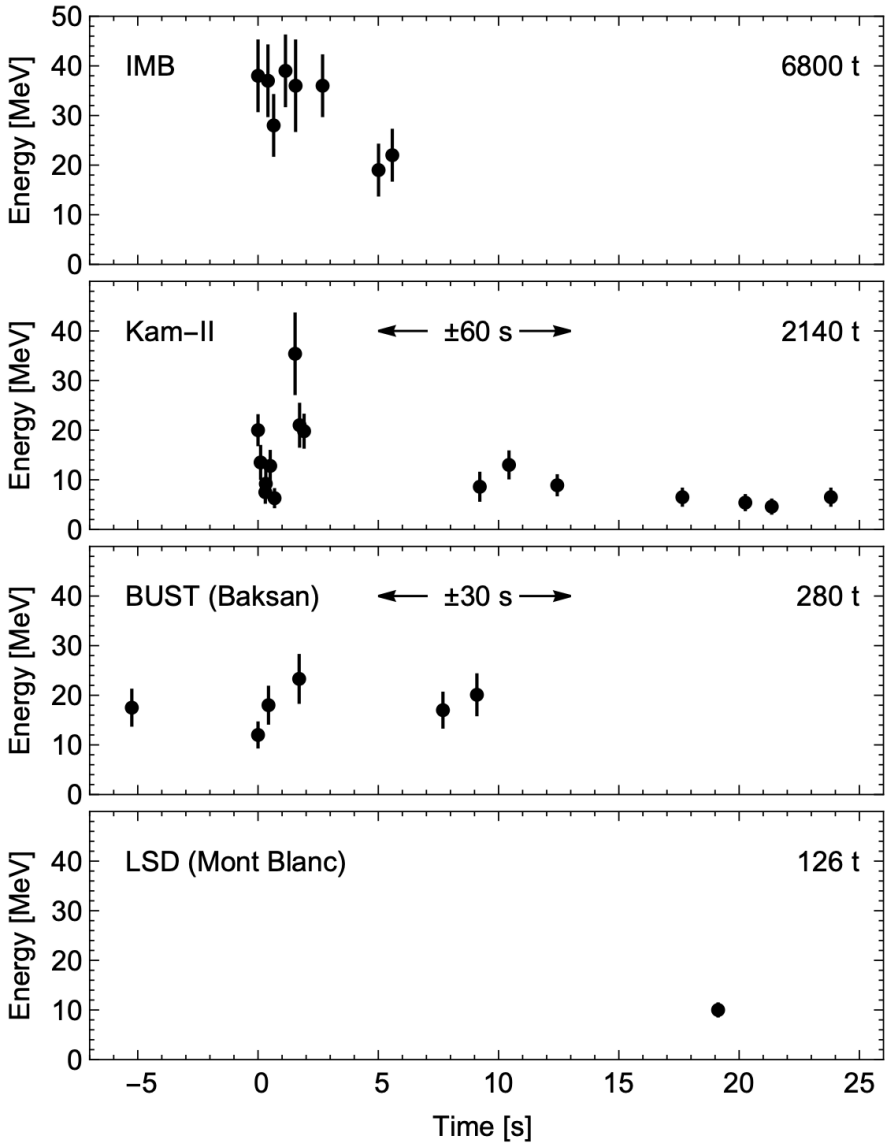

Figure 1.7: Neutrino events from SN 1987A detected at at IMB (*top panel*), KII (*middle-top panel*), BUST (*middle-bottom panel*) and LSD (*bottom panel*). Figure taken from Fiorillo, Heinlein, et al., 2023.

confirms the main aspects characterizing the CC SN explosion mechanism and the associated neutrino emission (Raffelt, 1990b). Indications for the presence of a NS inside one of the brightest dust clumps close to the expected position of the SN remnant (Page, Beznogov, et al., 2020; Greco et al., 2021) can be interpreted as further confirmation of the standard explosion scenario.

Despite the exiguous number of events detected, this observation have been widely employed to study neutrino properties (see, e.g., Loredo et al., 1989; Raffelt, 1990b; Raffelt, 1996; Yuksel et al., 2007; Pagliaroli et al., 2009; Gallo Rosso et al., 2018; Li et al., 2023; Fiorillo, Heinlein, et al., 2023) and, more importantly, to set some of the most stringent astrophysical constraints on non-standard cooling mechanisms associated to the existence of novel exotic particles (Raffelt and Seckel, 1988; Ellis and Olive, 1987; Raffelt, 1996; Caputo et al., 2022a; Caputo and Raffelt, 2024; Carenza, Giannotti, et al., 2025).

In this context, it is worth mentioning the recent re-analysis of the SN 1987A neutrino data performed in Fiorillo, Heinlein, et al., 2023 based on the state-of-the-art spherically-symmetric SN models, which include energy transport by PNS convection via a mixing-length treatment. This study confirmed once again that the time-integrated number of detected neutrino events and their mean energies agree with numerical predictions from simulations. However, the situation changes when considering the time structure of the signal. Indeed, despite the neutrino flux is in agreement with predictions from simulations in the first seconds of the burst, the three KII events after 9 s and and the two BUST events after 8 s (see Fig. 1.7) are difficult to explain by means of these simulations. This is due to the fact that the neutrino cooling process should not produce events in such detectors after 6 s due to a shortening of the cooling time window induced by PNS convection. This discrepancy may hide hints for non-standard physics, such as late phase transitions in the SN nuclear medium (Fiorillo, Heinlein, et al., 2023). Another fascinating scenario, well-justified in the perspective of 3D simulations, consists in additional late-time neutrino emission from fallback accretion. Hopefully, a future Galactic SN event would largely increase statistics thanks to the employment of current neutrino detectors (Scholberg, 2012; Mirizzi et al., 2016; Li et al., 2018). This detection would help to answer to many of questions left open by SN 1987A, especially regarding the late-time signal.

1.4.3 Gravitational waves from core-collapse supernovae

Similarly to neutrinos, CC SNe are expected to be a powerful source of GWs. Indeed, general relativity (GR) predicts that temporal variations of the mass-energy quadrupole momentum tensor of a given system source

gravitational-wave emission. Therefore, asymmetric mass motions and highly time-dependent anisotropic emission of neutrinos in SN events can trigger the emission of gravitational radiation. We stress that, while the main features of the neutrino signal are already observable by employing 1D simulations, the prediction of the GW signal from SN events intrinsically requires the development of long-lasting multi-D SN simulations. Indeed, time-dependent distortions from spherical symmetry are a key ingredient to seed the GW emission. In this regard, the growing number of multi-D simulations allowed systematic studies of the SN GW signal, which typically displays a significant variability in its features. However, some signal components are well-identified and common to all the analysis developed (see Ott, 2009a; Kotake, 2013; Kotake and Kuroda, 2017; Kalogera et al., 2021; Abdikamalov et al., 2022; Mezzacappa and Zanolin, 2024 for some review articles). Schematically, in the SN GW signal one can distinguish two main contributions, which we discussed in details below.

- *GWs from non-radial mass flows.* Hydrodynamical instabilities developed during the stellar collapse and explosion imprint asymmetries which act as a source of GWs in all the multi-D SN models developed. Fig. 1.8, taken from Vartanyan, Burrows, et al., 2023, shows time evolution of the matter GW signal from various 3D models produced by the Princeton group. We report the GW amplitudes $A_{+,\times} = D\, h_{+,\times}$ expressed in cm and defined as the product between the the GW strain $h_{+,\times}$ times the source distance D. In these expressions, $+$ and $\times$ refer to the two GW polarization states. Matter GW production can be directly connected to prompt post-bounce convection (for tens of ms) due to a negative entropy gradient behind the decelerating shock, SASI and violent convective overturn in the postshock layers (for hundreds of ms) and PNS oscillations (lasting many seconds) excited by accretion downflows of matter hitting the PNS from the outside and, less effectively, by PNS convection from the inside (see Andresen, Müller, Müller, et al., 2017; Radice et al., 2019; Torres-Forné et al., 2019; Powell et al., 2020; Andresen, Glas, et al., 2021; Vartanyan, Burrows, et al., 2023; Choi, Burrows, et al., 2024; Powell et al., 2024 for recent works on the topic). Finally, at $t_{\rm pb} \gtrsim 1$ s a long-term GW strain or "memory" (Braginsky et al., 1987a; Christodoulou, 1991; Favata, 2010) is triggered by asymmetries in the expanding explosion ejecta.

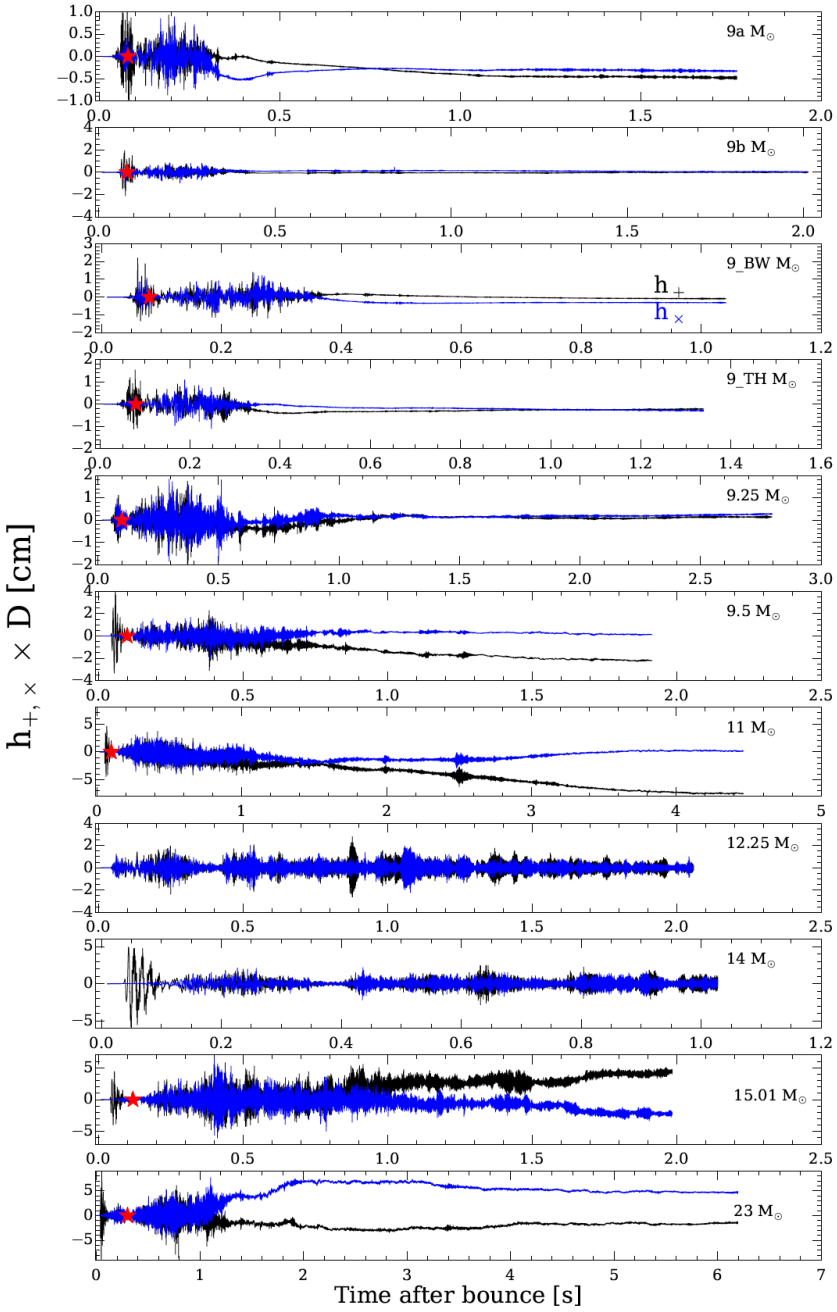

Figure 1.8: Time series of the GW strain due to non-radial mass flows from various 3D SN models by Princeton group. Black and blue curves refer to the + and × GW polarization states, respectively. The red star indicates the time of explosion. Figure taken from Vartanyan, Burrows, et al., 2023.

This component manifests in the models in Fig. 1.8 as a large-offset of the signal varying over relatively large time-scales. Moreover, long-lasting PNS convection and fallback accretion induce small-excursion highly-time dependent oscillations of the signal on top of the memory component. Typical distance independent GW strains associated with matter motions in 3D simulations are in the order of several centimeters. Moreover, the matter GW emission cover a wide frequency range from $\lesssim 50$ Hz to several ~ 1000 Hz. In particular, memory components power GWs at $\lesssim 50$ Hz, while post-shock instabilities (convection and SASI) excite GW modes at $\sim 100-200$ Hz. Moreover, PNS oscillation modes trigger broad-band GW emission, whose frequency characteristically increases from a few 100 Hz after the core bounce to more than 1000 Hz after 1 s due to the contraction of the PNS. This oscillation mode is typically associated to the fundamental PNS quadrupolar oscillation mode (f-mode) (Torres-Forné et al., 2019; Andresen, Glas, et al., 2021; Bruel et al., 2023).

- *Neutrino memory.* Asymmetries in the time-dependent emission of neutrinos are able to source GWs as well. Fig. 1.9 reports the time behavior of GWs amplitudes generated by anisotropic neutrino emission for the same models considered in Fig. 1.8. In the case of neutrino GWs, the signal can reach amplitudes up to several ~ 100 cm and in case massive progenitors with highly-asymmetric neutrino flows or large radiated neutrino energies, amplitudes can grow up to few ~ 1000 cm (Vartanyan, Burrows, et al., 2023; Choi, Burrows, et al., 2024).The neutrino GW signal is characterized by a rise over time scales of a few ~ 100 ms followed by a flat long-term evolution. The absence of high-frequency modes implies that almost all of the power radiated in neutrino GW is concentrated in the memory component at frequencies $\lesssim 10$ Hz. Thus, the neutrino memory signal dominates GW emission in the low-frequency band. With the employment of planned deciHertz interferometers, such as DECIGO (Kawamura et al., 2008), the presence of the neutrino memory component becomes crucial for the detection of the GW signal for SN events up to distances of a few ~ 10 Mpc (Mukhopadhyay, Cardona, et al., 2021).

A detailed GW measurement from a future galactic SN enlarges perspectives

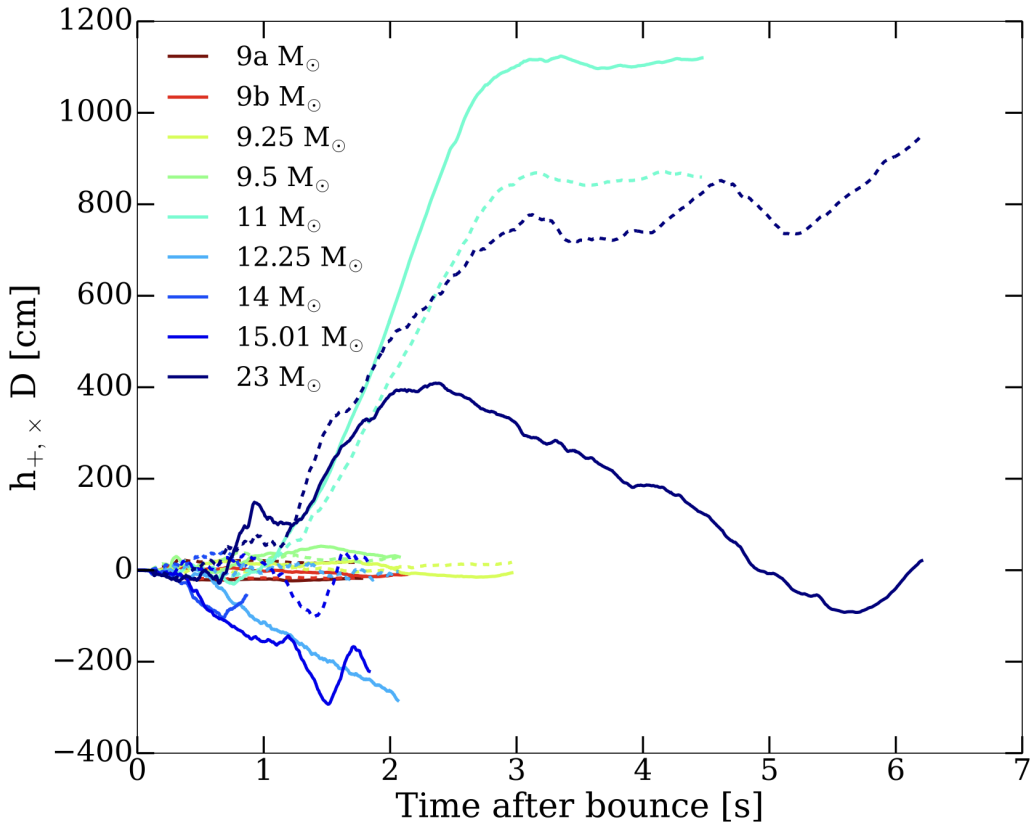

Figure 1.9: Time evolution of the GW strain due to anisotropic neutrino emission from various 3D SN models by Princeton group. Figure taken from Vartanyan, Burrows, et al., 2023.

for observations of such rare events. Specifically, SN GWs would allow one to study otherwise inaccessible effects in the core of collapsing stars, e.g., contraction of the PNS, stochastic matter shock motions, the onset time of the explosion, PNS oscillations modes and the asymmetric morphology of inner ejecta. All of these aspects are complementary to the information that can be extracted from the observation of the neutrino burst (Kuroda, Kotake, et al., 2017), highlighting the importance of characterizing CC SNe under a truly multimessenger point of view.

1.4.4 Feebly-interacting particles from Supernovae

CC SNe have been proposed as unique astrophysical laboratories to probe the emission of novel FIPs, such as such as axions (Brinkmann et al., 1988; Burrows et al., 1989; Burrows et al., 1990; Keil, Janka, Schramm, et al., 1997; Chang et al., 2018; Carenza et al., 2019; Caputo et al., 2022a), dark photons (DeRocco et al., 2019; Chang et al., 2017), sterile neutrinos (Dolgov et al., 2000; Mastrototaro et al., 2020), Kaluza-Klein gravitons (Hannestad and Raffelt, 2001), unparticles (Hannestad et al., 2007), etc. Similarly to SN neutrino emission, the series of catastrophic events occurring in the interior of the collapsing star set extreme thermodynamical conditions, which may dramatically enhance the production of exotic particles (see, e.g., Caputo et al., 2022a). The production of FIPs becomes efficient when the SN core reaches both high temperatures and densities, so that the cooling phase represents a preferred stage to investigate FIP emission. Since 3D SN simulations have been extended to the cooling phase only recently, FIP emission has always been set over 1D SN models. Nevertheless, the SN cooling phase is less affected by hydrodynamical instabilities and deviations from spherical symmetry. Therefore, the key aspects of the FIP emission process can be already understood by characterizing their production on the basis of 1D SN simulations. In the following of this Thesis work, when discussing SN production of a given FIP we will always refer to spherically-symmetric SN profiles.

Depending on the strength of its coupling to ordinary matter g_X, a generic FIP X may undergo different regimes when attempting to escape the dense SN core. In particular, if X is extremely-weakly coupled (i.e., small g_X), it can escape the SN core unimpeded, introducing an additional exotic energy sink from the SN core. In this regime, dubbed *free-streaming* regime, reabsorption in the PNS is completely negligible, since the FIP mean-free path in the inner core is typically larger than the size of the PNS. Therefore, X emission can be considered volumetric (Caputo et al., 2022a), since it takes contributions from the entire PNS volume (with larger rates from regions where temperature is higher, see Section 5.3). Streaming freely outside from the SN volume, FIP emission may reduce the energy budget available for neutrinos emitted from the PNS, leading to a seizable reduction of the SN neutrino burst duration. A shorter neutrino burst, would result in fewer

events from the observed SN 1987A, leading to a strong tension between the neutrino flux predicted by standard SN simulations and measurements of IMB, KII and BUST (Raffelt and Seckel, 1988; Raffelt, 1990a; Raffelt, 1996). This criterion is commonly known as *energy-loss* or *cooling* criterion and it is widely used to constrain FIP properties. In particular, the SN 1987A neutrino burst is compatible with a total energy released in neutrinos of $1 - 4 \times 10^{53}$ s over a time window ~ 10 s, where equipartition of energy among the different species is typically assumed. Thus, as estimated in seminal papers as Ellis and Olive, 1987; Raffelt and Seckel, 1988, an exotic energy sink might steal at most $\sim 2 \times 10^{53}$ erg in ~ 10 s, resulting in a total luminosity in exotic particles constrained by $L_X \lesssim 2 \times 10^{52}$ erg s^{-1} (Raffelt, 1990a). In classical literature, this constrain can be conveniently recast in terms of the FIP emissivity, namely the luminosity per unit mass:

$$\epsilon_X \lesssim 10^{19} \text{ erg s}^{-1} \text{ g}^{-1}, \tag{1.3}$$

obtained for a PNS mass ≈ 1 M$_\odot$ and for typical SN conditions $T = 30$ MeV, $\rho = 3 \times 10^{14}$ g cm^{-3} and $Y_e = 0.3$. This criterion is known as "Raffelt criterion". At a given coupling g_{min}, FIP luminosity becomes larger than the neutrino one L_ν, so that the cooling argument allows one to exclude values $g_X \gtrsim g_{\text{min}}$ for which $L_X \gtrsim L_\nu$. This criterion, based on simple estimations, has been calibrated on different 1D SN simulations taking into account exotic particles (Carenza, Giannotti, et al., 2025), providing the same constraints on the total energy drained by exotic particles. However, it is worth mentioning that no state-of-the-art simulation including a 1D treatment of PNS convection (which can shorter the cooling time scale to $\sim 5 - 9$ s) has been employed to test the validity of the cooling criterion. Furthermore, as already mentioned in Sec. 1.4.2, we remark that recent analysis have pointed out some tension between late-time events observed by KII and BUST and recent 1D simulations (Fiorillo, Heinlein, et al., 2023). This observation supports the insights in Raffelt and Seckel, 1988, which proposed to use only IMB events to derive the cooling bound, obtaining a factor ~ 2 of difference with respect to results accounting for other detector measurements. As a rough estimation, this value sets the range of couplings where the SN cooling bound can be considered sufficiently robust.

As shown in Fig. 1.10, FIP luminosity increases quadratically with g_X until

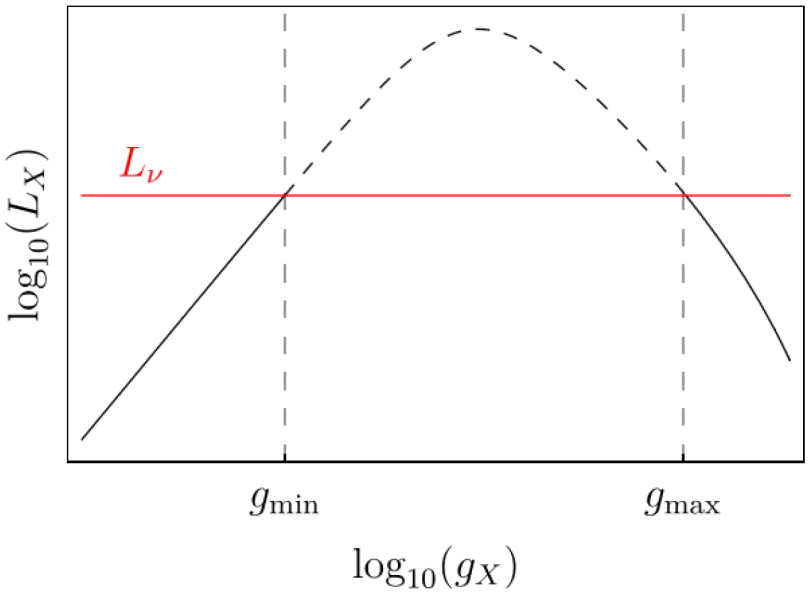

Figure 1.10: Schematic representation of the SN luminosity of a given FIP as a function of its coupling to ordinary matter g_X. Horizontal red line sets the neutrino luminosity. The dashed line highlights the range of couplings $g_{\rm min} \lesssim g \lesssim g_{\rm max}$ excluded by the SN cooling argument. Figure taken from Carenza, Giannotti, et al., 2025.

the emitted FIP becomes so strongly coupled that reabsorption is not negligible anymore. Then, SN FIPs enter the *trapping* regime (Raffelt, 1996; Caputo et al., 2022a; Fiorillo, Pitik, et al., 2025a). Similarly to the neutrino case, in this regime FIP emission switches from volumetric to surface emission and takes place from a last-scattering surface with radius R_X dubbed "X-sphere" in analogy to the neutrino-sphere. Thus, assuming thermal production, FIP luminosity can be estimated through the Stefan-Boltzmann law

$$L_X = 4\pi R_X^2 \frac{\pi^2}{120} T^4(R_X)\,, \tag{1.4}$$

where $T(R_X)$ is the temperature on the X-sphere located at radius R_X. As long as the coupling increases, the SN core becomes more optically thick for the emitted FIPs. Thus the X-sphere moves towards outer regions where temperature is lower, so that the FIP emission spectrum is peaked at lower energies. This trend reflects in the FIP luminosity in Fig. 1.10, which is rapidly decreased in the trapping regime when increasing the coupling. When

the luminosity becomes lower than the neutrino one at $g_X \gtrsim g_{\max}$, the energy release via SN FIPs is again compatible with the standard case based only on neutrino energy-loss. Globally, the energy-loss argument rules out all the couplings $g_{\min} \lesssim g_X \lesssim g_{\max}$. Nevertheless, FIPs in the trapping regime are provided with a quite reach phenomenology. Indeed, they can take part to energy transfer processes together with neutrinos and convection (see, e.g., Lucente et al., 2020), depositing radiative energy from the inner regions of the PNS to the PNS surface. Moreover, FIPs emitted from the X-sphere can deposit some energy behind the shock front and, for sufficiently strong couplings, they can give rise to a detectable signal in large underground neutrino detectors (Engel et al., 1990; Carenza, Co, et al., 2024).

Chapter 2

Axions and Axion-Like Particles: theory and constraints

In this Chapter we introduce the axion, a new particle postulated to solve the *strong CP problem* of Quantum ChromoDynamics (QCD) in terms of the introduction of the Peccei-Quinn symmetry. Apart from the QCD axion, we will also discuss how many other pseudoscalar particles, dubbed *axion-like particles*, may emerge in different extension of the Standard Model of particle physics. Here, we briefly review the phenomenology of axions and axion-like particles, which lies at the interface of particle physics, astrophysics and cosmology. In Sec. 2.1 we present the strong CP problem and its solution in terms of the Peccei-Quinn mechanism, as illustrated in Sec. 2.2. This mechanism leads to the introduction of the axion as a new pseudo Nambu-Goldston boson emerging from a broken global symmetry. The axion interaction Lagrangian is described in Sec. 2.3, with a focus on the main theoretical models introducing axions and axion-like particles (Sec. 2.3.1). Finally, in Sec. 2.4 we review the main strategies to search for axions, which can be classified into two main line of research: direct searches (Sec. 2.4.1) and astrophysical searches (Sec. 2.4.2).

2.1 The strong CP problem

QCD is the most complete theory attempting to describe strong interactions. Despite its wide success in explaining phenomenological results, it soon be-

came apparent that QCD was plagued by a subtle theoretical problem, the so-called "strong CP problem". A generic QCD Lagrangian for N quark flavors shows a global symmetry $U(N)_V \times U(N)_A$ in the limit of vanishing quark masses (Peccei, 2008), where V and A stand for vector and axial, respectively. Below the QCD phase-transition scale $\Lambda_{\rm QCD} \approx 250$ MeV, we are allowed to consider just the two light quarks, namely the up (u) and down (d) quarks. Since these quarks can be considered massless with good approximation ($m_u, m_d \ll \Lambda_{\rm QCD}$), the two-quark QCD Lagrangian below $\Lambda_{\rm QCD}$ is provided with the global symmetry previously mentioned. This can be translated into a $U(1)_V \times SU(2)_V \times U(1)_A \times SU(2)_A$ symmetry. The vector part gives rise to nucleon and pion multiplets and it implies the conservation of isospin and and baryon number, which is consistent with experiments. Conversely, the axial part is not manifest since it should be dynamically broken by quark condensates. This symmetry breaking would introduce four light pseudoscalar Nambu-Goldstone bosons related to the four broken generators of the $U(1)_A \times SU(2)_A$ symmetry. The existence of three pions, light compared to the QCD scale, can be associated to the $SU(2)_A$ breaking. On the other hand, an additional fourth light pseudoscalar was missing in the hadronic spectrum, since the η' is much heavier than pions. This problem was known as the "$U(1)_A$ problem" (Weinberg, 1975).

This was solved by 't Hooft, who first realized that the vacuum structure of QCD is not trivial ('t Hooft, 1976b; 't Hooft, 1976a). In particular, under a $U(1)_A$ transformation of parameter α the QCD Lagrangian for N flavors acquires an extra term due to the chiral anomaly affecting the action (Adler, 1969; Bardeen, 1969; Bell et al., 1969)

$$\delta\mathcal{L} = \alpha \, \frac{g^2 N}{32\pi^2} G_a^{\mu\nu} \tilde{G}_{\mu\nu a} \, , \tag{2.1}$$

where g is the quark charge, $G_a^{\mu\nu}$ is the gluon field strength tensor and $\tilde{G}_{\mu\nu a} = \frac{1}{2}\epsilon_{\mu\nu\rho\sigma} G_a^{\rho\sigma}$ its dual. In an abelian theory, this term does not have any observable effect, since it consists in a total derivative which vanishes on the boundary of the integration domain. This condition is always verified for gauge fields exactly vanishing at spatial infinity, making the action really invariant under $U(1)_A$ transformations. However, 't Hooft showed that the correct condition requires that the gauge fields of the theory must behave as pure gauge fields even at spatial infinity, i.e. they must be either zero or a gauge transformation of zero at the boundary. Each of this vac-

uum configurations can be directly related to an integer number n, known as *winding number*, so that the true QCD vacuum configuration $|\theta\rangle$ consist in a superposition of all of this vacua $|\theta_n\rangle$ (Peccei, 2008)

$$|\theta\rangle = \sum_n e^{-in\theta}|\theta_n\rangle \,. \tag{2.2}$$

This configuration is commonly called θ-vacuum. This implies the presence of an additional term in the QCD Lagrangian related to QCD vacuum structure:

$$\delta\mathcal{L} = \theta_{\rm QCD}\frac{\alpha_s}{8\pi}G_a^{\mu\nu}\tilde{G}_{\mu\nu a}\,, \tag{2.3}$$

where $\alpha_s = g^2/4\pi$ is the fine-structure constant for strong interactions. Physics becomes even more involved when including weak interactions. Indeed, the quark mass matrix M_q is complex in general. Therefore, in order to make the mass matrix real and diagonal it is necessary to introduce an additional term which shifts $\theta_{\rm QCD}$ by a quantity ArgDetM_q. In conclusion, the additional term in the QCD Lagrangian can be written as

$$\begin{aligned} \delta\mathcal{L} &= \overline{\theta}_{\rm QCD}\frac{\alpha_s}{8\pi}G_a^{\mu\nu}\tilde{G}_{\mu\nu a}\,, \\ \overline{\theta}_{\rm QCD} &= \theta_{\rm QCD} + {\rm ArgDet}M_q\,. \end{aligned} \tag{2.4}$$

This extra-term changes sign under charge conjugation (C) and parity (P) transformations, breaking the expected CP invariance of the QCD Lagrangian. Indeed, the term $G_a^{\mu\nu}\tilde{G}_{\mu\nu a}$ has the form of a scalar product between a a true and a axial vector $\mathbf{E}_{\rm color}\cdot\mathbf{B}_{\rm color}$, thus it is CP odd. Nevertheless, there are strong experimental evidences showing that CP-invariance is preserved by strong interactions at very high-precision level. The most accurate one is related to to the absence of a neutron electric dipole moment (EDM). Indeed, the presence of the $\overline{\theta}$-term in the QCD Lagrangian induces a neutron EDM given by (Dragos et al., 2021)

$$|d_n| \simeq 1.52(71)\times 10^{-16}\, e\,{\rm cm}\;\overline{\theta}_{\rm QCD}\,. \tag{2.5}$$

Accurate experimental measurements of the nEDM constrained its absolute value to $|d_n| < 1.8\times 10^{-26}\, e\,{\rm cm}$ (Abel et al., 2020), thus the magnitude of the $\overline{\theta}_{\rm QCD}$ parameter must be $\overline{\theta}_{\rm QCD} \lesssim 10^{-10}$. Since $\overline{\theta}_{\rm QCD}$ is given by the sum of two terms, the smallness of this parameter would require an extremely accurate

fine-tuning between two unrelated quantities, threatening the naturalness of the QCD theory. This problem is commonly known as the *strong CP problem*. There have been many proposed solutions to solve this problem. A first attempt assumes an unconventional QCD dynamics (Schierholz, 1994) with non trivial QCD effects. The main works in this direction suggested that the boundary conditions inducing the non trivial structure of the θ-vacuum are numerical artifacts (Khlebnikov et al., 1988). However, these assumptions often spoil the solution of the $U(1)_A$ problem. Another interesting possibility would consists in introducing a spontaneous breaking of the CP symmetry (Beg et al., 1978; Georgi, 1978; Nelson, 1984; Barr, 1984; Mohapatra et al., 1983; Feruglio et al., 2023). In this scenario, if CP is a sponatneously broken symmetry of nature, we are allowed to set $\theta = 0$ at the Lagrangian level (Peccei, 2008). However, 1-loop corrections introduce back the θ-term and recondite physics is required to artificially constrain these corrections and agree with observations (Dine and Draper, 2015; Vecchi, 2017). Finally, an ultimate natural solution leads to the introduction of a novel chiral symmetry, which rotates the θ-term away. Two suggestions have been proposed in this direction. The first one requires that one of the light-quark fields is massless, but this is in strong tension with lattice predictions and measurements of light-quark masses (Navas et al., 2024). The second one assumes the presence of a novel $U(1)$ chiral global symmetry in the SM Lagrangian which cancels the θ-term through the dynamics of a novel pseudoscalar boson. This is the first ingredient of the so called *Peccei-Quinn (PQ) mechanism*, which represents the most elegant solution up to date to the Strong CP problem.

2.2 The Peccei-Quinn Mechanism

At the end of the '70s Roberto Peccei and Helen Quinn proposed to introduce a new global chiral symmetry $U(1)_{\rm PQ}$ (Peccei and Quinn, 1977b; Peccei and Quinn, 1977a; Weinberg, 1978; Wilczek, 1978) to tackle the severe issue imposed by the strong CP problem. This symmetry is spontaneously broken at a given energy scale f_a, setting the fundamental energy scale of the theory. From symmetry breaking a novel pseudo-Nambu Goldston boson emerges: this is the so-called *QCD axion* a. Under a $U(1)_{\rm PQ}$ transformation with

parameter α, the axion field translates as

$$a(x) \to a(x) + \alpha f_a \,. \tag{2.6}$$

The $U(1)_{\rm PQ}$ symmetry is anomalous in the QCD sector introducing a non-vanishing divergence for the the associated PQ current

$$\partial_\mu J^\mu_{\rm PQ} = \zeta \frac{\alpha_s}{8\pi} G^{\mu\nu}_a \tilde{G}_{\mu\nu a} \,, \tag{2.7}$$

where ζ is a model-dependent constant. In order to satisfy Eq. (2.7), the QCD Lagrangian must include a novel term in addition to the θ-term in Eq. (2.4)

$$\mathcal{L}_a = \left(\bar{\theta}_{\rm QCD} - \zeta \frac{a}{f_a} \right) \frac{\alpha_s}{8\pi} \tilde{G}_{\mu\nu a} G^{\mu\nu}_a \,, \tag{2.8}$$

related to an axion-gluon interaction vertex with the same structure of the CP-odd part in the QCD Lagrangian. By shifting the axion field as $a \to f_a \bar{\theta}_{\rm QCD}/\zeta$, the $\bar{\theta}_{\rm QCD}$ parameter assumes now the form of a dynamical variable proportional to the axion field. Specifically, the introduction of the $U(1)_{\rm PQ}$ symmetry allows one to make the replacement

$$\bar{\theta}_{\rm QCD} \to \zeta \frac{a}{f_a} \,. \tag{2.9}$$

Axion interactions with the gluon field introduce an effective potential on the axion field. Taking into account non-perturbative QCD effects, the axion potential acquires the form

$$V_{\rm eff}(a) = m_a^2 f_a^2 \left[1 - \cos\left(\frac{a}{f_a} \right) \right] \,, \tag{2.10}$$

which is schematically depicted in Fig. 2.1. This potential is periodic in a/f_a, and it is minimized at $a = 0$. Thus, sitting in the minimum of its potential, the axion field washes out the CP-odd term in the QCD Lagrangian and solves dynamically the strong CP problem.

Moreover the effective QCD potential in Eq. (2.10) induce an effective mass term m_a for the axion field:

$$m_a^2 = \left\langle \frac{\partial^2 V_{\rm eff}}{\partial^2 a} \right\rangle \Bigg|_{\langle a \rangle = 0} \,. \tag{2.11}$$

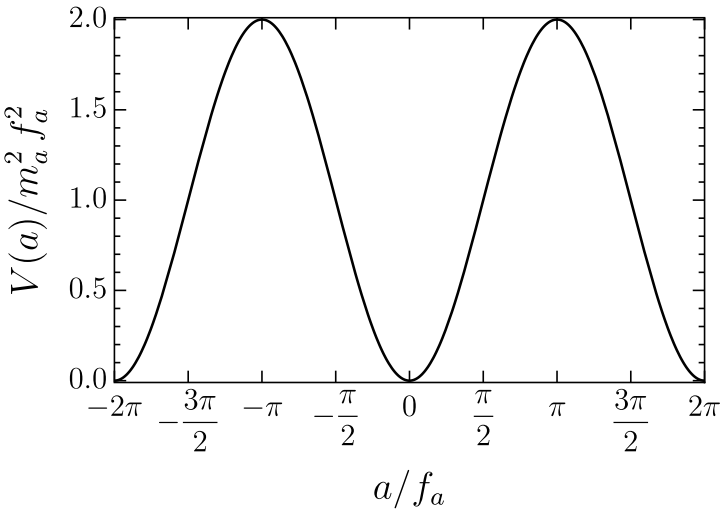

Figure 2.1: Schematic representation of the axion potential in Eq. ((2.10)).

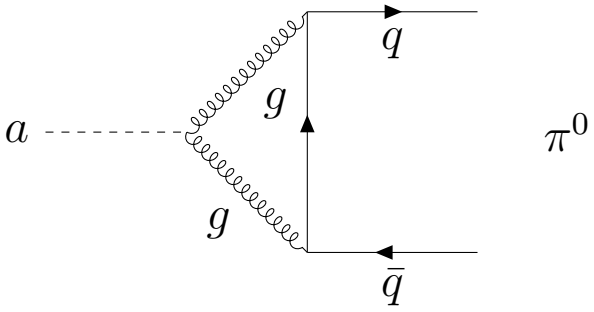

Figure 2.2: A scheme of the axion-neutral pion mixing due to the coupling with gluons.

Indeed, even if the axion is introduced massless, its coupling with gluons induce the mixing with neutral pions below $\Lambda_{\rm QCD}$. This non-perturbative effect, illustrated in Fig. 2.2, would induce a tiny axion mass. The value of the axion mass is calculated to the next-to-next-to-leading order by employing chiral perturbation theory (Gorghetto and Villadoro, 2019) and lattice QCD (Borsanyi et al., 2016)

$$m_a = 5.691(51)\ \text{meV} \left(\frac{10^9\,\text{GeV}}{f_a} \right) . \tag{2.12}$$

The mechanism that solves the strong CP problem and gives mass to the axion can be pictorially described with Fig. 2.3. At energies higher than

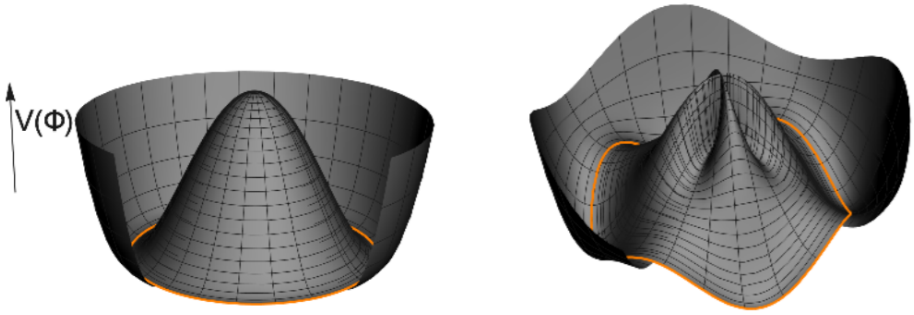

Figure 2.3: The Mexican-hat potential of the axion field before (left) and after (right) the QCD phase transition. Figure taken from Chadha-Day et al., 2022.

the PQ scale f_a the axion field is located on the wells of the mexican hat potential, and every configuration is equivalent. When energy lowers the axion field rolls down the hill and when the energy scale gets lower than f_a and the $U(1)_{PQ}$ symmetry is broken, it sits in one one of the equivalent minima on the orange circle. The emerging configuration of the field as a pseudo-Nambu Goldston boson is the QCD axion. At this level, the strong-CP problem is still unsolved, since there is no reason for the axion the choose a configuration close to zero. Here, the QCD phase transition plays a crucial role. As the energy gets also lower than $\Lambda_{\mathrm{QCD}} \sim 150 - 170$ MeV (Gottlieb et al., 1997), quarks and gluons are confined into hadrons. Meanwhile, the axion acquires an effective potential induced by QCD effects which deforms its own potential, setting new local minima in the valley and providing the axion with an effective mass due to processes as in Fig. 2.2. The deformed potential ultimately drives the axion to the null configuration, which solves the strong CP problem.

2.3 Axion models and interactions

The extension of the Standard Model (SM) with the $U(1)_{\mathrm{PQ}}$ introduces novel terms in the SM Lagrangian. The most general Lagrangian, accounting for

all possible axion interaction vertices, reads (Peccei, 2008)

$$\begin{aligned}\mathcal{L}_a =& \mathcal{L}_{\rm SM} + \bar{\theta}_{\rm QCD}\frac{\alpha_s}{8\pi}\tilde{G}_{\mu\nu a}G_a^{\mu\nu} - \frac{1}{2}\partial_\mu a \partial^\mu a + \mathcal{L}_{\rm f}\left[a,\Psi\right] + \\ &+ \zeta\frac{a}{f_a}\frac{\alpha_s}{8\pi}\tilde{G}_{\mu\nu a}G_a^{\mu\nu} + \zeta_\gamma\frac{a}{f_a}\frac{\alpha_{\rm em}}{4\pi}\tilde{F}_{\mu\nu}F^{\mu\nu}\ ,\end{aligned} \tag{2.13}$$

where $\mathcal{L}_{\rm SM}$ is the SM Lagrangian, $F^{\mu\nu}$ is the electromagnetic field strength tensor, $\tilde{F}^{\mu\nu}$ its dual, $\alpha_{\rm em}$ is the electromagnetic fine-structure constant and ζ and ζ_γ are model dependent constant. $\mathcal{L}_{\rm f}[a,\psi]$ encodes axion interactions with SM fermions

$$\mathcal{L}_{af} = \frac{C_{af}}{2\,f_a}\partial_\mu a \bar{\psi}_f \gamma^\mu \gamma_5 \psi_f\,, \tag{2.14}$$

where ψ_f is the fermion field with mass m_f, and C_f is a model-dependent coefficient. Thus, the dimensionless combination

$$g_{af} = C_{af}\,\frac{m_f}{f_a} \tag{2.15}$$

plays the role of a Yukawa coupling. Below the QCD phase transition, axions couple to nucleons and model dependent constants C_{aN} (with $N = n, p$ for neutrons and protons, respectively) can be defined in terms of couplings to quarks C_q (with $q = u, d, s, c, b, t$) (Grilli di Cortona et al., 2016):

$$\begin{aligned}C_{ap} =& -0.47 + 0.88c_u - 0.39c_d - 0.038c_s - 0.012c_c - 0.009c_b - 0.0035c_t\,,\\ C_{an} =& -0.02 + 0.88c_d - 0.39c_u - 0.038c_s - 0.012c_c - 0.009c_b - 0.0035c_t\,.\end{aligned} \tag{2.16}$$

The axion-photon coupling $g_{a\gamma}$ is the main channel for axion detection at low energy. It can be conveniently defined as (Grilli di Cortona et al., 2016)

$$g_{a\gamma} = C_{a\gamma}\,\frac{\alpha}{2\pi f_a}\,, \tag{2.17}$$

where

$$C_{a\gamma} = \frac{E}{N} - 1.92(4). \tag{2.18}$$

Here, E and N are the electromagnetic and color anomalies of the PQ current in the given model, respectively, while $C^0_{a\gamma} = -1.92(4)$ accounts for the model-independent contribution due to the axion-gluon interaction.

As a general property, all the axion interactions with SM particles in Eq. (2.13) are always suppressed by $1/f_a$, so that the larger the PQ scale is the weaker

axion couplings result to be. The most important consequence is that the axion decay rate in photon pairs (Raffelt, 1996)

$$\Gamma_{a\to\gamma\gamma} = \frac{g_{a\gamma}^2 m_a^3}{64\pi} = 7.55\times 10^{-26}\,\mathrm{s}^{-1}\left(\frac{g_{a\gamma}}{10^{-10}\,\mathrm{GeV}^{-1}}\right)^2\left(\frac{m_a}{\mathrm{eV}}\right)^3\,, \tag{2.19}$$

is suppressed for small values of the axion-photon coupling. Thus, axions with masses $m_a \lesssim 20$ eV are stable over cosmological time-scales.

Relevant for cosmological implications, axions can also couple with pions through the following Lagrangian

$$\mathcal{L}_{a\pi} = \frac{C_{a\pi}}{f_\pi f_a}\left(\pi^0\pi^+\partial_\mu\pi^- + \pi^0\pi^-\partial_\mu\pi^+ - 2\pi^+\pi^-\partial_\mu\pi^0\right)\partial_\mu a\,, \tag{2.20}$$

where $f_\pi = 92.4$ MeV is the pion decay constant, while $C_{a\pi}$ is a model-dependent constant.

2.3.1 "Canonical" QCD axions and axion-like particles

The solution of the strong CP problem is intrinsically related to the presence of the $\sim aG\tilde{G}$ term in the Lagrangian in Eq. (2.13). Nevertheless, the QCD axion degree of freedom can be introduced through UV completions of the SM provided by many different axion models (see, e.g., Di Luzio et al., 2020 for a review). Below, we briefly outline the main features of the most studied models, which are commonly dubbed *canonical* QCD axion models.

- *Peccei-Quinn-Weinberg-Wilczek (PQWW) model* (Peccei and Quinn, 1977b; Peccei and Quinn, 1977a; Weinberg, 1978; Wilczek, 1978). This was the first proposed model for the realization of the PQ mechanism. It proposes to enrich the SM only with an extra Higgs doublet whose complex phase coincides with the axion degree of freedom. The appealing feature of this model lies in a natural choice for the PQ scale, which should be in the order of the electroweak scale $f_{\mathrm{EW}} \simeq 246$ GeV. Therefore, axions should be provided with seizable couplings to SM fermions. This model was soon ruled out by beam dump experiments (Donnelly et al., 1978) and searches for "invisible decays" as $K \to \pi\, a$ (Hall et al., 1981), $J/\Psi \to \gamma a$ and $\Upsilon \to \gamma a$ (Wilczek, 1977).

The rejection of this model led to development of the so-called *invisible axion* models introduced below, in which the PQ scale is much larger than electroweak scale $f_a \gg f_{\rm EW}$, leading to extremely weak axion interactions since $1/f_a \ll 1/f_{\rm EW}$.

- *Kim-Shifman-Vainshtein-Zakharov (KSVZ) model* (Kim, 1979; Shifman et al., 1980). In this model, the SM content is extended by the introduction of new heavy vector-like fermion in the fundamental of color, singlet under $SU(2)_L$ and neutral under hypercharge, and a complex scalar field. The latter couples to the heavy fermion providing it with a mass proportional to the scalar vacuum expectation value in the order of f_a. Since the mass of the heavy fermion can be very large, in this model $f_a \gg 100$ GeV. In the KSVZ axion model, the axion couples to SM fields only via the model-independent $aG\tilde{G}$ term. Thus, the ratio between electromagnetic and color anomalies is null $E/N = 0$ and $C_{a\gamma} = -1.92$. The KSVZ axion does not couple at tree level to any SM fermion. A strongly suppressed coupling to electrons can be radiatively generated at one loop (Srednicki, 1985; Chang and Choi, 1993)
$$C_{ae} \simeq \frac{3\alpha^2}{4\pi^2}\left[\frac{E}{N}\log\left(\frac{f_a}{m_e}\right) - 1.92\,\log\left(\frac{\Lambda_\chi}{m_e}\right)\right], \tag{2.21}$$
in which $\Lambda_\chi \simeq 1$ GeV is the chiral symmetry breaking scale. The KSVZ axion model is an example of *hadronic* axion model, since its low-energy phenomenology is determined by its coupling to hadrons. In particular, for hadronic axions the axion-nucleon coupling is the only non-vanishing coupling to fermions and it is given by (Grilli di Cortona et al., 2016)
$$C_{ap} = -0.47 \qquad C_{an} = -0.02\,, \tag{2.22}$$
with n and p for neutron and proton, respectively. Finally, in hadronic axion models $C_{a\pi} = (1-z)/3(1+z)$ (Di Luzio et al., 2020), with $z = 0.48(3)$ being the ratio between the up and down quark masses (Grilli di Cortona et al., 2016).

- *Dine-Fischler-Srednicki-Zhitnitsky (DFSZ) model* (Zhitnitsky, 1980; Dine, Fischler, and Srednicki, 1981). In the DFSZ axion model two Higgs doublets and a singlet complex scalar field are introduced. This model

allows for Yukawa couplings between the Higgs fields and SM fermions, inducing tree-level axion-fermion couplings. Thus, in DFSZ axion models the PQ current is in general characterized by a non-vanishing electromagnetic anomaly. In the minimal DFSZ model $E/N = 8/3$, but this ratio can vary over a wide range of values for more complicated DFSZ models introducing a larger number of Higgs doublets (see, e.g., Di Luzio et al., 2020). Remarkably, the DFSZ axion shows a seizable coupling to electrons at tree level (Srednicki, 1985)

$$C_{ae} = \frac{\sin^2 \beta}{3}\,, \tag{2.23}$$

where $\tan\beta$ is the ratio of the vacuum expectation values of the two Higgs doublets, constrained to be $0.28 < \tan\beta < 140$ from the requirement of perturbative unitarity of the Yukawa couplings of SM fermions (Di Luzio et al., 2020; Grilli di Cortona et al., 2016). Analogously, axion couplings to nucleons can be written as

$$\begin{aligned} C_{ap} &= -0.435\,\sin^2\beta + (-0.182 \pm 0.025)\,, \\ C_{an} &= 0.414\sin^2\beta + (-0.160 \pm 0.025)\,, \end{aligned} \tag{2.24}$$

and they never vanish simultaneously. Finally, in the DFSZ axion model the model dependent axion-pion coupling constant is given by $C_{a\pi} = (1-z)/3(1+z) - 1/9\cos 2\beta$ (Di Luzio et al., 2020).

As discussed in previous sections, the QCD axion emerges in the context of the PQ mechanism to solve the strong CP problem. However, many others UV completions of the SM, such as Grand Unified Theories (GUT) and string theory (ST), predict additional global axial symmetries whose spontaneous breaking introduces novel pseudoscalar Nambu-Goldston bosons. Since they typically share many of the properties of the QCD axion, these novel pseudoscalar particles are dubbed *axion-like particles* (ALPs) (Masso, 2008). ALPs can arise in low-effective field theories descending from ST (Witten, 1984; Choi and Kim, 1985; Choi, Nilles, et al., 2009; Arvanitaki, Dimopoulos, Dubovsky, et al., 2010; Cicoli et al., 2012; Halverson et al., 2017), in models with broken supersymmetries (Bellazzini et al., 2017), in extended Higgs sectors (Branco et al., 2012; Dolan et al., 2015) and in quantum field theory on torsion manifolds (Duncan et al., 1992; Mercuri, 2009; Castillo-Felisola et al.,

2015). Typically, ALP couplings are characterized by the same interaction vertices as the QCD axion. The main difference between the QCD axion and a generic ALP is in the relation between their mass and couplings. Indeed, while for the QCD axion both mass and couplings are set by a single free parameter, namely the PQ energy scale f_a, ALP couplings are in general unrelated to their masses. Thus the ALP mass spectrum stretches over a large range of scales from $m_a \lesssim 10^{-10}$ eV up to $m_a \gtrsim 1$ GeV, featuring a wide phenomenology. In the following we will generically refer to ALPs and QCD axions as "axions" and we will discuss the main line of research undertaken to constrain the axion parameter space.

2.4 Axion Searches

The extremely feeble interactions of the axions with SM particles make their detection extremely challenging. Since the axion proposal as a solution of the strong CP problem, many strategies have been proposed to search for such elusive particles. These can be classified into two main line of research: *a) direct searches* in laboratory experiments and *b) indirect signatures* from astrophysics and cosmology. The majority of the probes employs the axion coupling to photons $g_{a\gamma}$. As shown in the left panel of Fig. 2.4, this interaction may trigger axion production in the electric field of charged particles $\gamma + Ze \to a + Ze$, called Primakoff effect (Dicus et al., 1978). This process is relevant for axion production in stellar plasmas. In parallel, the axion-photon coupling allows for axion-photon conversions in an external magnetic field (see right panel of Fig. 2.4). This mechanism represents the basis of the main experiments designed to search for the *invisible* axion (Sikivie, 1983). Furthermore, in presence of light axions traveling in large scale astrophysical magnetic fields, the axion-photon coupling gives rise to the phenomenon of axion-photon oscillations (Raffelt and Stodolsky, 1988). On the other hand, heavy axions coupled to photons can decay in photon pairs over astrophysical distances, giving rise to observable signatures. Thus, astrophysical searches of axions are conducted in synergy with multiwavelength astronomy. Despite the axion-photon coupling is the basis for axion searches, in recent years more general models allowing for other couplings to SM particles have been investigated. In this Thesis work we will focus on the axion-nucleon coupling g_{aN}, which opens the most efficient axion production channels in

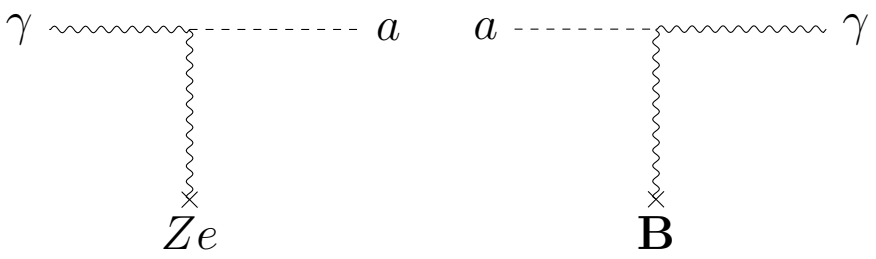

Figure 2.4: Left panel: axion production via the Primakoff process $\gamma + Ze \rightarrow a + Ze$. Right panel: axion-photon conversion in an external magnetic field.

CC SNe and other compact objects, leading to some of the most stringent astrophysical constraints. In the following, we mainly focus on bounds for axions coupled to photons and nucleons by following the collection in O'Hare, 2020. This section is not meant to be an exhaustive review of all the present constraints on the axion parameter space. The reader is invited to look at the references provided in O'Hare, 2020 for further details and information on constraints not discussed in this Thesis work. We point out Navas et al., 2024 for a general review on axion limits, Irastorza et al., 2018; Sikivie, 2021 for more details on experimental limits and Sikivie, 2008; Cadamuro et al., 2011; Cadamuro and Redondo, 2012 on cosmological bounds.

2.4.1 Direct Searches

The quest for the axion in dedicated laboratory experiments have been developed since the axion proposal, when the PQWW axion model was soon ruled out (see Sec. 2.3.1). Historically, the first proposed experiments looked for axions produced in astrophysical sources or in a cosmological context, and then detected through their conversion into photons in large magnets installed in laboratory experiments (Sikivie, 1983). These ideas led to development of the first *helioscopes* and *haloscopes*, searching for axions produced in the Sun or composing in the dark matter (DM) Galactic halo, respectively. The uncertainties related to axion fluxes of astrophysical and cosmological origin suggested the introduction of *pure laboratory experiments*, where axions are produced directly in laboratories (Irastorza et al., 2018). All of these types of experiments rely on the axion-photon coupling inducing axion-photon conversions in long-baseline magnetic fields. In particular,

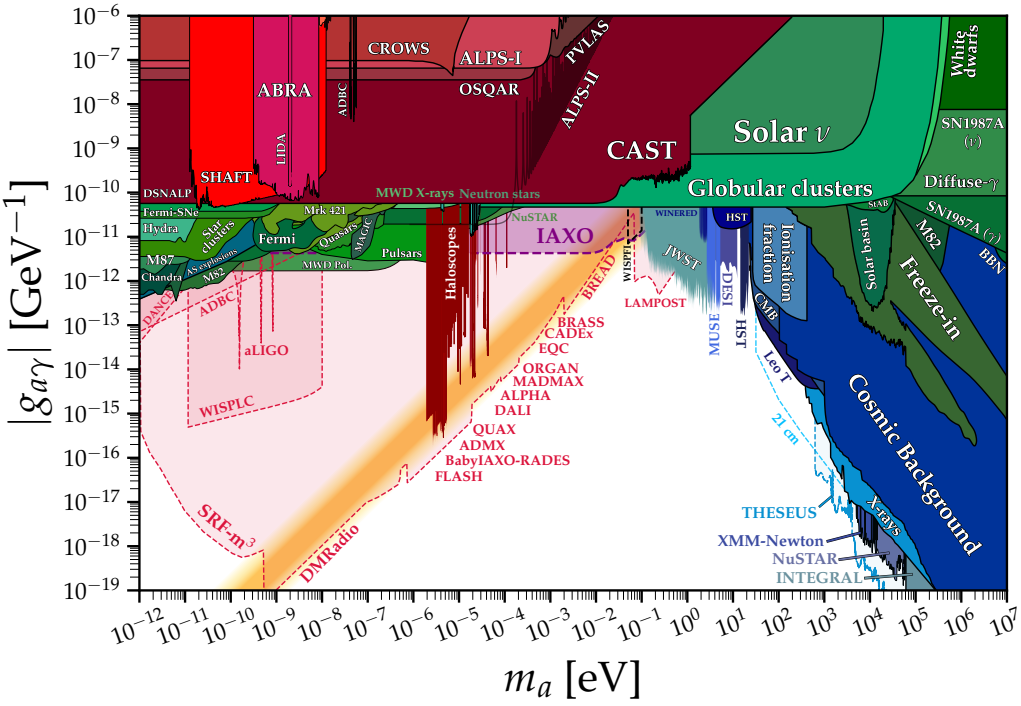

Figure 2.5: Overview plot of the bounds and future-experiments sensitivities in the axion parameter space (m_a, $g_{a\gamma}$). The yellow band represents the variability of possible QCD axion models. Reddish zones are experimental bounds, greenish areas are constraints based on astrophysical arguments, while the bluish ones are excluded via cosmological probes. Shaded red areas represents projection for future experiments. Figure taken from O'Hare, 2020.

light axions (with mass $m_a^2\, L/2\omega \ll 2\pi$, where ω is the axion energy and L the length of the magnetic region) can convert into photons with a probability $P_{a\gamma} \simeq g_{a\gamma}^2\, B^2\, L^2/4$ (Sikivie, 1983; Raffelt and Stodolsky, 1988). An alternative to this kind of searches is related to the oscillation of the nuclear EDM and the precession of the nuclear spins, which might be induced by oscillation of the axion field in the DM halo (Navas et al., 2024). Current experimental bounds on the axion-photon and axion-proton coupling are reported as reddish regions in Fig. 2.5, Fig. 2.7 and Fig. 2.8. In these figures the variability of QCD axion models is depicted as a yellow band.

Pure-laboratory experiments

Light-Shining-through-Walls (LSW) experiments represent one of the most constraining pure-laboratory probes for light axions. All of this kind of experiments are based on the setup depicted in Fig. 2.6. They consists in a laser beam propagating towards an optical barrier within a strong magnetic field. If the axion exist, a fraction of the light beam might be converted in axions. Then, due to the extremely suppressed axion interaction with matter, the axion flux is able to overcame the optically-thick medium, entering the region where a new magnetic field is applied. Here axions may reconvert back in photons, giving rise to a peculiar signal probing the existence of the axion (Anselm, 1985; Van Bibber et al., 1987). The first LSW experiment was performed by the BFRT (Brookhaven-Fermilab-Rochester-Trieste) collaboration, setting a limit on the axion-photon coupling $g_{a\gamma} < 6.7 \times 10^{-7}$ GeV^{-1} at 95% confidence level (CL) for $m_a < 1$ meV (Ruoso et al., 1992; Cameron et al., 1993). For many years, the leading constraint introduced by a LSW experiment was the one set by the OSQAR (Optical Search for QED Vacuum Birefringence, Axions, and Photon Regeneration) experiment, which employed two 9 T magnet from LHC to exclude $g_{a\gamma} > 5.7 \times 10^{-8}$ GeV^{-1} at 95% confidence level (CL) for $m_a < 0.3$ meV (Ballou et al., 2014). Moreover, the ALPS (Any Light Particle Search) experiment at DESY set a limit competitive with OSQAR by exploiting the HERA dipole magnet to provide a field intensity of $B = 5\,\mathrm{T}$ in a length of 8.8 m. In particular, ALPS excluded $g_{a\gamma} > 6.5 \times 10^{-8}$ GeV^{-1} at 95% confidence level (CL) for $m_a < 1$ meV (Ehret et al., 2010). A novel frontier for LSW experiments is represented by the ALPS II experiment currently running at DESY, which employs 24 superconducting dipole magnets installed in 122 m long optical cavities. The first run of the experiment set the limit $g_{a\gamma} \lesssim 6 \times 10^{-10}$ GeV^{-1} at 95% confidence level (CL) for $m_a < 0.1$ meV (Wei, 2024), but the experiment in the full operational regime is expected to be sensitive to axion-photon couplings down to $g_{a\gamma} \simeq 2 \times 10^{-11}$ GeV^{-1}.

Other types of searches related to the axion-photon coupling, look for dichroism or birefringence effects induced by the axion electrodynamics. Indeed, if the axion couples to a single photon polarization state, this can be depleted (dichroism) or dephased (birefringence) compared to the other state (Maiani et al., 1986). However, experiments exploiting this mechanism typically set

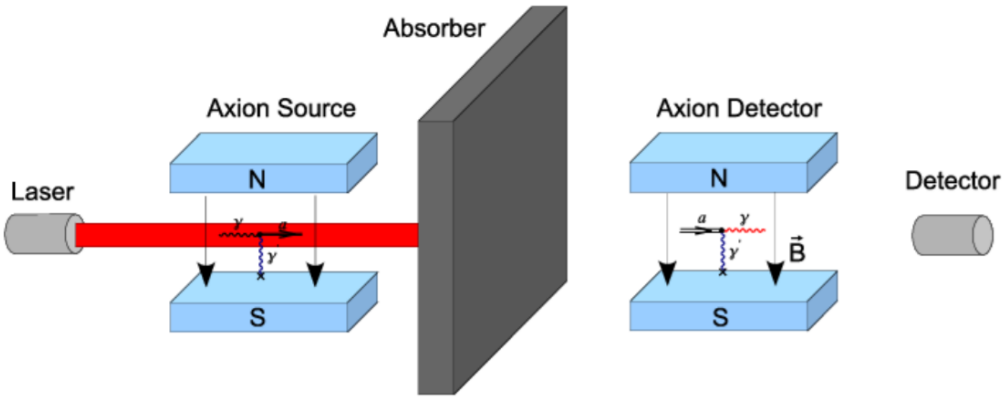

Figure 2.6: Schematic representation of a LSW experiment. Figure taken from Kim and Carosi, 2010.

constraints weaker than LSW experiments. Latest results from PVLAS (Polarizzazione del Vuoto con LASer) exclude $g_{a\gamma} \gtrsim 6.7 \times 10^{-8}$ GeV^{-1} at 95% confidence level (CL) for $m_a < 0.2$ meV.

If axions are also coupled to fermions, especially nucleons, they can also mediate long-range forces. Effects induced by these forces are employed in "fifth force" experiments (Fischbach et al., 1992) to search for new mass-spin couplings, which set the limit derived from torsion balance tests in Fig. 2.7. Furthermore, the oscillating Galactic DM axion field may induce oscillations in nuclear EDMs, which might cause the precession of nuclear spin in a spin-polarized sample in presence of an external electric field (Navas et al., 2024). This mechanism is exploited in experiments as CASPEr (Cosmic Axion Spin Precession Experiment)(Budker et al., 2014), NASDUCK (Bloch, Ronen, et al., 2022) and K-^{3}He (Bloch, Hochberg, et al., 2020; Vasilakis et al., 2009) to introduce stringent constraints on sub-μeV axions coupled to nucleons.

Finally, particle accelerators are the most viable experimental tool to probe axions interacting with photons in the MeV-GeV mass (see purple regions in Fig. 2.8). The axion-photon coupling can be constrained by e^+e^- colliders, such as LEP (Large Electro-Positron collider) (Jaeckel and Spannowsky, 2016) and Belle II (Abudinén et al., 2020). In particular, axions can be produced via Primakoff process in electron beam dump (Bjorken, Ecklund, et al., 1988; Dolan et al., 2017; Döbrich, 2018; Banerjee et al., 2020) and

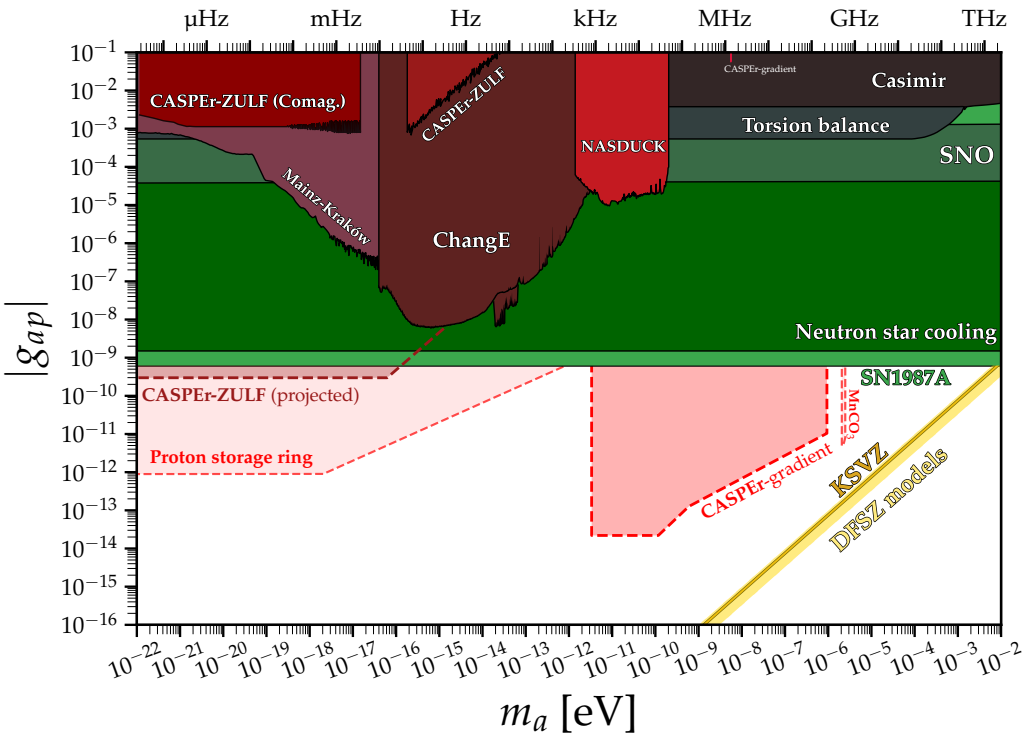

Figure 2.7: Overview plot of the bounds and future-experiment sensitivities in the axion parameter space (m_a, g_{ap}). The color scheme is the same as in Fig. 2.5. Figure taken from O'Hare, 2020.

proton beam dump (Blumlein et al., 1992; Gninenko, 2012) experiments, and then decay into photons which can be collected by detectors. Finally, axions with larger masses 5 GeV $\lesssim m_a \lesssim$ 100 GeV are also studied at LHC (Large Hadron Collider) by the ATLAS (A Toroidal LHC ApparatuS) and CMS (Compact Muon Solenoid) experiments (Aad et al., 2016; Aaboud et al., 2016; Knapen et al., 2017a; Knapen et al., 2017b; Bauer, Neubert, and Thamm, 2017; Sirunyan et al., 2019; Aad et al., 2021).

Helioscopes

The Sun is expected to be a powerful natural source of axions close to the Earth. This huge axion flux, originating from the hottest regions of the stellar core, can be employed to conduct axion searches on the Earth. This idea is at the basis of the development of helioscopes (Sikivie, 1983; Van Bib-

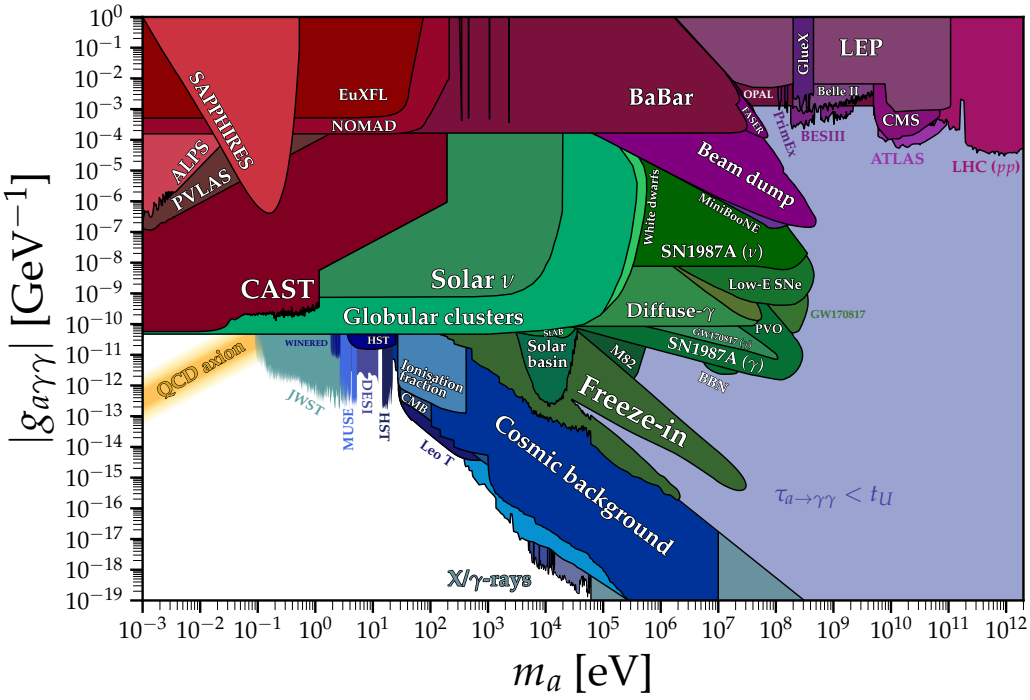

Figure 2.8: Overview plot of the bounds and future-experiment sensitivities in the axion parameter space (m_a, $g_{a\gamma}$). This plot, is the extension of Fig. 2.5 to higher axion masses $m_a \gtrsim 10$ MeV. Purple regions refer to collider searches for heavy axions. Figure taken from O'Hare, 2020.

ber et al., 1987), which aim to detect solar axions by means of conversion in X-rays within strong magnetic fields. A schematic view of the functioning of a helioscope is provided in Fig. 2.9. The first running helioscope was located at the Brookhaven National Laboratory (BNL) (Lazarus et al., 1992) subsequently followed by the SUMICO axion helioscope at the University of Tokyo, which allowed to constrain the axion-photon coupling to $g_{a\gamma} \lesssim 6 \times 10^{-10}$ GeV^{-1} at 95% CL for $m_a < 30$ meV (Moriyama et al., 1998; Inoue et al., 2002). The most recent running axion helioscope is the CAST (CERN Axion Solar Telescope) experiment at CERN, which employed a more powerful decomissioned LHC magnet with a magnetic region filled with gas to keep coherence in axion-photon conversion till $m_a \sim 20$ meV. The absence of a positive signal placed a bound at $g_{a\gamma} \lesssim 6.6 \times 10^{-11}$ GeV^{-1} at 95% CL for $m_a < 20$ meV (Anastassopoulos et al., 2017). Moreover, filling the cavity with gases as ^{3}He and ^{4}He allowed the extension of the

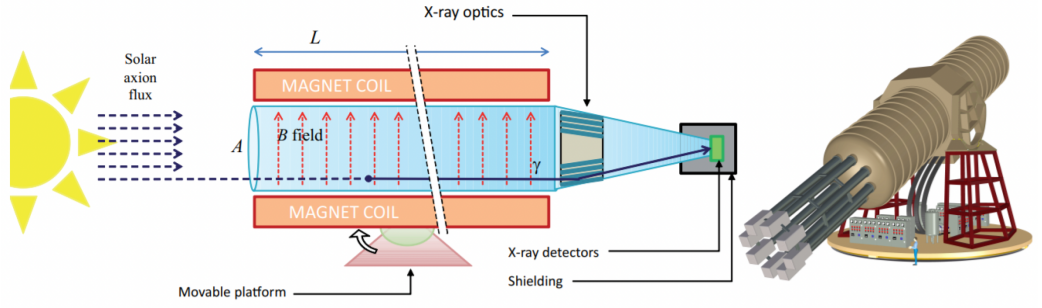

Figure 2.9: Schematic view of an axion helioscope, in particular IAXO. Solar axions are converted into photons in the transverse magnetic field inside the large magnet. The converted photons are then focused in a low-background detector. Figure taken from Graham, Irastorza, et al., 2015.

bound towards higher axion masses, excluding $g_{a\gamma} \lesssim 3 \times 10^{-10}$ GeV^{-1} at 95% CL for $0.04\,\text{eV} < m_a < 1.17$ eV (Arik et al., 2014). A new run of the experiment employing a Xe-based micromegas detector improved the limit to $g_{a\gamma} \lesssim 5.8 \times 10^{-11}$ GeV^{-1} at 95% CL for $m_a < 20$ meV (Altenmüller et al., 2024). The next frontier of axion helioscopes is represented by the International AXion Observatory (IAXO). This experiment will be able to improve helioscope sensitivities down to few $\sim 10^{-12}$ GeV^{-1} for axion masses $m_a \lesssim 20$ meV, allowing one to probe canonical QCD axion models in the mass range 1 meV $\lesssim m_a \lesssim$ 100 meV, a region mostly unexplored by other probes. This region is of particular interest for some axion DM models. For these reasons, the IAXO experiment is expected to lead experimental axion searches in the next future.

Haloscopes

Axions might have been copiously produced in the early Universe. The present behavior of axions produced on cosmological scales depends on their mass and production mechanism. In particular, QCD axions that interact sufficiently strongly may have been in thermal equilibrium with the primordial plasma, undergoing thermal production. These axions behave as hot dark matter (HDM) for masses $m_a \sim \mathcal{O}(1)$ eV and as dark radiation for $m_a \lesssim 0.1$ eV. On the other hand, lighter QCD axions with masses $m_a \lesssim \mathcal{O}(\mu\,\text{eV})$, interact so weakly that they can never be considered in

thermal equilibrium with the plasma (Masso et al., 2002). However, they can be produced by means of non-thermal mechanisms, such as misalignment (Preskill et al., 1983; Abbott and Sikivie, 1983; Dine and Fischler, 1983; Arias et al., 2012) or the decay of cosmological defects (Klaer et al., 2017; Gorghetto et al., 2021; Saikawa et al., 2024; Benabou, Bonnefoy, et al., 2024), contributing to the cold dark matter (CDM) content of the Universe. CDM axions are the main target of haloscope experiments, which employ microwave cavities with high quality factors and a tunable plasma frequency (Sikivie, 1983; Sikivie, 1985; Bradley et al., 2003). When the cavity plasma frequency matches the axion mass, resonant axion-to-photon conversions are triggered, allowing one to probe extremely weak couplings down to canonical QCD axion models. The current strongest haloscope limit has been set by the ADMX (Axion Dark Matter eXperiment) experiment, excluding KSVZ axions in the mass range $1.9 - 3.3\,\mu$eV (Asztalos et al., 2004) and both the KSVZ and DSFZ models in the mass range $2.7 - 4.2\ \mu$eV (Du et al., 2018; Braine et al., 2020; Bartram et al., 2021a; Bartram et al., 2021b). Future improvements of this experiment would allow one to cover KSVZ axion masses in the range $4.5 - 6\,\mu$eV and $14 - 25\,\mu$eV and DFSZ axions in the range $2 - 40\,\mu$eV (Stern, 2016). Furthermore, a huge experimental program is undergoing with the aim to develop novel haloscope designs to cover complementary regions of the QCD axion band in the range 10^{-10} eV $\lesssim m_a \lesssim 10$ eV (see Fig. 2.5). In particular, the proposed MADMAX (MAgnetized Disk and Mirror Axion eXperiment) experiment would probe the range $40\ \mu\text{eV} \lesssim m_a \lesssim 200\ \mu\text{eV}$ (Caldwell et al., 2017; Brun et al., 2019), the ALPHA (Antihydrogen Laser Physics Apparatus) (Lawson et al., 2019) haloscope experimental setup would cover masses $40\ \mu\text{eV} \lesssim m_a \lesssim 400\ \mu\text{eV}$, while larger masses $50\ \text{meV} \lesssim m_a \lesssim 10$ eV, can be scanned by proposed optical dielectric haloscopes (Baryakhtar et al., 2018). For lower masses $1\ \text{neV} \lesssim m_a \lesssim 0.1\mu\text{eV}$, DM axions in strong magnetic fields may induce oscillating electric currents in cooled LC circuits (Sikivie et al., 2014; Kahn et al., 2016). These techniques are planned to be employed in future haloscopes experiments as DM-Radio which will target the $0.4\ \text{neV} \lesssim m_a \lesssim 800\ \text{neV}$ mass range (Brouwer et al., 2022a; Brouwer et al., 2022b).

2.4.2 Astrophysical searches

Since axions are extremely weakly coupled to SM particles, an abundant production can be achieved only under extreme conditions of temperature and densities. For these reasons, stellar plasmas are an ideal environment for axion searches, since they can possibly emit large fluxes of such elusive particles giving rise to observable signatures. If the stellar source is nearby, as for the Sun, the axion emission can be directly detected in axion helioscopes (Altenmüller et al., 2024; Armengaud et al., 2019), while for further stars the expected flux on the Earth is suppressed. Nevertheless, axion emission can affect many different astrophysical observables, giving rise to a huge variety of indirect probes for the existence of the axion (Raffelt, 1996). Limits set by astrophysical observables are depicted as greenish areas in Figs. 2.5, 2.7 and 2.8.

Stellar energy-loss

Once produced in the interior of stellar core, axions can freely escape the stellar volume due to their extremely weak interaction with matter. Thus, they can open an additional energy sink for stellar cooling which may significantly alter the standard stellar evolution. Thus, axion emission can be related to various probes which must not be in conflict with observations (Raffelt, 2008; Caputo and Raffelt, 2024; Carenza, Giannotti, et al., 2025), setting stringent constraints on the axion parameter space. In this context, observations of Globular Clusters (GC), gravitationally bound systems of almost coeval low-mass stars differing only for their mass, can allow one to measure the relative duration of the RG and HB phases through the number of stars in the two evolutionary stages. Since RGs are degenerate, the Primakoff axion production is more efficient in HB stars (Raffelt and Dearborn, 1988). Thus, if axions are coupled only to photons, the HB lifetime would be reduced without altering the duration of the RG phase. From the analysis of 39 GCs, this argument allowed Ayala et al., 2014 to place the bound $g_{a\gamma} \lesssim 6.6\times10^{-11}$ GeV^{-1} at 95% CL for $m_a \lesssim 10$ keV. This bound has been extended to higher axion masses (up to few ~ 10 keV) in Carenza et al., 2020. Conversely, the strong electron degeneracy expected in the RG core, makes them a powerful tool to probe the axion-electron coupling g_{ae}. In these environments, the most efficient axion production mechanism is electron-ion bremsstrahlung

$e^- + Z\,e \to e^- + Z\,e + a$, which can open an additional cooling channel of the He core, increasing the critical mass to trigger helium ignition. This would lead to brighter RGs at the tip of the red giant branch, i.e. the stages immediately before the abrupt transition to the HB phase. Studies in this direction ruled out axion-electron couplings $|g_{ae}| \gtrsim 4.3 \times 10^{-13}$ at 95% CL (Capozzi et al., 2020; Straniero et al., 2020). The coupling to electrons opens efficient energy loss channels also in other electron degenerate environments as the interior of WDs. Analysis of the WD luminosity function, i.e. the number of stars per unit volume and luminosity interval, excluded $g_{ae} \gtrsim 3 \times 10^{-13}$ (Isern et al., 2008; Isern et al., 2009). Furthermore, CC SNe provide unique conditions to study axion couplings to SM particles. Indeed, the extremely high temperatures ($T \sim 30$ MeV) expected in the interior of a SN core may allow the production of axions up to masses $\sim \mathcal{O}(100)$ MeV. In this case, the physical observable consists in the duration of the neutrino burst deduced from SN 1987A, which would be shortened in case of an excessive energy-loss in exotic particles. The SN energy-loss argument places relevant constraints for massive axions coupled to photons (Lucente et al., 2020; Caputo et al., 2022a) and to electrons (Lucente and Carenza, 2021; Ferreira et al., 2022; Fiorillo, Pitik, et al., 2025b). Remarkably, SNe represents the most constraining system up to date for axions coupled to nucleons. Indeed, the dense nucleon-rich SN core hosts ideal conditions for the production of axions via nuclear processes as NN bremsstrahlung $N + N \to N + N + a$ and pionic Compton-like processes $N + \pi \to N + a$. In Chapter 3 we will describe in details axion production mechanisms in the SN nuclear medium. Here, it is worthwhile to mention that the SN cooling argument rules out axion-nucleon couplings such that (Lella et al., 2023)

$$g_{an}^2 + 1.10\, g_{ap}^2 - 0.26\, g_{an}\, g_{ap} > 7.8 \times 10^{-19}\,, \tag{2.25}$$

for $m_a \lesssim 10$ MeV. Within its uncertainties, this limit translates is the most stringent astrophysical constrain up to date on the QCD axion mass. In particular, in hadronic axion models, as the KSVZ model, the SN cooling argument excludes axions with masses $m_a \gtrsim 8$ meV. In parallel to SNe, NSs are another powerful laboratory to search for signatures of axions coupled to nuclear matter. In particular, Buschmann et al., 2022 studied the cooling light curves of a sample of five isolated NSs, imposing the bound $|g_{ap}| \lesssim 1.5 \times 10^{-10}$ ($|g_{an}| \lesssim 1.3 \times 10^{-10}$) on the axion-proton(neutron) cou-

pling. Moreover, observations of the NS in the SN remnants Cassiopeia A and HESS J1731-347 imply $g_{ap} \lesssim 5 \times 10^{-9}$ (Sedrakian, 2016) and $g_{an} \lesssim 3 \times 10^{-10}$ (Beznogov et al., 2018), respectively.

Axion-induced signatures in photon fluxes

Astrophysical environments can host powerful large-scale magnetic fields, where axions produced in astrophysical sources may efficiently convert in photons. Here we recall that the axion-photon conversion probability in the coherent regime goes as $P_{a\gamma} \propto g_{a\gamma} B^2 L^2$. Thus, seizable conversion probabilities can be achieved in magnetic domains either hosting strong magnetic fields B or showing long correlation lengths L. Extremely intense stellar magnetic fields are hosted by neutron stars and magnetic white dwarfs, where B-fields can reach values as high as $B \sim 10^{12}\,\mathrm{G}$ and $B \sim 10^{9}\,\mathrm{G}$ respectively (Raffelt, 1996). Conversely, magnetic fields hosted by galaxies are much weaker than stellar fields ($B \sim 1\,\mu\mathrm{G}$), but magnetic domains show much larger sizes $L \sim 10$ kpc, giving rise to efficient axion-photon conversions. Photon spectra from distant sources, as Active Galactic Nuclei (AGN), could show modulations due to axion-photon oscillations. Searching for these irregularities can place stringent bounds. In particular, Chandra observations at X-ray energies of the NGC 1275 galaxy, excludes $g_{a\gamma} > 8 \times 10^{-13}$ GeV^{-1} at 99.7% CL for $m_a \lesssim 10^{-11}$ eV (Reynolds et al., 2020). Furthermore, the cumulative axion flux emitted by the stellar population of nearby starburst galaxies as M82 can be converted in hard X-rays in the galaxy magnetic field. Searches for this X-ray excess conducted with the NuStar telescope place strong constraints, $g_{a\gamma} \lesssim 7 \times 10^{-13}$ GeV^{-1} at 95% CL for $m_a \lesssim 10^{-10}$ eV (Ning et al., 2025a). Axion-photon conversions may also affect other physical observables, as the polarization of light emitted from WDs. Recent observations of the WD J033320+000720 by the Lick Observatory allowed the exclusion of $g_{a\gamma} \gtrsim 1.7 \times 10^{-12}$ GeV^{-1} at 95% CL for $m_a \lesssim 2 \times 10^{-7}$ eV (Ning et al., 2025b), which is the most stringent constraint in the range of masses 10^{-10} eV $\lesssim m_a \lesssim 10^{-7}$ eV. Furthermore, observations of a population of 27 nearby pulsars to search for axion resonant conversions in pulsars magnetospheres imposed the limit $g_{a\gamma} \gtrsim 10^{-12}$ GeV^{-1} for $m_a \approx 10^{-6}$ eV (Noordhuis et al., 2022).

A widely-studied scenario relies on axions produced by Primakoff effect in the

SN core. Light axions may have produced a gamma-ray signal due to conversions in the Milky-Way magnetic fields in coincidence to SN 1987A neutrino burst. The absence of any signal in the Gamma-Ray Spectrometer (GRS) on board of the Solar Maximum Mission (SMM) constrains the axion-photon coupling to $g_{a\gamma} \lesssim 4.2 \times 10^{-12}$ GeV^{-1} for $m_a \lesssim 4 \times 10^{-10}$ eV (Brockway et al., 1996; Grifols, Masso, and Toldra, 1996; Payez et al., 2015; Hoof et al., 2023). On the other hand, heavy axions with masses $m_a \gtrsim 1$ MeV produced in the hot SN core may decay in photon pairs when traveling sufficiently long distances. Depending on their decay length, these axions may give rise to different observable signatures. When decaying outside from the star volume along their path to the Earth they can induce an observable gamma-ray signal. Once again, the non observation of such signal in SMM data following SN 1987A excluded 10^{-12} GeV$^{-1} \lesssim g_{a\gamma} \lesssim 10^{-10}$ GeV^{-1} for $m_a \sim 100$ MeV (Jaeckel et al., 2018; Hoof et al., 2023; Müller et al., 2023b). Conversely, when decaying in the stellar envelope, heavy axions might affect the measured explosion energy of low-energy SNe. This effect rules out 4×10^{-10} GeV$^{-1} \lesssim g_{a\gamma} \lesssim 3 \times 10^{-7}$ GeV^{-1} for $m_a \sim 100$ MeV (Caputo, Janka, et al., 2022; Fiorillo, Pitik, et al., 2025a). The parameter space in between the latter constraints is excluded by ruling out the axion-sourced fireball scenario in coincidence to the Binary Neutron Star (BNS) merger event GW170817 (Diamond, Fiorillo, Marques-Tavares, Tamborra, et al., 2024).

Chapter 3

Signatures of supernova axions: impact on the neutrino burst

In this Chapter we characterize the production of axions by means of their couplings to nuclear matter during a SN explosion. In this context, we will extend the results of previous literature to the case of axions with masses larger than the SN core temperature ($m_a \gtrsim T \sim 30$ MeV) and to the case of axions strongly-coupled with nuclear matter. In particular, in Sec. 3.1 we introduce the main axion production channels in the SN nuclear medium. In Sec. 3.2 we focus on weakly-coupled free-streaming (with axion-nucleon coupling $g_{aN} \lesssim 10^{-8}$) massive axions, detailing the corresponding emission spectrum in Sec. 3.2.1. Subsequently, in Sec. 3.2.2 we calculate the axion luminosity and compare it with the expected SN neutrino luminosity to exclude regions of the parameter space that would lead to an excessive axion production, shortening the SN ν burst (Sec. 3.2.2). In Sec. 3.3 we extend the analysis to strongly-coupled axions ($g_{aN} \gtrsim 10^{-7}$) which are trapped in the SN core. Moreover, we discuss the features of axion spectra in the trapping regime (Sec. 3.3.1) and we compute the modified luminosity to smoothly extend the cooling bound from the free-streaming to the trapping regime (Sec. 3.3.2). Uncertainties on the cooling bound are analyzed in Sec. 3.3.3. Finally, we discuss the implications on canonical QCD axion models in Sec. 3.3.4. This Chapter is mainly based on:

(P1) A. Lella, P. Carenza, G. Lucente, M. Giannotti, A. Mirizzi, *Protoneutron stars as cosmic factories for massive axionlike particles*, Phys.Rev.D

107 (2023) no.10, 103017 [arXiv:2211.13760 [hep-ph]].

(P2) A. Lella, G. Co', P. Carenza, G. Lucente, M. Giannotti, A. Mirizzi, T. Rauscher, *Getting the most on supernova axions*, Phys.Rev.D **109** (2024) no.2, 023001 [arXiv:2306.01048 [hep-ph]].

3.1 The state-of-the-art

Core-collapse supernovae (CC SNe) are among the most powerful astrophysical laboratories to probe axion physics (see, e.g., Raffelt, 1996; Raffelt, 2008; Caputo and Raffelt, 2024; Carenza, Giannotti, et al., 2025 for some reviews). Indeed, as discussed in Chapter 1, the series of catastrophic events occurring during a SN explosion can induce extreme thermodynamical conditions in the SN core, with temperatures $T \sim 30 - 40$ MeV and densities $\rho \sim 10^{14}$ g cm^{-3}. These would lead to a copious production of axions up to masses $m_a \sim 100$ MeV, since the emission of heavier axions would be significantly reduced due to Boltzmann suppression $\sim e^{-m_a/T}$. If axion emission from the protoneutron star (PNS) is too efficient, it may impact observably the SN neutrino burst, leading to a shortening of the duration of the signal expected from SN simulations, which is barely in agreement with SN 1987A observations (see Sec. 1.4.4). In this regard, the *energy-loss* or *Raffelt* criterion (see Sec. 1.4.4) has been widely employed in literature to constrain axion couplings to photons (Lucente et al., 2020; Caputo et al., 2022a), to electrons (Lucente and Carenza, 2021; Ferreira et al., 2022; Fiorillo, Pitik, et al., 2025b), to muons (Bollig, DeRocco, et al., 2020; Caputo et al., 2022a) and to set limits on the EDM coupling (Graham and Rajendran, 2013; Lucente et al., 2022). Nevertheless, if axions are coupled to nucleons, it was soon realized that production in the SN nuclear medium, composed by nucleons, pions and baryonic resonances, would dominate over all the other possible emission channels. This scenario has been intensively studied in a number of papers (Turner, 1988; Raffelt and Seckel, 1988; Mayle, Wilson, Ellis, et al., 1988; Burrows et al., 1989; Burrows et al., 1990; Raffelt, 1990a; Engel et al., 1990; Turner, 1992; Hanhart et al., 2001; Raffelt and Seckel, 1995; Keil, Janka, Schramm, et al., 1997; Fischer, Chakraborty, et al., 2016; Carenza et al., 2019; Carenza et al., 2021). We underline that all of these works focused on the case of free-streaming axions with axion-nucleon cou-

plings $g_{aN} \lesssim 10^{-8}$ (see Sec. 1.4.4). In particular, they focus on the case massless axions, i.e. axions with masses much smaller than the SN core temperature $m_a \ll T \sim 10$ MeV, and lack a proper approach to smoothly connect the free-streaming and trapping regimes.

3.1.1 Emissivity processes

At energy scales below the QCD phase transition $\Lambda_{\rm QCD} \sim 250$ MeV, axion interactions with hadrons can be derived in the context of the Heavy Baryon Chiral Perturbation Theory (HBChPT) (Jenkins et al., 1991). Following this approach, interaction vertices with hadrons relevant for axion production at SN temperatures are encoded in the following Lagrangian (Chang and Choi, 1993; Di Luzio et al., 2020; Choi et al., 2022; Ho et al., 2023)

$$\begin{aligned}\mathcal{L}_{\rm int} = g_a \frac{\partial_\mu a}{2m_N} \Bigg[& C_{ap} \bar{p}\gamma^\mu\gamma_5 p + C_{an}\bar{n}\gamma^\mu\gamma_5 n + \\ & + \frac{C_{aN\pi}}{f_\pi}(i\pi^+\bar{p}\gamma^\mu n - i\pi^-\bar{n}\gamma^\mu p) + \\ & + C_{aN\Delta}\left(\bar{p}\,\Delta^+_\mu + \overline{\Delta^+_\mu}\,p + \bar{n}\,\Delta^0_\mu + \overline{\Delta^0_\mu}\,n\right)\Bigg] ,\end{aligned} \tag{3.1}$$

where g_a is a dimensionless constant characterizing the axion coupling with nuclear matter,[1] $f_\pi = 92.4$ MeV is the pion decay constant, $C_{aN\pi} = (C_{ap} - C_{an})/\sqrt{2}g_A$ (Choi et al., 2022) and $C_{aN\Delta} = -\sqrt{3}/2\,(C_{ap} - C_{an})$, with $g_A \simeq 1.28$ (Navas et al., 2024) being the axial coupling. The first line in Eq. (3.1) contains axion-nucleon couplings already discussed in Sec. 2.3, while the second term gives rise to a four-particle interaction vertex, dubbed contact interaction vertex, whose contribution to the axion emissivity was originally discussed in Carena et al., 1989 and recently re-discussed in Choi et al., 2022. Finally, the last term describes the axion couplings to the Δ-resonance which has an observable impact on axion emissivity, as recently discussed in Ho et al., 2023. It is convenient to define the axion couplings with protons and neutrons as $g_{aN} = g_a\, C_{aN}$, for $N = p, n$, where C_{aN} are model-dependent coupling constants of order unity. The choice of the values assumed by these

[1] In the literature, especially that concerning QCD axions, it is common to find axion couplings expressed in terms of the axion decay constant, f_a. For axions interacting with nucleons, g_a and f_a are related as $g_a = m_N/f_a$.

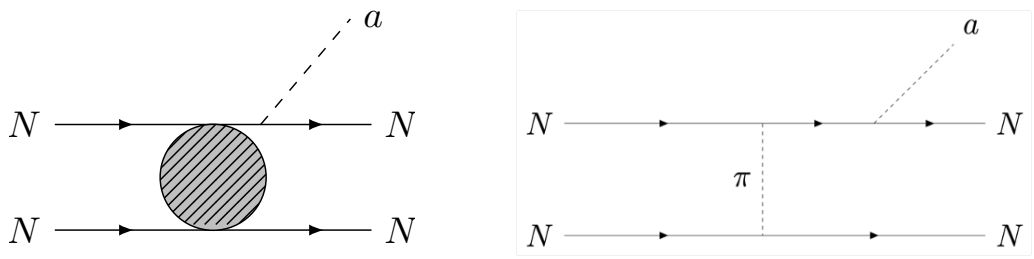

Figure 3.1: Schematic representation of axion emission via NN bremsstrahlung involving a generic nucleon interaction potential (left panel) and the OPE potential (right panel).

coupling constants leads to some uncertainties on the estimation of SN axion emission rates. Nevertheless, these are typically subleading compared to uncertainties introduced by the astrophysical modeling of the SN explosion event. Thus, to set the stage for our computations, in this Thesis work we will often refer to benchmark values inspired by the KSVZ axion model $C_{ap} = -0.47$ and $C_{an} = 0$ (Grilli di Cortona et al., 2016), unless otherwise stated.

Nucleon-nucleon bremsstrahlung

The first considered axion production channel in the SN nuclear medium is NN bremsstrahlung $N + N \to N + N + a$ (Iwamoto, 1984; Carena et al., 1989; Brinkmann et al., 1988; Turner, 1992; Keil, Janka, Schramm, et al., 1997). As shown by the Feynman diagram in the left panel of Fig. 3.1, in this process an axion is produced from a nucleon scattering mediated by strong interactions at finite density in the SN nuclear medium. The first naive computations for the NN bremsstrahlung emission rate relied on the One-Pion-Exchange (OPE) approximation (right panel), in which the nuclear interaction potential is modeled through the exchange of a single massless pion. A first attempt to take into account corrections beyond the OPE approximation has been performed in (Chang et al., 2018) by including phenomenological form factors in the axion emissivity. However, it was soon realized that this approach was overestimating the axion emissivity. The state-of-the-art calculation for the bremsstrahlung emission rate has been performed in Carenza et al., 2019, accounting for corrections beyond the OPE approximation directly in the nuclear interaction potential and matrix element. In particular,

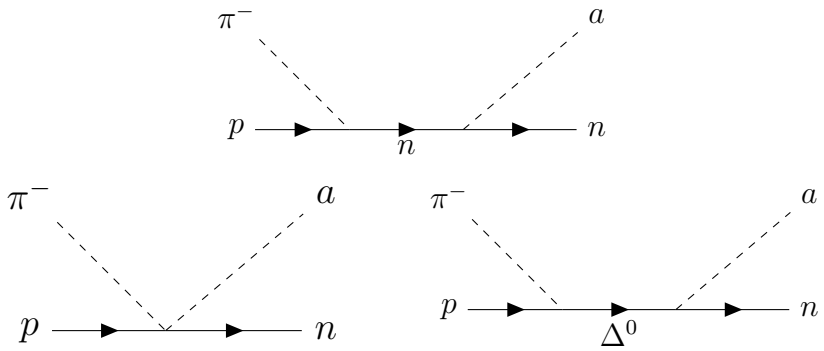

Figure 3.2: Feynmann diagrams for pionic Compton-like processes. The top panel illustrates nucleon mediated diagrams, the bottom-left panel refers to contact interaction diagrams and the bottom-right panel depicts Δ-mediated diagrams.

it was shown that non-vanishing mass for the exchanged pion (Stoica et al., 2009), effective in-medium nucleon masses (Iwamoto, 1984; Martinez-Pinedo et al., 2012; Hempel, 2015) and multiple nucleon scattering effects (Raffelt and Seckel, 1991; Janka, Keil, et al., 1996) have to be taken into account to obtain a reliable estimation of the bremsstrahlung emissivity. Furthermore, the nuclear potential must account for additional terms due to two-pion exchange, which can be modeled through nucleon interactions mediated by a meson ρ of mass $m_\rho \approx 600$ MeV (Ericson et al., 1989). These effects globally result in a reduction of factor $\sim$few of the SN axion emissivities compared to the OPE estimation, leading to the SN cooling constrain $g_{ap} \lesssim 1.2 \times 10^{-9}$ for axion masses $m_a \lesssim 1$ MeV. In this context, we also mention the work of Springmann et al., 2025 which employed a self-consistent approach to SN axion emissivity by taking into account the impact of finite-density effects on axion couplings.

Pionic Compton-like processes

Another possible axion production channel involving nuclear couplings relies on pionic Compton-like processes $\pi + N \to a + N$, in which a thermal pion in the nuclear medium is converted into an axion when scattering over a non-relativistic nucleon (Turner, 1992; Raffelt and Seckel, 1995; Keil, Janka, Schramm, et al., 1997). Since the fraction of thermal pions in the hot and

dense SN core was expected to be relatively small $Y_\pi \sim \mathcal{O}(10^{-4})$, the contribution to axion emissivity due to pionic processes has been overlooked for a long time. Afterwards, Fore and Reddy, 2020 pointed out that the number density of negatively charged pions can be significantly enhanced by strong interactions taking place at typical SN conditions. Thus, Carenza et al., 2021 re-estimated axion emissivity via $\pi^- + p \to a + n$ under the assumptions of Fore and Reddy, 2020, realizing that it may become competitive with NN bremsstrahlung. Moreover, while Carenza et al., 2021 took into account only nucleon mediated diagrams as the one depicted in the top panel of Fig. 3.2, recent works have shown that the contributions of the contact interaction diagram (lower-left panel) (Choi et al., 2022) and the $\Delta(1232)$-mediated diagrams (lower right panel) (Ho et al., 2023) can even enhance axion emissivities via pion conversions.

In the following sections we will discuss the extension of these results to the case massive axions with masses up to $m_a \sim 100$ MeV and to the case of trapped axions for axion-nucleon couplings $g_{aN} \gtrsim 10^{-7}$.

3.2 Supernova emissivities at finite axion mass

As discussed in the previous Sections, the role of the axion mass in the emission rates has been overlooked by classical literature investigating the case of SN axions coupled to nucleons. Nonetheless, the extremely-high temperatures expected in the inner SN core may allow an efficient production of axions up to masses $m_a \lesssim 3T \approx 90$ MeV. At larger masses, the production rate would be suppressed by the Boltzmann factor $e^{-m_a/T}$ and by the axion velocity $\beta_a \sim 3T/m_a$. In this regard, we highlight that the parameter space of axions coupled with nucleons at masses $m_a \gtrsim 10$ MeV is very poorly constrained. Therefore, CC SNe are unique laboratories to probe the axion-nucleon coupling in these regions of the parameter space. We highlight that in this Section we will always refer to free-streaming axions with $g_{aN} \lesssim 10^{-8}$, for which reabsorption effects in the SN nuclear medium are negligible.

Nucleon-nucleon bremsstrahlung

The effects of a finite mass in the axion emissivity have been first included in Giannotti et al., 2005, which focused on the NN bremsstrahlung process

within the OPE scheme. In Lella, Carenza, et al., 2023 we adopt the most general framework for axion interactions to go beyond this simplistic scenario, including all the relevant corrections beyond OPE in the emission rates , and introducing, for the first time, finite-axion-mass effects on pionic processes.

Starting from the interaction Lagrangian in Eq. (3.1), the spin-summed matrix element for massive axions with masses $m_a \lesssim m_N$ emitted via NN bremsstrahlung reads (Giannotti et al., 2005)

$$S \sum_{\text{spins}} |\mathcal{M}|^2 = \left(\frac{|\mathbf{p}_a|}{E_a} \right)^2 |\mathcal{M}^{(0)}|^2 \,, \tag{3.2}$$

where E_a and $|\mathbf{p}_a|$ are the axion energy and momentum, respectively. Here, $|\mathcal{M}^{(0)}|^2$ is the squared modulus of the spin-summed matrix element in the massless case introduced in previous works (see, e.g., Brinkmann et al., 1988; Carenza et al., 2019), which differs from the matrix element for massive axion only by velocity factor $\beta_a = |\mathbf{p}_a|/E_a$. The axion spectrum per unit volume and unit time can be written as

$$\left(\frac{d^2 n_a}{dE_a \, dt} \right)_{NN} = \frac{g_a^2}{16\pi^2} \frac{n_B}{m_N^2} \left(E_a^2 - m_a^2\right)^{\frac{3}{2}} e^{-E_a/T} \, S_\sigma \left(\frac{E_a}{T} \right) \Theta(E_a - m_a) \,, \tag{3.3}$$

where n_B is the baryon density in the SN core, and the Heaviside-Θ function guarantees that the minimum axion energy is given by its mass. The previous expression is written in terms of the nuclear structure functions S_σ which encode the nuclear part of the matrix element (Raffelt, 1996)

$$S_\sigma(E_a) = \frac{\Gamma_\sigma}{E_a^2 + \Gamma^2} s(E_a/T) \,, \tag{3.4}$$

where $s(x)$ and the spin-fluctuation rate Γ_σ are given in Appendix A, and the line-width Γ is chosen in such a way to have a properly normalized structure function (see Appendix A for details). In particular, the Lorentzian line shape in front of structure functions in Eq. (3.4) accounts for nucleon multiple scattering (Raffelt, 1996), which makes nucleon energies uncertain at the moment of the interaction. We remark that structure function contains all the corrections beyond the OPE approximation introduced in Carenza et al., 2019, accounting for two pion exchanges in the nuclear interaction potential (Ericson et al., 1989) and effective nucleon masses inside the SN core (Iwamoto, 1984; Martinez-Pinedo et al., 2012; Hempel, 2015). Our work

also took into account the contribution coming from the contact interaction term, neglected in (Carenza et al., 2019). In agreement with previous literature (Carena et al., 1989; Choi et al., 2022), we have obtained that this term has negligible impact on the axion emission rate since it gives contributions of higher order in $1/m_N$ compared to other diagrams.

Pionic Compton-like processes

In case of an enhanced abundance of negatively-charged pions as in the scenario outlined in Fore and Reddy, 2020, pionic Compton-like processes become competitive with NN bremsstrahlung for typical SN conditions. Therefore, it is worthwhile to extend also the results of Carenza et al., 2021 by including non-vanishing axion mass effects. In particular, the pion conversion axion emission spectrum per unit volume can be written as

$$\begin{aligned}\left(\frac{d^2 n_a}{dE_a\, dt}\right)_{N\pi} &= \frac{g_a^2 T^{3.5}}{2^{1.5}\pi^5 m_N^{0.5}} \left(\frac{g_A}{2f_\pi}\right)^2 \left(E_a^2 - m_a^2\right)^{\frac{1}{2}} \\ &\times \mathcal{C}_a^{p\pi^-} \frac{\Theta(E_a - m_\pi)\,\Theta(E_a - m_a)}{\exp\{(x_a - y_\pi - \hat{\mu}_\pi)\} - 1} \left(E_a^2 - m_\pi^2\right)^{\frac{1}{2}} \\ &\times \int_0^\infty dy\, y^2 \frac{1}{\exp\{(y^2 - \hat{\mu}_p)\} + 1} \frac{1}{\exp\{(-y^2 + \hat{\mu}_n)\} + 1}\,,\end{aligned} \tag{3.5}$$

where m_π is the pion mass, $y_\pi = m_\pi/T$, $x_a = E_a/T$, $\hat{\mu} = (\mu - m)/T$, with μ being the pion and nucleon chemical potentials, and the product of the Heaviside theta functions fixes the minimal threshold energy for the process. Here, $\mathcal{C}_a^{p\pi^-}$ can be written as

$$\mathcal{C}_a^{p\pi^-} = \frac{m_N^2}{g_A^2\, T^2}\, \beta_a^2\, \mathcal{G}_a(|\mathbf{p}_\pi|)\,, \tag{3.6}$$

in which $|\mathbf{p}_\pi| = \sqrt{E_a^2 - m_\pi^2}$ is the modulus of the pion three-momentum. The complete expression for $\mathcal{G}_a(|\mathbf{p}_\pi|)$ is given in Appendix A. We highlight that, analogously to NN bremsstrahlung, the squared matrix element for the emission of massive axions via pion conversion differ from the massless result in Carenza et al., 2021; Choi et al., 2022; Ho et al., 2023 by a factor β_a^2. Moreover, we observe that Δ-mediated and contact interaction diagrams give rise to terms of the same order as the ones related to nucleon-mediated diagrams. Therefore, these additional contributions enhance SN axion emissivity at least by a factor of ~ 2 in the whole mass range of interest $m_a \lesssim 300$ MeV.

3.2.1 The axion energy spectrum

When considering the emission for an observer at large distance from the production point, the strong gravitational potential inside the PNS may significantly affect the axion emission spectrum. These effects result in the time dilation of rates and in the red-shifting of axion energies (Caputo et al., 2022a; Calore et al., 2022a). In particular, the energy observed at infinity E_a^* is shifted with respect to the energy at the production point E_a as

$$E_a^* = \alpha(r)\, E_a \,, \tag{3.7}$$

where $0 < \alpha(r) \leq 1$ is the so-called "lapse factor", which encodes the effects due to the PNS gravitational potential $\Phi(r)$ in the PNS interior. The values of α are extracted directly from the SN simulation employed in the computation of the emission rates (see, e.g., Kuroda, Fischer, et al., 2022). Analogously, time intervals observed at infinity are dilated by the gravitational potential as follows

$$dt^* = \alpha^{-1}(r)\, dt \,, \tag{3.8}$$

where the dt refers to the local observer time interval at distance r from the center, while dt^* is the simulation time, corresponding to the time interval of a distant observer. With these definitions, the local axion emission spectrum integrated over the SN volume and over the given time window is computed as

$$\frac{dN_a}{dE_a}(E_a) = \int d^3r\, dt\, \frac{d^2 n_a}{dE_a dt}(r, t, E_a) \,. \tag{3.9}$$

Massive axions with $m_a \sim T$ can also interact gravitationally with the extremely-dense SN core. Thus, the only axions escaping the stellar gravitational field are those produced with sufficiently high kinetic energy. Relativistically, this effect translates in the condition $E_a > m_a/\alpha(r,t)$ (see, e.g., Caputo, Janka, et al., 2022).

The axion production spectra are here computed numerically by employing our benchmark spherically-symmetric `GARCHING` group's SN model SFHo-s18.8, described in details in Sec. 1.4.1. We underline that `GARCHING` group's simulations do not account for the presence of pions in the SN core, since the pion properties in PNS matter are still under debate. Therefore, we estimated the pion chemical potential and a pion abundance by employing the procedure proposed in Fore and Reddy, 2020; Fischer et al., 2021. In particular, pion abundances can be calculated by requiring thermal and chemical

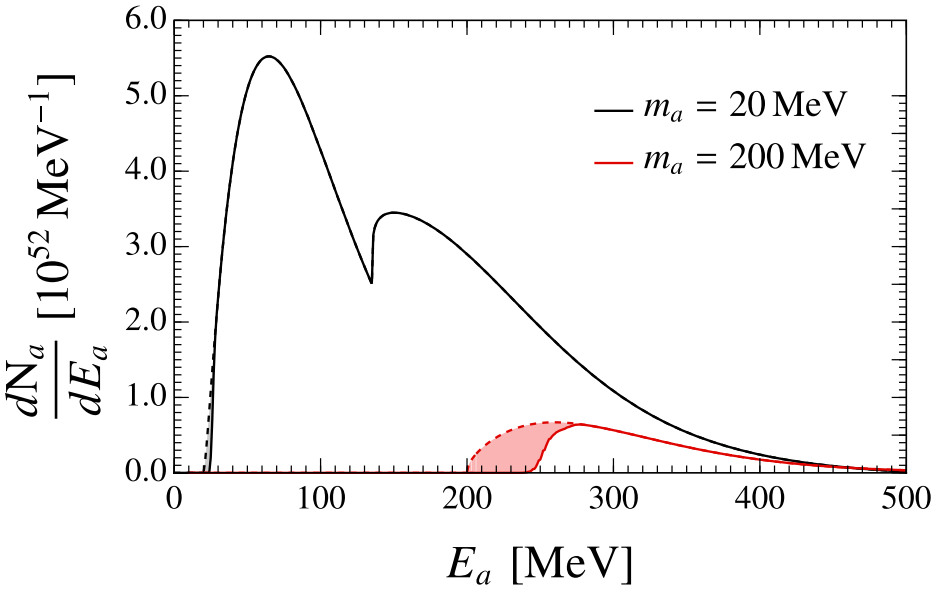

Figure 3.3: Axion energy spectra for $g_{ap} = 10^{-10}$ and $g_{an} = 0$ and for two representative masses, $m_a = 20$ MeV (black curve) and $m_a = 200$ MeV (red curve), integrated over 10 s after the core bounce. Dashed curves refer to the total production spectrum including gravitationally trapped axions while solid curves depict the spectrum of axions escaping the PNS gravitational potential (see text for details). The spectra of gravitationally trapped axions are depicted as shaded bands.

equilibrium conditions for a gas of massive and relativistic bosons. This implies that pions have a chemical potential $\mu_{\pi^\pm} = \mp\hat{\mu}$, where $\hat{\mu} = \mu_n - \mu_p$ is the difference between the neutron and the proton chemical potential, and $\mu_{\pi^0} = 0$ (Fischer et al., 2021). Therefore, due to the Boltzmann suppression factor, the abundance of negative pions $Y_{\pi^-} \propto \exp(\hat{\mu}/T)$ in the SN core is enhanced, compared to π^0 and π^+, when $\hat{\mu} \simeq m_\pi \simeq 139$ MeV (Carenza et al., 2021; Fischer et al., 2021). This post-processing addition of pions is justified as long as the impact of pionic matter on the PNS properties is not larger than the impact of muons. Moreover, we refer to axions extremely weakly-coupled with nuclear matter $g_{ap} \lesssim 10^{-8}$, so that the axion feedback on the SN simulation can be reasonably neglected in the whole time domain under investigation, allowing us to employ the unperturbed SN profile.

In Fig. 3.3 we show the local axion production spectra integrated over a time

window of 10 s for two representative masses, $m_a = 20$ MeV (black curves) and $m_a = 200$ MeV (red curves). As in the KSVZ axion model, here we assume $g_{an} = 0$ and $g_{ap} = 10^{-10}$ for the axion-neutron and axion-proton coupling, respectively. Dashed lines display the local emission spectrum in absence of gravitational effects including axions trapped inside the PNS gravitational field, while solid lines depict the spectrum of axions escaping the PNS gravitational potential. Thus, shaded regions in the figure delimit the energy range of gravitationally-trapped axions with $m_a < E_a < m_a/\alpha$. Remarkably, the axion spectrum corresponding to $m_a = 20$ MeV shows a bimodal shape, with peak at $E_a \sim 80$ MeV due to the NN bremsstrahlung, and the peak at $E_a \sim 200$ MeV associated to the pionic production. This behavior is not present for the $m_a = 200$ MeV case where, bremsstrahlung is completely subdominant with respect to pion conversion, because of Boltzmann suppression.

3.2.2 The axion luminosity and the cooling bound

The energy per unit time released in axions, i.e. the axion luminosity, is obtained by integrating the emission spectra over the SN volume and over the axion energy

$$L_a(t, m_a) = \int d^3r \;\; \alpha^2(r,t) \int dE_a \, E_a \frac{d^2 n_{\rm a}}{dE_a dt}(r, t, E_a, m_a) \;\; . \tag{3.10}$$

The behavior of the axion luminosity as a function of the axion mass for our benchmark SN profile at post-bounce time $t_{\rm pb} = 1$ s is displayed in Figure 3.4. The curves are obtained by assuming $g_{ap} = 6.5 \times 10^{-10}$ and $g_{an} = 0$. Interestingly, we observe that even at $m_a \lesssim 30$ MeV the contribution to luminosity given by pion conversion dominate over NN bremsstrahlung, since pionic processes produce axions with higher energies. Furthermore, the NN Bremsstrahlung rate becomes more and more subdominant as the axion mass increases, due to Boltzmann suppression. On the other hand, the energy threshold imposed by the pion mass m_π allows pion conversion production to be efficient up to masses $m_a \sim m_\pi$.

In a model-independent way, the axion luminosity can be expressed as a function of the axion-nucleon couplings through the following fitting formula

$$L_a \simeq \epsilon_0 \, (g_{an}^2 + b \, g_{ap}^2 - c \, g_{an} g_{ap}) \;\times 10^{70} \, {\rm erg \, s^{-1}} \, , \tag{3.11}$$

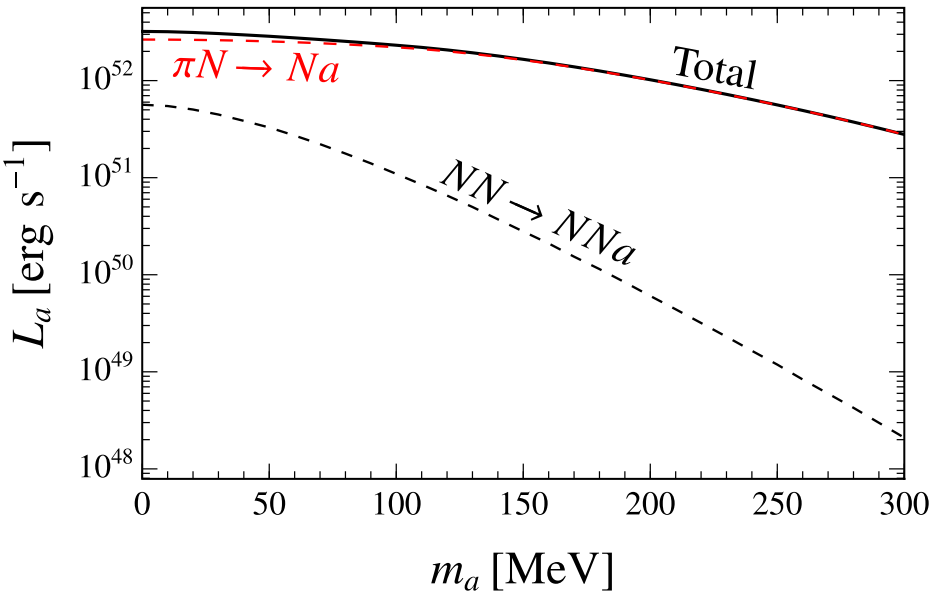

Figure 3.4: Axion luminosity at $t_{\rm pb} = 1$ s as a function of the axion mass for $g_{ap} = 5 \times 10^{-10}$ and $g_{an} = 0$. Black dashed line refer to NN Bremsstrahlung, red dashed line to pion conversion πN, while the total luminosity is displayed as a black solid line.

m_a (MeV)	ϵ_0	b	c
0	10.07	1.20	0.59
30	9.72	1.26	0.68
90	6.87	1.41	1.02
150	4.46	1.49	1.30

Table 3.1: Fitting parameters of axion luminosity in Eq. (3.11) for representative values axion masses.

where the values of the fitting parameters $\{\epsilon_0, b, c\}$ for some representative axion masses are given in Tab. (3.1). Notice that, differently from the result in Carenza et al., 2019, the minus sign in front of the mixed term parameter is due to the dependence of $C_{aN\pi}$ and $C_{aN\Delta}$ on C_{ap} and C_{an}.

The luminosity calculated in Eq. (3.10) con be employed to constrain the axion-nucleon couplings through the Raffelt criterion (Raffelt, 1990a; Caputo et al., 2022a). Indeed, to avoid an excessive shortening of the duration of the

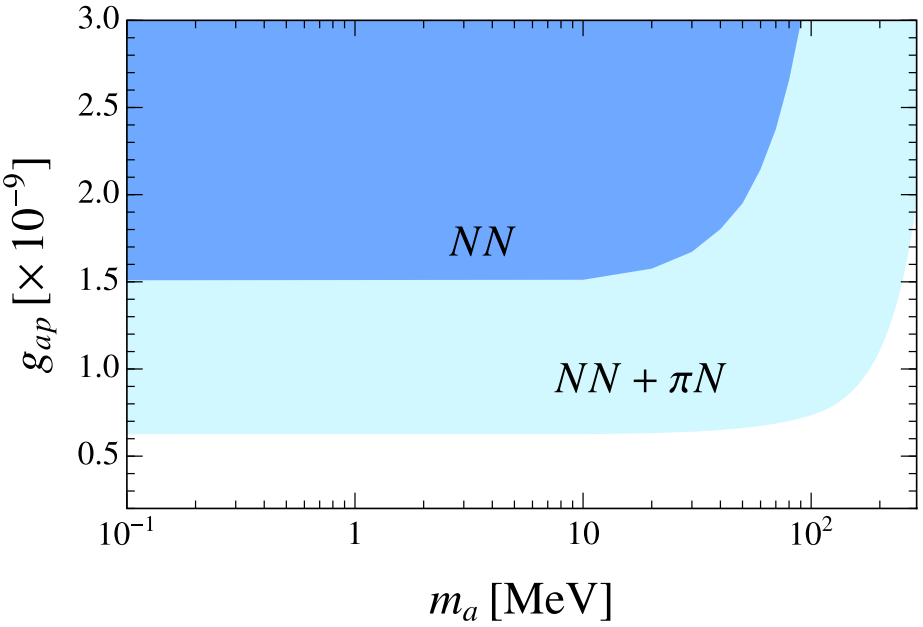

Figure 3.5: The SN cooling bound in the plane g_{ap} *vs* m_a placed in this work. The dark blue region refers to NN Bremsstrahlung only, while the light blue is referred to the total luminosity including also pionic processes.

neutrino burst expected from SN simulations, which is barely in agreement to SN 1987A observations, we require that

$$L_a \lesssim L_\nu \tag{3.12}$$

at $t_{\rm pb} = 1$ s. In particular, for the SN model employed in this work we have $L_\nu \simeq 5 \times 10^{52}$ erg s^{-1} at $t_{\rm pb} = 1$ s. Assuming $g_{an} = 0$ as in the KSVZ axion model, we exclude the light-blue region in Fig. 3.5, ruling out $g_{ap} \lesssim 6.5 \times 10^{-10}$ for $m_a \lesssim 30$ MeV. As expected, the exclusion region shrinks when including only NN in the computation of the emission rate (dark-blue region). We highlight that for axion masses $m_a \gtrsim m_\pi$ the cooling bound is set solely by pion conversion. These results update and extend to the case of axion masses $m_a \gtrsim 30$ MeV the outcomes of Carenza et al., 2019; Carenza et al., 2021.

3.3 The trapping regime

The SN cooling bound introduced in the previous Section, $g_{aN} \lesssim 6.5 \times 10^{-10}$ (Lella, Carenza, et al., 2023), cannot be extended to arbitrarily large values of the coupling strength. Indeed, at $g_{aN} \gtrsim 10^{-8}$ the SN nuclear medium becomes "optically thick" for propagating axions and we are not allowed to neglect absorption effects in axion emissivities anymore. In particular, axions produced in the inner regions of the PNS cannot freely escape the PNS volume and become trapped inside the inner SN core, analogously to neutrinos (Raffelt and Seckel, 1988).

The behavior of axions coupled with nuclear matter in the *trapping regime* has been investigated in some seminal papers after SN 1987A (Raffelt and Seckel, 1988; Burrows et al., 1990) and, more recently, in Carenza et al., 2019. However, all of these works treated free-streaming and trapped axions separately, lacking for a proper approach to smoothly connect the two regimes. To cover this gap, in Lella et al., 2023 we have applied the recently-formulated "modified luminsity criterion" (Chang et al., 2017; Chang et al., 2018; Lucente et al., 2020; Caputo et al., 2022a), which we will describe in details below, to the case of axions coupled to nucleons. This procedure allowed us to properly compute the axion luminosity in the case of strongly-coupled axions, extending the SN cooling bound introduced in Lella, Carenza, et al., 2023 to the case of axion trapping.

The behavior of the axion luminosity at $t_{\rm pb} = 1$ s as a function of the axion-proton coupling g_{ap} is displayed in Fig. 3.6 for some representative axion masses. For illustration purposes, here we assume $g_{an} = 0$, in analogy with the KSVZ axions, that we adopted as our benchmark model. Notably, the axion luminosity in the free-streaming regime grows quadratically with the coupling, and their emission can be considered volumetric (see Sec. 1.4.4). After reaching the luminosity peak, axions start to be efficiently reabsorbed in the medium suppressing the energy per unit time released in axions from the PNS. Under these conditions, massless-axion emission takes place in the form of blackbody radiation from a thin layer around a last-scattering surface at radius R_a and local temperature T_a. Thus, the axion luminosity in this regime scales $L_a \sim R_a^2 \, T_a^4$. As the axion coupling increases, the axion-sphere radius R_a increases while the temperature T_a rapidly decreases and the luminosity may eventually reach a plateau as already observed in other works employing

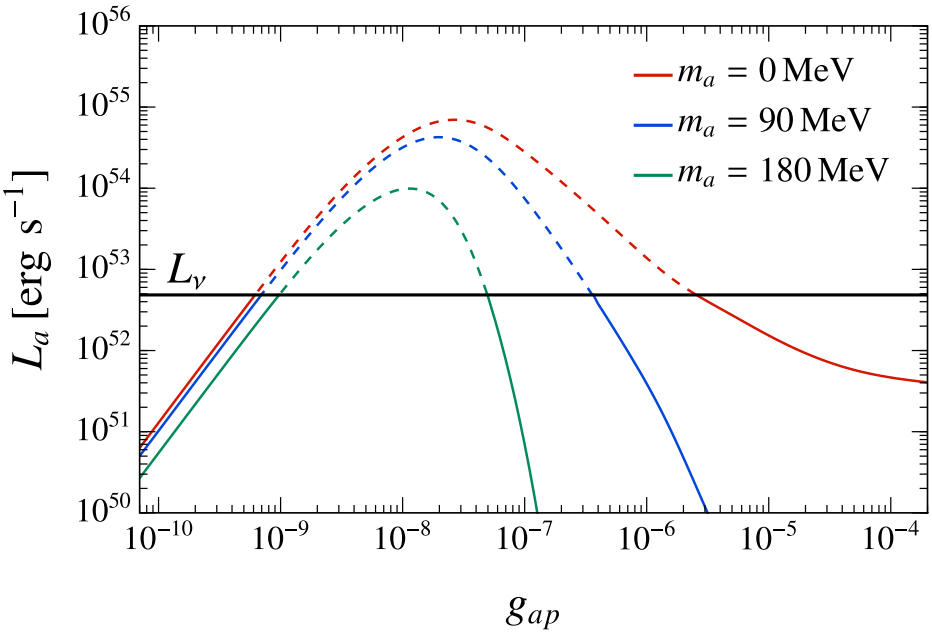

Figure 3.6: Axion luminosity at $t_{\rm pb} = 1$ s as a function of the axion-proton coupling g_{ap} for three different masses, assuming $g_{an} = 0$. The black line sets the value of the neutrino luminosity. Dashed lines depict the range of couplings where the axion luminosity exceeds the neutrino one.

the modified luminosity approach (Lucente et al., 2022). Conversely, the production of axions with masses $m_a \gtrsim 10$ MeV is dramatically suppressed in the trapping regime, since temperatures outside from the PNS never reach values high enough to permit the thermal production of such heavy particles.

3.3.1 Axion spectra in the trapping regime

For sufficiently high values of axion-nucleon couplings, axions produced via NN bremsstrahlung and pion conversion can be reabsorbed in the SN nuclear medium by means of the inverse processes, namely $N + N + a \to N + N$ and $N + a \to N + \pi$. The related axion mean free path (MFP) $\lambda_a(E_a, r)$ is immediately derived from the emission spectra introduced in Eq. (3.2) and Eq. (3.5) (Lella et al., 2023). All the details are provided in Appendix A. Accounting for axion reabsorption, the axion emission spectrum integrated over a spherically symmetric SN profile is given by (Chang et al., 2018;

Chang et al., 2017; Caputo et al., 2022a; Caputo et al., 2022b)

$$\frac{d^2N_a}{dE_a dt} = \int_0^\infty 4\pi r^2 dr \left\langle e^{-\tau(E_a^*,r)} \right\rangle \frac{d^2n_a}{dE_a dt}\,, \tag{3.13}$$

where r is the radial position with respect to the center of the SN core and $\tau(E_a^*, r)$ is the optical depth at a given axion energy and position. The exponential term $\langle \exp[-\tau(E_a^*, r)] \rangle$ encodes the absorption effects on SN axion emission. To account for axion emission in any direction, including backward, at each radial location, we take the average over the cosine of the emission angle μ (Caputo et al., 2022a),

$$\left\langle e^{-\tau(E_a^*,r)} \right\rangle = \frac{1}{2}\int_{-1}^{+1} d\mu\, e^{-\int_0^\infty ds\, \Gamma_a\left(E_a^*, \sqrt{r^2+s^2+2rs\mu}\right)}\,. \tag{3.14}$$

In this expression,

$$\Gamma_a(E_a, r) = \lambda_a^{-1}(E_a, r)\left[1 - e^{-\frac{E_a}{T(r)}}\right] \tag{3.15}$$

is the reduced absorption rate defined as in Caputo et al., 2022a. Notice that the optical depth is evaluated at

$$E_a^* = E_a \times \frac{\alpha(r)}{\alpha\left(\sqrt{r^2+s^2+2rs\mu}\right)} \tag{3.16}$$

to take into account the gravitational redshift from the point of axion production to the point of absorption.

The axion spectra displayed in Fig. 3.7 are computed numerically by employing the SFHo-s18.8 SN profile at $t_{\rm pb} = 1$ s, which we adopted as a benchmark. The variation of the spectral behavior of axion emission at different values of the axion-nucleon coupling can be appreciated from the the various curves referring to different coupling regimes. In particular, free-streaming axions ($g_{ap} = 3 \times 10^{-10}$, solid thick line) are characterized by the bimodal spectrum already illustrated in Sec. 3.2.1, where the peaks at $E_a \simeq 50$ MeV and $E_a \simeq 200$ MeV are associated to NN bremsstrahlung and pion conversion, respectively. As the coupling grows, both absorption and emission processes become efficient. When kinematically allowed ($E_a \geq m_\pi$), inverse pion conversion dominates over inverse bremsstrahlung, resulting in a significant reduction of the axion MFP. See Appendix A for further details.

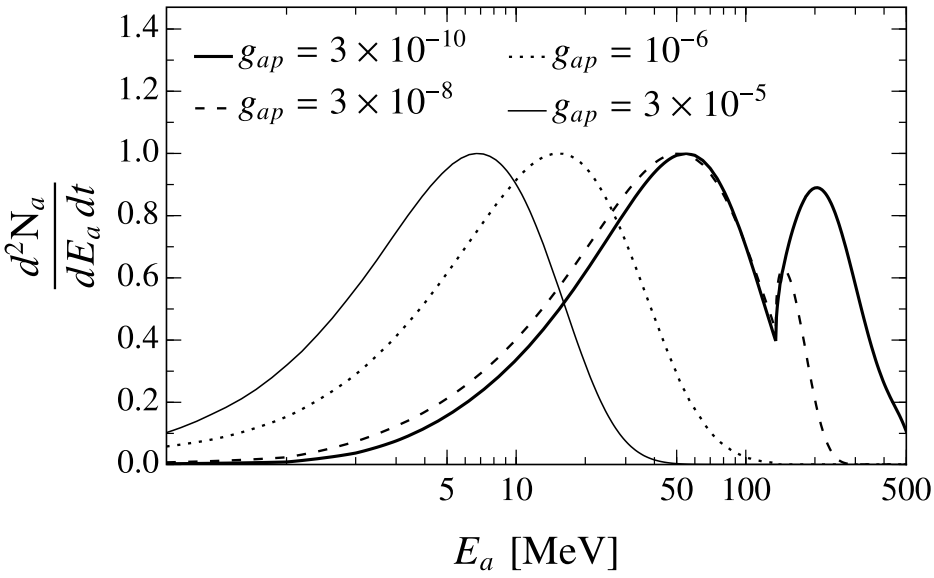

Figure 3.7: Normalized axion spectrum in the massless case at $t_{\rm pb} = 1$ s for different values of the axion-proton coupling g_{ap} and for $g_{an} = 0$.

Thus, the emission of axions with energies $E_a \geq m_\pi$ is suppressed, lowering the pion conversion peak for $g_{ap} = 3 \times 10^{-8}$ (dashed curve) while it is completely washed out for $g_{ap} = 10^{-6}$ (dotted curve) and $g_{ap} = 3 \times 10^{-5}$ (solid thin curve). Conversely, NN bremsstrahlung is a quasi-thermal process. Thus, the features of bremsstrahlung emission in the trapping regime reflect the behavior of the temperature profile in the layers where escaping axions are produced. Indeed, as the coupling increases, axions are more and more trapped inside the inner PNS and their emission takes place from outer layers, where temperature is lower. Thus, the axion average energy is reduced. For this reason, the energy range of bremsstrahlung-produced axions shift from $E_a \sim 50$ MeV for $g_{ap} = 3 \times 10^{-10}$ in the free-streaming case, down to $E_a \sim 6$ MeV for $g_{ap} = 3 \times 10^{-5}$ in the strongly-coupled case.

3.3.2 The modified luminosity criterion

Following the treatment in Caputo et al., 2022a; Chang et al., 2017; Lucente et al., 2020, the axion luminosity accounting for absorption effects can be

computed as

$$L_a = \int_0^{R_\nu} 4\pi r^2 dr \int_{m_a/\alpha}^{\infty} dE_a \, E_a \, \alpha(r)^2 \left\langle e^{-\tau(E_a,r)} \right\rangle \frac{d^2 n_a}{dE_a \, dt} \,, \tag{3.17}$$

where the lower limit of integration m_a/α cuts off the amount of massive axions trapped in the PNS gravitational potential (Caputo, Janka, et al., 2022; Lella, Carenza, et al., 2023; Lucente et al., 2020) and the integration over the radial coordinate extends up to the neutrino-sphere radius R_ν to take into account only the energy carried away by axions which can impact the neutrino burst. By applying the Raffelt criterion expressed by Eq. (3.12), we require that the modified luminosity computed in Eq. (3.12) does not exceed the neutrino luminosity at $t_{\rm pb} = 1$ s for the given SN model (Raffelt, 1996; Chang et al., 2017). By assuming vanishing axion-neutron coupling, we are allowed to rule out blue region in Fig. 3.8. In particular we exclude $6 \times 10^{-10} \lesssim g_{ap} \lesssim 2.5 \times 10^{-6}$ for $m_a \lesssim 10\,\text{MeV}$ and $7 \times 10^{-10} \lesssim g_{ap} \lesssim 3.5 \times 10^{-7}$ for $m_a \sim \mathcal{O}(100)\,\text{MeV}$. Interestingly, we observe the presence of an allowed region between the bound placed from searches for solar axions by the SNO (Solar Neutrino Observatory) experiment and the SN cooling bound introduced in Lella et al., 2023. As we will discuss in Sec. 4.1.3, this region of the parameter space can be excluded from the non observation of axion-induced events in KII in coincidence to SN 1987A.

The behavior of the cooling bound in the free streaming regime $g_{ap} \lesssim 10^{-8}$ has been already analyzed in Sec. 3.2.2. Thus, here we discuss the behavior of the contours in the trapping regime. Focusing on the mass range $m_a \lesssim 10$ MeV, in Sec. 3.3.1 we observed that at $g_{ap} \gtrsim 10^{-7}$ the only axions able to escape the SN core are those with energies energies lower than the pion mass $E_a \lesssim m_\pi$. In this energy range, the only kinematically-allowed absorption process is inverse bremsstrahlung, which is less efficient than pionic absorption (see Appendix A). Therefore, strong couplings are required to suppress enough the axion luminosity, thus saturating the cooling condition in Eq. (3.12) at $g_{ap} \simeq 2.5 \times 10^{-6}$. This bound updates the results of Carenza et al., 2019, in which a less refined criterion based on a rough calculation of the axion-sphere radius is employed to set the constrain in the trapping regime. Furthermore, Lella et al., 2023 also improves the results in Chang et al., 2018, which employed the modified luminosity criterion but did not take into account all the phenomenological corrections to the emission rates considered in this work.

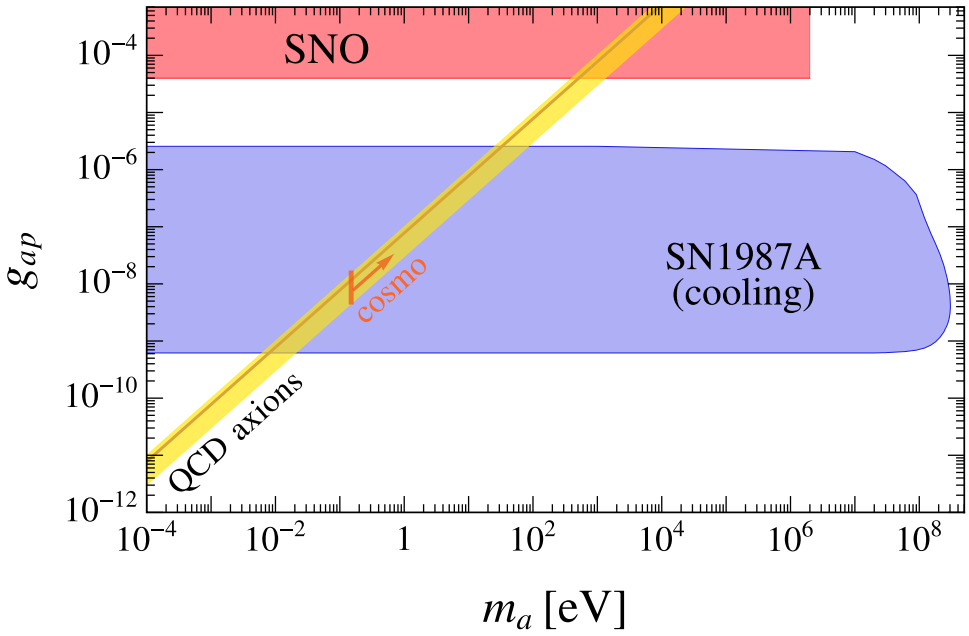

Figure 3.8: Summary plot of the bounds in the g_{ap} vs m_a plane together with the QCD axion band (in yellow). The region labeled SNO is excluded by the search for $p + d \to {}^3\mathrm{He} + a\,(5.5\,\mathrm{MeV})$ solar axion flux in SNO data (Bhusal et al., 2021). The blue region labeled SN 1987A is ruled out the SN cooling argument. The orange line with the arrow within the QCD axion band shows the sensitivity of current and future cosmological experiments, $m_a \gtrsim 0.15\,\mathrm{eV}$ (Archidiacono et al., 2015; D'Eramo et al., 2022). See the text for more details.

On the other hand, for axions with masses $m_a \gtrsim m_\pi$ pionic reabsorption is always kinematically allowed, thus the axion luminosity is dramatically reduced by reabsorption in the nuclear medium. Moreover, in this mass range Boltzmann suppression becomes effective, leading to a strong suppression of the production rates. For these reasons, both constraints in the trapping and free streaming regimes progressively relax, until the contour closes around $m_a \simeq 240$ MeV.

3.3.3 Uncertainties on supernova bounds

The SN cooling argument introduces one of the most stringent astrophysical constraint on the axion parameter space. Nevertheless, it might be affected by many sources of uncertainties. These are mainly related to the astrophysical modeling of the SN event, since axion emission rates in the dense PNS are expected to be extremely sensitive to the stellar properties. Thus, we devote this section to a discussion about the robustness of our results under variations in the SN profiles employed in the analysis. In particular, we focus on two important aspects: the dependence of SN bounds on the SN model used in computations and the presence of a relatively large fraction of pions inside the SN core.

Supernova models

As discussed in the previous Sections, the emission rates of axions coupled to nuclear matter are strongly dependent on the SN temperature and density profiles, which might change significantly from one SN model to the other. Therefore, it is worthwhile to estimate the impact on the SN cooling bound due to the choice of the simulation employed in the analysis. For this purpose, in addition to the study carried out with the `GARCHING` SFHo-18.8 SN model, we have also characterized axion emissivity by using a 1D spherically-symmetric general-relativistic SN model based on the `AGILE-BOLTZTRAN` code (Mezzacappa and Bruenn, 1993; Liebendoerfer et al., 2004) and launched from a 18 $M_\odot$ progenitor (Woosley, Heger, and Weaver, 2002), with a similar mass to the `GARCHING` SFHo-18.8 progenitor. The `AGILE-BOLTZTRAN` code enriches the set of neutrino weak interaction processes, but, on the contrary of the `GARCHING` model, does not account for any 1D treatment of convection. We also highlight that the `AGILE-BOLTZTRAN` model shows lower temperature and density in the SN core at $t_{\rm pb} = 1$ s compared to the `GARCHING` model. This is mainly due to the fact that the `AGILE-BOLTZTRAN` simulation is characterized by a cooling phase lasting for longer than the one predicted in `GARCHING` models, in which convection speeds up the cooling of the PNS. Therefore, at $t_{\rm pb} \simeq 1$ s the core of `AGILE-BOLTZTRAN` model has not reach the peak temperature yet.

In the upper panel of Fig. 3.9 we show the SN bounds obtained by employing the `GARCHING` model (blue regions delimited by solid lines) and the

AGILE-BOLTZTRAN model (delimited by dashed lines). We observe that the lower part of the contour is slightly relaxed when employing the AGILE -BOLTZTRAN profile. Indeed, due to the strong dependence of the axion emission rates on the SN temperature [see Eq. (3.2) and Eq. (3.5)], the higher temperature in the inner SN core predicted by GARCHING model enhances the production of weakly-coupled axions. Moreover, higher temperatures increase the fraction of negatively charged pions, resulting in a further enhancement of pion conversion emission rates. Nevertheless, higher temperatures and densities power neutrino emission as well, so that the neutrino luminosity from the GARCHING simulation at $t_{\rm pb} = 1$ s results to be 70% higher than in the AGILE-BOLTZTRAN simulation. Thus, the increase in neutrino luminosity partially counterbalances the enhancement of the axion luminosity in Eq. (3.12). Globally, we find that changing the SN model induces uncertainties in the order 25% percent on the SN cooling bound in the free streaming regime. Conversely, the two models show similar temperature profiles in the outer layers of the core. Therefore, since the emission of strongly-coupled axions takes place from the outer core, we do not observe any significant difference on the SN cooling constrain in the trapping regime as well.

This discussion highlights that differences in SN models, featuring different temperature and density profiles, impact axion and neutrino luminosities in a similar way. This implies that the cooling bound derived by setting the limit with the neutrino luminosities extracted from the given simulation is not expected to be dramatically affected by changes in the SN model employed.

Abundance of pions in the supernova core

The abundance of pions in dense environments close to the nuclear saturation density is strictly dependent on the EoS describing the environment. Despite pion abundances in the order of 1% are not expected to impact the standard explosion scenario, SN simulations still lack a self-consistent treatment for pionic matter in the EoS involved (see, e.g., Ref. Fore, Kaiser, et al., 2024 for recent developments). An estimate of the maximum uncertainty over the SN cooling bound related by the abundance of pions in the SN core can be obtained by switching off the pion conversion production channel, which is equivalent to assume a "worst case scenario" in which the pion fraction in the core is extremely suppressed. In absence of pions, the only viable axion pro-

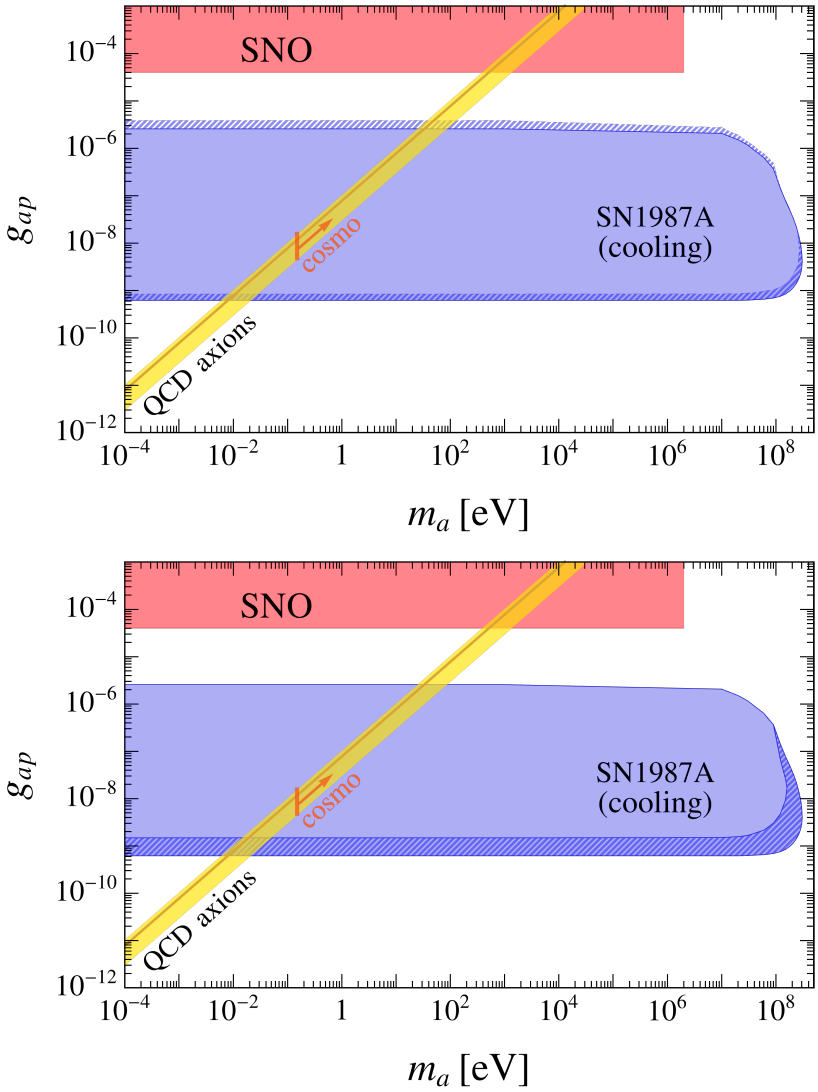

Figure 3.9: Summary of the uncertainties on the SN cooling bound in the g_{ap} vs m_a plane together with the QCD axion band. The color code is the same as Fig. 3.8. *Upper panel*: Solid thin lines delimit the region excluded by the `GARCHING` model while the dashed thick lines delineate the one excluded using the `AGILE-BOLTZTRAN` code. Uncertainties related to changes in the SN model are depicted as an hatched blue region. *Lower panel*: The blue hatched region shows the uncertainty related to the abundance of pions in the SN core.

duction channel is NN bremsstrahlung and axion emissivity is significantly reduced. As shown by the right panel of Fig. 3.9, the SN cooling bound in the free streaming regime is weakened by a factor ~ 2 in the mass range $m_a \lesssim 10$ MeV, setting at $g_{ap} \lesssim 1.6 \times 10^{-9}$. Moreover, since bremsstrahlung is more effected by Boltzmann suppression than pion conversion, in absence of pions the SN cooling argument does not allow one to probe axion masses $m_a \gtrsim 150$ MeV. On the other hand, in Sec. 3.3 we observed that pionic production is not relevant in the trapping regime. Therefore, the SN cooling bound at strong couplings $g_{aN} \gtrsim 10^{-7}$ is not affected by the absence of pions.

3.3.4 Implications for QCD axions

Canonical QCD axion models, described in Sec. 2.3.1, lie on the yellow band in Fig. 3.8. In case of QCD axions, the SN cooling bound can be translated in terms of constraints on the QCD axion mass. In particular, at given axion-nucleon coupling g_{aN}, the corresponding QCD axion mass can be obtained as (Navas et al., 2024)

$$m_a \simeq 6.06 \left(\frac{g_{aN}}{10^{-6}\, C_{aN}} \right) \text{eV} \,, \tag{3.18}$$

where the variability on the different axion models is encoded in the model dependent constants C_{aN}. The KSVZ axion model, here depicted as a dark yellow line, assumes fixed values for the model dependent constants (see Sec. 2.3.1). Thus, the SN cooling constraint on the KSVZ axion mass can be directly read from Fig. 3.9. Depending on the presence of pions inside the SN core, the upper bound imposed on the QCD axion mass varies in the range

$$m_a \in [8, 19] \text{ meV} \,. \tag{3.19}$$

The upper limit introduced in this work is comparable, within the uncertainties, to the results of Buschmann et al., 2022, in which the sutdy of the cooling lightcurves of isolated neutron stars has been employed to rule out QCD axions with $m_a \gtrsim 16$ meV. Since KSVZ axions are also provided with a coupling to photons, here we also mention the bound placed from observations of Globular Cluster (Ayala et al., 2014; Carenza et al., 2020) excluding $g_{a\gamma} \gtrsim 0.66 \times 10^{-10}$ GeV^{-1}, which can be translated in the bound $m_a \lesssim 440$ meV in the case of KSVZ axions. However, we highlight this

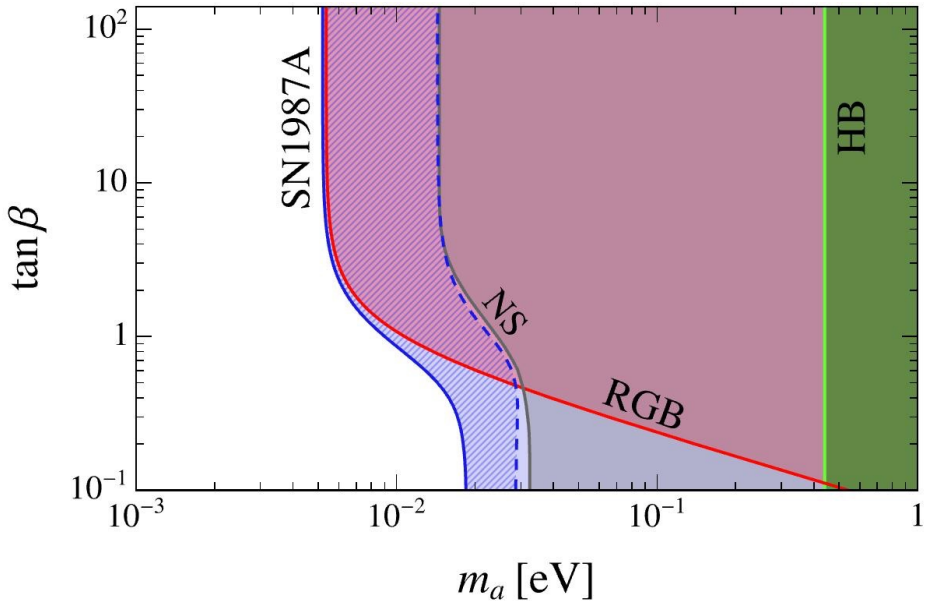

Figure 3.10: Summary plot of the bounds in the $\tan\beta$ *vs* m_a plane for the DFSZ axion model. The blue shadowed region, delimited by the blue solid line, displays the region excluded by the SN bounds placed in Lella et al., 2023. The hatched blue region between the solid and the dashed blue lines represents uncertainties related to the presence of pions. The red shadowed area shows the region of the parameter space ruled out by the RGB tips bound (Capozzi et al., 2020), while the grey and green shadowed regions refer to the bound placed by isolated neutron star cooling (Buschmann et al., 2022) and the duration of the HB phase in Globular Clusters (Carenza et al., 2020).

bound is at least one order of magnitude weaker than the one introduced from the study of SN cooling.

For DFSZ axion models, axion-nucleon model dependent constants can be parametrized through the ratio of the vacuum expectation values of the two Higgs bosons involved in the theory $\tan\beta$, with $\tan\beta$ confined to $0.28 < \tan\beta < 140$ by perturbative unitarity constraints (Grilli di Cortona et al., 2016; Di Luzio et al., 2020). This range outlines the variability of DFSZ axion models on the QCD axion band. As displayed by the solid blue line in Fig. 3.10, the SN cooling argument excludes $m_a \gtrsim 5\,\text{meV}$ for $\tan\beta \gtrsim 5$ and $m_a \gtrsim 18$ meV for $\tan\beta \lesssim 1$. In absence of pions (dashed blue line)

the bound is relaxed to $m_a \gtrsim 14\,\text{meV}$ for $\tan\beta \gtrsim 5$ and $m_a \gtrsim 28$ meV for $\tan\beta \lesssim 1$. We highlight that DFSZ axions are also coupled to leptons, thus we also consider the bound derived from observations of the RGB tip (solid red line) (Straniero et al., 2020; Capozzi et al., 2020), which is comparable to the SN cooling bound in presence of pions.

Remarkably, the SN cooling bound introduced in this work rules out the presence of an "hadronic axion window" (Moroi et al., 1998; Chang and Choi, 1993) around $\sim$ 1 eV, which was unprobed by either astrophysical observations or experimental searches. Moreover, QCD axions with masses $m_a > 10$ meV would play the role of hot dark matter (HDM), if thermally-produced in the early universe. Since, the SN cooling bound is significantly stronger than the reach of current and future cosmological experiments (orange arrow in the plots) (Archidiacono et al., 2015; D'Eramo et al., 2022), we can assert that it is unlikely that future cosmological probes would find signatures of HDM QCD axions. Nevertheless, below the SN bound, thermally-produced QCD axions with masses $m_a \lesssim 10$ meV may contribute to cosmological dark radiation (D'Eramo et al., 2022), which is in the reach of future cosmological surveys (see Ref. Baumann et al., 2016).

Chapter 4

Signatures of supernova axions: direct detection

In this Chapter we discuss some possibilities for direct detection of axions emitted from CC SNe. In this regard, we will refer to probes requiring that the axion interact itself in the considered detector, without demanding any axion-photon conversion along the path covered from the SN to the Earth. Specifically, in Section 4.1 we study possible axion-induced signatures in water Čherenkov detectors due to absorption and excitation of oxygen nuclei. In Section 4.1.1 we introduce the axion-oxygen excitation cross section, which we will use to estimate the expected number of axion events in KII during SN 1987A in Section 4.1.2. The non observation of such events can set novel constraints on the parameter space of axions coupled to nucleons, as illustrated in Section 4.1.3. Finally, Section 4.2 we investigate the physics potential of the International AXion Observatory (IAXO) in the detection of SN axions. This Chapter is based on the following articles.

(P3) P. Carenza, G. Co', M. Giannotti, A. Lella, A. Mirizzi, T. Rauscher, "Cross section for supernova axion observation in neutrino water Čherenkov detectors", Phys.Rev.C **109** (2024) no.1, 015501 [arXiv:2306.17055 [hep-ph]].

(P8) P. Carenza, J. A. Garcia Pascual, M. Giannotti, I. G. Irastorza, M. Kaltschmidt, A. Lella, A. Lindner, G. Lucente, A. Mirizzi, M. J. Puyuelo, "Detecting Supernova Axions with IAXO", 2502.19476 [hep-ph].

4.1 Supernova axions in water Čherenkov detectors

The discussion developed in Chapter 3 highlights that CC SNe are potentially powerful sources of axions coupled to nucleons. In particular, for typical values of the axion-nucleon coupling $g_{aN} \gtrsim 10^{-7}$, axions result to be trapped in the inner regions of the hot and dense SN core, similarly to neutrinos. Indeed, when the strength of axion-nucleon interactions, encoded in the ratio g_{aN}/m_N^2, becomes comparable to the Fermi constant $G_{\rm F} \simeq 10^{-5}$ GeV^{-2} modeling effective neutrino weak interactions at temperatures $T \ll M_W \sim 100$ GeV (Griffiths, 2008), axion emission and absorption cross sections in the SN environment are expected to be comparable to neutrino ones. Motivated by this argument, one may wonder if also a SN burst of trapped axions can lead to an observable signal in large underground neutrino detectors, in analogy to the detection of the SN 1987A neutrino burst (see Section 1.4.2).

In this regard, the *direct detection* of SN axions coupled to nucleons in relation to the SN 1987A event has been studied for the first time in the seminal paper by Engel *et al.* (Engel et al., 1990). In this work, the authors studied axion-induced excitations of oxygen nuclei, which are the most abundant target in water Čherenkov detectors. The detection is then achieved by searching for the photon emitted by the oxygen nucleus in order to relax the excited state of the system

$$a + {}^{16}\mathrm{O} \rightarrow {}^{16}\mathrm{O}^{*} \rightarrow \begin{cases} {}^{16}\mathrm{O} + \gamma \\ {}^{15}\mathrm{O} + \mathrm{n} + \gamma \\ {}^{15}\mathrm{N} + \mathrm{p} + \gamma \end{cases} . \tag{4.1}$$

If axions were coupled to nucleons strongly enough, this process may have led to a sizeable number of detectable events in the Kamiokande II (KII) water Čherenkov detector (Hirata et al., 1987; Hirata et al., 1988), allowing the authors of Engel et al., 1990 to place novel constraints on the value of g_{aN}. Nevertheless, this computation relies on nuclear models which are now outdated, and, more importantly, on a naive treatment for axion emission in the trapping regime based on schematic SN profiles. Therefore, in Carenza, Co, et al., 2024 we have revised the calculation of the axion-oxygen cross

section by employing the most updated nuclear models. Then, by deriving the incoming axion flux from our state-of-the-art 1D SN models, we set novel constraints on the axion parameter space, probing regions complementary to the ones ruled out by the SN cooling argument (Lella et al., 2023).

4.1.1 The axion-nucleus cross section

The axion-nucleon interaction Lagrangian, introduced in Sec. 3.1.1, can be conveniently recast in the following form

$$\mathcal{L}_{aN}(\boldsymbol{r},t) = \frac{g_{aN}}{2m_N}\bar{\psi}_N(\boldsymbol{r},t)\gamma^\mu\gamma^5(C_0 + C_1\tau_3)\psi_N(\boldsymbol{r},t)\partial_\mu a(\boldsymbol{r},t)\,, \tag{4.2}$$

where g_{aN} is the axion-nucleon coupling constant, m_N is the nucleon mass, $\psi_N = (p,n)^T$ is the nucleon doublet and $\tau^3 = \mathrm{diag}(1,-1)$ is the third Pauli matrix. Moreover, the iso-scalar coupling C_0 and the iso-vector coupling C_1 can be related to the model dependent constants C_{ap} and C_{an} as $C_0 = (C_{ap} + C_{an})/2$ and $C_1 = (C_{ap} - C_{an})/2$. As done in previous Sections, in the following we will assume $C_p = -0.47$ and $C_n \simeq 0$, as in the canonical KSVZ axion model (see Sec. 2.3.1).

Starting from Eq. (4.2), we can introduce the Hamiltonian

$$\begin{aligned}\mathcal{H}_{aN}(\boldsymbol{r},t) &= -\frac{g_{aN}}{2m_N}\bar{\psi}_N(\boldsymbol{r},t)\gamma^k\gamma^5(C_0 + C_1\tau_3)\psi_N(\boldsymbol{r},t)\partial_k a(\boldsymbol{r},t) \\ &\equiv -\frac{g_{aN}}{2m_N}\mathcal{J}^k(\boldsymbol{r},t)\partial_k a(\boldsymbol{r},t)\,,\end{aligned} \tag{4.3}$$

in which we have defined the hadronic current operator $\mathcal{J}^k(\boldsymbol{r},t)$ and the index k ranges from 1 to 3. Then, the transition matrix element from system initial state $|i\rangle$ and the final state $|f\rangle$ can be expressed as

$$\begin{aligned}\mathcal{M}_{if} &= \int d^3\boldsymbol{r}\, dt\, \langle f|\, \mathcal{H}_{aN}(\boldsymbol{r},t)\, |i\rangle \\ &= -\frac{g_{aN}}{2m_N}\int d^3\boldsymbol{r}\, dt\, \langle \Psi_f|\, \mathcal{J}^k(\boldsymbol{r},t)\, |\Psi_i\rangle\, \langle 0|\, \partial_k a(\boldsymbol{r},t)\, |\boldsymbol{p}\rangle\ ,\end{aligned} \tag{4.4}$$

where $|\Psi_i\rangle$ and $|\Psi_f\rangle$ are the nucleus initial and final eigenstates, $|\boldsymbol{p}\rangle$ describes a single axion of momentum $\boldsymbol{p}$ and $|0\rangle$ is the physical vacuum of the axion field. The full derivation of the cross section is illustrated in details in Appendix B.

Once performed this computation, the axion absorption cross section reads

$$\begin{aligned}\sigma(\epsilon_p) &= \int \frac{d\omega}{\mathcal{T}} \sum_J \left(\frac{d\rho}{d\omega}\right)_J |M_{if}|^2 \\ &= \frac{4\pi^2 g_{aN}^2}{m_N^2} \sum_J \epsilon_p \, (2J+1) \left|\left\langle J^P \right| |T_J| \left|0^+\right\rangle\right|^2 \delta(\epsilon_p - E_J) \,,\end{aligned} \tag{4.5}$$

where $\mathcal{T}$ is the observation time, J is the total angular moment of the oxygen nucleus, P its parity, so that $|0^+\rangle$ and $\left|J^P\right\rangle$ denotes the nucleus ground state and the state excited by axion absorption, respectively. Moreover $(d\rho/d\omega)_J = 4\,\delta(\omega - E_J)$ is the density of nuclear states for the excitation level J^P with energy E_J.

The computation of the nuclear transition matrix element requires a dedicated treatment, described in details in Carenza, Co, et al., 2024. In particular, three main problems have to be tackled. First, SN axions in the trapping regime with typical energies $\mathcal{O}(10)$ MeV excite the oxygen nucleus in an energy range where collective and single-particle excitation modes overlap. Therefore, a theory describing both kinds of excitation with a unified treatment is required. Second, since the transferred axion energies allow also for nucleon emission, the theory describing the nuclear system have to take into account also this kind of effects. Finally, a more subtle issue is connected to the dynamics of axion-nucleon interactions. Indeed, being the axion a pseudoscalar particle, it allows for the excitation of unnatural parity states, which are poorly known, since their cross section is typically suppressed compared to natural parity states. Thus, experimental data cannot be employed to set up a phenomenological treatment for this kind of excitations. We address these problems by employing the Continuum Random Phase Approximation (CRPA) theory, which is able to describe excitations of the continuum spectrum, accounting for single-nucleon emission. Moreover, the ground state as well as the excited states are determined by employing the same sets of nucleon-nucleon interactions (De Donno et al., 2011). In particular, we have considered three different parametrizations for the description of the nuclear model: the D1S parametrization (Berger et al., 1991) also used in the compilation of the AMEDEE data base (Hilaire et al., n.d.; Hilaire et al., 2007), the D1M model (Goriely et al., 2009), fitting a wider set of data with respect to D1S, and the D1MT model which is obtained by adding to the D1M parametrization one tensor and one tensor-isospin term.

The comparison among the results obtained with the different interaction models gives an estimation of the theoretical uncertainties on the nuclear model used in our calculations. The total axion absorption cross sections up to 30 MeV, obtained with the three different interaction set-ups, is shown in Fig. 4.1, displaying all the contributions from the the 0^-, 1^+ and 2^- multipole excitations. In particular, here we assume $g_{aN} = 2 \times 10^{-9}$ with the ratio between axion-proton and axion-neutron couplings fixed as in the KSVZ axion model. We observe that the 2^- cross section dominates the absorption up to energies $\sim 20\,\text{MeV}$, while a peak related to a 0^- excitation is important around energies $22 - 23\,\text{MeV}$.

Then, the final step consists in the modeling the de-excitation of the ^{16}O excited states, including both γ-cascades and particle emission (protons, neutrons and α-particles), since the energy of the excited levels is above the typical nucleon separation energies. Moreover, secondary nuclides created after the first-particle emission may still be in excited states above their nuclear separation energies. Therefore, a model describing the de-excitation of these secondary nuclides is also required. We obtained the summed de-excitation spectra by using with the SPECTRUM code (Rauscher, 2018) based on the SMARAGD Hauser-Feshbach reaction code (Rauscher, 2010 - 2022; Rauscher, 2011). Then, the spectra computed following this procedure can be employed to estimate the number of axion-induced events in KII, as we illustrate in the following section.

4.1.2 Axion-induced events in Kamiokande II

Once computed the axion-oxygen cross section and the oxygen de-excitation spectrum, we have all the ingredients to estimate the expected number of events in KII water Čherenkov detector in coincidence to SN 1987A, revising the computation performed in Engel et al., 1990 in light of the state-of-the-art nuclear models. Despite also the IMB experiment detected the neutrino burst from SN 1987A (Bionta et al., 1987; Bratton et al., 1988), our analysis will be based only on the KII setup. This choice is due to the lower energy threshold characterizing the KII detector in comparison to IMB. In particular, KII was able to observe Čherenkov photons with energies down to $E_{\text{thr}} \simeq 4\,\text{MeV}$, allowing for the detection of the de-excitation photons from all the oxygen excited levels. On the other hand, IMB had a too high energy threshold

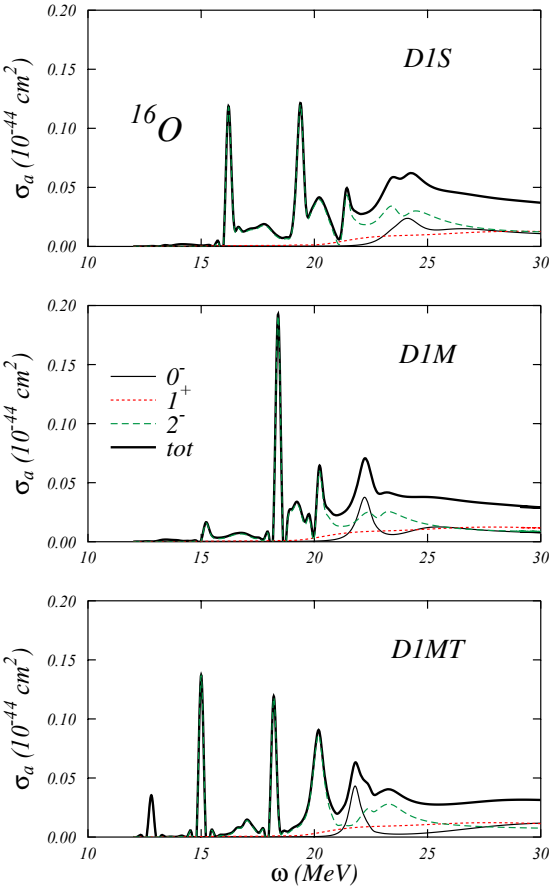

Figure 4.1: Total cross section for the absorption of an axion by the ^{16}O nucleus in the energy range up to 30 MeV, calculated with $g_{aN} = 2 \times 10^{-9}$. The three panels show the results obtained by using the three parametrization considered for the modeling of the oxygen nucleus. We show separately the contributions of the multipoles 0^- (thin continuous black lines), 1^+ (dotted red lines) and 2^- (dashed green lines). The thick continuous black lines show the total cross section obtained by summing all the unnatural parity state contributions.

$E_{\rm thr} \simeq 19$ MeV (Fiorillo, Heinlein, et al., 2023) to achieve an axion detection in regions of the parameter space not already excluded by other experiments, as searches for solar axions in the SNO experiment (Bhusal et al., 2021). The number of axion-induced events in the detector is thus obtained as (Fischer, Chakraborty, et al., 2016)

$$N_{\rm ev} = F_a \otimes \sigma \otimes \mathcal{R} \otimes \mathcal{E}\,, \tag{4.6}$$

where F_a is the predicted axion flux from SN 1987A, folded with the detection cross section σ, the detector energy resolution $\mathcal{R}$ and the detector efficiency $\mathcal{E}$. We point out that the detector response to oxygen de-excitation has not previously taken into account in Engel et al., 1990. From this expression, the differential number of events $dN_{\rm ev}/dE$ is then obtained as (Lunardini et al., 2004)

$$\frac{dN_{\rm ev}}{dE} = N_{\rm T} \int_0^{+\infty} d\epsilon\, \mathcal{R}_\epsilon(E)\, \mathcal{E}(E)\, F_a(\epsilon)\, \sigma(\epsilon)\,, \tag{4.7}$$

where ϵ and E are the energy of the incident axion and the detected energy of the de-excitation photon, respectively. Moreover, we introduced the number of targets $N_{\rm T}$ given by the ratio between the Avogadro's number $N_{\rm A} = 6.02 \times 10^{23}$ and oxygen molar mass $M_{\rm mol} = 18.1\,{\rm g}$ and multiplied by the total detector mass $M = 2.4$ kton. The detector resolution $\mathcal{R}$ is taken from Fogli et al., 2005:

$$\mathcal{R}_\epsilon(E) = \sum_{E_\gamma(\epsilon)} \frac{1}{\sqrt{2\pi\sigma_\gamma^2}}\, e^{-(E-E_\gamma(\epsilon))^2/2\sigma_\gamma^2}\, BR(E_\gamma(\epsilon))\,, \tag{4.8}$$

in which $E_\gamma(\epsilon)$ is the energy of the photon emitted to relax the oxygen nucleus from an excited state of energy ϵ, while $BR(E_\gamma(\epsilon))$ is the branching ratio related to the process. This approach allows us to take into account non-radiative de-excitation processes, which are not detectable. In particular, we observe that the sum of branching ratios for all possible radiative channels is in the order of 50%. Moreover, we also take into account Gaussian dispersion for detected energies E around the true de-excitation energy $E_\gamma(\epsilon)$, with $\sigma_\gamma = \sqrt{0.6\, E_\gamma(\epsilon)/\,{\rm MeV}}$. Finally, we introduce the detector efficiency (Fiorillo, Heinlein, et al., 2023)

$$\mathcal{E} = \begin{cases} 0 & x < 4 \\ \frac{0.932}{\sqrt{1+\left(\frac{34}{12-7x+x2}\right)^2}} & x \geq 4 \end{cases}\,, \tag{4.9}$$

where $x = E/\,\mathrm{MeV}$. The predicted axion flux from SN 1987A reads

$$F_a(\epsilon) = \frac{1}{4\pi d^2}\frac{dN_a(\epsilon)}{d\epsilon}\,, \tag{4.10}$$

where $d = 51.4$ kpc is SN 1987A distance, while the axion energy spectra $dN_a/d\epsilon$ are described in details in Chapter 3. As discussed in Carenza, Co, et al., 2024 the detected photon de-excitation energies mainly lie in the energy $4 - 10$ MeV, peeking around $E \sim 6 - 7\,\mathrm{MeV}$ since the oxygen nuclei mainly relax by emitting photons of energies between $E \simeq 4.4$ MeV and $E \simeq 8.2$ MeV. To compare our results to the outcomes of Engel et al., 1990, in Fig. 4.2 we plot the total number of events expected in KII as a function of the axion-proton coupling g_{ap}. The number of axion-induced events predicted in our work is comparable to the estimation of Engel et al., 1990 around $g_{ap} \sim 10^{-6} - 10^{-5}$, while it is higher for $g_{ap} \gtrsim 10^{-5}$. In particular, we observe that in our case N_{ev} quadratically increases with the coupling for $g_{ap} \gtrsim 10^{-5}$, while in Engel et al., 1990 it results to be suppressed. This difference is mainly related to the determination of the incoming axion flux employed in the two different works. Indeed, while in Engel et al., 1990 the axion luminosity L_a is determined with a naive argument based on the location of the axion sphere leading to a rapid suppression of axion emission for $g_{ap} \gtrsim 10^{-4}$, in Section 3.3 we have shown that L_a approaches a plateau in this range of couplings. Thus, the behavior of the event number is essentially determined by the dependence of the cross section on g_{ap}, namely $\sigma \propto g_{ap}^2$. Finally, comparing the results obtained from the different nuclear models considered, we can observe that a different modeling of nuclear interactions in the oxygen nucleus may imply uncertainties of 40% in the weak coupling regime and up to 80% for strongly-coupled axions.

4.1.3 Constraining SN axions with KII observations

The estimation of the number of axion-induced events introduced in the previous Section allows us to constrain the axion parameter space by looking at KII observations, which did not observe any evidence for axion-induced events in coincidence to the SN 1987A explosion. As detailed in Section 1.4.2, KII detected 11 neutrino events from the SN 1987A neutrino burst. However, following the recent analysis performed in Fiorillo, Heinlein, et al., 2023, in our analysis we consider only the time window associated to the first nine

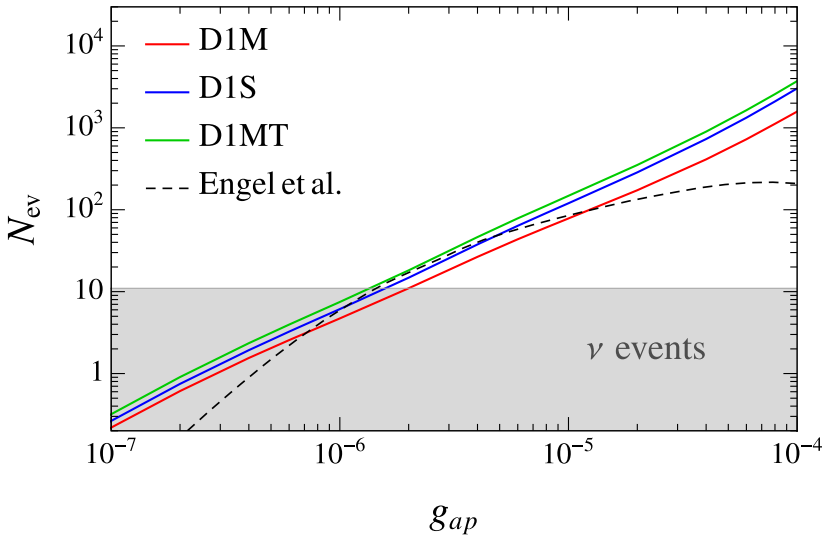

Figure 4.2: Predicted number of axion-induced events in KII water Čherenkov detector for the three different nucleon-nucleon interactions employed in the CRPA calculations as a function of the axion-proton coupling. The solid lines are obtained by exploiting the results for cross section introduced in this work and the spectra computed in Lella et al., 2023, while the dashed lines displays the number of events estimated in Engel et al., 1990. The grey band defines the region where the number of events due to axions is submerged by neutrino events.

events detected, which turned out to be in good agreement with recent 1D SN simulations, while we neglect the last three-events at $t_{\rm pb} \sim 10$ s being in tension with state-of-the-art simulations. During 2.7 days before the SN 1987A time, the average background event rate in KII was measured to be $\overline{n}_{\rm bkg} \simeq 0.02$ events/ s (Hirata et al., 1988; Hirata et al., 1987). Therefore, assuming Poissonian priors for the distribution of the background events in the detector, a positive axion signal would have been associated to the detection of a number of axion-induced events $N_{\rm ev} \gtrsim 2\sqrt{\overline{n}_{\rm bkg}\Delta t_a}$ in the time window Δt_a of the axion signal. In particular, axions with masses $m_a \lesssim 20$ eV, the time of flight necessary to cover the distance between the SN to us is comparable with the entire neutrino burst duration[1], thus

[1]As illustrated in Raffelt, 1996, the duration of the SN 1987A can be employed to set the constrain $m_\nu \lesssim 20$ eV on neutrino masses

in this case we assume $\Delta t_a = \Delta t_\nu \simeq 10$ s. As shown by the green region in Fig. 4.3, this argument allows us to exclude value of the axion-proton coupling $g_{ap} \gtrsim 3 \times 10^{-7}$ in this mass range. Conversely, higher-mass axions would have arrived at Earth with time delay with respect to the first detected neutrino event. The time necessary for an axion of energy E_a and mass m_a to travel the distance $D = 51.4$ kpc from SN 1987A to the Earth can be estimated as $t = D\, m_a^2 / 2E_a^2$ (Raffelt, 1996). Moreover, incoming axions can excite different oxygen excited levels in the range $E \in [9.55, 28]$ MeV, depending on their energy. Since less energetic axions travel slower, the spread in energy of the oxygen excited level implies that the axion signal would have been smeared over a time window

$$\Delta t_a\,(m_a) \approx t\,(E_{\rm min}, m_a) - t\,(E_{\rm max}, m_a) \approx 1.82\,{\rm s}\,\left(\frac{m_a}{10\ {\rm eV}}\right)^2\,, \tag{4.11}$$

over which we have to evaluate the number of expected background events. In particular, in this expression we denoted $E_{\rm min} = 9.55$ MeV, $E_{\rm max} = 28$ MeV and we have neglected the intrinsic dispersion of the ALP signal. Thus, for increasing axion masses the condition constraining the number of axion-induced events $N_{\rm ev} \lesssim 2\sqrt{\overline{n}_{\rm bkg} \Delta t_a}$ relaxes, ruling out progressively larger values of the the axion-proton coupling.

The constraint placed by the non-observation of axion-induced events during SN 1987A turns out to be nicely complementary to the region excluded by the SN cooling argument detailed in Section 3.3.2, ruling QCD axion masses 30 eV $\lesssim m_a \lesssim$ 500 eV, a region of the parameter space which cannot be probed by neither the SN cooling argument nor by observations of the SNO experiment searching for solar axions emitted through $p + d \rightarrow {}^3{\rm He} + a\,(5.5\,{\rm MeV})$ (Weinberg, 1978, see also Lucente, Nath, et al., 2022 for a recent work on the topic). Ultimately, the combination of arguments related to SN 1987A observations allows us to rule out, within their uncertainties of factor ∼few, QCD axions with masses $m_a \gtrsim 10\,{\rm meV}$ (Lella et al., 2023), consolidating the role of CC SNe as unique laboratories to search for these elusive particles.

4.2 Detecting SN axions with IAXO

As highlighted in previous Chapters, Galactic CC SNe are very rare events, with current estimates predicting a rate in the order of $\sim 1 - 3$ SNe per

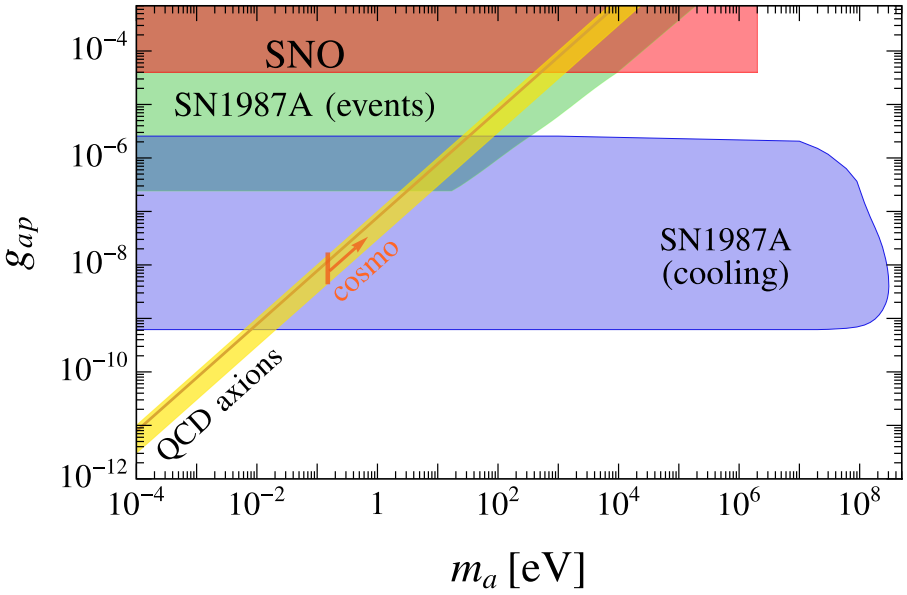

Figure 4.3: Summary plot of the bounds in the g_{ap} vs m_a plane. The color scheme is the same as in Fig. 3.8. To the exclusion limits already discussed in Section 3.3.2 we add the green region labeled *SN 1987A (events)*, which is ruled out by the non-observation of extra axion-induced events inside the KII experiment during the SN 1987A neutrino burst.

century in the Milky-Way (Rozwadowska et al., 2021). Since they represent a once-in-a-lifetime opportunity for the possible discovery of the axion, it is imperative to ensure the highest possible level of preparedness for such an eventuality, exploiting as much as possible all the facilities proposed for axion searches. In this regard, the proposed IAXO experiment plays a central role in the extensive experimental program in place to achieve such a discovery (see Section 2.4.1). Though the experiment is designed as an *helioscope* aiming for the the emission of axions from the Sun, in Carenza, García Pascual, et al., 2025 we prove its potential also as an axion *SN-scope*, widening the physics cases in the reach of this experiment.

This idea, originally proposed in Raffelt and otheres, 2011; Ge et al., 2020, relies once again on the extreme temperature and density conditions in the SN core, permitting the emission of axion fluxes large enough to be detected by the next generation of helioscopes. In particular, even if the nearest SN candidates are located much further away from the Sun at distances $\mathcal{O}(100)$ pc,

the incoming flux of axions produced by means of nuclear processes in the SN core might be even larger than the predicted solar axion flux. Nonetheless, a possible detection can be achieved only if axions are also provided with a coupling to photons, allowing a fraction of the incoming flux to convert into gamma-ray photons within the large conversion volume engineered for the experiment.

Many technical challenges have to be tackled to maximize the sensitivity prospects. A first issue is related to the duration of the SN event, lasting in a few seconds. Therefore, the capability of pointing the IAXO telescope towards the SN event is intrinsically related to the possibility of predicting the occurrence of a Galactic SN event in the sky far enough in advance. Methodologies for pre-SN alerts practically rely on the detection of pre-SN neutrinos emitted during the Silicon-burning stage of Red SuperGiants (RSG) (see, e.g., Asakura et al., 2016; Al Kharusi et al., 2021), which precedes the onset of the gravitational collapse. Furthermore, SN axions are emitted with energies within the range $10 - 250\,\mathrm{MeV}$, which is out of the reach of detectors conceived for helioscope searches, which typically target the X-ray energy range characterizing axions emitted from the Sun. Thus, the detection of SN axions requires the installation of a highly-efficient gamma-ray detector on the body of the experiment, in addition to the X-ray detector. In this context, the intriguing possibilities of detecting the SN axions and axions emitted from processes as $p + d \rightarrow {}^3\mathrm{He}{+}a(5.5\ \mathrm{MeV})$ in the Sun strongly motivate the construction of this MeV detector.

Below we propose a first detection strategy for SN-axion searches with IAXO and discuss the related sensitivity prospects.

4.2.1 Detection strategy

The IAXO experiment will be provided with a novel tracking system allowing the telescope to point towards a specific target in just few minutes (Abeln et al., 2021). Nevertheless, if the alert was triggered by the first incoming SN neutrino event, IAXO would miss the possible axion burst which is predicted to last in a few seconds. Therefore, the detection startegy has to rely on the detection of pre-SN neutrinos emitted during the Silicon-burning stage of the SN progenitor lasting in ~ 2 days. An extended catalog of RSGs in the Milky-Way is provided in Mukhopadhyay, Lunardini, et al., 2020, and might

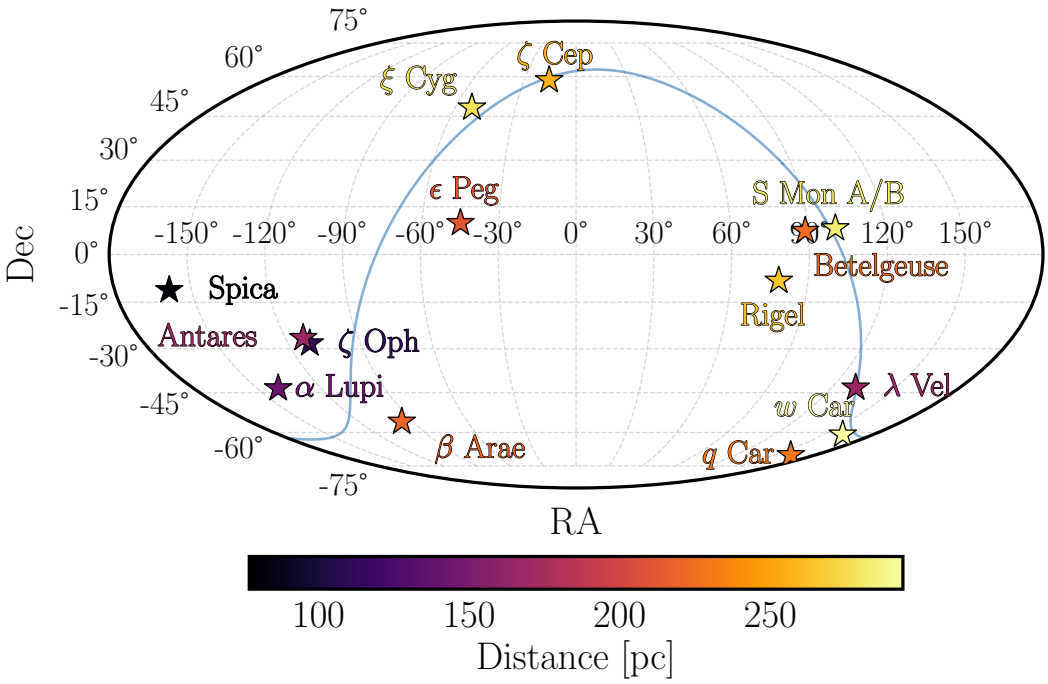

Figure 4.4: Mollweide projection of the SN candidates considered in our analysis. The Galactic plane, defined by latitude 0 in the Galactic coordinate system, is depicted as a continuous blue line across the sky. The color scheme encodes the distance of the stars from Earth.

be integrated with the more recent RSG catalog presented in Healy et al., 2024 crosschecked with the `simbad` database (Wenger et al., 2000). In our analysis, we focus on SN candidates at distances $d < 300$ pc, since the axion flux from more distant stars is expected to be undetectable with IAXO. The complete list of RSGs considered in this work is represented in Mollweide projection in Fig. 4.4, in which the color scheme encodes the distance of the star from the observer.

The capabilities in achieving an efficient pointing towards the SN event is intrinsically related to the identification of the candidate sufficiently in advance from the onset of the gravitational collapse . For this purpose, one has to rely on an early-alert system based on the observation of pre-SN neutrinos, since the neutrino production rapidly rises during the Silicon burning phase, which anticipates the onset of the collapse (Mukhopadhyay, Lunardini, et al., 2020). These neutrino fluxes are expected to be significantly less abundant than neutrinos emitted during the SN event and characterized by lower energies in the

range $\sim 0.1 - 5$ MeV. Nevertheless, in case of a close-by SN event, they are expected to be observable in dedicated detectors, providing the desired early alert. For example the study carried out in Abe et al., 2024 showed that the combined analysis of KamLAND and Super-Kamiokande (SK) observations permits to detect SN neutrinos up to distances ~ 500 pc, leading to an early warning up to ~ 12 hours before the SN event. On the other hand, the reconstruction of the direction of the incoming pre SN-neutrino flux is way more challenging. Indeed, the direction sensitivity for this kind of events is relatively low, due to the weak forward-backward asymmetry of inverse beta decays used to look for neutrino events (Mukhopadhyay, Lunardini, et al., 2020). By employing currently available liquid scintillators the capability in determine the direction of the neutrino flux is moderate, translating in an angular resolution of around 60° when ~ 200 events are detected, which is a realistic value for a star like Betelegeuse few hours before the SN event. Nevertheless, the advent of lithium-loaded liquid scintillators (LS-Li), which would increase the forward-backward asymmetry, would push the angular resolution down to 15°[2].

Despite the moderate angular resolution, in most cases observations of pre-SN neutrinos would be sufficient to discriminate the SN candidate close to the explosion among the list of near RSGs (see Fig. 4.4). If the identification is achieved, IAXO (and its precursor BabyIAXO) would have sufficiently-high pointing accuracy for the observation of the event. In this regard, we recall that the required pointing accuracy for the (Baby)IAXO experiment to follow the Sun is within $\leq 30''$[3]. A more serious issue would occur if multiple potential targets fall within the angular cone suggested by pre-SN neutrinos. In this case, a decision on which candidate the IAXO telescope would point at has to be made. Despite a decision-making protocol has not been already discussed within the IAXO collaboration, the most natural choice would consist in pointing towards the closest candidate, which is expected to yield the strongest signal.

[2]Although currently there is no existing or funded large-volume LS-Li detector specifically optimized for pre-SN neutrino detection, ongoing developments indicate their feasibility. In this regard, experiments like PROSPECT (Ashenfelter et al., 2019) have successfully demonstrated lithium-loaded scintillator technology at multi-ton scales.

[3]This estimations are performed for the X-ray telescopes installed on IAXO. Nevertheless, for typical IAXO geometries, the pointing accuracy for MeV photons will not be larger than $\sim 2° - 4°$.

4.2.2 Sensitivity prospects

Light axions ($m_a \lesssim 1$ eV) emitted from the exploding SN with energies 10-250 MeV would travel at relativistic velocities reaching the Earth in coincidence to the SN neutrino burst. If these particles are coupled to both nucleons and photons, once produced in the SN core by means of their nuclear couplings (see Section 3.1) they may convert into gamma-rays when entering the magnetic volume of the IAXO experiment. In order to study the sensitivity prospects on the axion-photon coupling $g_{a\gamma}$, in the following we will set axion-nucleon couplings at values which are always allowed by the leading astrophysical constraints (Lella et al., 2023; Buschmann et al., 2022), and leave only $g_{a\gamma}$ as a free parameter. In this context, the axion-to-photon conversion probability within an approximately constant magnetic field of magnitude B and length L can be estimated as (Raffelt and Stodolsky, 1988; Bibber et al., 1989)

$$P_{a\to\gamma} = \left(\frac{g_{a\gamma} B L}{2}\right)^2 \left[\frac{\sin\left(\frac{qL}{2}\right)}{\frac{qL}{2}}\right]^2 , \tag{4.12}$$

where we have introduced the momentum transfer between the axion and photon $q = m_a^2/2E_a$ for relativistic axions. Given the conversion probability, the number of counts S_γ related to an axion burst lasting in about ~ 10 s, is given by

$$S_\gamma = \frac{1}{4\pi D^2} \int_{E_i}^{E_f} dE \, \frac{dN_a}{dE_a} \, P_{a\to\gamma} \, \epsilon \, A = g_{a\gamma}^2 \, g_{aN}^2 \int_{E_i}^{E_f} dE \, \frac{dn_\gamma}{dE}, \tag{4.13}$$

where ϵ is the detector efficiency and A is the magnet bore area. In this expression, dN_a/dE_a is the emitted axion spectrum integrated over ~ 10 s

$$\frac{dN_a}{dE_a} = g_{aN}^2 \left[F_{NN}(E_a) + \delta \, F_{\pi N}(E_a)\right] , \tag{4.14}$$

in which we have separated the contributions from NN bremsstrahlung (F_{NN}) and pion conversion ($F_{\pi N}$), and we have introduced a variable δ to parametrize the relative impact of the pionic production channel with respect to the scenario outlined in Carenza et al., 2021; Lella, Carenza, et al., 2023, which relies on the estimation of the pion fraction introduced in Fore and Reddy, 2020, still under debate (see Section 3.3.3). Moreover, we have explicitly written the dependence on the axion nucleon coupling g_{aN}^2. Finally,

	B (T)	L (m)	A (m^2)
BabyIAXO	2	10	0.77
IAXO	2.5	20	2.3
IAXO+	3.5	22	3.9

Table 4.1: Magnetic field strength B, length L, and cross sectional area A for BabyIAXO, IAXO and IAXO+ (Abeln et al., 2021).

the quantity dn_γ/dE parametrizes the number counts per energy divided by the coupling strength $g^2_{a\gamma}$. It is then convenient to split this function into the bremsstrahlung and pion-induced signals:

$$n_\gamma = n_\gamma^{NN} + \delta \cdot n_\gamma^{\pi N} \,, \tag{4.15}$$

which follows from the definition in Eq. (4.14). Since almost zero background is expected for MeV photons, the IAXO sensitivity to a SN axion signal at 95% of C.L. can be placed by requiring

$$S_\gamma = g^2_{a\gamma}\, g^2_{aN} \int_{E_i}^{E_f} dE\, \frac{dn_\gamma}{dE} \leq \ln(20) \tag{4.16}$$

In Fig. 4.5 we report the sensitivity curves in the plane $g_{a\gamma}$ vs m_a for two representative SN progenitors, namely Spica (α Virginis) at distance $d = 77\,\mathrm{pc}$ and Betelgeuse (α Orionis) at distance $d = 222\,\mathrm{pc}$, and considering both scenarios in which we have axion production by means of NN bremsstrahlung only (NN) and both bremsstrahlung and pion conversion ($NN+\pi N$). These plots are obtained by assuming $g_{an} = 0$ and by setting g_{ap} to the maximum allowed value by the SN cooling bound, i.e. $g_{ap} = 10^{-9}$ for the bremsstrahlung only case and $g_{ap} = 5 \times 10^{-10}$ for the $NN + \pi N$ scenario. Moreover, we report the curves computed for different helioscope upgrades, from the first prototype BabyIAXO up to IAXO+, which is an enhanced version of IAXO. These helioscope designs are outlined in Abeln et al., 2021, while the features useful for our analysis are summarized in Table 4.1.

Interestingly, for both SN candidates considered, IAXO as a SN-scope is able to probe values of axion-photon coupling $g_{a\gamma}$ beyond the current bound placed by the CAST experiment (except for the $NN + \pi N$ scenario for Betelgeuse)

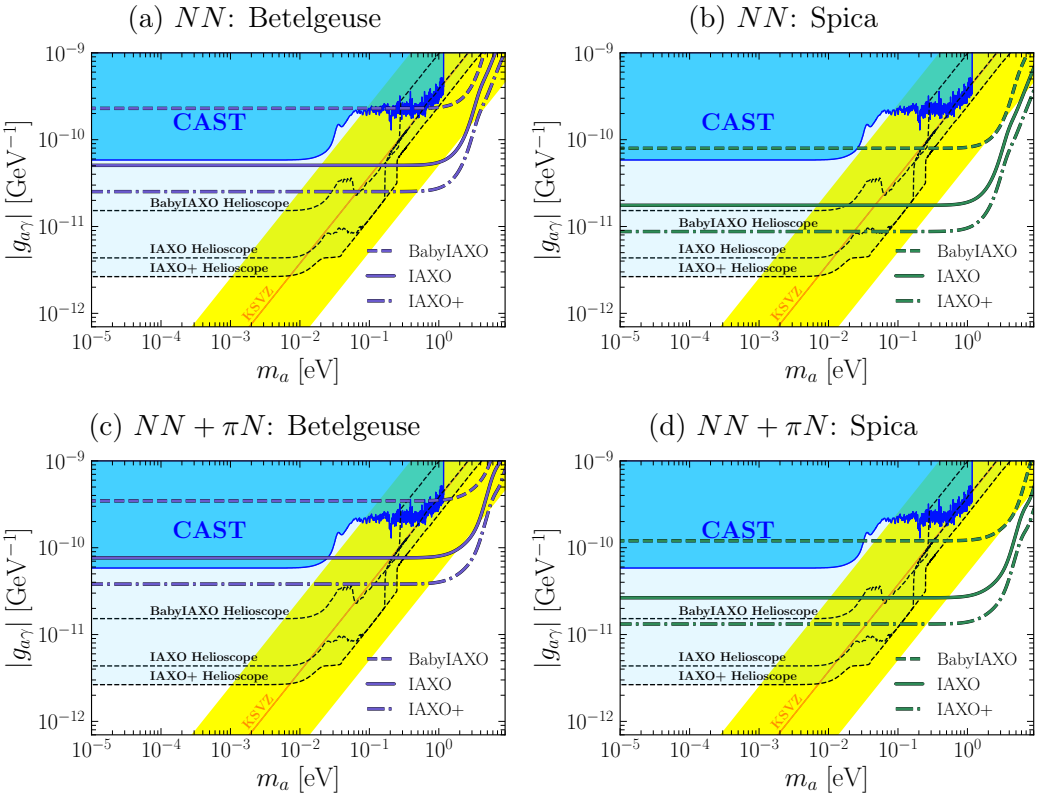

Figure 4.5: Sensitivity prospects for BabyIAXO, IAXO and IAXO+ as SN scopes for Betelgeuse (violet, *left panel*) and Spica (green, *right panel*) in the ALP free streaming regime considering bremsstrahlung emission and both bremsstrahlung and pion conversion emission. In the upper panels, we set the ALP-nucleon coupling to $g_{aN} = 10^{-9}$, while in the lower panels we set it to the maximum value allowed by the the SN cooling argument $g_{aN} = 5 \times 10^{-10}$. The black transparent regions show the sensivity prospects of IAXO, BabyIAXO and IAXO+ as helioscopes.

in the massless axion limit $m_a \lesssim 10^{-2}$ eV. We also highlight that, despite the sensitivity prospects for the SN-scope mode are worse than the sensitivity of the helioscope mode at low axion masses, the high energies characterizing SN axion emission allow the signal to keep coherence up to large masses $m_a \sim \mathcal{O}(1)$ eV, probing regions of the QCD axion band to which IAXO helioscope is not sensitive.

4.2.3 Parameter reconstruction

In case a of a positive axion signal, the energy spectrum of the events detected would provide precious information about the axion production mechanism during core-collapse SNe. In particular, we have argued before that the number of axions emitted via pionic processes at energies $E_a \sim 200$ MeV is effectively dependent on the pion abundance in the SN core, which is still under debate. To perform a binned analysis of the expected axion signal, we can introduce a two-dimensional likelihood in which the probability density function is given by the Poissonian distribution

$$L = \frac{1}{L_0} \prod_{i=1}^{n} e^{-\mathrm{s}_i} \frac{\mathrm{s}_i^{ni}}{n_i!}, \qquad L_0 = \prod_{i=1}^{n} e^{-n_i} \frac{n_i^{ni}}{n_i!}, \tag{4.17}$$

where L_0 is the normalization factor, n_i is the number of counts measured in the ith energy bin and s_i is the expected number of signal counts in the ith bin. Given the definition in Eq. (4.13), the number of axion events in the ith energy bin is given by

$$\mathrm{s}_i = g_{a\gamma}^2 \, g_{aN}^2 \int_{E_i}^{E_i+\Delta E} dE \, \frac{dn_\gamma^{NN}}{dE} \; + \; g_{a\gamma}^2 \, g_{aN}^2 \, \delta \int_{E_i}^{E_i+\Delta E} \frac{dn_\gamma^{\pi N}}{dE} dE, \tag{4.18}$$

where the integration is performed over an energy bin of width ΔE =1 MeV with boundaries E_i and $E_i + \Delta E$.

According to Wilks' theorem (Wilks, 1938), for a sufficiently-high number of counts in the detector, the minimum of $-2 \ln L$ approaches to a χ^2 distribution

$$-\frac{\chi^2}{2} = \ln L = \sum_{i=1}^{n} n_i - \mathrm{s}_i + n_i \log \frac{\mathrm{s}_i}{n_i}. \tag{4.19}$$

The likelihood analysis is performed for a fixed axion mass in the coherence region $m_a = 10^{-2}$ eV, by keeping as free parameter the product $g_{a\gamma}^2 \times g_{aN}^2$, which defines the intensity of the signal in our detector. In particular we vary the squared product of couplings in the range $g_{a\gamma}^2 \times g_{aN}^2 \in [0, 50] \times 10^{-40}$ GeV^{-2}. Moreover, we also let δ vary within the range $\delta \in [0, 3]$ to test the capabilities of the detector in discriminating the impact of the pionic contribution over the incoming axion spectrum. We then perform the simulation in the detector by assuming $g_{aN} = 5 \times 10^{-10}$ and $\delta = 1$, which is the standard scenario considered in this work. In Fig. 4.6 we show our

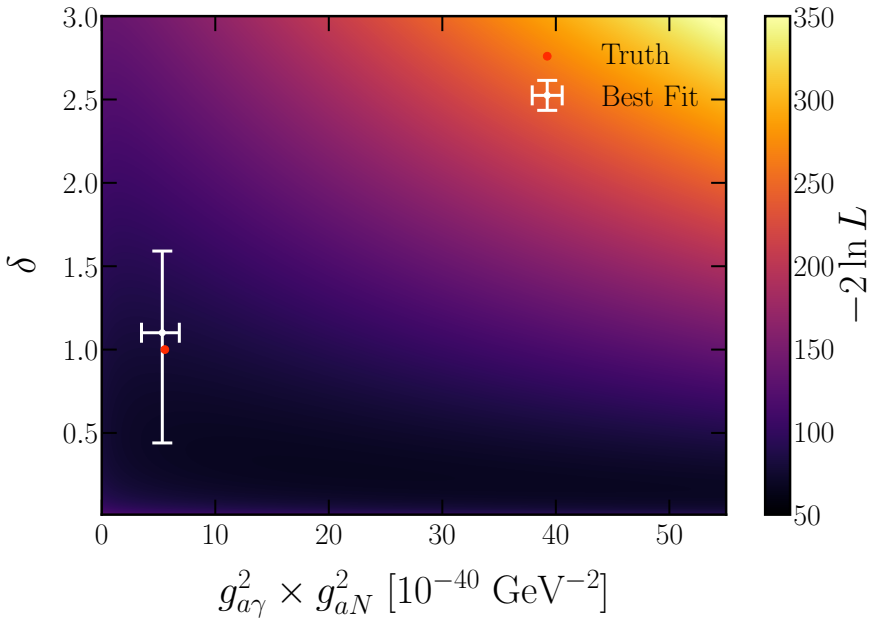

Figure 4.6: Likelihood analysis results in the $g^2_{a\gamma} \times g^2_{aN}$ and δ parameter space, in which the color palette shows the value of the $-2 \ln L$ distribution. The red dot represents the truth value of the SN axion model used as input for the calculations, while the white marker shows the minimum of the likelihood analysis in which the error bars correspond to one standard deviation (σ).

results for 10 detected axion events. We observe that the values of the reconstructed parameters are well compatible with the truth values assumed in the simulation.

These results probe the physics potential of IAXO as a SN scope, not only for a groundbreaking axion detection but also in reconstructing properties of the axion spectrum intrinsically related to SN physics. In particular, the detection of a large number of SN axion events at energies $E_a \sim 200$ MeV would probe the presence of a relatively high fraction of pions in the SN core, which is a matter of research. While other proposals exist in the literature (Lella, Calore, Carenza, Eckner, et al., 2024, see Section 5.3), they primarily focus on ultra-light axion-like particles. Remarkably, IAXO SN-scope would target the strongly-motivated case of QCD axions.

Chapter 5

Signatures of supernova axions: Gamma-rays

Axions emitted from CC SNe via their nuclear couplings can give rise to various observable signatures if they also couple to photons and electrons. In this Chapter we will focus on gamma-ray signals produced in different processes. In Section 5.1 we characterize the gamma-ray signal for axions with masses $m_a \gtrsim 1$ MeV decaying in photons pairs. In Section 5.2 we study observable gamma-ray signatures for heavy axions coupling to electrons. Finally, in Section 5.3 we examine the case of ultralight axions ($m_a \lesssim 0.1$ neV) converting into photons in the Galactic magnetic field, illustrating how this axion-induced gamma-ray burst can be employed to probe relevant properties of the SN core.

This chapter is based on the following research articles:

(P1) A. Lella, P. Carenza, G. Lucente, M. Giannotti, A. Mirizzi, "Proto-neutron stars as cosmic factories for massive axionlike particles", Phys.Rev.D **107** (2023) no.10, 103017 [arXiv:2211.13760 [hep-ph]].

(P4) A. Lella, E. Ravensburg, P. Carenza, M.C.D. Marsh, "Supernova limits on QCD axionlike particles", Phys.Rev.D **110** (2024) no.4, 043019 [arXiv:2405.00153 [hep-ph]].

(P6) A. Lella, F. Calore, P. Carenza, C. Eckner, M. Giannotti, G. Lucente, A. Mirizzi, "Probing protoneutron stars with gamma-ray axionscopes", JCAP **11** (2024) 009, JCAP 11 (2024) 009 [arXiv:2405.02395 [hep-ph]].

(P7) S. Balaji, P. Carenza, P. De la Torre Luque, A. Lella, L. Mastrototaro, "In-flight positron annihilation as a probe of feebly interacting particles", Phys.Rev.D **111** (2025) no.8, 8, [arXiv:2501.07725 [hep-ph]].

5.1 Gamma-rays from radiative decays of heavy axions

In the previous Chapters of this Thesis we have discussed the phenomenology of axions with masses up to $m_a \sim \mathcal{O}(100)$ MeV assuming a minimal model in which axions are only coupled to nuclear matter. In this context, we have shown that the combination of indirect probes, as the shortening of the observed SN neutrino burst (see Chapter 3), and direct signatures, as the non-observation of axion-induced events in KII during SN 1987A [see Chapter (4)], rules out values of the axion-nucleon coupling $g_{aN} \gtrsim 10^{-9}$ for axion masses $m_a \lesssim 300$ MeV. Nevertheless, the phenomenology of heavy axions significantly widens if they are also provided with the coupling to photons.

In this regard, the axion-photon couplings is typically modeled through the following Lagrangian (Di Luzio et al., 2020)

$$\mathcal{L}_{a\gamma} = -\frac{1}{4} g_{a\gamma} F^{\mu\nu} \tilde{F}_{\mu\nu} a \,, \tag{5.1}$$

where $g_{a\gamma}$ is the axion-photon coupling (in units of inverse energy), $F^{\mu\nu}$ is the electromagnetic tensor and $\tilde{F}_{\mu\nu} = \frac{1}{2}\epsilon_{\mu\nu\rho\sigma} F^{\rho\sigma}$ its dual. In the following Sections we will give some insights about the possible origin of this coupling in the UV theory describing a generic axion coupled to nuclear matter, and discuss the phenomenological consequences related to the axion-photon coupling.

5.1.1 The UV origin of the axion-photon coupling

The interaction vertex in Eq. (5.1) may arise from different UV completions of the effective low-energy Lagrangian describing axion interactions at typical SN temperatures $T \sim 30$ MeV. A first possible approach consists in assuming that generic axion-like particles are furnished with tree-level couplings to

both photons and nucleons having different origins in the high-energy theory. In this scenario, it is licit to infer that couplings to photons and nucleons are mutually unrelated, as done in Calore et al., 2020; Lella, Carenza, et al., 2023. In these studies, it is customary to set axion production in the SN core, governed by nuclear processes, by assuming the maximum allowed value of the axion-nucleon coupling which does not perturb the duration of the SN neutrino burst, namely $g_{aN} \simeq 10^{-9}$ (Lella et al., 2023). For definiteness, in the following when assuming unrelated couplings to photon and nucleons, we will set $g_{ap} = 10^{-10}$ and $g_{an} = 0$. Conversely, the axion-photon coupling will be allowed to vary freely, investigating the sensitivity of the different probes in the plane $g_{a\gamma}$ vs m_a.

Nonetheless, in Lella, Ravensburg, et al., 2024 we prove that, even in the absence of a tree-level axion-photon coupling, MeV-scale axions coupled to nuclear matter are naturally provided with an additional coupling to photons. This is due to the fact that the low-energy effective Lagrangian describing nuclear interactions in Eq. (3.1) is expected to be generated at higher energies by the fundamental degrees of freedom of QCD, namely quarks and gluon fields. In this context, the interaction Lagrangian for a generic axion-like particle (not necessarily a QCD axion) coupling to QCD has the form

$$\mathcal{L}_{\text{aQCD}} = c_g \frac{g_s^2}{32\pi^2} \frac{a}{f_a} G^a_{\mu\nu} \tilde{G}^{a\mu\nu} + \sum_q c_q \frac{\partial_\mu a}{2 f_a} \bar{q} \gamma^\mu \gamma_5 + \frac{(m_{a,0})^2}{2} a^2 \,, \tag{5.2}$$

where g_s is the coupling constant of QCD, $G^a_{\mu\nu}$ is the gluon field strength tensor, $\tilde{G}^a_{\mu\nu} = \frac{1}{2} \epsilon_{\mu\nu\rho\sigma} G^{a\rho\sigma}$ its dual, c_g and c_q are $\mathcal{O}(1)$ model-dependent constants, and $q = u, d, s, c, t, b$ runs over the quark species. Moreover, here f_a denotes a generic energy scale defining the dynamics of the axion-like particle considered, which is in general not related to the Peccei-Quinn scale. Notice that in this equation we also introduced a mass term $m_{a,0}$. Since we are interested in axions with masses $m_a \gtrsim 1$ MeV, we assume the contribution to the axion mass coming from the QCD dynamics to be negligible. In this regard, we highlight that, due the large mass difference between the canonical QCD axion and MeV-scale axions coupling to nucleons considered here, the latter are in general decoupled from the dynamics resolving the strong CP problem (see Appendix C for more details). The Lagrangian in Eq. (5.2) would induce model dependent couplings to nucleons given by Eq. (3.1). Although Eq. (5.2) does not include a tree-level photon coupling

as in Eq. (5.1), such coupling is generated in the low-energy theory through fermion loops and axion-pion mixing, reading

$$g_{a\gamma} = \frac{\alpha_{\rm em}}{2\pi f_a} C_\gamma \,, \tag{5.3}$$

where $\alpha_{\rm em}$ is the electromagnetic fine-structure constant and (Bauer, Neubert, and Thamm, 2017; Bauer, Neubert, Renner, et al., 2022)

$$C_\gamma(c_g, c_u, c_d) = -1.92\, c_g - \frac{m_a^2}{m_\pi^2 - m_a^2}\left[c_g \frac{m_d - m_u}{m_d + m_u} + (c_u - c_d)\right], \tag{5.4}$$

holding for $m_a \lesssim 1$ GeV and away from the strong mixing regime $|m_\pi^2 - m_{a,0}^2| \gg m_\pi^2 f_\pi / f_a$ (Bauer, Neubert, Renner, et al., 2021). Moreover, we have neglected the contribution from quarks heavier than u, d (Bauer, Neubert, Renner, et al., 2022; Bauer, Neubert, and Thamm, 2017), and m_u and m_d are the masses of the light quarks whose ratio is measured from lattice estimates $m_u/m_d = 0.48$ (Divitiis et al., 2013; Basak et al., 2015; Horsley et al., 2016; Grilli di Cortona et al., 2016). We remark that this photon coupling is "irreducible" for MeV-scale axions coupled to nuclear matter, since it has the same origin as the axion nucleon-couplings (see also the study in Benabou, Manzari, et al., 2025 which takes advantage of the same arguments discussed in Lella, Ravensburg, et al., 2024 and reported in this Thesis work). In general, the induced photon-couplings depend on the values of $\{c_g, c_u, c_d\}$, which might be fixed once specifiying the UV model. To simplify the expressions, we fix $c_u(c_g, c_d)$ by setting $C_n \simeq 0$ as in the KSVZ model, which we assume as our benchmark model in most of previous Chapters. Moreover, we assume as a benchmark case $c_g = 1$ and $c_d = 0$ to display our results. This assumption is justified by the study carried out in Lella, Ravensburg, et al., 2024, showing that constraints can change at most by factors $\mathcal{O}(1)$ in the different scenarios. Thus, the axion-photon coupling can be related to the axion-proton coupling as follows

$$g_{a\gamma} \simeq 9.5 \times 10^{-4}\, g_{ap}\ \text{GeV}^{-1} \times \left[4.64 + 0.73 \frac{m_a^2}{m_\pi^2 - m_a^2}\right]. \tag{5.5}$$

We highlight this expression shows a pole at $m_a = m_\pi$. However, in the range of couplings considered here $g_{aN} \lesssim 10^{-8}$, we have $f_a \gtrsim 10^{-8}$ GeV^{-1} and Eq. (5.5) hold for $|m_a - m_\pi|/m_\pi \gtrsim 10^{-9}$ (Di Luzio, Guerrera, et al.,

2024). Thus, this limitation does not meaningfully affect our results in the phenomenologically interesting parameter range. Finally, we observe that, for values of the model dependent constants assumed here, C_γ may vanish for a tuned value of the axion mass around $m_a \simeq 147$ MeV.

5.1.2 SN production and decays

In the core of an exploding SN, the coupling to photons introduced in Eq. (5.1) would allow for the production of MeV-scale axions by means of Primakoff process on free photons $\gamma + p \to p + a$ and photon coalescence $\gamma + \gamma \to a$ (see, e.g., Lucente et al., 2020 which places $g_{a\gamma} \lesssim 5 \times 10^{-9}\,\mathrm{GeV}^{-1}$ from the standard SN cooling argument). Nevertheless, these production channels are dramatically suppressed compared to nuclear production channels in regions of the parameter space currently allowed by astrophysical constraints (see Fig. 2.7 and Fig. 2.8). Therefore, we can safely neglect the photon coupling when considering SN axion production.

Although the photon coupling is irrelevant in the axion emissivity, it may allow for axion decays. The axion decay rate in the particle rest frame is given by

$$\Gamma_{a\gamma\gamma} = g_{a\gamma}^2 \frac{m_a^3}{64\pi}\,, \tag{5.6}$$

corresponding to a decay length in the laboratory reference frame (Calore, Carenza, Giannotti, et al., 2021)

$$\begin{aligned}\lambda_{a\gamma\gamma} = \frac{\gamma_a \beta_a}{\Gamma_{a\gamma\gamma}} \simeq 1.3\,\mathrm{kpc} \left(\frac{\omega_a}{100\,\mathrm{MeV}}\right) \left(\frac{m_a}{10\,\mathrm{MeV}}\right)^{-4} \\ \times \left(\frac{g_{a\gamma}}{10^{-13}\,\mathrm{GeV}^{-1}}\right)^{-2} \sqrt{1 - \left(\frac{E_a}{m_a}\right)^2}\,,\end{aligned} \tag{5.7}$$

where E_a is the axion energy, γ_a is the Lorentz factor and β_a is the axion velocity. The possibility of radiative decays of heavy axions with typical energies $\sim 10 - 250$ MeV opens many different phenomenological scenarios to constrain axion properties. In particular, depending on the value of the axion decay length, they can decay either inside the star envelope of radius $R_{\mathrm{env}} \simeq 3 \times 10^{14}$ cm (Ouchi et al., 2017; Goldberg et al., 2020), depositing energy in the stellar mantle, or outside from the star volume, giving rise to gamma-ray signatures which may be directly detected after the SN explosion

or contributing to a diffuse gamma-ray background generated by SN axions. All of these scenarios can be exploited to set stringent constraints on different regions of the axion parameter space, as we illustrate in the following Sections.

5.1.3 Energy Deposition in the SN envelope

Axions with masses $m_a \gtrsim 100$ MeV can escape the PNS and then decay before leaving the stellar volume, since their typical decay length is shorter than the SN envelope radius $\lambda_\gamma \lesssim R_{\rm env}$. By means of this mechanism, the decay of such axions may dump a large amount of energy inside the envelope of the progenitor star (Caputo, Janka, et al., 2022). If the energy deposition is too large, this phenomenon would power the ejection of the outer layers of the stellar mantle independently of any hypothetical SN explosion mechanism (Falk et al., 1978; Sung et al., 2019), especially the neutrino heating process in the delayed explosion scenario which is in agreement to observations of SN 1987A. Thus, this argument immediately provides a "calorimetric" constrain on the properties of heavy axions. In this context, observations of low-energy SNe, a class with particularly low explosion energies, can be exploited to severely constrain this scenario (Yang and Chevalier, 2015; Stockinger et al., 2020). For these systems, one should require that the energy deposited in the mantle by heavy-axion decays has to be less than $\sim 0.1\,\mathrm{B}$, which is one order of magnitude smaller than explosion energy expected for standard SNe, $E_{\rm exp} \simeq 1\,\mathrm{B} = 10^{51}$ erg.

The total energy released by decays in the SN envelope is given by

$$\begin{aligned} E_{\rm dep} =& 4\pi \int dt \int_0^{R_{\rm PNS}} dr\, r^2 \int_{m_a}^{\infty} dE_a\, E_a\, \frac{d^2 n_a}{dE_a\, dt}(r, t, E_a^{\rm loc}) \\ & \times \left[\exp\left(-\frac{R_{\rm PNS} - r}{\lambda_a} \right) - \exp\left(-\frac{R_{\rm env} - r}{\lambda_a} \right) \right] , \end{aligned} \tag{5.8}$$

where $d^2 n_a / dE_a\, dt$ is the axion spectrum per unit time and unit volume, E_a is the local production energy and the radial integration accounts for the total axion production in the PNS of radius $R_{\rm PNS} \simeq 30$ km. In this expression $E_a = \alpha \times E_a^{\rm loc}$ is the axion energy measured by a distant observer, red-shifted by the gravitational lapse factor $\alpha(r, t)$ (Rampp et al., 2002). Notice that the combination of the exponentials in Eq. (5.8) accounts for axion decays

occurring between the PNS and photosphere radius. We also observe that in this expression we did not take into account axion reabsorption in the PNS nuclear medium, since it is negligible in the range of couplings considered here $g_{ap} \lesssim 10^{-8}$ (see Section 3.3).

Furthermore, at axion masses $m_a \gtrsim 3m_\pi$ axion decays in three pions, $a \to 3\,\pi^0$ and $a \to \pi^+\,\pi^-\,\pi^0$ are also allowed. The decay rate associated to this process is given by (Bauer, Neubert, and Thamm, 2017)

$$\Gamma_{a3\pi} = \frac{m_a m_\pi^4\,(\Delta c_{ud})^2}{6144\,\pi^3 f_\pi^2 f_a^2}\Theta(m_a - 3m_\pi)\left[g_0\left(\frac{m_\pi^2}{m_a^2}\right) + g_1\left(\frac{m_\pi^2}{m_a^2}\right)\right]\,, \tag{5.9}$$

where

$$g_n(r) = \frac{2\cdot 6^n}{(1-r)^2}\int_{4r}^{(1-\sqrt{r})^2} dz\,\sqrt{1-\frac{4r}{z}}(z-r)^{2n}\sqrt{1+z^2+r^2-2z-2r-2zr} \tag{5.10}$$

and

$$\Delta c_{ud} = c_u - c_d + c_g\frac{m_d - m_u}{m_d + m_u}\,. \tag{5.11}$$

Therefore, in this range of masses, the total axion decay length is given by

$$\lambda_a^{-1} = \lambda_{a\gamma\gamma}^{-1} + \lambda_{a3\pi}^{-1} \tag{5.12}$$

Notice that, once produced, neutral pions decay immediately in photon pairs, while charged pions tend to be reabsorbed in the nuclear medum by means of strong interactions. Thus, also this decay channel would contribute to energy deposition. By requiring that $E_{\rm dep} \lesssim 0.1\,\mathrm{B}$, we have obtained the constraints shown in Fig. 5.1 and Fig. 5.2 labeled as "Explosion energy". In particular, Fig. 5.1 displays constraints obtained by fixing axion production in the SN core at values of the nucleon couplings $g_{ap} = 10^{-10}$ and $g_{an} = 0$. Conversely, in Fig. 5.2 we set constraints on g_{ap} by assuming that it is related to the QCD-induced photon coupling as in Eq. (5.5). Notice that the latter bound is rapidly relaxed around masses $m_a \simeq 147$ MeV, where the induced axion-photon coupling vanishes when assuming $c_g = 1$ and $c_d = 0$. Remarkably, the energy-deposition argument extends the exclusion region of the SN 1987A cooling bound up to masses $m_a \sim 600$ MeV (Caputo, Janka, et al., 2022).

5.1.4 Gamma-ray bursts from SN 1987A

Axions with masses $m_a \sim 10 - 100$ MeV have typical decay lengths larger than the stellar radius $\lambda_a \gtrsim R_{\rm env}$, thus they can leave the star unimpeded and

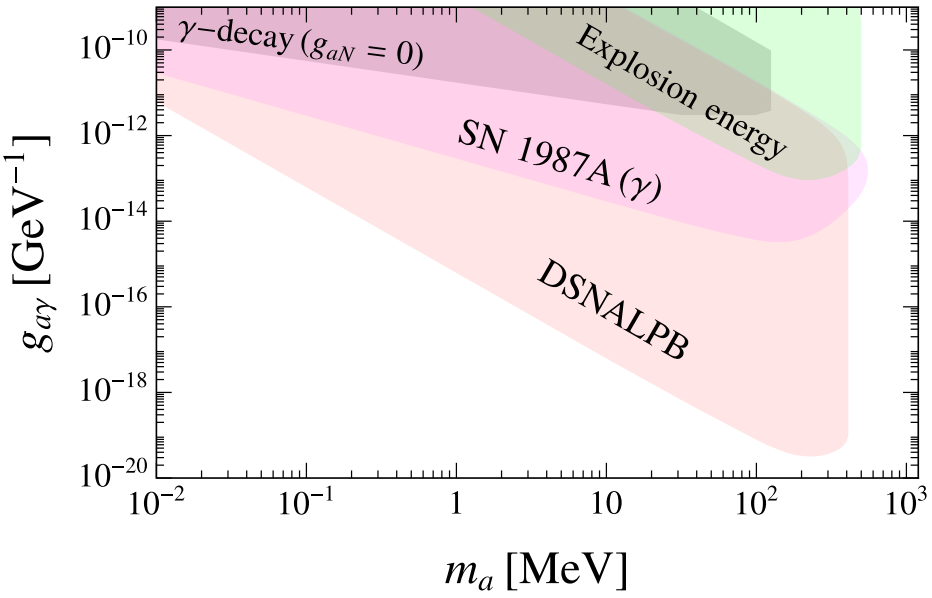

Figure 5.1: Bounds on the axion-photon coupling $g_{a\gamma}$ for massive axions from SNe setting $g_{ap} = 10^{-10}$ and $g_{an} = 0$. The green area is referred to the energy deposition constrain, the magenta region is associated to radiative decays of axions from SN 1987A, the pink area is the excluded region by observations of the DSALPB. Finally, the gray region is the excluded region discussed in Jaeckel et al., 2018, considering γ-decays of massive axions produced by Primakoff processes.

then decay in the interstellar medium between the SN and the Earth. If the SN is sufficiently close, some of the photons produced in radiative decays may eventually reach gamma-ray detectors, which would observe a time-delayed (due to the finite time of flight of heavy axions) axion-induced gamma-ray burst following the observation of the neutrino burst. Once again, the most constraining system to date for this scenario is SN 1987A at a distance $d_{\rm SN} = 51.4$ kpc. Gamma-ray observations of the SN event were due to the Gamma-Ray Spectrometer on board of the Solar Maximum Mission (SMM) satellite, taking data in the direction of SN 1987A for $\Delta t = 223$ s after the first neutrino signal reaching the Earth. In particular, the operational energy range of this experiment was $[25, 100]$ MeV.

The photon fluence due to axion decays F_γ, defined as the number of photons per unit area reaching Earth within the SMM observational time, can be

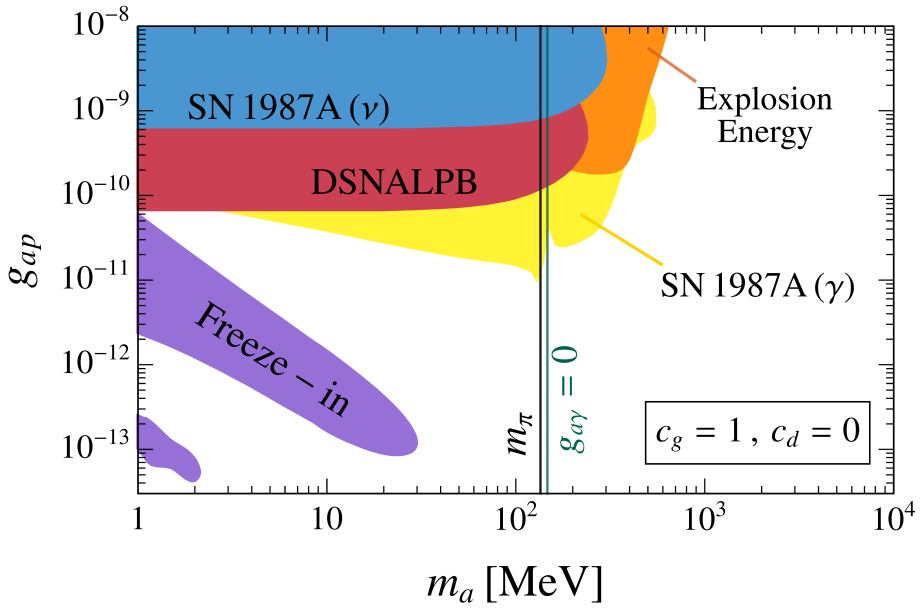

Figure 5.2: Summary plot of the bounds placed in this work for axions coupling to nuclear matter and provided with an irreducible photon coupling induced by QCD. Here we assume $c_g = 1$ and $c_d = 0$ (see text for details). The blue region displays the SN 1987A cooling bound placed in Lella et al., 2023, while the violet region has been obtained by converting the limit on axion-photon interactions placed in Langhoff et al., 2022 by searching for signatures of an irreducible axion background to a constraint on g_{ap}. The other bounds have been calculated in Lella, Ravensburg, et al., 2024 from the non observation of a DSNALPB (red region), the non observation of gamma-rays from SN 1987A (yellow region) and the energy deposition argument (orange region). The dark green vertical lines depict the value of the axion mass for which the QCD induced axion-photon coupling vanishes in the considered cases.

estimated as (Oberauer et al., 1993; Jaffe et al., 1997; Müller et al., 2023b):

$$F_\gamma = \int_{m_a}^{\infty} dE_a \int_{E_\gamma^{\min}}^{E_\gamma^{\max}} dE_\gamma \, \Theta(\Delta E_\gamma) \frac{\mathrm{BR}_{a\to\gamma\gamma}}{2\pi d_{\mathrm{SN}}^2} \, p_a^{-1} \, \frac{dN_a}{dE_a} \times \left[\exp\left(-\frac{m_a R_*}{\tau_a p_a} \right) - \exp\left(-\frac{2E_\gamma \, \Delta t}{\tau_a m_a} \right) \right] , \tag{5.13}$$

where $R_* = 3 \times 10^{12}$ cm is the radius of the progenitor of SN 1987A (which, as a blue supergiant, was relatively small) and dN_a/dE_a is the total axion spectrum integrated over the emission time window and over the stellar volume

$$\frac{dN_a}{dE_a} = 4\pi \int dt \int dr \, r^2 \, \alpha(r,t)^{-1} \frac{d^2 n_a}{dt \, dE_a}(r, t, E_a^{\mathrm{loc}}) \, . \tag{5.14}$$

As discussed in Müller et al., 2023b, conservation of energy-momentum in the observer frame defines the limits for integration on the photon energies in the reach of SMM

$$\begin{aligned} E_\gamma^{\min}(p_a) &= \max\left(25 \text{ MeV}, \, \frac{1}{2}(E_a - p_a), \, \frac{m_a^2 \, R_*}{2 \, p_a \, \Delta t} \right) , \\ E_\gamma^{\max}(p_a) &= \min\left(100 \text{ MeV}, \, \frac{1}{2}(E_a + p_a) \right) , \\ \Delta E_\gamma(p_a) &= E_\gamma^{\max}(p_a) - E_\gamma^{\min}(p_a) \end{aligned} \tag{5.15}$$

in which p_a is the modulus of the axion three-momentum. Notice that in Eq. (5.13) we have also scaled the flux by the branching ratio for axion decays in photon pairs $\mathrm{BR}_{a\to\gamma\gamma}$ to take into account only axion radiative decays.

Since no significant excess was observed by SMM, the axion-induced photon fluence arriving at the detector must not exceed a 3-σ variation of the observed background data, i.e. $F_\gamma < 1.78 \text{ cm}^{-2}$ (Jaeckel et al., 2018; Hoof et al., 2023). Resulting constraints are labeled as "SN 1987A (γ)" in Fig. 5.1 and Fig. 5.2. Interestingly, from Fig. (5.2) we can observe that constraints from the absence of gamma-rays from SN 1987A are the leading bounds in the mass range 10 MeV $\lesssim m_a \lesssim$ 300 MeV, ruling out axion-proton couplings down to $g_{ap} \lesssim$ few$\times 10^{-11}$. Moreover, we can also observe the occurrence of resonant effects when the axion mass approaches the pion mass, while the bound is suddendly relaxed for values of the axion mass around $m_a \simeq 147$ MeV, where the induced axion-photon coupling vanishes.

Finally, we recall that Diamond, Fiorillo, Marques-Tavares, and Vitagliano, 2023 pointed out that in some regions of parameter space seemingly excluded by this decay bound, axion-decay may eventually lead to the formation of a dense "fireball" QED-plasma, from which no gamma-ray can escape, and SMM observations cannot be employed to rule out these region. Nevertheless, this portion of the parameter space can be typically closed through the non-observation of fireball-sourced photons by the Pierre Venus Orbiter experiment.

5.1.5 Diffuse SN ALP Background

The superposition of the axion fluxes produced in the core of all past SNe occurred within the observable Universe may have lead to a diffuse SN Axion-Like-Particle background (DSALPB) (Raffelt and otheres, 2011), analogous to the diffuse neutrino background (Beacom, 2010). Then, radiative decays over cosmological time scales of axions composing the DSALPB would lead to an additional contribution to the diffuse gamma-ray background measured by gamma-ray telescopes as the *Fermi*-Large Area Telescope (LAT).

The contribution to the diffuse gamma-ray flux due to decays of axions in the DSALPB is obtained by integrating over the red-shift z the fluxes coming from all the expected CC SNe within the event-horizon (Calore et al., 2020):

$$\frac{d\phi_\gamma^{\rm dif}}{dE_\gamma} = \int_0^\infty dz \left|\frac{dt}{dz}\right| (1+z) R_{\rm SN}(z) \frac{dN_\gamma(E_\gamma(1+z))}{dE_\gamma}\,, \tag{5.16}$$

where E_γ is the energy of the emitted photon. Here $R_{SN}(z)$ is the SN explosion rate, taken from Priya et al., 2017, with a total normalization for the core-collapse rate $R_{\rm cc} = 1.25 \times 10^{-4}\,{\rm yr}^{-1}\,{\rm Mpc}^{-3}$ and computed assuming an average progenitor mass of about 18 $M_\odot$, as in the SN simulation employed in this work. Furthermore, $|dt/dz|^{-1}$ is given by $|dt/dz|^{-1} = H_0(1+z)[\Omega_\Lambda + \Omega_M(1+z)^3]^{\frac{1}{2}}$ with the cosmological parameters $H_0 = 67.4\,{\rm km\,s^{-1}\,Mpc^{-1}}$, $\Omega_\Lambda = 0.7$ and $\Omega_M = 0.3$. Since daughter photons can acquire any energy in the range $(\omega_a - p_a)/2 < E_\gamma < (\omega_a + p_a)/2$, corresponding to a unique angle between the axion and photon momenta, the gamma-ray flux sourced by SN

axion decays at redshift z is given by

$$\frac{dN_\gamma(E_\gamma)}{dE_\gamma} = \int_{p_a^{\rm min}}^{\infty} \frac{dp_a}{\omega_a}\, 2 \times {\rm BR}_{a\to\gamma\gamma}\, \frac{dN_a}{d\omega_a} \times \left[\exp\left(-\frac{R'_{\rm env} m_a}{p_a \tau_a}\right) - \exp\left(-\frac{d(z) m_a}{p_a \tau_a}\right)\right], \tag{5.17}$$

where $d(z)$ is the cosmological distance for SN occurred at redshift z, $p_a^{\rm min} = E_\gamma + m_a^2/4E_\gamma$ is the minimal axion momentum contributing to the flux at photon energy E_γ and dN_a/dE_a is the spectrum of the axions emitted.

To avoid an excessive distortion of the measured isotropic gamma-ray background provided in the Pass 8 R3 processed dataset (8-yr dataset) for the ULTRACLEANVETO event class section by the *Fermi*-LAT Collaboration, we have to require that in the energy range $E_\gamma \gtrsim 50\,{\rm MeV}$ DSALPB-sourced gamma-ray fluxes do not exceed (Calore et al., 2020)

$$\frac{d\phi_\gamma(E_\gamma)}{dE_\gamma} \simeq 2.2 \times 10^{-3} \left(\frac{E_\gamma}{\rm MeV}\right)^{-2.2} {\rm MeV}^{-1}\,{\rm cm}^{-2}\,{\rm s}^{-1}\,{\rm sr}^{-1}\,. \tag{5.18}$$

At lower energies, photon fluxes have to be compared to the measurements from the COMPTEL experiment (Stacy et al., 2008)

$$\frac{d\phi_\gamma(E_\gamma)}{dE_\gamma} \simeq 1.05 \times 10^{-4} \left(\frac{E_\gamma}{5\ {\rm MeV}}\right)^{-2.4} {\rm MeV}^{-1}\,{\rm cm}^{-2}\,{\rm s}^{-1}\,{\rm sr}^{-1}\,. \tag{5.19}$$

Some examples of the expected diffuse gamma-ray fluxes due to radiative decays in the DSALPB are illustrated in Fig. 5.3 in comparison to the fitted isotropic gamma-ray background observed by *Fermi*-LAT.

The phenomenological consequences of the existence of a DSALPB in the case of axions coupled to photons only and axions coupled to both photons and nucleons have been first analyzed in Eckner et al., 2021; Calore et al., 2022a. Subsequently, in Lella, Carenza, et al., 2023 we have re-evaluated these results by including both contributions from NN bremsstrahlung emission and pion conversion emission processes. Constraints introduced in this work by setting $g_{ap} = 10^{-10}$ are depicted as a pink region in Fig. 5.1. Subsequently, these arguments have been also employed in Lella, Ravensburg, et al., 2024 to constrain the axion-proton coupling g_{ap}, in light of the outcomes summarized in Section 5.1.1, which outlined the existence of an irreducible photon coupling for heavy axions coupled to nuclear matter. From Fig. 5.2 we can

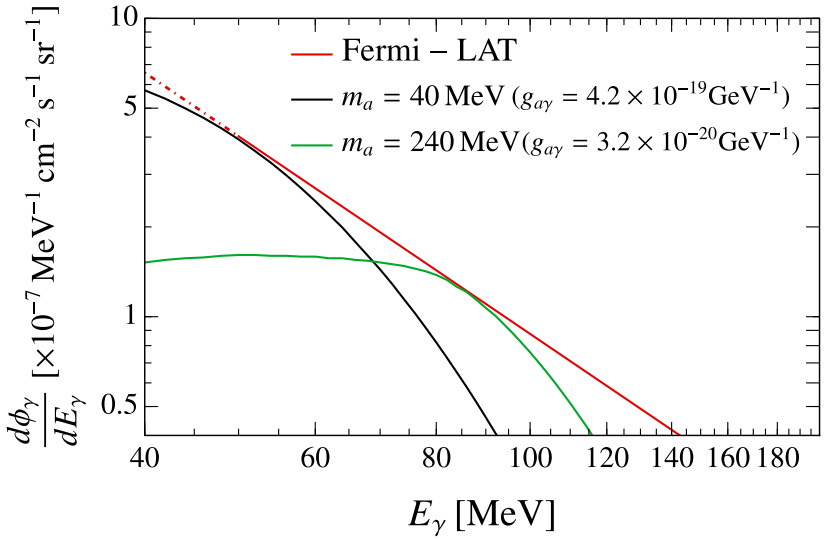

Figure 5.3: Diffuse gamma-ray fluxes induced by the decay of DSALPB for two different axion masses. In this figure we fix $g_{ap} = 10^{-10}$ and $g_{an} = 0$. The red line refers to the diffuse gamma-ray background measured by *Fermi*-LAT. The dot-dashed part of the line is an extrapolation of the Fermi line at energies $30\,\text{MeV} \leq E \leq 50\,\text{MeV}$.

observe that the non-observation of any evidence for the DSALPB allows us to constrain axion masses $1\ \text{MeV} \lesssim m_a \lesssim 5\ \text{MeV}$ excluding values of $g_{ap} \gtrsim 7 \times 10^{-11}$.

5.2 Gamma-rays from leptonic decays of heavy-axions

As for the case of axions coupled to photons, the presence of leptonic couplings may open novel perspectives for the phenomenology of axions produced in the nuclear medium of the PNS. In this Section, we will focus on the case of axions coupled to electrons, which may provide characteristic indirect signatures. However, in Lella, Carenza, et al., 2023 we also consider the case of SN axions coupled to muons. The axion-electron coupling is described through the following Lagrangian

$$\mathcal{L}_{ae} = \frac{g_{ae}}{2m_e}(\bar{e}\gamma_\mu\gamma_5 e)\partial^\mu a\,. \tag{5.20}$$

The presence of an axion-electron coupling can source axion production by means of electron-proton Bremsstrahlung ($e^- + p \to e^- + p + a$), electron-positron fusion ($e^- + e^+ \to a$) and Semi-Compton scatterings ($\gamma + e^- \to a + e^-$) (Lucente and Carenza, 2021; Ferreira et al., 2022; Fiorillo, Pitik, et al., 2025b). However, in models in which both g_{ae} and g_{aN} are switched on, the axion production rate via processes triggered by the axion-electron coupling is completely negligible in the currently available parameter space with respect to nuclear production rates. Nevertheless, MeV-scale axions coupling to electrons can efficiently decay in electron positron pairs $a \to e^+ + e^-$ with a typical decay length (Altmann et al., 1995; Jaeckel et al., 2018):

$$\lambda_{aee} = \frac{8\pi}{g_{ae}^2 m_a} \frac{\omega_a}{m_a} \sqrt{\frac{1 - m_a^2/\omega_a^2}{1 - 4m_e^2/m_a^2}} = \\ = 0.16\,\mathrm{kpc} \left(\frac{g_{ae}}{10^{-15}}\right)^{-2} \left(\frac{m_a}{1\,\mathrm{MeV}}\right)^{-1} \sqrt{\frac{\omega_a^2 - m_a^2}{m_a^2 - 4m_e^2}}\,. \tag{5.21}$$

Once produced in the PNS nuclear medium, heavy axions can decay in electron-positron pairs within or outside the stellar volume, depending on their decay length. If the decay length is shorter than the SN envelope radius, axions produce electrons and positrons which rapidly thermalize in the stellar plasma, taking part to the energy deposition process in the same way as photons from axion radiative decays (see Section 5.1.3). On the other hand, when decaying outside from the SN volume, they can lead to the injection of positrons in the interstellar medium, giving rise to observable signatures as the 511 keV line or gamma-rays from in-flight electron-positron annihilation.

As for the irreducible photon coupling discussed in Section 5.1.1, axions coupling to nucleons are also naturally supplied with an electron coupling sourced by QCD effects, which shares the same UV origin of nuclear couplings. The induced axion-electron coupling reads

$$g_{ae} = \frac{3\alpha_{\mathrm{em}}\, m_e}{4\pi} K\, g_{a\gamma} \sim 8.7 \times 10^{-7} K \left(\frac{g_{a\gamma}}{\mathrm{GeV}^{-1}}\right)\,. \tag{5.22}$$

where $g_{a\gamma}$ is the induced photon coupling, $K = \log\left(f_a^2/m_e^2\right) + \delta_1 + g(m_a)$ and the renormalization-scheme dependent constant δ_1, as well as the function

$g(m_a)$, are provided in Bauer, Neubert, and Thamm, 2017. In particular, K is an $\mathcal{O}(10)$ factor at scales $f_a \sim 10^9$ GeV and masses $m_a \gtrsim 10$ MeV. Nevertheless, when evaluating the branching ratio for electron-positron decays

$$\begin{aligned} \mathrm{BR}(a \to e^+e^-) &= \frac{\lambda_e^{-1}}{\lambda_e^{-1} + \lambda_\gamma^{-1}} \simeq \frac{\lambda_e^{-1}}{\lambda_\gamma^{-1}} \\ &\simeq 6.1 \times 10^{-6} \left(\frac{m_a}{10\ \mathrm{MeV}}\right)^{-2} \sqrt{1 - \frac{4m_e^2}{m_a^2}} \ll 1\,, \end{aligned} \tag{5.23}$$

one realizes that electronic decays triggered by the QCD-induced electron coupling are extremely suppressed compared to radiative decays due to the induced photon coupling. Thus, effects due to the induced electron coupling are irrelevant for our study. Therefore, in the following we will study the phenomenology of MeV-scale axions coupled to nuclear matter which are also provided with a tree-level electron coupling, assuming that nuclear and electron couplings are not correlated one to each other.

5.2.1 The 511 keV line

Axions decaying in electron-positron pairs outside from the SN envelope may inject a large amount of positrons in the intergalactic medium (Calore, Carenza, Giannotti, et al., 2021). The energetic positrons emitted cannot escape the Galaxy since they are trapped by the Galactic magnetic field in the order of $B \sim \mathcal{O}(1)\,\mu$G. In particular, positrons with energies $\lesssim 100$ MeV are expected to travel no more than ~ 1 kpc (Jean et al., 2006; Jean et al., 2009; Martin et al., 2012). While traveling within the intergalactic medium, positrons loose most of their energy through Bhabha e^+e^- scatterings, before annihilating almost at rest into two photons, each of energy of $\simeq 511$ keV. Depending on the free-electron number density in the Galaxy and the ionization condition, the average time necessary for annihilation at rest can range between $\tau_e \in [10^3, 10^6]$ years (Wang et al., 2006; Kalemci et al., 2006). Nevertheless, part of the positron flux can also annihilate in-flight giving rise to signatures in the MeV energy range. For the moment we will neglect the contribution due to the in-flight positron annihilation, which will be reconsidered in the following Section to complement constraints set by observations of the 511 keV line.

Measurements of the angular distribution of the Galactic 511 keV X-ray line are provided by the SPI gamma-ray spectrometer on the INTEGRAL satellite (Strong et al., 2005; Bouchet et al., 2010; Siegert et al., 2016; Siegert et al., 2019). Interestingly, a full understanding of the observed characteristics of this monochromatic emission is still challenging. Nevertheless, the angular analysis of the 511 keV signal can be directly translated in a bound on the total number of positrons injected inside the Galaxy (Calore, Carenza, Giannotti, et al., 2021)

$$N_{\rm pos} \lesssim 1.4 \times 10^{52} \,. \tag{5.24}$$

The number of positrons released within the Milky-Way by axions, produced by means of nuclear processes inside the core of Galactic SNe and then decaying in electron-positron pairs outside from the SN envelope, is given by

$$N_{\rm pos} = \int dE_a \, {\rm BR}_{a\to e^+e^-} \, \frac{dN_a}{dE_a} \left(\epsilon_{II} e^{-R^{\rm II}_{\rm env}/\lambda_a} + \epsilon_I \, e^{-R^{\rm I}_{\rm env}/\lambda_a} \right) \left[1 - \exp\left(-\frac{r_{\rm G}}{\lambda_a} \right) \right] . \tag{5.25}$$

Following the treatment described in DeRocco et al., 2019, we consider the contribution of both type Ib/c and type II SNe, characterized by envelope radii $R^{\rm I}_{\rm env} = 2 \times 10^{12}$ cm and $R^{\rm II}_{\rm env} = 10^{14}$ cm (DeRocco et al., 2019), and average fractions $\epsilon_I = 0.33$ and $\epsilon_{II} = 1 - \epsilon_I$ (Li et al., 2011), respectively. Moreover $r_{\rm G} = 1$ kpc is the typical positron escape radius from the Galaxy. The total axion decay length $\lambda_a^{-1} = \lambda_{a\gamma\gamma}^{-1} + \lambda_{aee}^{-1}$ takes into account also the contribution from the QCD-induced photon coupling present for MeV-scale axions coupling to nucleons, while ${\rm BR}_{a\to ee}$ is the related branching ratio for the decay in electron-positron pairs.

Limits obtained by applying the condition in Eq. (5.24) on the injected number of positrons are displayed as blue regions in Fig. 5.4 and Fig. 5.5. In particular, Fig. 5.4 shows limits in the plane g_{ae} vs m_a by assuming axion-nucleon couplings allowed by the constraints introduced in Fig. 5.2, namely $g_{an} = 0$ and $g_{ap} = 2 \times 10^{-11}$. The 511 keV line observations allow us to exclude axion electron couplings $g_{ae} \gtrsim 10^{-16}$ in the range of masses 1 MeV $\lesssim m_a \lesssim$ 100 MeV. Notice that the limit is relaxed around $m_a = m_\pi$ due to the rapid enhancement in $g_{a\gamma}$ (see discussion in Section 5.1.1) leading to more efficient decays into photons than into electrons, while limits becomes stronger around $m_a = 147$ MeV where the induced photon coupling vanishes. Conversely, in Fig. 5.5 we fix the axion mass at $m_a = 100$ MeV and study limits in the g_{ap} vs g_{ae} plane. Here we also report in grey limits

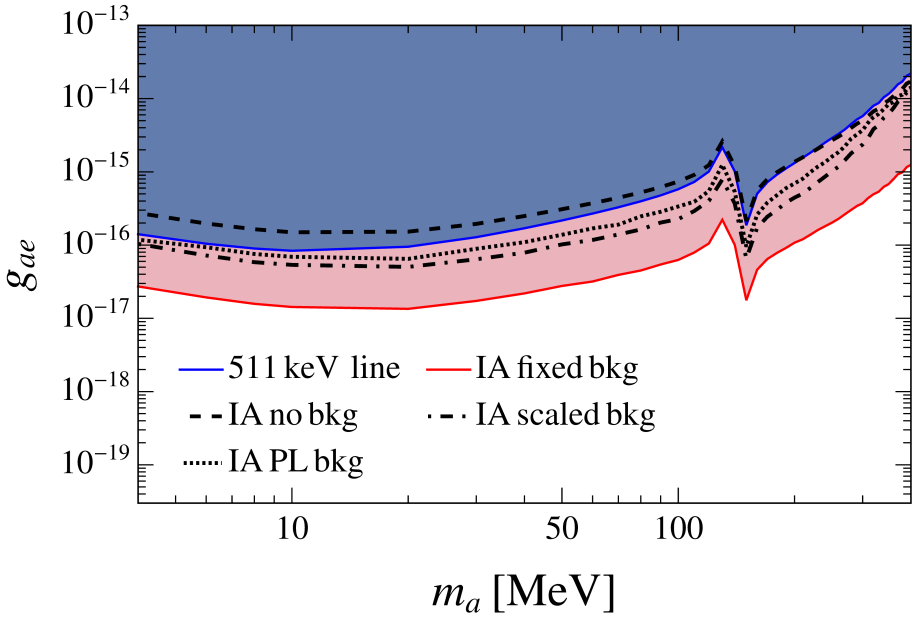

Figure 5.4: Upper limits, at 2σ confidence level, for the case of axions coupled to nucleons and electrons with $g_{ap} = 2 \times 10^{-11}$. We show the limits obtained in the different analyses performed: including our background model ("fixed bkg"), with the same background model but letting it's normalization be free in the fit ("scaled bkg"), including a background described as a simple power-law ("PL bkg") and, the most conservative case, without accounting for any background ("no bkg"). The limit obtained from the analysis of the 511 keV emission is displayed as a blue solid line.

set by other arguments, as the SN cooling bound on g_{ae}, the loop-induced gamma-decay bound introduced in Ferreira et al., 2022, the explosion energy bound and the gamma-decay bound taken from Fig. 5.2. The hatched blue region displays the uncertainty region for the 511 keV bound (De la Torre Luque, Balaji, et al., 2025). We observe that, in the most optimistic scenario, observations of 511 keV line rule out $10^{-15} \lesssim g_{ae} \lesssim 4 \times 10^{-13}$ for $g_{ap} \simeq 10^{-11}$.

5.2.2 In-flight positron annihilation

Interactions of the injected positrons with the interstellar medium, produce not only a diffuse monochromatic signal as the 511 keV line, but could also lead to a continuum emission above and below 511 keV (De la Torre

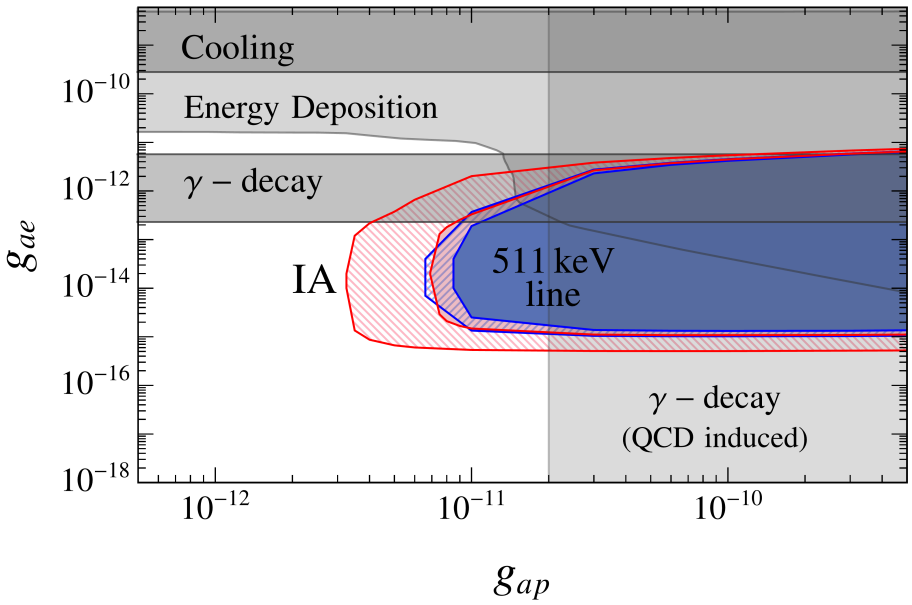

Figure 5.5: IA annihilation bounds in the g_{ae} vs g_{ap} plane for an axion mass $m_a = 100\,\text{MeV}$. We report in red, regions of the parameter space excluded by the arguments related to positron IA, while blue regions are excluded by observations of the 511 keV line. Hatched regions display the uncertainty bands for these limits, ranging from the most conservative to the most optimistic cases discussed in De la Torre Luque, Balaji, et al., 2025. We also report in gray, regions of the parameter space excluded by other arguments, namely the SN cooling bound and the loop-induced γ-decay bound on g_{ae} discussed in Ferreira et al., 2022. Moreover, we also display constraints from energy deposition in the SN envelope (Caputo, Janka, et al., 2022), which here takes into account axion production by means of electron and nucleon couplings, and the γ-decay constraint related to the axion-photon coupling induced by QCD effects, taken from Lella, Ravensburg, et al., 2024 (see Fig. 5.2).

Luque, Balaji, et al., 2025). In particular, high-energy positrons can produce gamma-ray signatures through the following processes:

- relativistic positrons can loose energy by scattering over free and bounded electrons in the intergalactic medium, inducing a continuum gamma-ray spectrum at energies $E_\gamma \sim 1-100$ MeV (De la Torre Luque, Balaji, et al., 2025). This process is dubbed in-flight annihilation (IA);

- 25% of thermalized positrons at rest produce a para-positronium bound states with free electrons, which rapidly decays into two gammas at energies of 511 kev each;
- the 75% of thermalized positrons produce a ortho-positronium state with free electrons, which decays in three photons at energies smaller than 511 keV.

In Balaji et al., 2025 we showed that constraints on the spectrum of in-flight annihilating positrons may eventually strengthen significantly bounds on axions coming from observations of the 511 keV signal.

Following the treatment of Beacom and Yuksel, 2006; De la Torre Luque, Balaji, et al., 2025, the IA emission can be evaluated by scaling the intensity of the 511 keV line as

$$\frac{d\phi^{\rm IA}}{d\Omega dE_\gamma} = \frac{d\phi^{\rm IA}}{d\Omega}\frac{n_H}{P(1-\frac{3}{4}f)}\int_{E_\gamma}^{E_{\rm max}} dE' \frac{1}{N_{\rm pos}}\frac{dN_{\rm pos}}{dE'}\int_{m_e}^{E'} P_{E'\to E}\frac{d\sigma}{dE_\gamma}\frac{dE}{|dE/dx|}\,, \tag{5.26}$$

where $d\phi^{\rm IA}/d\Omega$ is the flux per solid angle of the 511 keV signal directly depending on the morphology of the distribution of Galactic CC SNe, as described in Calore, Carenza, Giannotti, et al., 2021; Calore et al., 2022b. In this expression, n_H is the number of targets over which photons scatter and loose energy, while $f = 0.967 \pm 0.022$ (Jean et al., 2006) is the fraction of propagating positrons generating a positronium state and P is the probability of a positron to annihilate at rest. Thus, the factor $P(1-3f/4)$ rescales the 511 keV flux by the fraction of positrons producing 511 keV photons. The integral over E' accounts for the energy distribution of the injected photons and runs from the minimum positron energy producing photons with energies E_γ up to $E_{\rm max}$ which is the highest energy used in simulations for photon propagation. Moreover, $\frac{1}{N_{\rm pos}}\frac{dN_{\rm pos}}{dE'}$ is the positron number spectrum at energy E' normalized at the total number of injected positrons $N_{\rm pos}$. The second integral describes the energy loss of a positron injected with energy E' down to energy E, whose lowest possible value is of course the electron mass m_e. In particular $P_{E'\to E}$ is the probability for a positron with energy E' to loose energy down to E, $d\sigma/dE_\gamma$ is the differential cross section for a positron of energy E to perform IA generating photons of energy E_γ and $|dE/dx|$ is the ionization energy loss (see De la Torre Luque, Balaji, et al., 2025 for details).

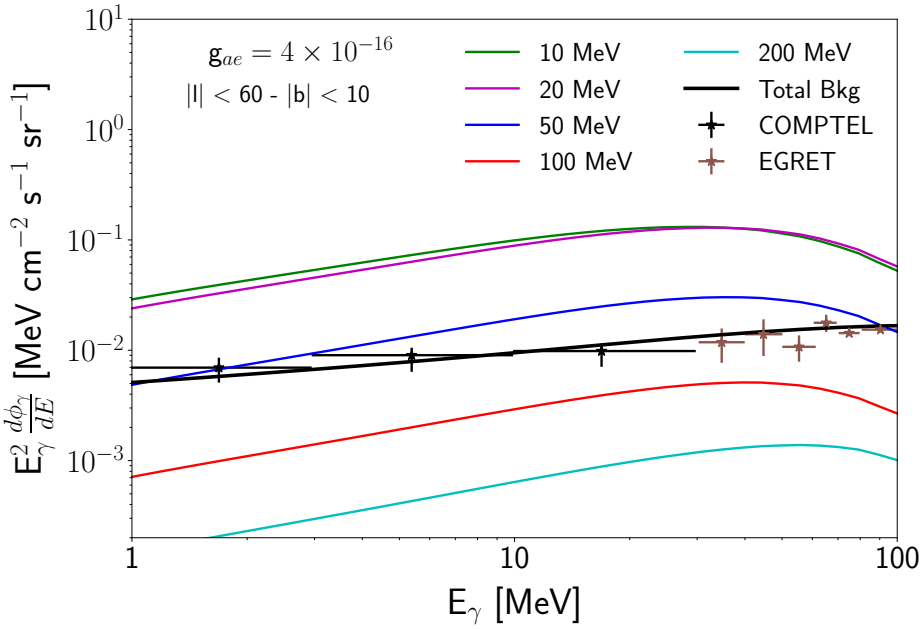

Figure 5.6: IA emission from axions coupling to baryons and electrons. SN axion production is here set by fixing the axion-proton coupling at $g_{ap} = 2 \times 10^{-11}$. The predicted signals are compared to COMPTEL (Strong, Bennett, et al., 1994a; Strong, Bennett, et al., 1994b) and EGRET (Strong, Moskalenko, et al., 2004) measurements of the diffuse γ-ray flux in the MeV range for a region of interest covering the Galactic plane ($|\ell| < 60°$ and $|b| < 10°$). The black line in both panels refers to the expected Galactic background emission (from Inverse-Compton and bremsstrahlung of cosmic ray electrons).

The predicted gamma-ray fluxes for different possible axion masses are shown in Fig. 5.6 for different axion masses and assuming $g_{ae} = 4 \times 10^{-16}$ and $g_{ap} = 2 \times 10^{-11}$. These spectra can be compared to COMPTEL (Strong, Bennett, et al., 1994a; Kappadath, 1998; Strong, Bennett, et al., 1994b) and EGRET (Strong, Moskalenko, et al., 2004) measurements of the diffuse γ-ray flux in the MeV range. In particular, we refer to the region of the sky $|\ell| \leq 60$ and $|b| \leq 10$, where (ℓ, b) are the Galactic latitude and longitude. This region of the sky leads to the strongest constraints among the few regions where COMPTEL data are available, since it is an extended region covering the Galactic plane where the CC SN rate is expected to be higher, providing the strongest signals. We observe that these data, can be well explained by

emission models relying on bremsstrahlung and inverse-Compton emission from cosmic-ray electrons, which are the dominant gamma-ray production channel at energies below few hundreds of MeV. The reference background model considered in this work is taken from Torre Luque et al., 2022; De la Torre Luque, Loparco, et al., 2023, showing strong agreement with data down to energies ~ 100 keV.

Constraints from SN axion injection of positrons accounting for our reference background model are derived at 95% confidence level by requiring compatibility with observations of the COMPTEL experiment. We highlight that we did not includ EGRET measurements in our analysis due to the poor angular resolution of the experiment in the given energy. Our limits at fixed g_{ap} are displayed in Fig. 5.4 in the g_{ae} vs m_a plane as a red solid line ("fixed bkg"). Notice that by employing our reference background model we are able to improve limits from observations of the 511 keV signal by ~ 1 order of magnitude. In order to show the variability of our results for different assumptions for the background model, we show limits by assuming also a simple power-law background ("PL bkg"), the same background as our reference model but leaving free its global normalization ("scaled bkg") and by assuming no background modeling at all ("no bkg"). From Fig. 5.5, we can also appreciate the improvement of our limits in the g_{ae} vs g_{ap} provided by searches of IA annihilation gamma-rays compared to the 511 keV signal. Also in this case, we display as a blue hatched region the maximal uncertainty band related to our constraints.

5.3 Light Axions as probes of the SN core

Ultralight axions coupled to photons with masses $m_a \lesssim 0.1$ neV have typical decay times larger than the age of the Universe. Nevertheless, when propagating inside large scale astrophysical magnetic fields, light axions can efficiently convert in photons (Raffelt and Stodolsky, 1988). In particular, the Milky Way host a large scale magnetic field of magnitude $|B| \sim \mathcal{O}(1)\,\mu G$ and active over distances of the typical size of the Galaxy $L \sim \mathcal{O}(10)$ kpc, which can represent a powerful laboratory to study the conversions of light axions produced in the core of Galactic SNe with typical energies $E_a \sim 100$ MeV. In this context, the non-observation of axion-induced signatures

in the SMM experiment in coincidence to SN 1987A rules out values of the axion-photon coupling $g_{a\gamma} \gtrsim 10^{-15}$ GeV^{-1} for axions coupled to nucleons with $g_{aN} \simeq 10^{-9}$ (Calore et al., 2020).

In this context, the *Fermi*-LAT experiment would represent a powerful facility to detect gamma-ray signatures of SN axions emitted from a next future Galactic SN (see, e.g., Meyer et al., 2017; Calore, Carenza, Eckner, et al., 2024 for some works on the topic). Motivated by these results, in Lella, Calore, Carenza, Eckner, et al., 2024 we studied the capability of *Fermi*-LAT to investigate the spectral properties of the axion-sourced gamma-ray burst in coincidence to a future Galactic SN. In particular, we consider the scenario in which axions in the free streaming regime $g_{aN} \lesssim 10^{-8}$ are produced in the inner regions of the SN core due to their nuclear couplings, they escape the SN volume unimpeded and then are converted within the Galactic magnetic field producing gamma-ray photons detectable in *Fermi*-LAT. Given the axion production spectrum per unit time introduced in Chapter 3 $d^2N_a/dE\,dt$, the expected photon flux at Earth is given by:

$$\frac{d^2\phi_\gamma}{dE\,dt} = \frac{1}{4\pi d^2}\frac{d^2N_a}{dE\,dt}P_{a\gamma}(E)\,, \tag{5.27}$$

where d is the distance from the SN event. In this expression, $P_{a\gamma}$ is the conversion probability in the Galactic magnetic field, which has to be determined by solving 3-dimensional axion-photon propagation equations, due to the complex structure of the Milky Way magnetic field (see, e.g., De Angelis et al., 2011). In the following, we will consider the case of coherent axion-to-photon conversions, which occur for axion masses

$$m_a \ll 0.36\,\text{neV}\left(\frac{E}{100\ \text{MeV}}\right)^{1/2}\left(\frac{L}{10\ \text{kpc}}\right)^{-1/2}\,. \tag{5.28}$$

Under these conditions, axion-photon conversions are energy-independent and the conversion probability is well approximated by

$$P_{a\gamma} \simeq (\Delta_{a\gamma}L)^2\,, \tag{5.29}$$

where

$$\Delta_{a\gamma} \simeq 1.5\times10^{-6}\left(\frac{g_{a\gamma}}{10^{-15}\ \text{GeV}^{-1}}\right)\left(\frac{B_T}{10^{-6}\,\text{G}}\right)\text{kpc}^{-1}\,, \tag{5.30}$$

and B_T is the average value of the transverse component of the magnetic field along the given line of sight. As an exemplary case, here we assume

a Galactic SN at fiducial distance $d = 10$ kpc in the direction of $(\ell, b) = (199.79°, -8.96°)$, which coincides with the sky location of Betelgeuse, which is one of the closest Galactic SN candidates (Leeuwen, 2007). The Galactic magnetic field is here modeled by employing Jansonn and Farrar model (Jansson et al., 2012) with the updated parameters from Adam et al., 2016, for which $B_T \simeq 0.58\,\mu$G in the given direction. A different choice for the magnetic field model would only imply a different normalization of the photon flux arriving at Earth without affecting its spectral features, which are the goal of this study. Moreover, the predicted flux would also depend on the location of the SN event. In this case, we refer to Fig. 7 of Calore et al., 2022a which shows how the conversion probability can be considered barely constant along the Galactic disk and outside of the Galactic center, where many Galactic red supergiants are located (Healy et al., 2024). Thus the choice of the location of the SN event will not significantly affect our results.

Eq. (5.27) shows that, in the energy-independent regime, the photon flux arriving at Earth would faithfully embody all the spectral properties of the axion production spectrum in the interior of the PNS. In this regard, Fig. 5.7 clearly shows that axion production in the SN core is typically concentrated in the inner regions of the PNS, to which neutrinos are blind since they are emitted from a thin layer around the *neutrino-sphere* at $R_\nu \sim 20$ km. Thus, if a detection of the SN axion burst is achieved by *Fermi*-LAT in coincidence to future Galactic SN, the study of the features of the axion-sourced gamma-ray signal would furnish a large amount of information about typical conditions of the PNS interior. In particular, the lower panel suggests that axions are efficiently emitted from the region $6 - 10$ km, which is located around the temperature peak at $R \simeq 8$ km due to the stiff dependence of the axion emission rate on the SN temperature. Therefore, it is licit to expect that the average energy characterizing axion spectra could be directly related to the average temperature in the inner SN core. Moreover, in Chapter 3 we have argued that in presence of a relatively large fraction of pions within the SN core ($\sim 1 - 3\%$ of the nucleon fraction), pionic production processes become efficient. Thus, the observable axion spectrum would be characterized by two peaks at energies $E_a \sim 50\,\text{MeV}$ and $E_a \sim 200\,\text{MeV}$, for NN bremsstrahlung and pion conversion, respectively. Conversely, the presence of such small pionic fraction in the core is expected to have no impact on the neutrino signal. Thus, as already suggested in Section 4.2, the presence of a peak

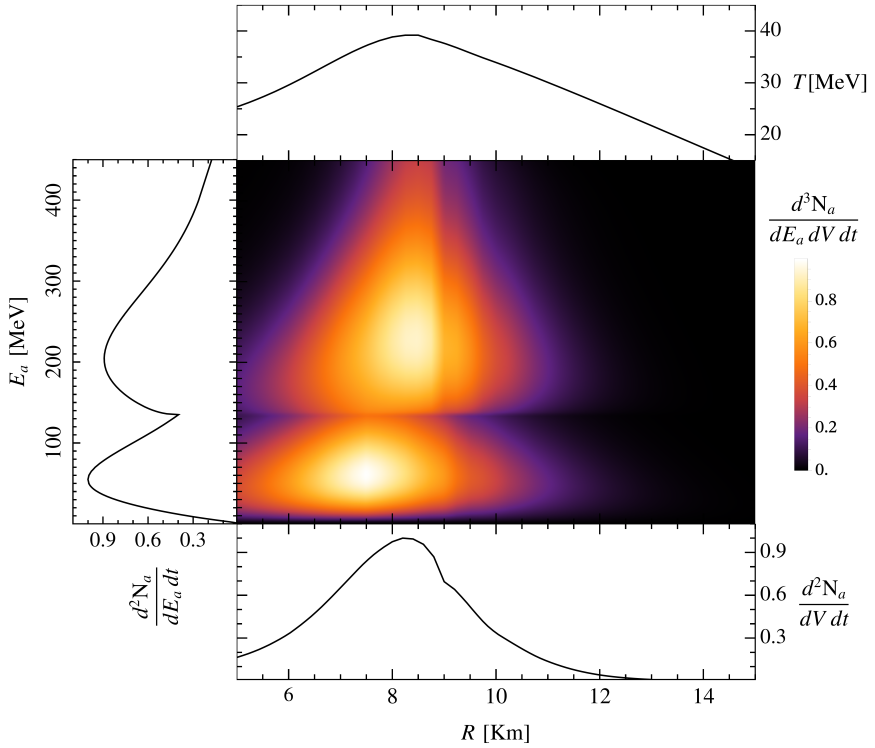

Figure 5.7: Axion production density (normalized at its peak value) for our benchmark SN model at $t_{\rm pb} = 1$ s, displayed as a function of the PNS radius and of the energy of the produced axion. *Lower panel*: Energy-integrated axion production density (normalized at its peak value) as a function of the production radius. *Left panel*: Volume-integrated axion production spectrum (normalized at its peak value). *Upper panel*: Temperature profile of the SFHo-s18.8 model.

at 200 MeV in the detectable axion-induced photon flux would represent a unique opportunity to answer the question related to the pion abundance in the PNS, since there is no other messenger sensitive to this feature. In the following, we will outline some simple procedures to connect the main features distinguishable in the axion emission spectrum to the relevant properties characterizing the PNS interior.

5.3.1 Fitting expressions for the emission spectra

In order to study the features of the axion signal, it is convenient to introduce some simple fitting expression for axion spectra[1], which are able to encode the main spectral properties of the axion signal within a reduced number of fitting parameters. As done in previous Sections, here we will assume the axion-neutron coupling to be $g_{an} \simeq 0$ as in the KSVZ axion model.

Since NN bremsstrahlung is a quasi-thermal process (see Ref. Lella et al., 2023), the behavior of the volume-integrated emission rate can be fit through a Gamma-distribution function (Payez et al., 2015)

$$\left(\frac{d^2 N_a}{dE_a\, dt}\right)_{NN} = A_{NN} \left(\frac{g_{ap}}{5\times 10^{-10}}\right)^2 \left(\frac{E_a}{E^0_{NN}}\right)^{\beta_{NN}} \exp\left[-(\beta_{NN}+1)\,\frac{E_a}{E^0_{NN}}\right], \tag{5.31}$$

where E_a is the red-shifted axion energy observed at large distances from the SN core, and A_{NN}, E^0_{NN} and β_{NN} are free fitting parameters. The expression in Eq. (5.31) describes a quasi-thermal spectrum with average energy E^0_{NN} and spectral shape parameter β_{NN}. We highlight that $\beta_{NN} \simeq 1.5$ in the first seconds of emission, suggesting that axion NN bremsstrahlung can be considered a *quasi*-thermal process ($\beta_{NN} = 2$ describes a perfectly thermal spectrum of ultra-relativistic particles). Conversely, pion conversions are highly non-thermal process due to energy budget associated to the pion mass which is directly trasfered to the outgoing massless axion. Indeed, assuming pions to be in thermal equilibrium with the plasma in the SN core the pion total energy can be estimated as $E_\pi \sim m_\pi + 3T \sim E_a$. In particular, the local production spectrum will show a lower energy cutoff at $E_a = m_\pi$. Moreover, when observing the spectrum at large distances from the SN core, axion energies are red-shifted by the strong gravitational potential inside of the PNS. Thus, also the lower cutoff of the axion spectrum will be red-shifted to $\omega_c \simeq \alpha\, m_\pi$, where α is the lapse factor. Ultimately, the fitting expression for the pion conversion emission rate would consist in a Gamma distribution function evaluated at energies shifted by ω_c:

$$\left(\frac{d^2 N_a}{dE_a\, dt}\right)_{\pi N} = A_{\pi N} \left(\frac{g_{ap}}{5\times 10^{-10}}\right)^2 \left(\frac{E_a-\omega_c}{E^0_{\pi N}}\right)^{\beta_{\pi N}} \exp\left[-(\beta_{\pi N}+1)\,\frac{E_a-\omega_c}{E^0_{\pi N}}\right], \tag{5.32}$$

[1] Complete expressions for axion spectra are provided in Sec. 3.2.

with $A_{\pi N}$, $E^0_{\pi N}$, $\beta_{\pi N}$ and ω_c as free fitting parameters.

In our analysis, we have computed the axion emission spectra over three different SN models taken from the GARCHING group SN archive (*Garching core-collapse supernova research archive* n.d.) considering for each of them 8 different time snapshots separated by $\Delta t = 1$ s in the time window $t_{\rm pb} \in [1, 8]$ s, where $t_{\rm pb}$ is the time after the core bounce. Besides our benchmark SN model SFHo-s18.8, already described in previous Sections, we also employ two other different 1D SN models, which we will label SFHo-s20 and LS220-s20. In particular, SFHo-s20 is characterized by the same EoS as SFHo-s18.8, but it is launched from a $20\,M_\odot$ progenitor and leads to PNS baryonic mass $M_{\rm NS} \simeq 1.95\,M_\odot$ (Woosley and Heger, 2007). LS220-s20 employs the LS220 EoS (Lattimer et al., 1991), characterized by a different behavior in the cooling phase with respect to SFHo-type simulations due to a different convective activity connected to the nuclear symmetry energy (Roberts et al., 2012). As for SFHo-s20, this model is developed from a $20\,M_\odot$ progenitor and produces a NS with baryonic mass $M_{\rm NS} \simeq 1.93\,M_\odot$ (Woosley and Heger, 2007). These two models, characterized by high PNS masses, show higher temperatures and densities compared to the SFHo-s18.8 model. Moreover, we observe that, as the SN core temperature drops and the density increases during the cooling phase, the thermal distribution of pions may undergo Bose-Einstein condensation. In this case, axion emission from a bosonic condensate would require a dedicated treatment which is still missing in present literature. Therefore, we will simplistically set to zero axion production in regions of the SN core where we observe the formation of the pion condensate.

The values of the fitting parameters for all the models considered in the analysis are provided in Appendix D.

5.3.2 Axion spectra from one-zone models

As highlighted in the previous Sections, the features characterizing the axion emission spectra are expected to be strictly dependent on typical conditions characterizing the interior of the PNS at $R < 10$ km, where nuclear processes take place. Remarkably, the temperature of the inner SN core plays a relevant role in determining the average energy of thermal processes for axion production, as NN bremsstrahlung. Conversely, the neutrino emission spectra are not sensitive to the temperature profile in these regions, since their

emission takes place from a shell around $R_\nu \sim 20$ km. Therefore, the axion emission spectrum may offer the unique opportunity to indirectly measure the temperature of the inner PNS.

In order to determine how the fitting parameters are related to the SN core temperature, we have fit through Eq. (5.31) and Eq. (5.32) the spectra obtained from an exemplary one-zone SN model, in which the temperature is assumed to be constant for $R \leq 13$ km and null elsewhere. The temperature of this region is varied in the range $T \in [10, 55]$ MeV, while all the other quantities necessary to compute the emission spectra are kept fixed by assuming the mass density $\rho = 3 \times 10^{14}$ g cm^{-3} and the electron fraction $Y_e = 0.3$. Notice that the value of the radius is chosen to have a PNS of mass $M_{\rm NS} \simeq 1.4\, M_\odot$, which is a typical value for the compact object at the center of an exploding SN (Raffelt, 1996). Then, all the other outputs of the SN simulation can be obtained by characterizing the nuclear medium through the SFHo EoS, which we use as a benchmark for this analysis. In particular, in Section 5.3.1 we observed that NN bremsstrahlung spectrum shows a quasi-thermal line-shape, therefore its average energy E_0^{NN} has to be directly correlated to the core temperature (Lujan-Peschard et al., 2014; Gallo Rosso et al., 2018). Therefore for each given value of the temperature of the one-zone model we have extracted the analytical fits through Eq. 5.31.

By employing this methodology we produced the plot in Fig. 5.8, which shows a clear linear correlation between E_0^{NN} and T:

$$\frac{E^0_{NN}}{\rm MeV} = 15.4 + 2.2 \frac{T}{\rm MeV}\,. \tag{5.33}$$

Thus, since the observed gamma-ray signal triggered by axion conversions in the Galactic magnetic field preserves the same spectral properties of the emitted spectrum, the reconstruction of the average energy of the observed gamma-ray spectrum would provide an immediate estimation of the average temperature in the core.

Nevertheless, we recall that energies observed at large distances from the core would suffer from the gravitational red-shift encoded in the lapse factor the $0 < \alpha < 1$. Thus, the correct expression for temperature reconstruction is given by

$$\frac{T}{\rm MeV} \simeq -6.93 + \frac{0.45}{\alpha} \left(\frac{E^0_{NN}}{\rm MeV} \right)_{\rm obs}\,. \tag{5.34}$$

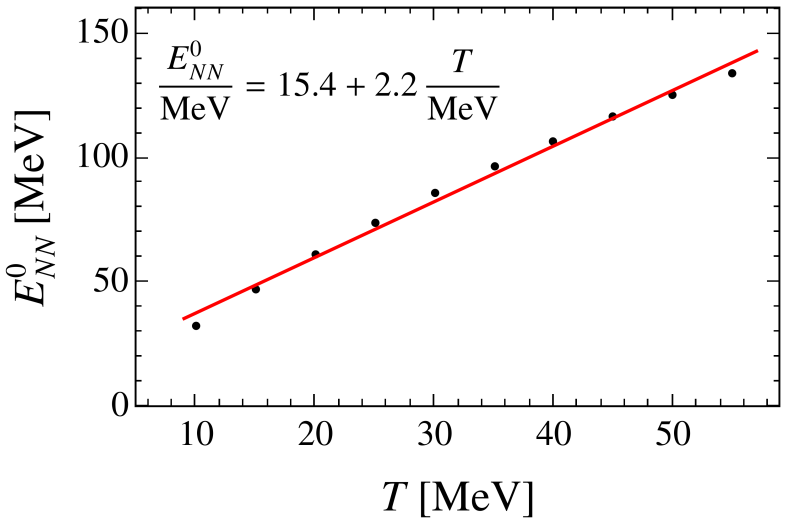

Figure 5.8: Values of E^0_{NN} for the fitting spectra obtained from our schematic one-zone SN model at different temperatures. The red solid line depicts the linear fit in the temperature range $T \in [10, 55]$ MeV.

We observe that the lapse factor does not vary significantly in regions where axion production is efficient at $R \sim 5 - 10$ km, thus for our estimations it is possible to assume an average value assumed by α. In particular, we use the value $\alpha \approx 0.78$ for the SFHo-s18.8 model and $\alpha \approx 0.67$ for the SFHo-s20 and LS220-s20 models. The difference in the values assumed is due to the different PNS masses characterizing the different models. In particular gravitational effects are more relevant for more massive remnants and, thus, α is smaller. Since the value of α depends on the PNS mass, the determination of this parameter represents an additional source of uncertainty for our analysis. However, the mass of the PNS can be roughly estimated from observations of the neutrino signal (Gallo Rosso et al., 2017).

5.3.3 *Fermi*-LAT simulations and results

The axion spectra integrated over the complete 1D SN models considered in the analysis give rise to gamma-ray photons as a consequence of their conversion in the Galactic magnetic field. In order to have a realistic idea of how these spectra would appear in case of a detection by the *Fermi*-LAT experiment in coincidence to the next Galactic SN, we simulate the axion-

induced gamma-ray signals and reconstruct their parameters in a *Fermi*-LAT data analysis chain closely following the procedure explained in Calore, Carenza, Eckner, et al., 2024. As discussed before, we consider the case of a SN event taking place at 10 kpc from the Earth in the direction $(\ell, b) = (199.79°, -8.96°)$. The normalization of this spectrum is fixed once setting the values of the axion-nucleon coupling, describing the axion production, and the axion-photon coupling, determining the conversion probability in the Galactic magnetic field. In particular, in our analysis we fix $g_{ap} = 5 \times 10^{-10}$ and $g_{a\gamma} = 3 \times 10^{-15}$. We remark that these values are currently allowed by all astrophysical constraints on the axion parameter space.

Then, the induced gamma-ray spectrum is simulated for 8 seconds with the Fermi Science Tools[2]. In particular, due to the transient nature of the SN axion burst, all the simulations are performed for the `P8R3_TRANSIENT020_V3` event class and `FRONT+BACK` type, for energies ranging in the interval $E_\gamma \in [60, 600]$ MeV with an additional cut on the zenith angle $< 80°$ of the reconstructed events. All the technical details of the analysis for the reconstruction of the spectral line-shape and the fitting parameters are reported in Lella, Calore, Carenza, Eckner, et al., 2024.

Presence of pions in the SN core

Fig. 5.9 displays the behavior of the spectrum simulated by assuming the aforementioned analysis set-up. In the left panel we consider a snapshot of the spectrum on the one-second time bin after the core bounce. As expected, the contribution from NN bremsstrahlung is peaked around energies $E \sim 90$ MeV, just above the energy threshold for the experiment considered in our analysis. Since *Fermi*-LAT suffer from a dramatic reduction in its effective area in the energy range $E \lesssim 80$ MeV where the bremsstrahlung contribution lies, we observe a suppression of the bremsstrahlung peak compared to the pion emission spectrum. Indeed, pion conversion emission is effective in the energy range $E \sim 100 - 200$ MeV, where *Fermi*-LAT detection is optimized. Conversely, in the time window $t_{\rm pb} \in [2, 3]$ s (right panel) the contribution due to pion conversion ceases to be significant and the emission is dominated by the bremsstrahlung component. This is due to effects related to bosonic condensation, which becomes more and more effective as the SN core cools

[2] https://fermi.gsfc.nasa.gov/ssc/data/analysis/software/

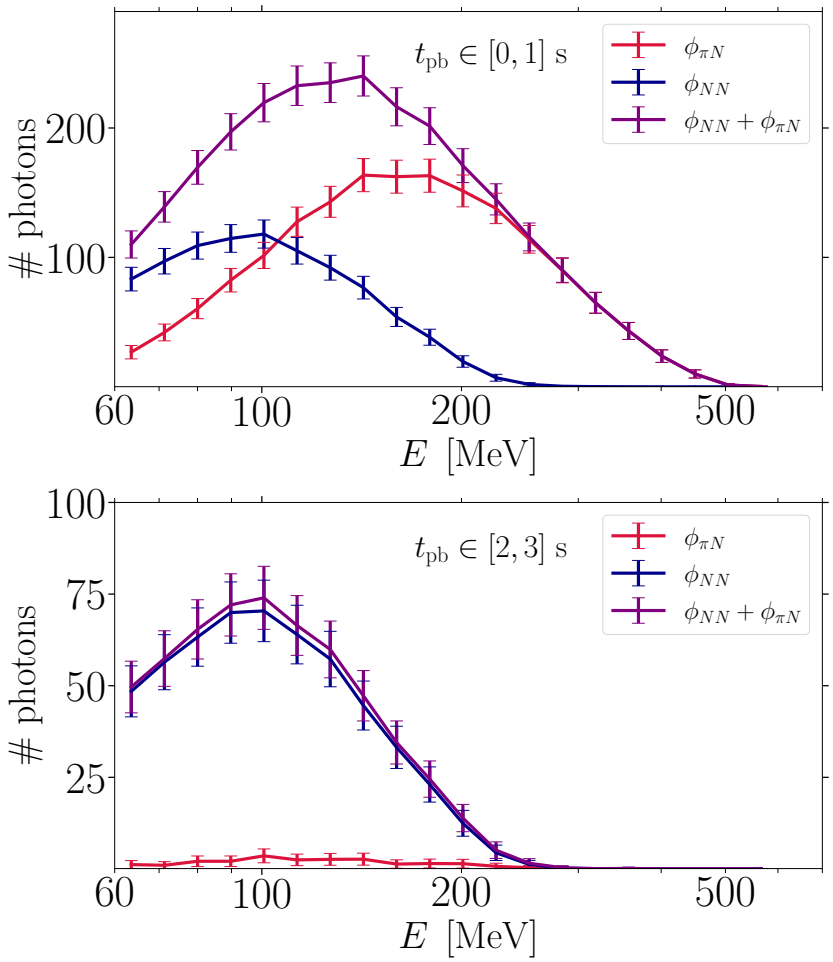

Figure 5.9: *Fermi*-LAT spectra of the axion-induced gamma-ray burst from a core-collapse SN in the time slices $t_{\rm pb} \in [0, 1]$ s (*upper panel*) and $t_{\rm pb} \in [2, 3]$ s (*lower panel*) after the bounce. We fixed $g_{a\gamma} = 3 \times 10^{-15}$ GeV^{-1} and $g_{ap} = 5 \times 10^{-10}$ to compute the average expectation for the number of gamma-ray photons associated with the bremsstrahlung (blue) and pion conversion (red) components. The sum of both contributions is shown in purple. The simulation conditions follow the details provided in Lella, Calore, Carenza, Eckner, et al., 2024

down. Hence, already after a few seconds, employing only the bremsstrahlung contribution is an excellent description of the emission process.

Due to the suppression of the bremsstrahlung contribution related to the poor *Fermi*-LAT effective area in the given energy range, we do not clearly

observe the presence of a double peak in the time window $t_{\rm pb} \in [0, 1]$ s, when pion conversion emission is still active. Nevertheless, the presence of a large number of axion-induced events at energies $E \gtrsim 200$ MeV, where bremsstrahlung is not active, can be solely interpreted as a signature of axion emission via pionic processes. This feature would provide a striking evidence for the presence of pions in the SN core, supporting the scenario outlined in Fore and Reddy, 2020. To quantify the physical evidence relating the number of events at energies $E \gtrsim 200$ MeV and the impact of the pion conversion contribution, in Lella, Calore, Carenza, Eckner, et al., 2024 we carried out a Bayesian analysis for model comparison, pointing out there is a strong evidence for the model including both pionic processes and NN bremsstrahlung being a better fit to the data.

This discussion highlights that a dedicated analysis may point out the presence of an additional contribution due to pion conversion on top of NN bremsstrahlung in the first seconds of emission, making the axion-signal a unique probe to inspect the abundance of pions in the inner PNS.

Reconstruction of the SN temperature

The analysis of the *Fermi*-LAT signal may allow one to infer, within their uncertainties, the spectral parameters characterizing the axion-induced gamma-ray burst (see Lella, Calore, Carenza, Eckner, et al., 2024 for details). As outlined in Section 5.3.2, the E_0^{NN} parameter appears to be particularly relevant for our study, since it may allow to reliably reconstruct the temperature of the SN core in regions relevant for axion production $R \sim 5-10$ km. Values of the E_0^{NN} parameter inferred through the *Fermi*-LAT analysis in the whole time window examined and considering both the case of bremsstrahlung only and both pionic and bremsstrahlung emission are displayed in the upper panel of Fig. 5.10. We can observe that, due to the degeneracy induced on the spectrum when both bremsstrahlung and pion conversion contributions are active, *Fermi*-LAT is not able to reconstruct the input values of E_0^{NN} in this scenario. As the pion conversion contribution is progressively washed out, the capabilities of reconstruction significantly improve. In the lower panel of Fig. 5.10, we display the values of the SN temperature reconstructed by employing the procedure discussed in 5.3.2 (black markers), applied on our benchmark SN model SFHo-s18.8 in the case of bremsstrahlung only emis-

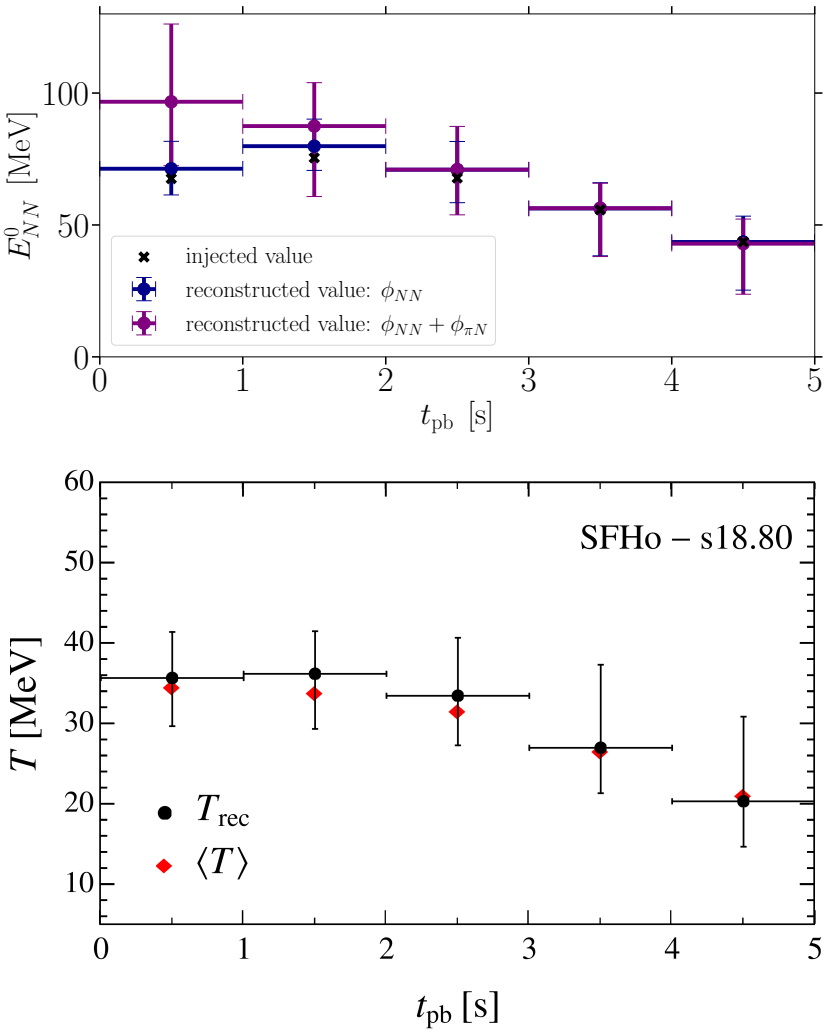

Figure 5.10: *Upper panel:* Time evolution of E^0_{NN} as reconstructed from a simulation of the SFHo-s18.8 SN model for up to five seconds after the core bounce. The injected values of the underlying model are marked with a black cross. We distinguish the two cases of a gamma-ray burst comprised of the summed emission of bremsstrahlung and pion conversion processes (purple) as well as only bremsstrahlung. *Lower Panel:* Values of the temperatures reconstructed by employing the procedure illustrated in Sec. 5.3.2 (black markers), together with the average temperatures in the regions of axion production computed as in Eq. (5.35) (red markers). In particular, the two panels refer to the first 5 snapshots of our reference SN model SFHo-s18.8.

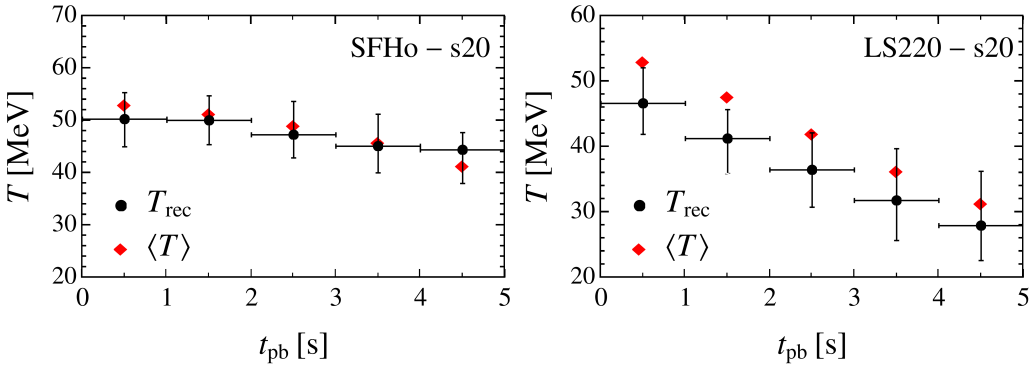

Figure 5.11: Values of the reconstructed temperature (black markers) for the SFHo-s20 and LS220-s20 SN models and for the first 5 time snapshots considered. Red markers depict the average temperature in the axion production region.

sion. These values have to be compared to the average SN temperature in the axion production region, which can be computed as

$$\langle T \rangle = \frac{\int_0^{R_c} T(r) \, \frac{d^2 N_a}{dV dt} \, dR}{\int_0^{R_c} \frac{d^2 N_a}{dV dt} \, dR} \,, \tag{5.35}$$

where $R_c = 15$ km and $d^2 N_a / dV dt$ is the axion production density. We observe that the values of the temperature reconstructed from the *Fermi*-LAT results are always 1-σ compatible with the corresponding values of $\langle T \rangle$. Hence, these results suggest that, in case of an observation of the axion burst from the future Galactic SN, the average energy of the axion emission spectrum of the E^0_{NN} can be considered as a good estimator of the SN core temperature.

To test the validity of our methodology for temperature reconstruction, we apply this procedure over the other two different SN models considered in the study. The left panel of Fig. 5.11 displays the results for the SFHo-s20 model. As we can appreciate, this model is characterized by higher values of the average PNS temperature, since it leads to a higher PNS mass compared to SFHo-s18.8. Nevertheless, also in this case we can reconstruct the temperature with very high precision, with discrepancies never larger than 1-σ in the first 5 s. Results obtained for the LS220-s20 SN model are shown in the right panel of Fig. 5.11. We notice that the reconstructed

values of the temperature for LS220 EoS show a larger discrepancy than what observed for the SFHo EoS, especially in the first instants after the core bounce. This difference is related to the behavior of the cooling lightcurves for LS220 EoS, which typically appear to be different with respect to the SFHo EoS(Lucente, Heinlein, et al., 2024), that we employed as benchmark in the temperature reconstruction procedure in Sec. 5.3.2. In this regard, we highlight that Fiorillo, Heinlein, et al., 2023; Lucente, Heinlein, et al., 2024 pointed out that DD2, SFHx and SFHo EoS lead to similar time evolution of the SN conditions and neutrino lightcurves, but slightly different from LS220. Despite these slightly larger deviations, our procedure provides temperature values barely 1-σ compatible (and always 2-σ compatible) with the average temperature of the core LS220-s20 simulation.

Chapter 6

The gravitational wave signature of core-collapse supernovae

This Chapter is devoted to the analysis of the GW signals from 3D SN simulations. This study highlights how a truly multimessenger approach for the observation of the signatures from a future SN event would allow us to shed light on the physics of the interior of exploding stars. In particular, in Sec. 6.1 we review the state-of-the-art for the analysis of GW signals extracted from 3D simulations currently available. Then, in Sec. 6.2 we analyze the GW signal sourced by anisotropic neutrino flows extracted from our models, while Sec. 6.3 is dedicated to the study of GW signatures triggered by non radial mass motions. Finally, in Sec. 6.4 we outline the detection prospects for current and planned GW experiments in case a future SN event.

This Chapter is based on the following work:

(P12) A. Lella, G. Lucente, D. Kresse, R. Glas, H.T. Janka, A. Mirizzi, "An analysis of the gravitational wave signals from three-dimensional supernova models", in preparation.

6.1 The state-of-the-art

Since the first detection of a GW signal from a binary black-hole merging (Abbott et al., 2016) in 2015, many other GW events from binary systems have been observed. Crucially, the observation of the GW170817 event, generated

by a binary neutron star inspiral (Abbott et al., 2017a), marked a milestone event for multimessenger astrophysics, since it was the first event observed under the eye of gamma-rays and GWs. Nevertheless, no GW event produced from isolated astrophysical systems has been observed to date. In this context, the detection of GWs emitted during a future Galactic SN event would open a new intriguing frontier in observational astrophysics, allowing one to study for the first time the physical phenomena characterizing these powerful events by employing all the known cosmic messengers, namely neutrinos, gamma-rays and GWs.

Notably, General Relativity (GR) predicts that each system able to develop a mass-energy quadrupole momentum tensor variable in time emits a GW signal. Therefore, SNe are expected to be powerful sources of GWs (see, e.g., Abdikamalov et al., 2020; Mezzacappa and Zanolin, 2024; Janka, 2025 for recent reviews) triggered by hydrodynamical instabilities (Finn et al., 1990; Wheeler, 1966; Ott, 2009b) and highly-time dependent anisotropies in neutrino radiation (Epstein, 1978; Turner, 1978). Specifically, the anisotropic emission of radiation from a given system causes a non-oscillatory permanent change in the space-time metric. Since the shape of the signal would depend on the properties of the emission phenomenon, the gravitational perturbation of the space-time would carry memory of the powerful astrophysical events which cause the emission. This effect is commonly known as *gravitational memory effect* (Zel'dovich et al., 1974; Braginsky et al., 1987b). On the other hand, anisotropic mass flows due to prompt post-shock overturning convection, neutrino-driven turbulence, turbulent accretion through the shock and onto the protoneutron star (PNS) and aspherical explosive mass flows also lead to time-variable deformations of the space-time metrics, triggering a broad-band emission of GWs (Finn et al., 1990; Wheeler, 1966; Ott, 2009b). As we show in this Chapter, the distinguishable features of this GW spectrum would permit to study features of the hydrodynamical instabilities to which neutrinos are unsensitive.

The main challenge in predicting the shape of the GW signal from SNe consists in developing multidimensional numerical simulations modeling the SN explosion continuously in 3D since the onset of the collapse to the SN cooling phase (see Janka, 2025 for a review). Thus, differently from the prediction of the SN neutrino signal whose main features can be already determined from 1D simulations introduced in the 90's (Burrows, 1990; Totani et al.,

1998; Keil, Janka, and Raffelt, 1995), the first extraction of the GW signal dates back early 2000 and was based on the first two-dimensional SN models (Ott, 2009b). Thereafter, the progress in the analysis of the SN GW signals followed the development of multidimensional SN simulations, allowing one to properly characterize the complex mechanisms leading to the explosion (Mueller, Janka, and Marek, 2013; Andresen, Müller, Müller, et al., 2017; Morozova et al., 2018; Radice et al., 2019; Vartanyan and Burrows, 2020; Takiwaki et al., 2021; Choi, Burrows, et al., 2024).

In this context, Burrows, Hayes, and Fryxell, 1995; Marek et al., 2009; Pajkos et al., 2019 realized that GW signatures may be released soon after the core-bounce for models showing prompt post-bounce convection and time-dependent rotating flattening. Nonetheless, the phase of most vigorous emission occur when hydrodynamical instabilities are powered during the accretion phase. Furthermore, infalling plumes of matter also excite PNS oscillations, which lead to the emission of GWs dominated by f/g modes (Murphy et al., 2009; Andresen, Müller, Müller, et al., 2017; Morozova et al., 2018; Torres-Forné et al., 2019; Andresen, Glas, et al., 2021; Afle et al., 2023). Finally, the anisotropic release of explosive ejecta would produce low-frequency GW signals at late times after the core bounce $t_{\rm pb} \gtrsim 0.6$ s (Vartanyan, Burrows, et al., 2023; Choi, Burrows, et al., 2024). In parallel, various works (Muller et al., 2012; Richardson et al., 2022; Mukhopadhyay, Lin, et al., 2022; Mukhopadhyay, Cardona, et al., 2021) underlined the crucial importance of the *neutrino memory effect* generated by anisotropic neutrino flows, which is the main component of the GW signal at low frequencies. This contribution plays a pivotal role for GW detection in next-future deci-Hertz GW interferometers (Mukhopadhyay, Cardona, et al., 2021; Mukhopadhyay, Lin, et al., 2022).

Remarkably, many detailed studies shed light on the relation between the different features of the GW signal and the EoS employed in the simulations (Marek et al., 2009; Sumiyoshi et al., 2005; Pan et al., 2018; Richers et al., 2017; Andersen et al., 2021), the mass density distributions (Vartanyan, Burrows, et al., 2023), the explosion energies (Powell et al., 2019), the state of rotation of the SN event progenitor (Andresen, Müller, Janka, et al., 2019; Powell et al., 2024) and the magnetic fields (Powell et al., 2024).

Motivated by the relevance of this line of research for SN physics, we study the GW signal sourced by two state-of-the-art supernova explosion models,

Model	EoS	$t_{\rm fin}$ [s]	$\xi_{1.75}$	$E^{\nu}_{\rm GW}$ $(t_{\rm fin})$ $[M_\odot\, c^2]$	$E^{\rm M}_{\rm GW}$ $(t_{\rm fin})$ $[M_\odot\, c^2]$
s12.28	SFHo	5.11	0.201	4.2×10^{-11}	6.4×10^{-10}
s18.88	LS220	1.675	0.780	7.0×10^{-11}	1.0×10^{-9}

Table 6.1: Details on the two simulations used in this work, showing the used EoS, the final post-bounce time $t_{\rm fin}$ and the compactness $\xi_{1.75}$ computed for a fixed value of the enclosed mass 1.75 $M_\odot$. We show also the energy radiated via GWs induced by anisotropic neutrino emission ($E^{\nu}_{\rm GW}$) and hydrodynamical instabilities ($E^{\rm M}_{\rm GW}$) until the time $t_{\rm fin}$.

with progenitor masses of 12.28 $M_\odot$ and 18.88 $M_\odot$, respectively. The main characteristics of these models have been already introduced in Section 1.3 and more details can be found in Janka and Kresse, 2024. Here we summarize in Tab. 6.1 the main properties of the two SN models, including the EoS employed, the final simulation time $t_{\rm fin}$ and the compactness of the model at the radius $R_{1.75}$ corresponding to an enclosed mass $M_{\rm enc} = 1.75\, M_\odot$ (O'Connor et al., 2011)

$$\xi_{1.75} \equiv \frac{1.75}{R_{1.75}/1000\ \text{km}}\,. \tag{6.1}$$

We also show the total energy radiated via GWs induced by anisotropic neutrino emission $E^{\nu}_{\rm GW}$ (see Sec. 6.2) and hydrodynamical instabilities $E^{\rm M}_{\rm GW}$ (see Sec. 6.2.1 and Sec. 6.3.1).

In the following Sections, we detail the features of the GW signals extracted from these two models focusing on both components of the signals sourced by anisotropic neutrino emission and non-radial mass motions.

6.2 GWs from anisotropic neutrino emission

6.2.1 Signals in the time domain

The GW signal sourced by the anisotropic emission of neutrinos is immediately related to the angle-dependent neutrino $dL_\nu(\Omega, t)/d\Omega$ which is directly extracted from SN simulations. In particular, the time profile of the gravitational signal, in the TT-gauge, can be written as (Epstein, 1978; Mukhopad-

hyay, Cardona, et al., 2021)

$$h_\sigma(t) = \frac{2G}{rc^4} \int_0^t dt' \, L_\nu(t') \, \alpha_\sigma(t') \, , \tag{6.2}$$

where $\sigma = +, \times$ are the two possible polarization states of the metric perturbation h_σ. Assuming a GW propagating in the z direction, $h_+ = h_{yy} = -h_{xx}$, and $h_\times = h_{xy} = h_{yx}$, while $L_\nu(t)$ is here the angle-averaged neutrino luminosity at infinity. Finally, $\alpha_\sigma(t)$ is the so-called anisotropy parameter, which includes the dependence on the angle-dependent neutrino luminosity:

$$\alpha_\sigma(t) = \frac{1}{L_\nu(t)} \int_{4\pi} d\Omega' \, W_\sigma(\theta', \phi' \, \alpha, \beta) \, \frac{dL_\nu(\Omega', t)}{d\Omega'} \, . \tag{6.3}$$

Here $d\Omega' = d\cos\theta' d\phi'$ is the solid angle element in the simulation frame and α and β are the astronomical coordinates of the SN event[1]. In particular, the angular functions W_+ and $W_\times$ weight the contribution of a given direction in the simulation frame (θ, ϕ) to observe the GW signal in the direction (α, β) in the observer frame. The complete expressions of the angular weight functions are given in Muller et al., 2012; Vartanyan, Burrows, et al., 2023.

Fig. 6.1 reports the time series of the anisotropy parameter for the two models considered in the analysis (left and right panels for the s12.28 and s18.88 models, respectively) and for both GW polarization states (upper and lower panels for the + and × polarization states, respectively). As an exemplary case, these results are obtained by assuming an observer located in the equatorial plane of the simulation ($\alpha = 0$, $\beta = \pi/2$). In particular, the anisotropy parameter for the total neutrino emission, accounting for all the species, is reported as a solid black line. We also show the anisotropy parameters related to the separate emission of ν_e in magenta, $\bar{\nu}_e$ in light blue and ν_x in dark yellow. Here, ν_x stands for a single generic flavor of all heavy-lepton (anti)neutrino species. We observe that immediately after the core bounce, all the anisotropy parameters acquire values compatible with zero, since the neutrino emission can be considered barely isotropic. At the beginning of the accretion phase at $t_{\rm pb} \sim 0.2\,$s, when post shock convection and Standing Accretion Shock Instabilities (SASI) (Blondin, Mezzacappa, et al., 2003; Foglizzo, 2002; Foglizzo, Scheck, et al., 2006; Foglizzo, Galletti, et al., 2007b;

[1] In particular, in the following we will refer to the coordinate set up depicted in Fig. 10 of Muller et al., 2012.

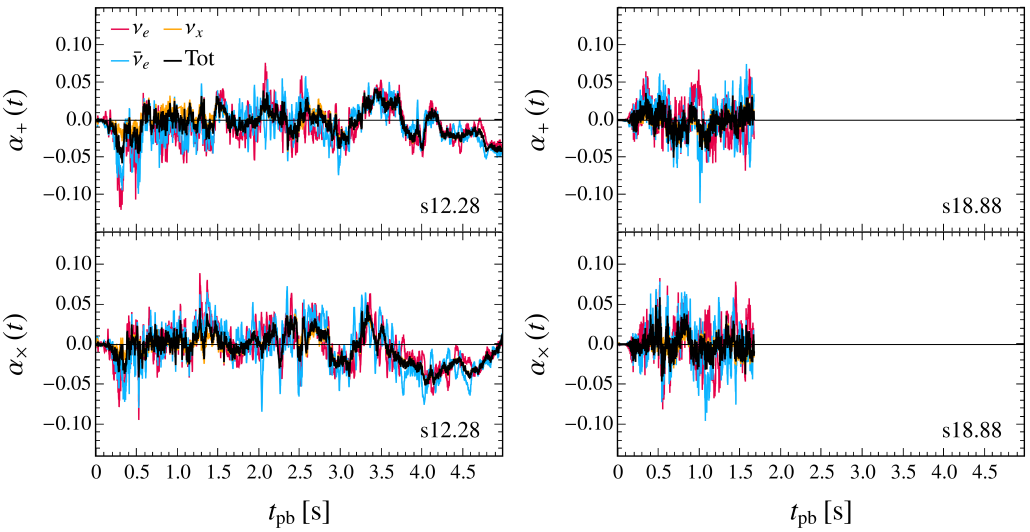

Figure 6.1: Anisotropy parameters for an observer located in the equatorial plane of the SN simulation. *Left* and *right panels* refer to the s12.28 and s18.88 SN models, respectively. *Upper* and *lower panels* display the "+" and "×" GW polarization states. The different colors refer to the contribution of the different neutrino species. In particular, "ν_x" represents a single generic flavor of all heavy-lepton (anti)neutrino species in green. The black solid line is obtained by taking into account the total anisotropic emission of all neutrinos species.

Blondin and Shaw, 2007; Foglizzo, Masset, et al., 2012) start imprinting observable time-dependent anisotropies in the neutrino flow, the anisotropy parameter is characterized by values in the range $|\alpha_\sigma| \lesssim 0.1$ (Kotake, Iwakami, et al., 2009; Vartanyan and Burrows, 2020).

The behavior of the anisotropy parameter is immediately reflected in the GW signal sourced by neutrino emission, displayed in Fig. 6.2. To make our results independent of the source distance r, here we show the gravitational wave amplitudes A_σ, given by $A_\sigma = r\, h_\sigma$. We can observe that there is no trace of GW emission till $t_{\rm pb} \sim 0.2$ s. Then, the signal is powered by post-shock convection and SASI accretion flows, rising over typical time-scales $\mathcal{O}(100)$ ms and acquiring values $A_\sigma \sim \mathcal{O}(100)$ cm. Thus, as argued in Kuroda, Kotake, et al., 2017, the correlation between the observed neutrino and GW signals from a future Galactic SN would provide strong evidences for vigorous SASI activity in the supernova core. At later times the GW amplitude manifests a

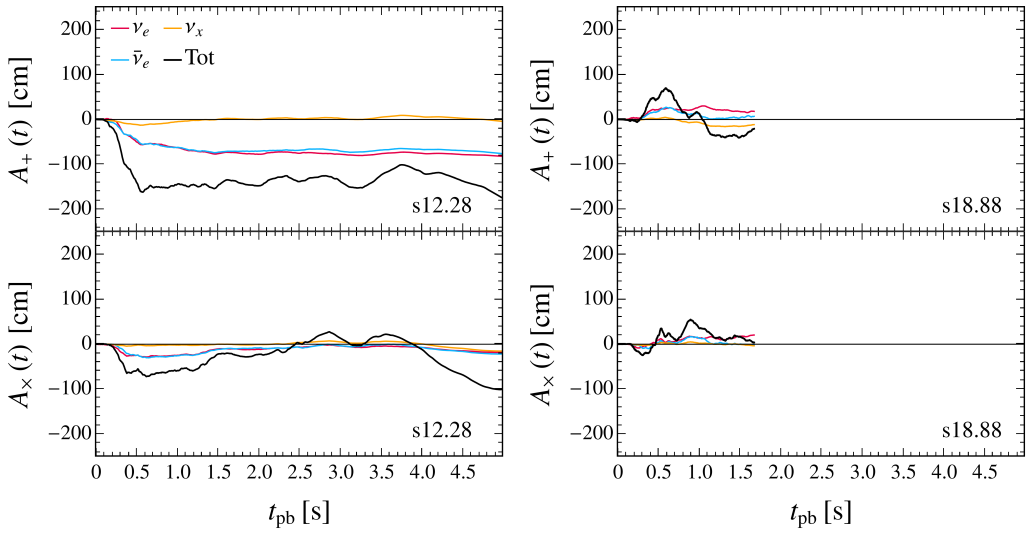

Figure 6.2: Amplitude $A_\sigma = r\, h_\sigma$ of the GW signal for an observer located in the source equatorial plane. *Left panels* refer to the s12.28 SN model, while *right panels* depict the case of the s18.88 model. *Upper* and *lower panels* display the time behavior of the signal for the + and × polarization states, respectively. We show contributions from ν_e in magenta, from $\bar{\nu}_e$ in light blue and from "ν_x" in dark yellow, representing a single generic flavor of all heavy-lepton (anti)neutrino species. The black lines display the total GW amplitude associated to the anisotropic emission of neutrinos of all species, obtained summing over the contributions from all the six neutrino species.

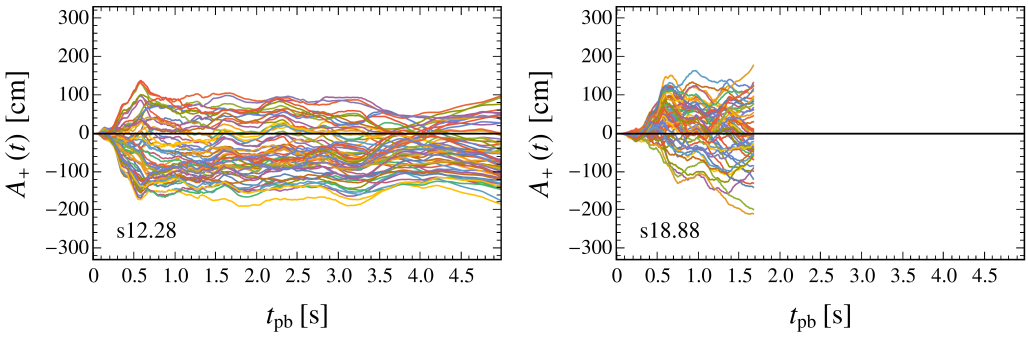

Figure 6.3: Neutrino GW amplitudes A_+ for the s12.28 $M_\odot$ model (*left panel*) and the s18.88 $M_\odot$ model (*right panel*). The different colors depict different randomly-chosen viewing angles of the large-distance observer.

barely-constant offset characterized by slowly-varying amplitudes, featuring in a nearly-permanent deformation of the space-time metric which is peculiar for memory effects (Epstein, 1978; Turner, 1978; Mukhopadhyay, Cardona, et al., 2021). Interestingly, our models are characterized by amplitudes in agreement to the results of (Mueller, Janka, and Marek, 2013; Powell et al., 2024), but show significantly smaller signals compared to the most extreme models considered in (Choi, Burrows, et al., 2024; Vartanyan, Burrows, et al., 2023; Vartanyan and Burrows, 2020), where simulations characterized by large radiated neutrino energies and large anisotropies in neutrino emission can source neutrino GWs with amplitudes up to ~ 2000 cm. We can also observe that the ν_x component shows smaller signals compared to electronic (anti)neutrinos. This effect is due to two main reasons. First of all, before the onset of the explosion, the single ν_x luminosity is ~ 50 % of the ν_e and $\bar{\nu}_e$ luminosities. Additionally, even after the onset of the explosion, the emission of heavy-lepton neutrino species is less affected by asymmetric accretion-flows onto the PNS since non-electron neutrinos come from a deeper neutrinosphere. This would lead to more-isotropic fluxes and smaller GW amplitudes. Finally, the strong dependence of the observed signal on the direction of observation can be deduced from Fig. 6.3, displaying that signals can range from -200 cm $\lesssim A_+ \lesssim 200$ cm depending on the location of the SN event in the sky.

The total energy energy radiated until time t in neutrino GWs is obtained by integrating over all the possible observation angles (Mueller and Janka, 1997; Mueller, Janka, and Marek, 2013)

$$E^{\nu}_{\rm GW}(t) = \frac{G}{4\pi c^5}\int_0^t dt' \int_{4\pi} d\Omega_{\alpha\beta}\left[l^2_+(t',\alpha,\beta) + l^2_\times(t',\alpha,\beta)\right] , \tag{6.4}$$

where

$$l_{+,\times}(t,\alpha,\beta) = L_\nu(t)\,\alpha_{+,\times}(t,\alpha,\beta)\,. \tag{6.5}$$

In particular, the time behavior of the radiated energy in neutrino GWs is displayed as dashed lines in Fig. 6.4. Interestingly, we observe that radiated energies rapidly rise in the time window $\sim 200 - 500$ ms, when plumes of matter due to large-scale accretion instabilities power highly time-dependent anisotropic neutrino emission. Following this large phase of emission, the total energy radiated saturates to $E^{\nu}_{\rm GW} \simeq 4.2\times10^{-11}\,M_\odot c^2 \approx 7.5\times10^{43}$ erg for the s12.28 model and to $E^{\nu}_{\rm GW} \simeq 7\times10^{-11}\,M_\odot c^2 \approx 1.2\times10^{44}$ erg for the s18.88 model.

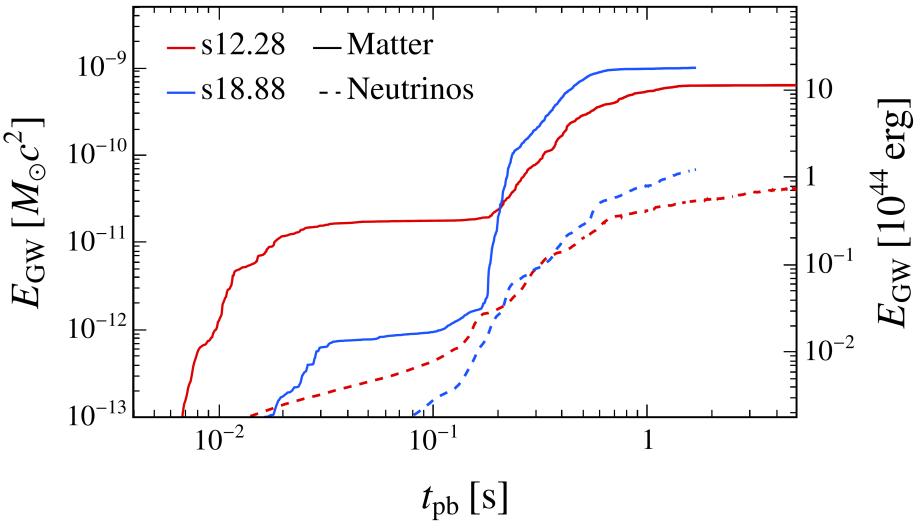

Figure 6.4: Total energy released in GWs induced by non-radial mass flows (solid lines) and anisotropic neutrino emission (dashed lines) radiated until time $t_{\rm pb}$ for the s12.28 (red) and s18.88 (blue) models.

6.2.2 Signals in the frequency domain

In order to examine the spectral features in the neutrino GW signal, it is convenient to introduce the amplitude spectra density (ASD) related to the GW emission

$$\mathrm{ASD} = 2\sqrt{f}\,h_c\,, \tag{6.6}$$

which is actually the quantity employed to compute the signal-to-noise ratio in GW detectors (see,e.g., Maggiore, 2007). In this expression we have introduced the characteristic strain h_c, which is here defined as in Takami et al., 2015

$$h_c = \sqrt{0.5\,\left(|\tilde{h}_+|^2 + |\tilde{h}_\times|^2\right)}\ . \tag{6.7}$$

Moreover, in this work we employ the discrete Fourier transform formalism for the GW strain $h_\sigma(t)$ sampled over a discrete time series as in Andresen, Müller, Janka, et al., 2019:

$$\tilde{X}_k(f_k) = \frac{T}{N}\sum_{n=1}^{N} x_n\, e^{i\,2\pi kn/N}\,, \tag{6.8}$$

where x_n is the time series obtained by sampling the signal at N equidistant discrete time instants labeled by the n index and $f_k = k/T$ is the frequency

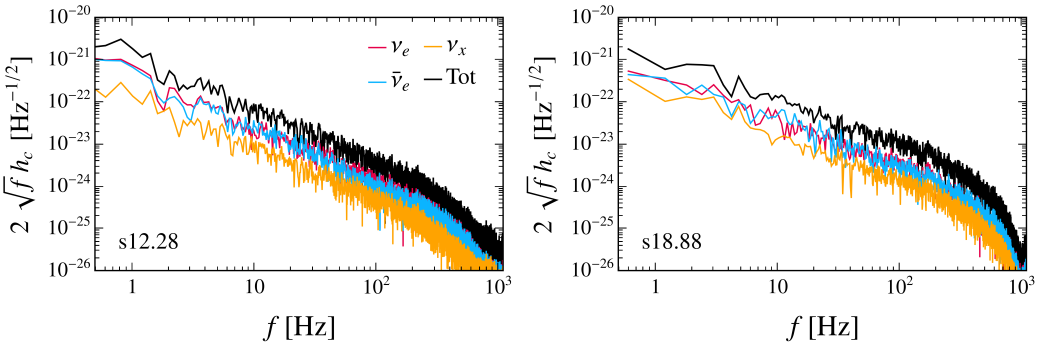

Figure 6.5: Behavior of the ASD for an observer located at a distance $r = 10$ kpc, for the s12.28 (*left panel*) and s18.88 (*right panel*) SN models. We show contributions from ν_e in magenta, from $\bar{\nu}_e$ in light blue and from ν_x in dark yellow, representing a single generic flavor of all heavy-lepton (anti)neutrino species. The solid black line shows the result obtained summing the contributions of all the six different neutrino species.

of bin k, with T the total duration of the analyzed signal. Moreover, in order to avoid the introduction of non-physical high-frequency noise due to a sharp cut-off of the signals at the boundaries of the time interval, we apply a Turkey window function (Willoughby, 1977) driving smoothly the GW signal to zero over time scales ~ 200 ms at the boundary of the given time domain.

The ASDs for the GW signals triggered by anisotropic neutrino emission for both models considered in this work are displayed in Fig. 6.5, in which we show in different colors contributions from different neutrino species. In agreement to previous studies (see, e.g., Müller, Janka, et al., 2011; Vartanyan and Burrows, 2020; Choi, Burrows, et al., 2024), most of the radiated power is concentrated in modes in the frequency range $f \sim 0.1 - 5$ Hz, where $2\sqrt{f}\,h_c \sim 10^{-21}$ Hz$^{-1/2}$ for both models. This behavior is related to the dominant contribution of memory effects in the neutrino GW signal analyzed in the time domain, manifesting in the long-term slowly-varying behavior of the amplitudes after the rise of the signals over time scales $t \sim 0.2 - 0.4$ s. Conversely, the ASD rapidly vanishes at higher frequencies. We point out that the peak values in our ASDs are a factor ∼few smaller than the values observed in models with comparable neutrino luminosities considered in Choi, Burrows, et al., 2024, as a consequence of the slightly smaller GW amplitudes predicted from our models.

6.3 GWs from hydrodynamical instabilities

6.3.1 Signals in the time domain

Large scale hydrodynamical instabilities and non-radial mass motions involving the dense plasma in the SN core may source broad-band emission of GWs during SN events. In this context, the GW strain can be directly related to second time-derivatives of the quadrupole momentum tensor of the system in the coordinate frame of the simulation. In a Cartesian orthonormal basis (spatial indices $i, j = 1, 2, 3$) the second-order time-derivatives of the quadrupole tensor can be expressed as (Müller, Janka, et al., 2011; Andresen, Glas, et al., 2021)

$$\ddot{Q}_{ij} = \mathrm{STF}\left[2\frac{G}{c^4}\int d^3x\,\rho\,(v_i v_j - x_i \partial_j \varphi)\right] , \tag{6.9}$$

where φ is the effective general relativistic gravitational potential, ρ the mass-density while v_i and ∂_i stands for the velocity components and derivatives in the Cartesian basis considered. Moreover, STF denotes the operator projecting the quadrupole momentum tensor onto its symmetric trace-free part. For illustration purposes, in the following we will consider the case of an observer located in the equatorial plane of the simulation frame $[(\phi, \theta) = (0, \pi/2)]$, for which the GW amplitudes can be simply expressed as (Muller et al., 2012)

$$\begin{aligned} A_+ &= \ddot{Q}_{xx} - \ddot{Q}_{yy} \ , \\ A_\times &= 2\,\ddot{Q}_{xy} \, . \end{aligned} \tag{6.10}$$

We refer the reader to Misner et al., 1973; O'Hare et al., 2020; Muller et al., 2012; Vartanyan, Burrows, et al., 2023 for expressions of the GW amplitudes for an observer along a generic (ϕ, θ) direction.

The time evolution of the GW signals triggered by matter motions is shown in Fig. 6.6 for both polarization states and for both models considered in our study. We observe that soon after the core bounce at $t_{\mathrm{pb}} \lesssim 50\,\mathrm{ms}$ the s12.28 model shows a prompt phase of emission of GWs, which is associated to the phenomenon of prompt post-bounce overturning convection (Burrows and Hayes, 1996; Marek et al., 2009; Müller, Janka, et al., 2011; Vartanyan, Burrows, et al., 2023). Conversely, the s18.88 model does not show traces of this phenomenon in the GW signal. In the time window $t_{\mathrm{pb}} \sim 50 - 200\,\mathrm{ms}$

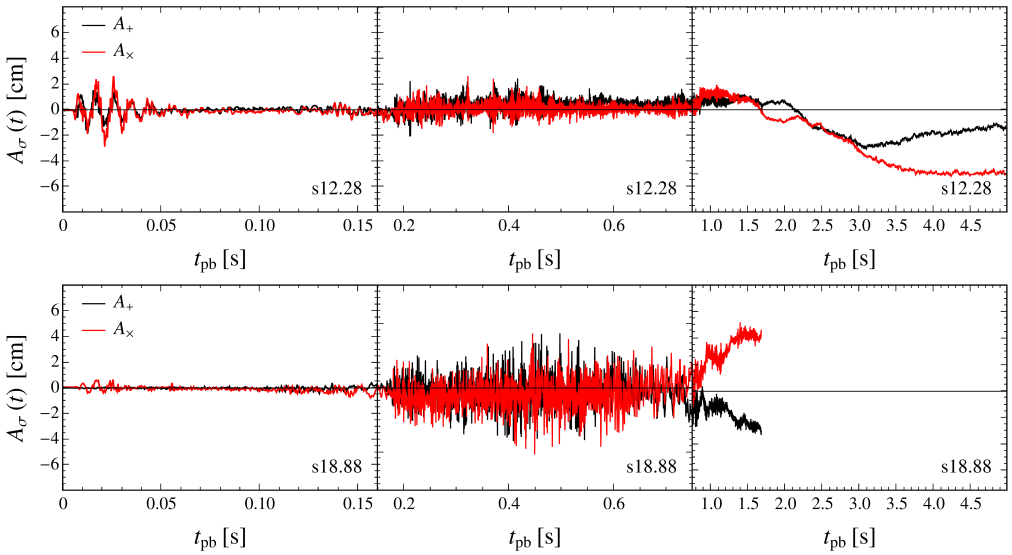

Figure 6.6: GW signals from mass motions for the s12.28 (*upper panels*) and s18.88 (*lower panels*) models. Black and red curves refer to the two possible GW polarization states. As an exemplary case, here we refer to an observer located in the the equatorial plane of the simulation frame. In particular, *left panels* focus on early phase of GW emission due to prompt convection while *middle panels* focuses on the powerful emission phase occurring in coincidence of SASI and post-shock convection activity. Finally, *right panels* display signals at late times during the anisotropic shock expansion when the matter memory component develops.

both models are characterized by a quiescent phase during which accretion instabilities in the neutrino-heated post-shock layers start to build up. Then, at $t_{\rm pb} \in [0.2, 0.7]$ s post-shock convective overturns and violent SASI activity stimulate a strong emission of a GWs at typical SASI frequencies. Moreover, accretion downflows of matter impacting the PNS surface induce oscillations of the near-surface layers, triggering broad-band emission of GWs. We observe that the s12.28 model is characterized by smaller amplitudes of signals compared to the s18.88 model, due to the different compactness characterizing the models. In particular, more compact models, as s18.88, are characterized by more powerful accretion leading to stronger GW emission (Vartanyan, Burrows, et al., 2023). As the SASI and convective activity attenuate after the shock revival $t_{\rm pb} \sim 0.7 - 1$ s, the amplitude of oscillations in the GW sig-

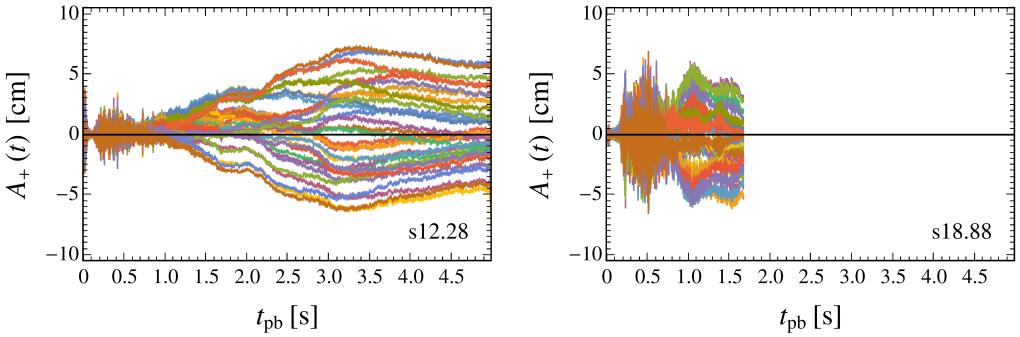

Figure 6.7: GW amplitudes associated to the A_+ polarization mode for the matter signal of model s12.28 (*left panel*) and model s18.88 (*right panel*), respectively. The different colors depict different randomly-chosen viewing angles of the large-distance observer.

nal is reduced. When the shock-wave resume its motion releasing the stellar mantle in the intergalactic medium, the asymmetric structure of expanding ejecta induce a slowly-growing long-lasting offset in the GW amplitudes associated to a memory behavior also in the matter signal (Burrows and Hayes, 1996; Müller, Janka, et al., 2011; Vartanyan, Burrows, et al., 2023; Janka, 2025). On top of the matter memory component we still observe the presence of high-frequency modes related to the presence of fall-back accretion and downflows of matter which keep hitting the PNS surface.

In Fig. 6.7 we plot matter-sourced GW amplitudes for different arbitrarily-chosen observer direction. In particular, at early times $t_{\rm pb} \lesssim 0.7$, the GW signals are barely independent on the observer location. Conversely, at late times $t_{\rm pb} \gtrsim 1$ s, the amplitudes effectively depend on the observer location, ranging within $-5\,{\rm cm} \lesssim A_+ \lesssim 5\,{\rm cm}$. This is due to the morphology of the expanding explosion ejecta, showing stronger anisotropies in some given direction compared to the others.

The angle-integrated energy radiated via GWs triggered by hydrodynamical instabilities until time t is obtained as (Misner et al., 1973; Muller et al., 2012; Vartanyan, Burrows, et al., 2023)

$$E^{\rm M}_{\rm GW}(t) = \frac{G}{c^5}\int_0^t dt' \sum_{ij} \dddot{Q}^2_{ij}\,(t') \ , \tag{6.11}$$

in which $\dddot{Q}_{ij}$ is the third time derivative of the symmetric trace-free part of the quadrupole momentum tensor. From Fig. 6.4 we can observe that

the energy emitted in matter-sourced GWs (solid lines) is at least one of magnitude larger than the energy released in neutrino GWs. Indeed, although GWs triggered by anisotropic neutrino emission are characterized by larger amplitudes, they dominate the emission only in the low-frequency range providing a negligible impact in the total GW energy radiated. The time behavior of the energy released in matter GWs is characterized by a sequence of abrupt jumps directly connected to the different phases characterizing GW emission. We notice that the prompt post-bounce emission due to post-bounce convection in the s12.28 implies a larger energy emitted until $t_{\rm pb} \lesssim 100$ ms. Then, when accretion instabilities power the GW emission reported in the central panel of Fig. 6.6, the larger amplitudes observed for the s18.88 model with higher compactness imply a larger amount of energy radiated compared to the s12.28 model. The matter memory component dominating at late times gives negligible contribution to the total energy, since it is typically associated to low frequencies. Thus, the $12.28\,M_\odot$ and $18.88\,M_\odot$ models have radiated the 95% of GW energy at the end of the accretion phase, at $t_{\rm pb} = 1.3$ s and $t_{\rm pb} = 0.6$ s respectively. In particular, the total released energy is $E^{\rm M}_{\rm GW} \simeq 6.4 \times 10^{-10}\, M_\odot c^2 \approx 1.1 \times 10^{45}$ erg and $E^{\rm M}_{\rm GW} \simeq 10^{-9}\, M_\odot c^2 \approx 1.8 \times 10^{45}$ erg for the s12.28 and s18.88 models, respectively. The hierarchy in the GW energies emitted by our models reflects the relation between the total power radiated in GWs and the compactness of the progenitor's core (which also correlates to the energy in post-shock layers and thus the explosion energy of the given model) highlighted in Müller, 2017; Powell et al., 2019; Vartanyan, Burrows, et al., 2023. In particular, Choi, Burrows, et al., 2024 points out that energies up to $\sim 10^{-7}\, M_\odot c^2$ are possible for more massive exploding progenitors, and even larger energies are possible for rapidly-rotating progenitor cores (Powell et al., 2024).

6.3.2 Signals in the frequency domain

Following the treatment outlined in Section 6.2.2, we have obtained the ASDs for the matter GW signal reported in Fig. 6.8, which are computed by assuming an observer located in the equatorial plane of the simulation frame at a distance of $r = 10$ kpc from the SN event. Here, the maximum frequency displayed in the plots is fixed by the time-sampling employed in the two different models Δt, reading $\Delta t = 0.02$ and $\Delta t = 0.05$ for the s12.28 and s18.88

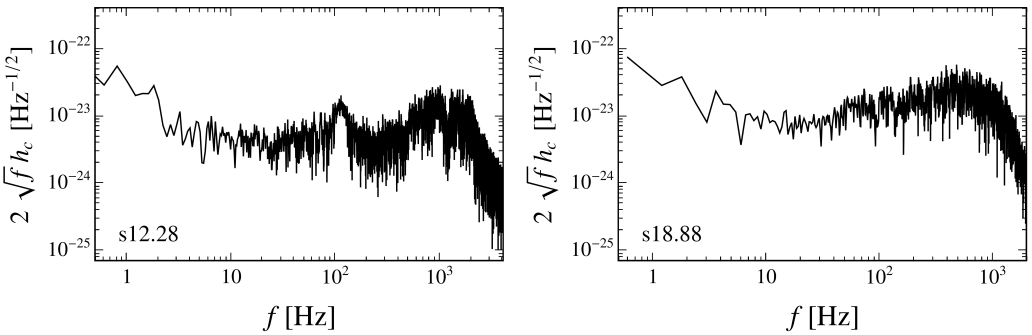

Figure 6.8: Behavior of the ADS for the matter-induced GW signal in function of the frequency f for an observer located in the equatorial plan of the simulation at a distance $r = 10$ kpc. *Left* and *right panels* refer to the s12.28 and s18.88 SN models, respectively.

models, respectively. In particular, numerical artifacts may affect the analysis when excited modes in the GW signal approach the Nyquist frequency of the simulation, given by $f_N = 1/(2\Delta t)$.

Differently from the case of neutrino-sourced signals concentrated around frequencies $f \sim \mathcal{O}(1)$ Hz, the GW emission due to non-radial mass motions involve a broader range of frequencies. Indeed, a large amount of power is here concentrated around frequencies $f \sim \mathcal{O}(10^3)$ Hz, with the ASDs associated with the s12.28 and s18.88 peaking in the range $f \sim 800 - 1500$ Hz and $f \sim 700 - 800$ Hz, respectively. The shift towards lower frequencies observed for the s18.88 model can be related to the lower Nyquist frequency for this simulation, implying that aliasing artifacts may affect our results at frequencies around $f \sim 1000$ Hz. Indeed, it is expected that more massive progenitors are characterized by higher-frequency peaks in their spectra (Vartanyan, Burrows, et al., 2023; Choi, Burrows, et al., 2024). The contribution at lower frequencies $f \sim \mathcal{O}(10)$ Hz is determined by the matter memory effect generated by the anisotropic expansion of explosive outflows of matter at $t_{\rm pb} \gtrsim 1$ s. Convection in the post-shock layers and SASI activity excite modes at typical frequencies around 100-200 Hz (Vartanyan, Burrows, et al., 2023; Janka, 2025). Interestingly, the bump at frequencies $f \sim 100$ Hz, observed for the s12.28 and absent in the s18.88 model, can be related to GW emission triggered by prompt post-bounce convection. Finally, excitations of the PNS oscillation modes source broad-band emission of GWs from $f \sim 100$ Hz up

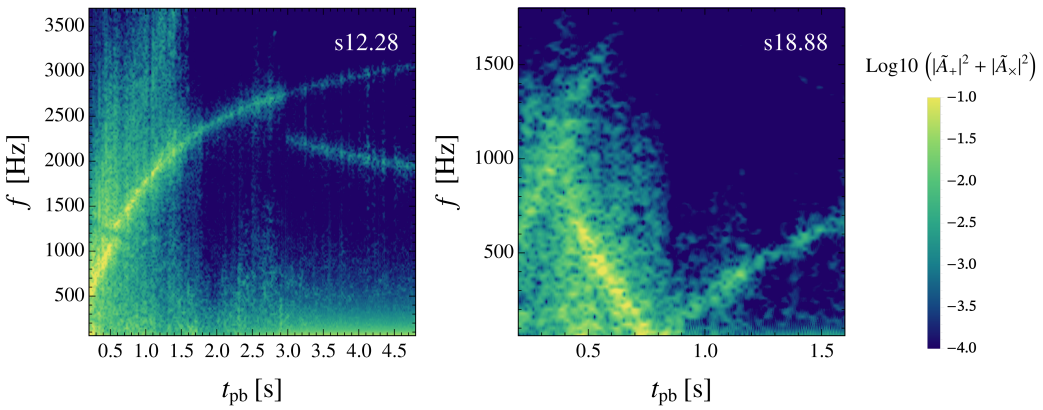

Figure 6.9: Amplitude spectrograms for the the s12.28 model (left panel) and s18.88 (right panel), for an observer located in the equatorial plane of the simulation frame. Aliasing artifacts due to the sampling rate of output data (with time intervals of 0.2 ms for s12.28 and 0.5 ms for s18.88) are visible when the GW frequency reaches 2500 Hz and 1000 Hz, respectively.

to $f \sim 2000$ Hz.

In order to characterize the dominant components in the matter GW signals during the different phases of emission, it is convenient to define the short-time Fourier transform (STFT) (Jacobsen et al., 2003) of the signals, obtained by convolving the Fourier transform in Eq. 6.8 with a sliding time window. In particular, for a discrete time series of the signal sampled at time-steps Δt, the STFT reads (Jacobsen et al., 2003)

$$\mathrm{STFT}[x]\,(t_n, f_k) = \frac{T}{N} \sum_{j=0}^{N-1} x_j \; w_{j-n} \; e^{i\,2\pi kj/N} \,, \tag{6.12}$$

where w_{j-n} is a window function centered at the n-th time instant $t_n = n\Delta t$, while other quantities involved are defined as in Eq. (6.8).

By applying this procedure, we obtained the amplitude spectrograms shown in Fig. 6.9 in which we report the modulus squared of the STFT of the wave amplitudes $|\tilde{A}_\sigma|^2 = |\mathrm{STFT}[A_\sigma]|^2$ summed over the possible GW polarization states. As highlighted before, the most relevant emission of GWs occurs during the accretion phase, in the time window $t_{\rm pb} \sim 0.2{-}1.3$ s and $t_{\rm pb} \sim 0.4{-}0.8$ s for the s12.28 and s18.88 models, respectively, when hydrodynamical instabilities in the neutrino-heated layer excite a haze of different modes. Indeed,

while typical frequencies for convective overturns of matter and SASI activity is limited around $f \sim \mathcal{O}(100)$ Hz, accretion downflows can also excite PNS vibrations generating GWs which span different frequency ranges. PNS oscillation eigenmodes can be classified on the basis of the number of nodes in the radial eigenfunctions describing the displacement of the fluid element with respect to its position at rest, and on the basis of the restoring force (Cowling, 1941; Torres-Forné et al., 2019; Rodriguez et al., 2023). Specifically, pressure is the dominant restoring force for the fundamental (f-)mode, characterized by the absence of nodes, and for generic p-modes, while for g-modes the restoring force is due to buoyancy. For both models, the largest amount of power is concentrated in the f-mode quadrupolar oscillation rising from frequencies of few 100 Hz shortly after the core bounce and reaching frequencies up to ~ 1000 Hz around $t \sim 1$ s. Notice that aliasing artifacts manifest in the presence of an additional branch mirroring the dominant PNS oscillation mode of the s12.28, rising when the f-mode approaches the Nyquist frequency of the simulation. Finally, as discussed in Torres-Forné et al., 2019; Morozova et al., 2018; Vartanyan, Burrows, et al., 2023, the presence of a dark band at early-times around frequencies $f \sim 1200 - 1400$ Hz in the spectrogram of the s12.28 model can be associated to an avoided mode crossing between the f-mode and a g-mode. This feature is also visible in the narrow deep present at these frequencies in the GW spectrum reported in the left panel of Fig. 6.8.

6.4 Detection prospects

To conclude the analysis of the GW signals derived from the 3D SN simulations considered in our study, we discuss the detection prospects in current and future GW detectors by considering a future Galactic SN event located within the Milky-Way at distance $d = 10$ kpc. For this purpose, in Fig. 6.10 we report the total ASDs referred to the two SN models considered taking into account both contributions due to anisotropic neutrino flows and aspherical mass motions. We observe that the power emitted at low frequencies $f \sim 1 - 10$ Hz is entirely determined by the neutrino memory effect, which is the most relevant component in the neutrino GW signal. Conversely, the contribution due to the matter memory signal reveals to be subdominant. At higher frequencies $f \gtrsim 10$ Hz, the neutrino memory component

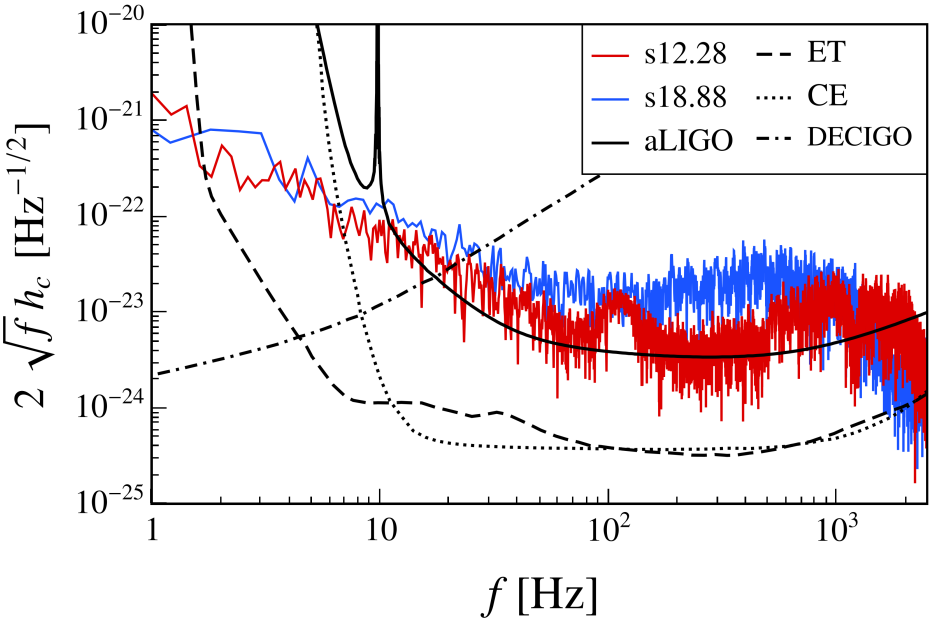

Figure 6.10: Combined neutrino and matter ASD for both SN models considered in this work, for a Galactic SN at $r = 10$ kpc. Black curves depict the sensitivity of current and programmed GW experiments operating in the frequency range of interest.

is rapidly suppressed and the the GW signal triggered by hydrodynamical instabilities dominates the emission. As highlighted before, the GW emission from the s18.88 is more powerful than the emission observed for s12.28, as a consequence of the fact that more massive progenitors typically show larger spectra (Mueller, Janka, and Marek, 2013; Vartanyan and Burrows, 2020; Vartanyan, Burrows, et al., 2023; Choi, Burrows, et al., 2024; Powell et al., 2024). In particular, the ASD for the matter component extracted from the s12.28 model is in good agreement to the outcomes for non-rotating models analyzed in Powell et al., 2024. Nevertheless, the relative amplitude of the high-frequency modes compared to the low-frequency component appears to be smaller than what observed in Vartanyan, Burrows, et al., 2023; Choi, Burrows, et al., 2024.

In Fig. 6.10 we also report the sensitivity curves for current and planned GW detectors in the frequency range of interest, namely advanced LIGO (aLIGO) (Aasi et al., 2015), Einstein Telescope (ET) (Hild et al., 2011; Punturo et al., 2010), Cosmic Explorer (CE) (Abbott et al., 2017b) and DECIGO (Kawa-

mura et al., 2008). We witness that the high-frequency modes of both of our models, around their spectral maxima, are in reach of aLIGO. The enhanced sensitivities of planned GW detectors, as CE and ET, would permit the detection of GW signatures at frequencies $f \gtrsim 10\,\mathrm{Hz}$ and $f \gtrsim 2\,\mathrm{Hz}$, respectively, for both models considered in our analysis. The detection of the high-frequency modes at $f \gtrsim 100\,\mathrm{Hz}$ would allow us to study many otherwise-inaccessible aspects characterizing the dynamics of the SN core. The analysis of the spectral features in the GW signal in correlation to the observed neutrino signal would shed light on many unprobed effects characterizing the hydrodynamics of the core of collapsing star, which are crucial ingredients in the SN explosion mechanism (see, e.g., Kuroda, Kotake, et al., 2017).

Finally, the advent of deci-Hertz interferometers, such as DECIGO, would significantly enhance the detection capabilities in the frequency range $f \lesssim 10\,\mathrm{Hz}$. In particular, we can observe that the neutrino memory component for both models considered is largely in the reach of such detector for Galactic SN events. Thus, deci-Hertz GW experiment would widen the horizon for the detection of SN events towards extragalactic distances (Mukhopadhyay, Lin, et al., 2022), inaccessible to observations of the neutrino burst, accomplishing the crucial task of triggering in time the occurrence of extra-galactic SN events.

Chapter 7

The energy-loss limit: core-collapse SNe or cold neutron stars?

In this Chapter we present a peculiar physics case in which cold isolated neutron stars (NSs) reveal to be more sensitive probes than the young and hot proto-NS at the center of the SN core. Specifically, we consider the emission of light scalar particles from the nuclear medium of NSs interiors, showing how the study of the cooling process of old NS may introduce the most stringent astrophysical limits on the parameter space of such particles. In Sec. 7.1 we take advantage of simple physical arguments to point out possible scenarios in which cold NSs can do better than CC SNe in constraining exotic physics. Sec. 7.2 is devoted to a brief summary of previous studies constraining the parameter space of scalars coupled to nucleons. Finally, in Sec. 7.2 we present our results deduced from the study of NS cooling when introducing an additional cooling channel due to the emission of light scalars.

This Chapter is based on the following research article:

(P11) D. F. G. Fiorillo, A. Lella, C A. J. O'Hare, E. Vitagliano, "Leading bounds on micro- to picometer fifth forces from neutron star cooling", 2506.19906 [hep-ph].

7.1 Supernovae *vs* cold neutron stars

In the previous Chapters we have extensively discussed the relevance of core-collapse SNe as unique astrophysical laboratories to probe new physics. This study has been carried out for the case of the axion, which, historically, represented the paradigmatic application of the celebrated SN cooling argument. Generally speaking, the argument requires that the luminosity in exotic particles emitted must not exceed the dominant cooling channel in the standard picture of the SN cooling phase, namely the neutrino burst (all the details are provided in 1.4.4). This argument applied to the case of axions allows one to place, within its uncertainties, the most stringent bound on the QCD axion mass $m_a \lesssim 8\,\text{meV}$ (Lella et al., 2023) (see Sec. 3.3.4), which is comparable to the results obtained from the analysis of the luminosity curves of isolated NSs, discussed in Buschmann et al., 2022. Nonetheless, the similarity between the results achieved by employing SNe and cold isolated NSs does not have to come as a surprise. Indeed, similarly to SNe, neutrino emission is also the dominant cooling channel for NSs with ages up to $\sim 10^5$ years, and both main axion and neutrino emission channels remain the same. Furthermore, as we can show on the basis of simple but fundamental physical arguments, axion and neutrino production rates depend on the temperature roughly in the same way. Indeed, both the emission of an axion and a neutrino pair is associated to the flip of the spin of one of the emitting nucleons. Such a spin flip introduces a factor $\sim p_a/m_N$ in the scattering amplitude, as it can be naturally deduced from the non-relativistic amplitude for the spin-flip operator which assumes the form $\boldsymbol{\sigma} \cdot \mathbf{p}_a/m_N$, with $\boldsymbol{\sigma}$ being the spin operator. Since the momentum of both the axion and the neutrino pair emitted in thermal nuclear processes grows with the temperature, it follows that both axion and neutrino emissivities scale with the temperature in the same way, and the ratio between the axion and neutrino luminosities L_a/L_ν should not be affected by the large difference in temperature between young and hot proto-NS [$T \sim \mathcal{O}(10)\,\text{MeV}$] and cold NSs [$T \sim \mathcal{O}(10)\,\text{keV}$]:

$$\left(\frac{L_a}{L_\nu}\right)_{\text{NS}} \sim \left(\frac{L_a}{L_\nu}\right)_{\text{SN}} . \tag{7.1}$$

As a consequence, the value of the axion coupling constant which can be constrained with the two systems remains essentially the same, and cold

NSs have primarily acted as complementary probes to CC SNe, with similar systematic uncertainties.

Nonetheless, the previous discussion highlighted how these results are uniquely related to the axial structure of axion interactions. Therefore, the similarity between the outcomes obtained with SNe and cold NSs for the axion case should not generically hold for all kind of exotic cooling channels, since different emission mechanisms show, in general, different dependence on the temperature of the system. Therefore, in some cases, looking at NSs which have already cooled down might improve the results obtained by studying hot proto-NSs at the beginning of their life. Motivated by these arguments in Fiorillo, Lella, et al., 2025 we demonstrate that cold NSs are the most constraining astrophysical system for light scalar particles coupled to nucleons with masses $m_\phi \lesssim 1\,\mathrm{MeV}$, superseding the constraints placed by the SN cooling argument by *few orders of magnitudes* in this mass range.

Once again, these results can be predicted on the basis of simple physical arguments. In particular, the emission of a scalar particle does not lead to a nucleon spin flip, therefore no suppression factor from the scalar momentum is present in the scattering amplitudes. Thus, the scalar emission from a system of non-relativistic particles can only occur in relation to a change in their quadrupole momentum, rather than to their charge. If we consider the case of a scattering process involving identical nucleons, both the total charge (i.e. number of nucleons) and current (i.e. flux of nucleons) are conserved, with only their quadrupole moment allowed to change to radiate the scalar particles. Therefore, the suppression factor in the scattering amplitude should take the form $\sim (p_N/m_N)^4$. Remarkably, this suppression factor depends only on the nucleons' momentum rather than the scalar one. Thus, the different nucleon degeneracy conditions in proto-NS and cold NS environments makes the difference in determining the flux of scalar particles emitted. Indeed, in SNe nucleons are only mildly degenerate and nucleon typical momentum can be estimated as $p_N \sim \sqrt{m_N T}$, leading to a suppression factor $\sim (p_N/m_N)^4 \sim (T/m_N)^2$ comparable to that present for axion and neutrino emission. Conversely, in cold NSs nucleons are strongly degenerate and their momenta lie over the Fermi surface. Crucially, these conditions lead to a dramatic enhancement of the scalar emission compared to neutrino emission.

Quantitatively, we estimate that

$$\left(\frac{L_\phi}{L_\nu}\right)_{\rm NS} \sim \left(\frac{L_\phi}{L_\nu}\right)_{\rm SN} \frac{p_{N,\rm NS}^4}{m_N^2 T_{\rm NS}^2} \sim 10^7 \left(\frac{L_\phi}{L_\nu}\right)_{\rm SN}, \tag{7.2}$$

where $T_{\rm NS} \sim 10$ keV is the typical temperature for NSs with ages $\sim 10^5$ years, and $p_{N,\rm NS} \sim 200$ MeV is the typical nucleon Fermi momentum in nuclear matter at nuclear saturation density $\rho \sim$ few $\times\, 10^{14}$ g cm^{-3}, which characterizes the NS interior. Since the scalar luminosity is proportional to the square of the coupling strengths, this implies that cold NSs would provide constraints on the scalar-nucleon coupling which are 3–4 orders of magnitude stronger than what expected from SNe.

Furthermore, we observe that if the exotic scalar particle is provided with different couplings with protons and neutrons, scalar emission would be further enhanced. Indeed, while in $np \to np$ scattering the total charge associated with the scalar field is conserved, the current (i.e. flux of protons or flux of neutrons) is not necessarily conserved. This would introduce a dipole suppression factor $\sim (p_N/m_N)^2$ in scalar emission, leading to even stronger enhancement for scalar emission compared to neutrino emission in cold NS environments:

$$\left(\frac{L_\phi}{L_\nu}\right)_{\rm NS} \sim \left(\frac{L_\phi}{L_\nu}\right)_{\rm SN} \frac{p_{N,\rm NS}^2}{T_{\rm NS}^2} \sim 10^8 \left(\frac{L_\phi}{L_\nu}\right)_{\rm SN}. \tag{7.3}$$

This discussion highlights that it is the fundamental structure of interactions, defining the microphysics of the novel exotic particle, which directly determines the best testbeds for the physics case under study. In the specific context of this Thesis work, this Chapter furnish a counter-example of how CC SNe are not always the best option to constrain all the possible extensions of the SM, and the exceptional probing power of such systems in the case of axions has to be considered as a peculiar feature. Focusing on the case of light scalar emission, in the following we will briefly outline present bounds on scalars and then discuss how to employ observations of cold isolated NSs to derive novel stringent constraints on the parameter space of such particles.

7.2 Current bounds on light scalar particles

Novel light CP-even scalars may arise in multiple extensions of the SM as dilatons (Damour et al., 1994; Taylor et al., 1988) or radions in theories

with extra dimensions (Arkani-Hamed et al., 2000), playing a role in the solution of some fundamental problems such as the generation of neutrino masses (Dev et al., 2017) and even the electroweak hierarchy problem (Graham et al., 2015; Flacke et al., 2017). Moreover, they could also constitute 100% of the dark matter content in our Universe if produced through, e.g., the misalignment mechanism (Hui et al., 2017; Arvanitaki, Dimopoulos, and Van Tilburg, 2018; Antypas et al., 2022; Cyncynates et al., 2024b; Cyncynates et al., 2024a) and act as mediators for interactions between the dark matter and the SM (Krnjaic, 2016; Knapen et al., 2017b). Interestingly, novel CP-even scalars could mediate hidden fifth forces, leading to deviations from well-established predictions of gravitational physics, like Newton's inverse-square law and the weak equivalence principle. Therefore, a wide experimental effort has taken place during the past few years, performing extremely sensitive tests to point out possible departures from such fundamental laws of nature (see, e.g., Adelberger et al., 2003; Will, 2014; Tino et al., 2020). These constraints are summarized in Fig. 7.1 in the plane scalar nucleon coupling g_S^N versus the mass of the scalar.

By assuming scalars with equal couplings to protons and neutrons, in the range of masses 10^{-5} eV $\lesssim m_\phi \lesssim 1$ eV leading constraints come from tests for violations of the Newtonian inverse square law. In particular, scalars in this mass range mediate long range forces implying violations in the inverse square law at typical scales 30 nm$\lesssim \lambda \lesssim 1$ cm. In particular, the leading constraint spanning $\lambda = 30$–8000 nm comes from a differential force measurement using a microelectromechanical torsional oscillator at the Indiana University–Purdue University Indianapolis (IUPUI) (Chen et al., 2016), which employs a source mass coated with a gold film to suppress the Casimir force between the source mass and the attractor due to background vacuum fluctuations. Fifth forces at sub-micron and sub-nm scales can also be tested by experiments employing levitated test masses (Blakemore et al., 2021; Venugopalan et al., 2024), using analogous setups to those used to measure the Casimir effect (Chiu et al., 2009; Bezerra et al., 2010; Sushkov et al., 2011; Banishev et al., 2013; Banishev et al., 2014; Mostepanenko et al., 2020; Klimchitskaya, Mohideen, et al., 2013; Klimchitskaya and Mostepanenko, 2023) and neutron scattering (Pokotilovski, 2006; Haddock et al., 2018; Heacock et al., 2021; Kamiya et al., 2015; Bogorad et al., 2023) (see also Klimchitskaya and Mostepanenko, 2023 for a recent summary). Nevertheless, these probes

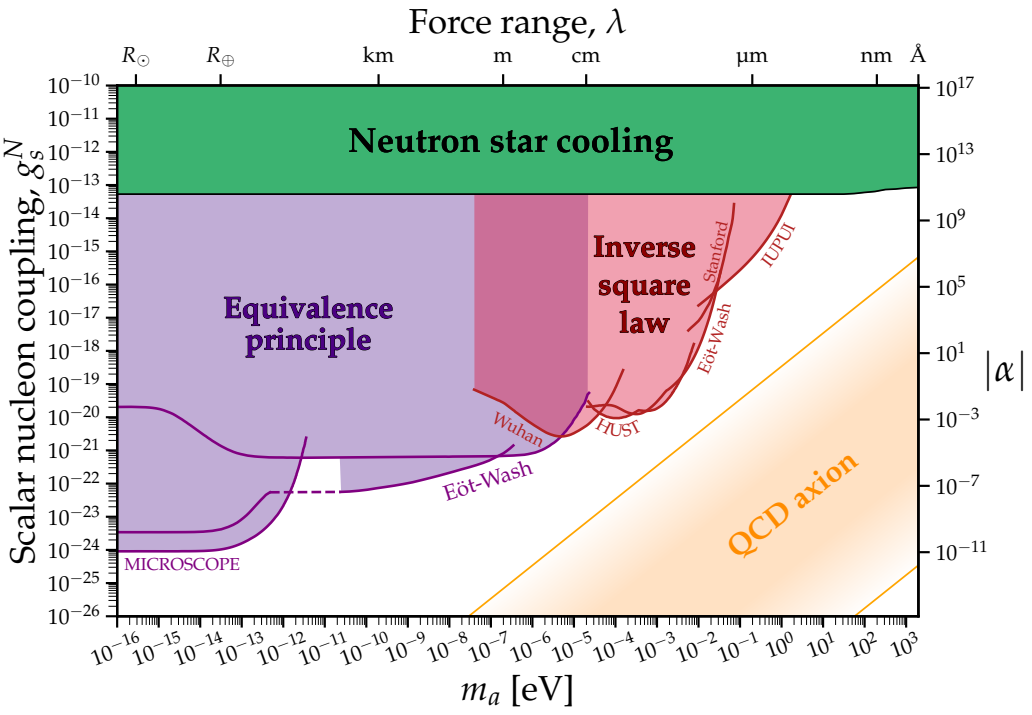

Figure 7.1: Full landscape of constraints on the scalar-nucleon coupling for scalar masses smaller than ∼keV. The bound introduced in Fiorillo, Lella, et al., 2025 from isolated NS cooling is shown in green. Laboratory constraints from tests of the violation of the inverse square law and the weak equivalence principle are shown in red and purple, respectively. The references for these bounds are as follows: MICROSCOPE (Bergé, Brax, et al., 2018; Bergé, Pernot-Borràs, et al., 2022; Touboul et al., 2022), Eöt-Wash (Smith et al., 2000; Kapner et al., 2007; Lee et al., 2020), Wuhan (Ke et al., 2021), HUST (Tu et al., 2007; Yang, Zhan, et al., 2012; Tan et al., 2016; Tan et al., 2020), IUPUI (Chen et al., 2016).

are typically sensitive to equivalent strengths of a Yukawa force relative to gravity $\alpha \sim 10^{11}$–10^{22} between $\lambda \sim 100$–0.1 nm, revealing to be much weaker than current astrophysical constraints. At lower masses, tests of the inverse square law between two masses dominate at force ranges 10 m $\gtrsim \lambda \gtrsim$ μm, while tests of the equivalence principle using torsion balances (Kapner et al., 2007; Lee et al., 2020; Smith et al., 2000; Smith et al., 2000; Yang, Zhan, et al., 2012; Tan et al., 2020; Hoskins et al., 1985) and satellite-borne accelerometers (Bergé, Brax, et al., 2018) dominate for much longer-range forces. All the references for bounds displayed are reported in the caption of Fig. 7.1.

At larger scalar masses, background fluctuations of the vacuum dramatically reduce the sensitivity of such experiments so that the leading sensitivities at masses $m_\phi \gtrsim 1$ eV is set by astrophysical bounds. In particular, scalars emitted from the nuclear plasmas composing stars may escape the stellar volume introducing an exotic cooling channel, which may eventually modify the course of life of stars with respect to the standard evolutionary picture (Grifols and Masso, 1986; Grifols, Masso, and Peris, 1989; Raffelt, 1996). Main astrophysical constraints on the parameter space of scalars coupled to nucleons are reported in Fig. (7.2). For instance, the production of scalars through resonant conversion of plasmons would affect the brightness RGB tip, severely constraining the scalar nucleon coupling down to $g_N \lesssim 1.1 \times 10^{-12}$ (Hardy and Lasenby, 2017). Similarly, scalar production through electron-nucleus bremsstrahlung would modify the WD luminosity function (Bottaro, Caputo, Raffelt, et al., 2023). This argument rules out $g_N \lesssim 7 \times 10^{-13}$ for $m_\phi \lesssim 100$ eV. At masses $m_\phi \gtrsim 10\,\mathrm{keV}$ leading constraints are due to observations of the lifetime of HB stars (Hardy and Lasenby, 2017), while larger masses are probed by the standard SN cooling argument which requires that scalar emission from the young and hot PNS does not affect the duration of the neutrino burst from SN 1987A (Ishizuka et al., 1990; Krnjaic, 2016; Hardy, Sokolov, et al., 2025).

An interesting application for all of the constraints previously discussed also involves axion physics. Indeed, although the axion is a pseudoscalar particle, it has been argued that it might be provided with CP-violating (i.e. scalar) couplings to fermions in addition to its usual CP-preserving couplings (Moody et al., 1984; Georgi and Randall, 1986; Pospelov, 1998; Pospelov and Ritz, 2005; Plakkot et al., 2023; Dekens et al., 2022; Di Luzio, Levati, et al., 2024). In this context, it is possible to introduce a range of values for

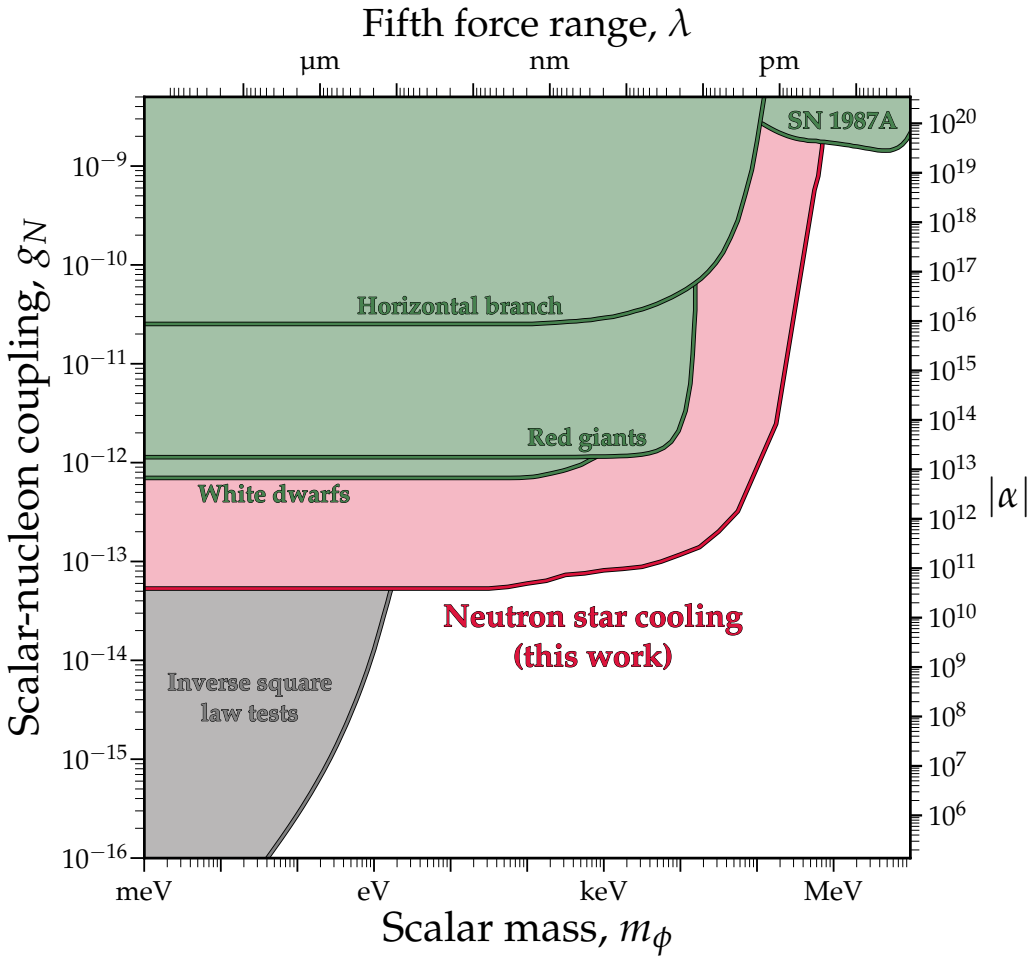

Figure 7.2: Our new limit on the scalar-nucleon coupling g_N at 95% CL as a function of the scalar mass from NS cooling. We show the limit alongside other astrophysical bounds (green) (Hardy and Lasenby, 2017; Bottaro, Caputo, Raffelt, et al., 2023; Hardy, Sokolov, et al., 2025) and laboratory tests of the inverse square law (gray) (Chen et al., 2016). For comparison with the conventional parameterization of fifth forces, we also show the coupling in terms of the equivalent strength of a Yukawa force relative to gravity, $|\alpha|$, along the right-hand axis, and the range of that force $\lambda = m_\phi^{-1}$ along the top axis. We assume equal coupling to protons and neutrons.

g_s^N expected in QCD axion models by estimating how much the QCD θ angle might be shifted with respect to the CP-preserving value at zero (Bigazzi et al., 2020; Bertolini et al., 2020; Di Luzio, Gisbert, Levati, et al., 2023; Di Luzio, Gisbert, Nesti, et al., 2024). Thus, a "QCD axion band", as the one reported in Fig. 7.1, can be introduced in the context axion scalar couplings. In particular it is bounded from above by the current experimental upper limit on $\bar{\theta}$ from the absence of the neutron's electric dipole moment (Abel et al., 2020) and from below by the expected level of CP violation in weak interactions (Georgi and Randall, 1986; Ellis and Gaillard, 1979; Khriplovich, 1986; Gérard et al., 2012; Okawa et al., 2022).

7.3 Light scalars from cold neutron stars

Following the study carried out in Buschmann et al., 2022 for the case of QCD axions, in Fiorillo, Lella, et al., 2025 we employed, for the first time, cold isolated NSs to derive novel constraints on light scalar particles. For our analysis we employ a set of five NSs with ages above $\sim 10^5$ years. In analogy to the rich literature developed on the topic for the axion case (Iwamoto, 1984; Page, Prakash, et al., 2011; Leinson, 2014; Sedrakian, 2016; Hamaguchi et al., 2018; Buschmann et al., 2022; Gómez-Bañón et al., 2024), we derive our new constraints by studying deviations in the NS cooling lightcurves induced by the introduction of an additional exotic cooling due to scalar emission from the nuclear medium in the NS interior. Motivated by the discussion in Sec. 7.1, we show that cold isolated NSs would allow to probe regions of the scalar parameter space to which other astrophysical systems, as CC SNe, are unsensitive. In the following sections we describe the NS dataset employed in this work and outline the main feature of NS cooling theory. Then, we detail the statistical procedure used to search for deviations of NS cooling lightcurves when introducing the exotic cooling channel due to the emission of light scalars, and compare our new constraint to other astrophysical bound present in previous literature.

7.3.1 Cold isolated NSs: data and modelling

In this work we employ data referring to five isolated NSs with ages $\sim 10^5$ years, for which thermal luminosity and kinematic data are available.

Table 7.1: Parameters of the NSs considered in this work. Values of the core temperature T_c, the core density ρ_c and the NS radius R are obtained from the best-fit models determined for each given NS.

Name	L_γ^∞ [10^{33} erg/s]	Age [Myr]	T_c [keV]	ρ_c [g cm^{-3}]	R [km]
J1856[a]	0.065 ± 0.015	0.42 ± 0.08	1.5	7.1×10^{14}	11.4
J1308[b]	0.32 ± 0.06	0.55 ± 0.25	9.4	1.2×10^{15}	11.2
J0720[c]	0.22 ± 0.11	0.85 ± 0.15	5.1	1.1×10^{15}	11.3
J1605[d]	0.4 ± 0.1	0.44 ± 0.07	8.1	1.2×10^{15}	11.2
J0659[e]	0.28 ± 0.14	0.35 ± 0.044	9.0	7.5×10^{14}	11.5

[a]Mignani et al., 2013; Ho et al., 2007; Sartore et al., 2012; [b]Motch et al., 2009; Hambaryan, Suleimanov, Schwope, et al., 2011; [c]Tetzlaff, Eisenbeiss, et al., 2011; Hambaryan, Suleimanov, Haberl, et al., 2017; [d]Tetzlaff, Schmidt, et al., 2012; Pires et al., 2019; [e]Suzuki et al., 2021; Zharikov et al., 2021.

Estimations for the NS thermal luminosities within their uncertainties are inferred on the basis of related X-ray observations interpreted in light of NS cooling theory (Potekhin et al., 2020), while quantitative estimations for their ages are obtained by analyzing the kinematic displacement of the remnant from the location of the supernova event giving birth to the pulsar (Suzuki et al., 2021). In analogy to Buschmann et al., 2022, we consider NSs in the same cooling epoch, in which light-scalar emission [$\propto T^4$ (Ishizuka et al., 1990)] is expected to be the dominant cooling channel compared to neutrino emissivity ($\propto T^8$), making NSs with these ages sensitive laboratories to constrain the properties of such particles. In this regard, we highlight that in the following we will always refer to measurements of the total thermal luminosity, since it is a more robust observable compared to surface temperature, which is affected by local inhomogeneities induced by the strong surrounding magnetic fields.

The relevant data for our analysis are listed in Tab. 7.1. J1856 and J1308 have originated in the Upper Scorpius OB (Motch et al., 2009; Mignani et al., 2013) and their luminosity data are inferred on the basis of a NS atmosphere model with a thin layer of partially-ionized hydrogen or double black body spectrum. These two approaches applied on J1856 suggest a lower luminosity bound at $L_\gamma \simeq 5 \times 10^{31}$ erg / s and an upper bound at $L_\gamma \simeq 8 \times 10^{31}$ erg / s. For J1308, the same models suggest $L_\gamma \simeq (3.3 \pm$

0.5) $\times 10^{32}$ erg / s and $L_\gamma \simeq 2.6 \times 10^{32}$ erg / s, respectively. In the case of J0720, born in the Trumpler association (Tetzlaff, Eisenbeiss, et al., 2011), both models lead to $L_\gamma \simeq 2 \times 10^{32}$ erg / s. The birth of the J1605 can be related to a binary disruption induced by a SN explosion (Tetzlaff, Schmidt, et al., 2012), and its present luminosity is obtained from a double blackbody fit, yielding $L_\gamma \simeq (4 \pm 1) \times 10^{32}$ erg / s. Finally, the pulsar J0659 is located within the large diffuse SN remnant Monogem Ring (Thorsett et al., 2003). Its emission is fit by a double blackbody spectrum including a broken power-law component to account for hard X-ray pulsed emission from the pulsar magnetosphere (Zharikov et al., 2021), leading to a total luminosity $L_\gamma \simeq (2.8 \pm 1.4) \times 10^{32}$ erg / s.

NS cooling process has been modeled by employing the publicly-available code `NSCool` (Page, 2016), which allows to trace NS cooling lightcurves from a one-dimensional NS profile since few seconds after the NS birth till several 10^6 years. In particular, `NSCool` solves the heat transport and energy balance equations in a full General Relativity (GR) framework, determining the surface temperature $T_s(T_b)$ as a function of the temperature in the NS interior T_b. Assuming the star interior to be isothermal, the thermal energy balance requires that

$$C\frac{dT_b^\infty}{dt} = -L_\gamma^\infty - L_\nu^\infty + H \tag{7.4}$$

where the photon luminosity is related to the surface temperature (T_s^∞) as $L_\gamma^\infty = 4\pi R_{*,\infty}^2 (T_s^\infty)^4$. In this expression t is the time, C is the heat capacity of the NS interior, L_ν^∞ is the neutrino luminosity and the superscript ∞ refer to quantities as measured by a distant observed. Moreover, H accounts for surface heating due to surrounding magnetic field. In our work we assume $H = 0$, since it is expected to play a subdominant role in constraining the emission of exotic particles (see the discussion in Buschmann et al., 2022). The solution of this equation determines the NS cooling lightcurve $L_\gamma^\infty(t, \boldsymbol{\theta})$, which is dependent on the NS simulation setup encoded in the $\boldsymbol{\theta}$ parameter vector. In particular, the NS model is determined once specified the NS mass $M_{\rm NS}$, the amount of light elements ΔM defining the envelope composition, the equation of state (EOS) modeling the NS interior and the choice for the superfluidity model. For the sake of simplicity, in the following we assume the APR EOS, built in the `NSCool` code, and the `0-0-0` superfluidity model,

which assumes no superfluidity by setting excitation gaps to zero. In this case we can rely on the detailed study of Buschmann et al., 2022, showing that different choices for the NS model may affect constraints by tens of percent, which is largely subdominant compared to the uncertainties related to the computation of scalar emissivities, entailing a factor $2-3$ uncertainty on the final constraints.

Furthermore, NS may accrete thin layers of light elements (H, He, C and O) on top of their crust. On the contrary to the superfluidity model, the fraction of light elements in accreted envelopes ΔM may significantly affect the relation between the core and surface temperatures $T_s(T_b)$ during both the neutrino- and photon-dominated cooling phases (Chabrier et al., 1997). In this regard, we highlight that the choice of proper values of ΔM allows for good agreement with observations independently of the superfluidity model employed in the analysis. Thus, in our work we varied ΔM over an interval of six discrete log-spaced values ranging from $\Delta M = 10^{-20}\,M_\odot$ (no light elements in accreted envelopes) to $\Delta M = 10^{-6}\,M_\odot$ (high-concentration of light elements in accreted envelopes), developing a dedicated NS simulation for each value assumed. Analogously, the total NS mass $M_{\rm NS}$ has been considered as a free parameter in our NS cooling simulations. In particular, we vary $M_{\rm NS}$ over six equally-spaced values ranging from $M_{\rm NS} = 1.0\,M_\odot$ to $M_{\rm NS} = 2.0\,M_\odot$.

7.3.2 Scalar emission: analysis and results

NSs at ages $t \sim 10^5$ years are characterized by typical core temperatures $T \sim 10^8\,\mathrm{K}$ and densities $\rho \sim 10^{15}$ g cm^{-3}. Under these conditions, the emission of hypothetical scalars with masses $m_\phi \lesssim 30$ keV may dominate NS cooling process at this stage, significantly affecting the photon lightcurves predicted by standard NS cooling theory. The main scalar production channels in the nucleon-rich matter of NS interiors are determined by their couplings to nucleons

$$\mathcal{L} \supset g_N \phi \overline{N} N\,, \tag{7.5}$$

where $N = p, n$ for neutrons and protons, respectively. In the following we will assume equal scalar couplings to protons and neutrons.

Scalars are produced in the core of cold NS by means of NN bremsstrahlung $N + N \to N + N + \phi$ (Ishizuka et al., 1990). In this work, we re-evaluate

the scalar bremsstrahlung emission rate, going beyond the usual one-pion exchange (OPE) or soft approximations employed in previous works. We describe nucleon scattering by using the effective interaction potential already employed in Friman et al., 1979; Bottaro, Caputo, and Fiorillo, 2024 to compute neutrino emissivities from NSs. These results for neutrino emissivities are the same built in `NSCool`, so that our treatment of the exotic production is on the same level of sophistication with that of standard processes. This potential models nucleon-nucleon interactions by means of an expansion in terms of Landau parameters, accounting for both short-range interactions and longer range contributions from OPE+ρ-meson exchange. All the details for the computation of the scalar emission rates are provided in the Supplemental Material of Fiorillo, Lella, et al., 2025. Nevertheless, the naive approximation in Ishizuka et al., 1990, valid for a completely-degenerate nuclear medium made up of neutrons only, can furnish an order of magnitude estimation for the scalar luminosity. At typical conditions for NS ages around $t \sim 10^5$ years, the scalar luminosity scales as

$$L_\phi \simeq 8 \times 10^{32}\,\mathrm{erg\,s^{-1}}\; g_{13}^2 \left(\frac{T}{10^8\,\mathrm{K}}\right)^4 \left(\frac{\rho}{10^{15}\;\mathrm{g\,cm^{-3}}}\right)^{5/3}, \tag{7.6}$$

where $g_{13} = g_N/10^{-13}$.

We have incorporated the complete expression for scalar emissivity within the `NSCool` code, taking into account both contributions from core and crust emission. An example of the cooling lightcurves related to photon, neutrino and scalar emission simulated through the `NSCool` code for an illustrative NS model is depicted in Fig. 7.3. If the scalar emission is too efficient, it may compete with photon and neutrino cooling channels, fastening the standard cooling process of NSs and making them cooler than what expected for their ages. In this scenario, lightcurves simulated through the `NSCool` code on the given set of NS models would not be able to reproduce isolated NS data anymore, allowing us to set upper limits on the scalar-nucleon coupling g_N for each value of the scalar mass m_ϕ. For the given NS EoS and superfluidity model, the set of simulated lightcurves describing the i^{th} NS $L(m_\phi, g_N, \boldsymbol{\theta}^i)$ is parametrized in terms of the scalar free parameters $\{m_\phi, g_N\}$ and in terms of the nuissance parameter vector $\boldsymbol{\theta}^i = \{M^i_{\mathrm{NS}},\, \Delta M^i,\, t^i\}$, which characterize the NS model. Thus, for each given NS we can write the likelihood function

$$\mathcal{L}_i\left(\boldsymbol{d}_i | m_\phi, g_N, \boldsymbol{\theta}^i\right) = \mathcal{N}\left[L(m_\phi, g_N, \boldsymbol{\theta}^i) - L^i_0,\, \sigma^i_L\right] \times \mathcal{N}\left[t^i - t^i_0,\, \sigma^i_t\right] \tag{7.7}$$

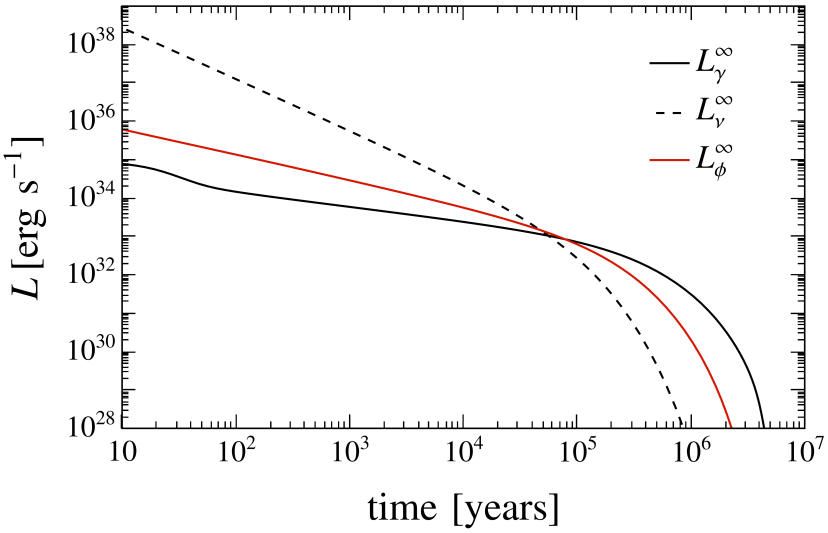

Figure 7.3: Cooling lightcurves for photons, neutrinos and scalars emitted from NSs simulated through the `NSCool` code. In this simulation we assume $M_{\rm NS} = 1.7\,M_\odot$ and $\Delta M = 10^{-20}$ (see text for details). The scalar-nucleon coupling is here set at $g_N = 10^{-13}$.

where we have introduced the dataset for the $i^{\rm th}$ NS $\boldsymbol{d}_i = \{L_0^i,\, \sigma_L^i,\, t_0^i,\, \sigma_t^i\}$, in which σ_L^i and σ_t^i are the 1-σ uncertainty for the measured NS luminosity L_0^i and age t_0^i, respectively. Moreover, $\mathcal{N}(x, \sigma)$ denotes the zero-mean Gaussian distribution function with standard deviation σ. Then, the joint likelihood for the set of NSs considered in the analysis $\mathcal{L}\,(\boldsymbol{d}|\, m_\phi,\, g_N,\, \boldsymbol{\theta})$ is defined by taking the product of the likelihood functions defined for each NS. Notice that in this expression $\boldsymbol{d} = \{\boldsymbol{d}_i\}_{i=1}^5$ and $\boldsymbol{\theta} = \{\boldsymbol{\theta}^i\}_{i=1}^5$ encode the total list of NS data and nuissance parameters. Once introduced the likelihood function, the Wilk's test statistics can be defined for each given scalar mass m_ϕ as (Cowan et al., 2011)

$$q(g_N; m_\phi) = \begin{cases} -2\ln \dfrac{\mathcal{L}\left(\boldsymbol{d}|m_\phi, g_N, \hat{\boldsymbol{\theta}}\right)}{\mathcal{L}\left(\boldsymbol{d}|m_\phi, \hat{g}_N, \hat{\boldsymbol{\theta}}\right)} & g_N \geq \hat{g}_N\,, \\ 0 & g_N < \hat{g}_N\,, \end{cases} \tag{7.8}$$

where $\hat{g}_N$ is the best-fit value of g_N and $\hat{\boldsymbol{\theta}} = \{\boldsymbol{\theta}^i\}_{i=1}^5$ denotes the set of nuissance parameters which individually maximize the likelihood function of each NS considered in the analysis. We determine the upper bound on the scalar-nucleon coupling at 95% confidence level by applying the Wilk's

theorem, which sets the limit at the value g_N^{95} for which the test statistics $q(m_\phi, g_N^{95}) = 2.71$. We point out that Buschmann et al., 2022 employs a different Monte Carlo (MC) procedure to set upper limits, since the distribution function of q computed over such a limited dataset has not approached yet to the expected χ^2 distribution in the asymptotic limit. Nevertheless, this assumption would produce at most a $\sim 50\%$ variations in final limits, which is again subdominant compared to uncertainties over the nuclear interaction model (see the discussion in Fiorillo, Lella, et al., 2025).

The limit derived with this analysis is reported in Fig. 7.2, ruling out $g_N \gtrsim 5 \times 10^{-14}$ for masses $m_\phi \lesssim 100\,\text{eV}$. This constrain supersedes all previous astrophysical limits in the range of masses $m_\phi \lesssim 700$ keV, overtaking by more than one order of magnitude previous constraints from observations of the WD luminosity function (Bottaro, Caputo, Raffelt, et al., 2023). As suggested in Sec. 7.1 our limit dominate over the SN cooling bound in the range of masses $m_\phi \lesssim 1$ MeV, improving upon the results of Hardy, Sokolov, et al., 2025 by ~ 4 orders of magnitude. Globally, constraints induced by NS cooling are now the leading bounds on light scalars mediating fifth forces over micro- to pico-meter distances, a region inaccessible to current experiments, emphasizing once more the complementarity between experimental and astrophysical searches.

Chapter 8

Conclusions

In this Thesis work we investigated the potential of CC SNe as powerful laboratories to probe both standard and non-standard physics, highlighting how the adoption of a truly multimessenger perspective may allow to shed light on the recondite physical phenomena occurring in the interior of exploding stars.

CC SNe have proven to be powerful tools for the study of various aspects of axion phenomenology, particularly in recent years, as these elusive particles have emerged as one of the most compelling and extensively studied BSM candidates fro Dark Matter. Hence, we devoted the first part of this work to a characterization of possible *direct* and *indirect signatures* sourced by axions produced in the SN core. In first place, we introduced the state-of-the-art computation of emission rates for axions coupled to nuclear matter and produced in the SN nuclear medium by means of NN bremsstrahlung, $N+N \to N+N+a$, and pion conversions, $N+\pi \to N+a$. In particular, we built upon the results obtained in previous literature (Turner, 1988; Raffelt and Seckel, 1988; Turner, 1992; Hanhart et al., 2001; Raffelt and Seckel, 1995; Keil, Janka, Schramm, et al., 1997; Carenza et al., 2019; Carenza et al., 2021; Choi et al., 2022; Ho et al., 2023) to the case of axions with masses up to $m_a \sim$ 100 MeV. These outcomes have been further generalized by the derivation of the axion absorption rate in the nuclear medium of the PNS, allowing us to employ the *modified luminosity criterion* to smoothly extend our results from the case of weakly-coupled axions in the free-streaming regime ($g_{aN} \lesssim 10^{-8}$) to the case axions trapped in the SN core ($g_{aN} \gtrsim 10^{-7}$). Since the copious emission of axions from the nuclear medium of the PNS may open

an efficient *energy-loss channel* shortening the duration of the SN cooling phase, observations of the SN 1987A neutrino burst set the bound $6\times10^{-10} \lesssim g_{ap} \lesssim 3\times10^{-6}$ for axions with masses $m_a \lesssim 10$ MeV and coupling to protons only ($g_{an} \simeq 0$).

Axions coupling to nucleons may also give rise to *direct signatures* in neutrino in neutrino water Čherenkov detectors due to their interactions with oxygen nuclei (Engel et al., 1990). In this work, we estimated the expected number of events within the Kamiokande II detector in coincidence to SN 1987A by employing the state-of-the-art nuclear interactions modeling the oxygen nucleus and realistic SN profiles to obtain a reliable estimation of the SN axion flux. Remarkably, the non-observation of axion-induced events during SN 1987A combined with the energy-loss argument rules out –within a factor $\sim 2-3$ of uncertainty– QCD axions with masses $m_a \gtrsim 8\,\text{meV}$, setting the most stringent bound on the QCD axion mass to date. We also studied the physics case of axions provided with an additional photon coupling. In this scenario, we investigated the potential of the IAXO experiment in discovering axions produced from a future nearby SN, pointing out that SN axion searches may probe regions of the parameter space that are complementary to those explored by the experiment in helioscope mode.

Axions coupling with photons and electrons may give rise to various *gamma-ray signatures*. Massive axions with $m_a \gtrsim 1$ MeV, once produced in the PNS nuclear medium, may efficiently decay in photon and electron pairs and, depending on their decay length, give rise to a large variety of probes. Specifically, axions decaying within the SN volume can be constrained by the limit imposed on energy injection in the SN mantle by observations of low-energy SNe (Caputo, Janka, et al., 2022). Conversely, when decaying outside from the photosphere they can produce an axion-induced gamma-ray burst, constrained by SMM observations during SN 1987A, or give rise to a contribution to the diffuse photon background measured by *Fermi*-LAT due to decays occurring in the DSALPB. Furthermore, heavy axion coupled to electrons may inject positrons in the intergalactic medium affecting the 511 keV signal measured by the SPI satellite (Siegert et al., 2019). Constraints obtained from the 511 keV line can be further improved by searches for signatures due to positrons in-flight annihilation. Noticeably, we showed that a proper modeling of the background in-flight annihilation gamma-ray signal may improve the 511 keV constraint by one order of magnitude. Finally we

discussed the case of light axions ($m_a \lesssim 10^{-9}$ eV) produced in the innermost regions of the PNS, which may escape the SN volume and then be converted in gamma-rays in the Galactic magnetic field. In this context, we illustrated how the analysis of axion-induced signals within the *Fermi*-LAT experiment in coincidence to a future Galactic SN may shed light on controversial properties characterizing the SN core, such as the average temperature of the PNS and the fraction of pions in the core interior.

A decisive imprint in the study of the physics of the SN core might be provided by observations of the *GW signal* emitted from a future Galactic SN. Hence, in the second part of this Thesis we developed a detailed analysis of GW signatures predicted from two state-of-the-art 3D SN simulations extended up to ∼few seconds. We account for both contributions sourced by the highly time-dependent anisotropic emission of neutrinos and aspherical mass flows, illustrating how peculiar features characterizing the signal may shed light on the impact of accretion downflows on the neutrino fluxes, the dynamics of post-shock convection and SASI, PNS oscillation modes and the anisotropic expansion of explosion ejecta. This analysis aims to highlight that the study of a future Galactic SN explosion must incorporate the interplay between the information carried by the neutrino and GW signals.

Finally, in the last Chapter we showed that CC SNe do not always provide the most stringent constraints for all classes of FIPs. We argued that the core of SNe, due to the extremely high temperature, is the most constraining astrophysical system for particles whose emission rates exhibit a strong dependence on temperature. This is the case for axions, whose emission rate scales similarly to neutrinos, due to the analogous axial nature of axion and neutrino interactions. Conversely, compact objects in more advanced evolutionary stages, as cold isolated neutron stars, set more stringent bounds on particles whose production is less temperature-dependent than neutrino's, such as scalar particles. In this context, we demonstrate that the analysis of NS cooling process places the most stringent astrophysical bound on light scalars coupled to nucleons, ruling out scalar-nucleon couplings $g_N \gtrsim 5 \times 10^{-14}$ for $m_\phi \lesssim 1$ MeV. This limit supersedes the constraint placed by the SN cooling argument by ~ 4 orders of magnitude.

The study carried out in this Thesis may set the stage for future promising directions of research. The advent of deci-Hertz interferometers may enable the detection of the GW signals from more frequent extragalactic SNe,

potentially allowing the time trigger of the onset of the explosion. In this scenario, the combination of electromagnetic and gravitational wave observations would significantly enhance our capabilities in pointing out axion signatures in extragalactic events characterized by extremely hot and dense environments as SNe and binary NS mergers (Lecce et al., 2025). Furthermore, we also leave to future work the characterization of the stochastic SN GW background arising from unresolved sources and based on the state-of-the-art 3D SN simulations, which would constitute a guaranteed signal correlated to the highly-energetic phenomena occurring in the SN core. Techniques developed in this work may also be applied to various other physics cases. In particular, the study of the impact of spin-2 particles on stellar systems is poorly explored (Cembranos et al., 2017) but will benefit of the extensive investigation of indirect axion signatures carried on in the last twenty years. Furthermore, searches for High-Frequency Gravitational Waves (HFGW), which would constitute a smoking gun for exotic physics, can be carried on using the same strategies originally thought for the axion quest. Alongside novel experimental proposals, HFGW conversions in photons within astrophysical magnetic fields may represent a valuable tool for searches in such high-frequency band (Lella, Calore, Carenza, and Mirizzi, 2024).

In conclusion, the study carried out in this Thesis underlines the power of multimessenger astrophysics in investigating the exotic physical phenomena taking place in the core of massive stars when undergoing a SN explosion. The study of SN axion phenomenology, impacting neutrino and gamma-ray observations, allows one to probe regions of the parameter space complementary to forthcoming ground-based experiments and cosmological surveys, revealing the importance of adopting a synergistic approach among astrophysics, cosmology and direct searches to outline a high-winning strategy for the discovery of the axion. In parallel, the characterization of signals carried by the various cosmic messengers sourced by the SN core enables us to be fully prepared to extract the highest possible amount of information from observations of the next nearby SN explosion event. In this context, the development of large underground neutrino detectors, the proposal of novel generation of gamma-ray detectors efficient in the MeV range and the advent of a new generation of GW detectors highlight the timeliness of this work, identifying CC SNe as a promising stage for future groundbreaking discoveries in fundamental physics.

Appendix A

Appendix: Details on axion emission rates from the SN nuclear medium

A.1 Explicit expressions for SN emission rates

The axion emission spectra expressed in terms of number of axions emitted per unit volume, unit time, and unit energy interval can be obtained as (Raffelt, 1996; Carenza, Giannotti, et al., 2025)

$$\frac{d^2 n_a}{d\omega_a dt} = \frac{|\mathbf{p}_a|}{4\pi^2} \int \prod_{i,j} \frac{d^3 p_i}{2E_{i,j}(2\pi)^3} f_i(1 \pm f_j) \\ S \sum_{\text{spins}} |\mathcal{M}|^2 (2\pi)^4 \delta^4 \left(\sum_i p_i - \sum_j p_j - p_a \right) , \tag{A.1}$$

where p_a and $\mathbf{p}_a$ are the axion four- and three-momentum, respectively. The index i and j run over incoming and outgoing, respectively, provided with $p_{i,j}$ four-momenta. $f_{i,j}$ are the distribution functions for the given particle and terms $(1 \pm f_i)$ account for Bose-enhancement or Pauli-blocking factors, for outgoing bosons and fermions, respectively. Moreover, $\sum |\mathcal{M}|^2$ is the squared matrix element for the process summed over the initial and final spins, S is the symmetry factor avoiding to double-counting in the summed

matrix element and the δ^4 distribution guarantees the conservation of the total four-momentum.

Given this definition, the axion emission rate via NN bremsstrahlung is given by

$$\left(\frac{d^2 n_a}{d\omega_a\, dt}\right)_{NN} = \frac{g_a^2}{16\pi^2}\frac{n_B}{m_N^2}\,(\omega_a^2 - m_a^2)^{\frac{3}{2}}\, e^{-\omega_a/T}\, S_\sigma\left(\frac{\omega_a}{T}\right)\,\Theta(\omega_a - m_a)\,, \quad \text{(A.2)}$$

in which the structure functions $S_\sigma(\omega_a)$ can be parametrized as

$$S_\sigma(\omega_a) = \frac{\Gamma_\sigma}{\omega_a^2 + \Gamma^2} s(\omega_a/T) \quad \text{(A.3)}$$

and the line-width Γ is chosen to have structure functions satisfying the normalization condition.

$$\begin{aligned}\int_{-\infty}^{+\infty}\frac{d\omega}{2\pi}S_\sigma &= \int_0^{+\infty}\frac{d\omega}{2\pi}(1+e^{-\omega/T})S_\sigma = \\ &= \frac{1}{n_B}\sum_{i=n,p}\frac{C_{ai}^2}{Y_n C_{an}^2 + Y_p C_{ap}^2}\int\frac{g_i d^3p_i}{(2\pi)^3}f_i(1-f_i)\,,\end{aligned} \quad \text{(A.4)}$$

In this context the nucleon spin-fluctuation rate Γ_σ can be expressed as

$$\Gamma_\sigma = \frac{4}{\pi^{3/2}}\left(\frac{g_A}{2f_\pi}\right)^4 {m_N^*}^{0.5}\, T^{0.5}\rho\,, \quad \text{(A.5)}$$

in which m_N^* is the effective nucleon mass in the SN medium, while T and ρ are the SN core temperature and density. Explicit expressions for the $s(x)$ function are introduced in Carenza et al., 2019 separating the contributions coming from pp, nn and np scattering processes:

$$s(x) = s_{nn}(x) + s_{pp}(x) + s_{np}(x)\,, \quad \text{(A.6)}$$

with

$$\begin{aligned}s_{nn}(x) =& \frac{1}{3}Y_n^2 C_{an}^2(s_{\mathbf{k}} + s_{\mathbf{l}} + s_{\mathbf{kl}} - 3s_{\mathbf{k}\cdot\mathbf{l}})\\ s_{pp}(x) =& \frac{1}{3}Y_p^2 C_{ap}^2(s_{\mathbf{k}} + s_{\mathbf{l}} + s_{\mathbf{kl}} - 3s_{\mathbf{k}\cdot\mathbf{l}})\\ s_{np}(x) =& \frac{4}{3}Y_n Y_p(C_+^2 + C_-^2)s_{\mathbf{k}} + \frac{4}{3}Y_n Y_p(4C_+^2 + 2C_-^2)s_{\mathbf{l}} + \\ &- \frac{8}{3}Y_n Y_p[(C_+^2 + C_-^2)s_{\mathbf{kl}} - (3C_+^2 - C_-^2)s_{\mathbf{k}\cdot\mathbf{l}}]\,,\end{aligned} \quad \text{(A.7)}$$

and Y_n and Y_p are the baryonic fractions of protons and neutrons inside the SN core, respectively. In particular, in this equation we have defined the following integrals

$$s_{\mathbf{k}} = \int \frac{d\cos\delta}{2}\frac{d\phi}{2\pi}\frac{\sqrt{w}dw}{\frac{\sqrt{\pi}}{2}}\frac{dz}{2}du \left[\frac{\rho Y_1}{2m_N}\left(\frac{2\pi}{m_N T}\right)^{\frac{3}{2}}\right]^{-1}\left[\frac{\rho Y_2}{2m_N}\left(\frac{2\pi}{m_N T}\right)^{\frac{3}{2}}\right]^{-1} e^{u-\eta_3}e^{w-\eta_4}\sqrt{u(u-x)}[H_u^+ H_u^- H_v^+ H_v^- F_+^2]_{v=u-x} \tag{A.8}$$

$$s_{\mathbf{l}} = \int \frac{d\cos\delta}{2}\frac{d\phi}{2\pi}\frac{\sqrt{w}dw}{\frac{\sqrt{\pi}}{2}}\frac{dz}{2}du \left[\frac{\rho Y_1}{2m_N}\left(\frac{2\pi}{m_N T}\right)^{\frac{3}{2}}\right]^{-1}\left[\frac{\rho Y_2}{2m_N}\left(\frac{2\pi}{m_N T}\right)^{\frac{3}{2}}\right]^{-1} e^{u-\eta_3}e^{w-\eta_4}\sqrt{u(u-x)}[H_u^+ H_u^- H_v^+ H_v^- F_-^2]_{v=u-x} \tag{A.9}$$

$$s_{\mathbf{kl}} = \int \frac{d\cos\delta}{2}\frac{d\phi}{2\pi}\frac{\sqrt{w}dw}{\frac{\sqrt{\pi}}{2}}\frac{dz}{2}du \left[\frac{\rho Y_1}{2m_N}\left(\frac{2\pi}{m_N T}\right)^{\frac{3}{2}}\right]^{-1}\left[\frac{\rho Y_2}{2m_N}\left(\frac{2\pi}{m_N T}\right)^{\frac{3}{2}}\right]^{-1} e^{u-\eta_3}e^{w-\eta_4}\sqrt{u(u-x)}[H_u^+ H_u^- H_v^+ H_v^- F_+ F_-]_{v=u-x} \tag{A.10}$$

$$s_{\mathbf{k}\cdot\mathbf{l}} = \int \frac{d\cos\delta}{2}\frac{d\phi}{2\pi}\frac{\sqrt{w}dw}{\frac{\sqrt{\pi}}{2}}\frac{dz}{2}du \left[\frac{\rho Y_1}{2m_N}\left(\frac{2\pi}{m_N T}\right)^{\frac{3}{2}}\right]^{-1}\left[\frac{\rho Y_2}{2m_N}\left(\frac{2\pi}{m_N T}\right)^{\frac{3}{2}}\right]^{-1} e^{u-\eta_3}e^{w-\eta_4}\sqrt{u(u-x)}\left[H_u^+ H_u^- H_v^+ H_v^- F_+ F_- \frac{\xi}{3}\right]_{v=u-x}. \tag{A.11}$$

Moreover, in these expressions we have introduced the functions

$$H_u^{\pm}(\eta) = \left(\exp\left\{\frac{u+w}{2} \pm \sqrt{uw}\cos\delta - \eta\right\} + 1\right)^{-1},$$
$$H_v^{\pm}(\eta) = \left(\exp\left\{\frac{u+w}{2} \pm \sqrt{uw}(\sin\delta\cos\phi\sin\theta + \cos\delta\cos\theta) - \eta\right\} + 1\right)^{-1},$$

$$
\begin{aligned}
F_+ &= \frac{u+v+2uv\sqrt{uv}z}{u+v+2uv\sqrt{uv}z+y} \\
F_- &= \frac{u+v-2uv\sqrt{uv}z}{u+v-2uv\sqrt{uv}z+y} \\
\xi &= 3\frac{(u-v)^2}{(u+v)^2-4uvz^2}\,.
\end{aligned}
\tag{A.12}
$$

The pion conversion axion emission spectrum per unit volume is given by

$$
\begin{aligned}
\left(\frac{d^2n_a}{d\omega_a\,dt}\right)_{N\pi} &= \frac{g_a^2T^{3.5}}{2^{1.5}\pi^5 m_N^{0.5}}\left(\frac{g_A}{2f_\pi}\right)^2\left(\omega_a^2-m_a^2\right)^{\frac{1}{2}} \\
&\times \mathcal{C}_a^{p\pi^-}\frac{\Theta(\omega_a-m_\pi)\,\Theta(\omega_a-m_a)}{\exp\{(x_a-y_\pi-\hat{\mu}_\pi)\}-1}\left(\omega_a^2-m_\pi^2\right)^{\frac{1}{2}} \\
&\times \int_0^\infty dy\,y^2\frac{1}{\exp\{(y^2-\hat{\mu}_p)\}+1}\frac{1}{\exp\{(-y^2+\hat{\mu}_n)\}+1}\,,
\end{aligned}
\tag{A.13}
$$

where m_π is the pion mass, $y_\pi = m_\pi/T$, $x_a = \omega_a/T$, $\hat{\mu} = (\mu - m)/T$, with μ the pion and nucleon chemical potentials, and the product of the Heaviside theta functions fixes the minimal threshold energy for the process. Notice that by neglecting nucleon recoil, energy conservation just requires the pion energy to be equal to the axion one $E_\pi = \omega_a$. Here, $\mathcal{C}_a^{p\pi^-}$ can be written as

$$
\mathcal{C}_a^{p\pi^-} = \frac{m_N^2}{g_A^2\,T^2}\,\beta_a^2\,\mathcal{G}_a(|\mathbf{p}_\pi|)\,,
\tag{A.14}
$$

in which $|\mathbf{p}_\pi| = \sqrt{\omega_a^2 - m_\pi^2}$ is the modulus of the pion three-momentum. The complete expression for $\mathcal{G}_a(|\mathbf{p}_\pi|)$ is provided in (Ho et al., 2023). Here we include only leading terms in $1/m_N$ as in (Carenza, 2023),

$$
\begin{aligned}
\mathcal{G}_a(|\mathbf{p}_\pi|) =& \frac{2g_A^2(2C_+^2+C_-^2)}{3}\left(\frac{|\mathbf{p}_\pi|}{m_N}\right)^2 + C_{a\pi N}^2\left(\frac{\omega_a}{m_N}\right)^2 \\
&+ \frac{2g_A^2C_{aN\Delta}^2}{9}\left(\frac{|\mathbf{p}_\pi|}{m_N}\right)^2\mathcal{F}_{aN\pi} - \frac{4\sqrt{3}g_A^2C_{aN\Delta}}{9}\left(\frac{|\mathbf{p}_\pi|}{m_N}\right)^2\mathcal{F}_{aN\Delta}
\end{aligned}
\tag{A.15}
$$

with

$$
\begin{aligned}
\mathcal{D} =& \left[(\Delta m-\omega_a)^2+\Gamma_\Delta^2/4\right]\left[(\Delta m+\omega_a)^2+\Gamma_\Delta^2/4\right] \\
\mathcal{F}_{aN\pi} =& \mathcal{D}^{-1}E_\pi^2\left(\Delta m^2+2\omega_a^2+\Gamma_\Delta^2/4\right) \\
\mathcal{F}_{aN\Delta} =& \mathcal{D}^{-1}E_\pi\left[\left(\Delta m^2-\omega_a^2\right)(C_+\Delta m+C_-\omega_a)+\Gamma_\Delta^2/4\,(C_+\Delta m-C_-\omega_a)\right]
\end{aligned}
\tag{A.16}
$$

where the width of the Δ-resonance is $\Gamma_\Delta = 117$ MeV, while the nucleon-Δ mass difference is $\Delta m = m_\Delta - m_N^*$.

A.2 Axion pionic absorption

As discussed in Sec. 3.1, only processes involving negatively charged pions are relevant for axion production (Carenza et al., 2021; Choi et al., 2022), since the abundance of π^+ and π^0 inside a SN core is strongly suppressed with respect to π^- (Fore and Reddy, 2020). However, since in axion absorption processes pions are present only in the final state, the concentration of the different species does not influence inverse pion conversion. Thus, to have a reliable estimation of axion absorption rates it is necessary to include the absorption contributions given by all the possible pionic processes

$$\begin{aligned} n + a &\to p + \pi^- \\ p + a &\to n + \pi^+ \\ n + a &\to n + \pi^0 \\ p + a &\to p + \pi^0 \,. \end{aligned} \tag{A.17}$$

Referring to Fig. A.1 and to the interaction Lagrangian introduced in Eq. (3.1), the scattering amplitudes for other processes can be easily computed from the matrix element for $n + a \to p + \pi^-$ following some simple prescriptions:

- To switch from $a + n \to p + \pi^-$ to $a + p \to n + \pi^+$ it is only needed to exchange $C_{ap} \leftrightarrow C_{an}$.
- The relative sign between the Compton diagrams and the contact interaction term is different in $a+p \to n+\pi^+$ with respect to $a+n \to p+\pi^-$. However, this is not relevant for us since the interference terms involving the contact diagram have been neglected in this work, being of higher order in $1/m_N$ (see Carena et al., 1989; Choi et al., 2022; Ho et al., 2023 for further details).
- In processes involving neutral pions, only Compton-like diagrams are possible. Moreover, it is necessary to divide by a factor of 2 with respect to the same contribution estimated for charged pions (Bjorken and Drell, 1965).

- The integral on the nucleons kinetic energies in the formulas in Eq. (5) of Lella, Carenza, et al., 2023 has to be generalized as follows

$$\int_0^\infty dy\, y^2 \frac{1}{\exp\{(y^2 - \hat{\mu}_{\rm in})\} + 1} \frac{1}{\exp\{(-y^2 + \hat{\mu}_{\rm out})\} + 1}\,, \tag{A.18}$$

  where $\hat{\mu}_{\rm in}$ is the relativistic chemical potential of the incoming nucleon while $\hat{\mu}_{\rm out}$ refers to the outgoing nucleon.

A.3 Mean free path

Starting from the expressions for the axion spectrum of production $d^2 n_a / d\omega_a\, dt$ introduced in Lella, Carenza, et al., 2023, the mean free path (MFP) λ_a associated with the inverse pion conversion and inverse bremsstrahlung can be computed as (Giannotti et al., 2005)

$$\begin{aligned} \lambda_a^{-1}(\omega_a) = \frac{1}{2|\mathbf{p}_a|} \frac{d^2 n_a(\chi\, \omega_a)}{d\Pi_a\, dt} = \\ 2\pi^2 \left(\omega_a^2 - m_a^2\right)^{-1} \frac{d^2 n_a(\chi\, \omega_a)}{d\omega_a\, dt}\,, \end{aligned} \tag{A.19}$$

where $d\Pi_a = d^3\mathbf{p}_a/(2\pi)^3 2\omega_a$ is the axion phase space and $\chi = \pm 1$ for pionic processes and bremsstrahlung respectively. This change in sign of the axion energy is due to the different role that the axion plays in the two processes. In bremsstrahlung processes, depending on whether the axion is absorbed or emitted, its energy is released to or soaked up from the nuclear medium and then it must change sign switching from the production to the absorption rate (see, e.g. Raffelt, 1996). On the other hand, in pionic processes the conservation of the energy for non-relativistic nucleons just requires that the axion and the pion involved must have the same energy and no change in sign is necessary. However, note that in pionic absorption the pion is present in the final state implying the substitution $f_\pi \to 1 + f_\pi$. Let us highlight that the expression of the MFP for inverse bremsstrahlung coincides with Eq. (4.27) in (Raffelt, 1996) extended to the case of massive axions. The behavior of the MFP in the massless case $m_a < 10$ MeV at $R \simeq 20$ km is depicted in Fig. A.2. In inverse bremsstrahlung the incoming axion just yields a certain amount of kinetic energy to the system of nucleons. As a consequence,

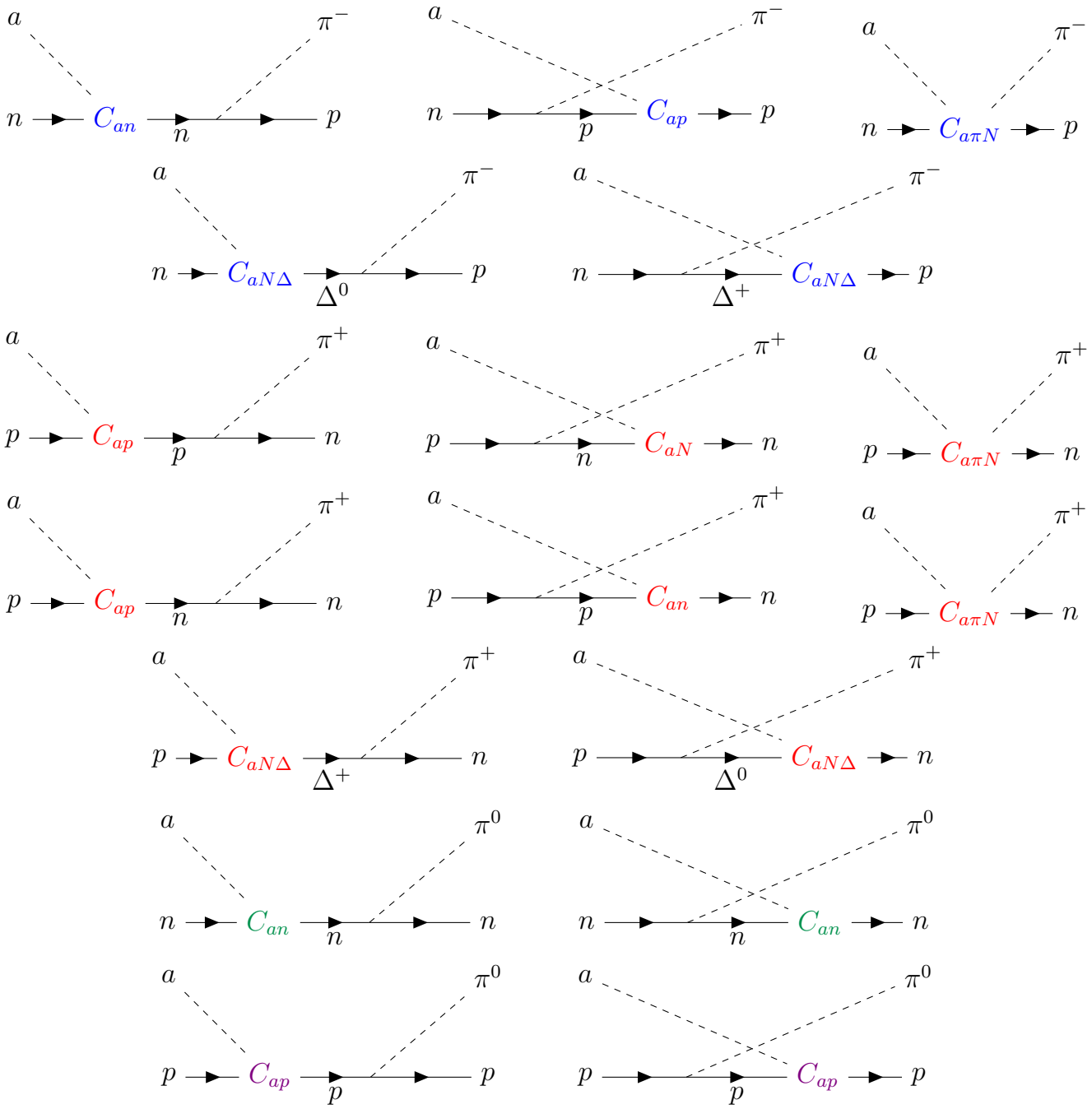

Figure A.1: Feynman diagrams of pionic Compton processes for axion absorption, including also the contact and the delta mediated diagrams.

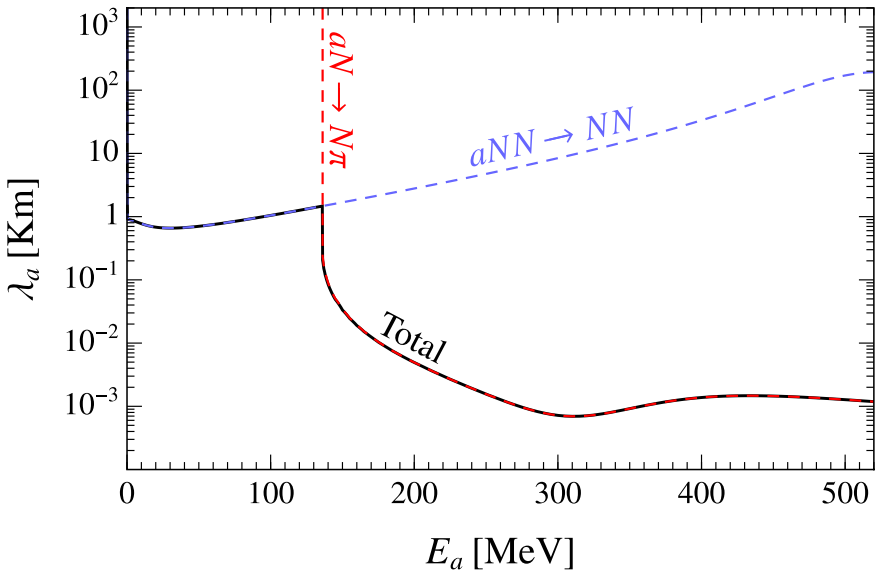

Figure A.2: Behavior of the axion mean free path at the value of the upper bound for the case of massless axions at $R \simeq 20$ km. In particular the dashed blue line describes the absorption length by means of inverse bremsstrahlung, the red one by means of inverse pion conversion and the black solid curve shows the total MFP.

bremsstrahlung absorptions are favored (shorter MFP) for axions with energies in the order of the nucleons mean kinetic energy $E_{\rm kin} \sim 3T \sim 20\,{\rm MeV}$. On the other hand, larger energies cannot be efficiently absorbed by nucleons since their phase space becomes smaller. Therefore, the axion MFP increases for energies larger than ~ 20 MeV.

On the contrary, the MFP associated to pionic processes decreases monotonically as the axion energy increases. Since these processes consist in the conversion of an axion into a pion (nucleons can be considered at rest), all the energy brought by the axion is available in the center of mass to produce the outgoing pion. Consequently, once exceeded the threshold energy $\omega_a = m_\pi$, as the axion energy increases the conversion process becomes more and more efficient.

Appendix B

Appendix: Derivation of the axion-oxygen cross section

The axion-nucleon interaction Lagrangian, introduced in Sec. 3.1.1, can be conveniently recast in the following form

$$\mathcal{L}_{aN}(\boldsymbol{r},t) = \frac{g_{aN}}{2m_N}\bar{\psi}_N(\boldsymbol{r},t)\gamma^\mu\gamma^5(C_0 + C_1\tau_3)\psi_N(\boldsymbol{r},t)\partial_\mu a(\boldsymbol{r},t)\,, \tag{B.1}$$

where g_{aN} is the axion-nucleon coupling constant, m_N is the nucleon mass, $\psi_N = (p,n)^T$ is the nucleon doublet and $\tau^3 = \mathrm{diag}(1,-1)$ is the third Pauli matrix. Moreover, the iso-scalar coupling C_0 and the iso-vector coupling C_1 can be related to the model dependent constants C_{ap} and C_{an} as $C_0 = (C_{ap} + C_{an})/2$ and $C_1 = (C_{ap} - C_{an})/2$.

Starting from Eq. (B.1), we can introduce the Hamiltonian

$$\begin{aligned}\mathcal{H}_{aN}(\boldsymbol{r},t) &= -\frac{g_{aN}}{2m_N}\bar{\psi}_N(\boldsymbol{r},t)\gamma^k\gamma^5(C_0 + C_1\tau_3)\psi_N(\boldsymbol{r},t)\partial_k a(\boldsymbol{r},t) \\ &\equiv -\frac{g_{aN}}{2m_N}\mathcal{J}^k(\boldsymbol{r},t)\partial_k a(\boldsymbol{r},t)\,,\end{aligned} \tag{B.2}$$

in which we have introduced the hadronic current operator $\mathcal{J}^k(\boldsymbol{r},t)$ and the index k ranges from 1 to 3. Then, the transition matrix element from system initial state $|i\rangle$ and the final $|f\rangle$ state can be expressed as

$$\begin{aligned}\mathcal{M}_{if} &= \int d^3\boldsymbol{r}\,dt\,\langle f|\,\mathcal{H}_{aN}(\boldsymbol{r},t)\,|i\rangle \\ &= -\frac{g_{aN}}{2m_N}\int d^3\boldsymbol{r}\,dt\,\langle\Psi_f|\,\mathcal{J}^k(\boldsymbol{r},t)\,|\Psi_i\rangle\,\langle 0|\,\partial_k a(\boldsymbol{r},t)\,|\boldsymbol{p}\rangle\ ,\end{aligned} \tag{B.3}$$

where $|\Psi_i\rangle$ and $|\Psi_f\rangle$ are the nucleus initial and final eigenstates, $|\boldsymbol{p}\rangle$ describes a single axion of momentum $\boldsymbol{p}$ and $|0\rangle$ is the physical vacuum of the axion field. By expanding the axion operator in terms of destruction and creation operators b_q and $b_q^\dagger$

$$a(\boldsymbol{r},t) = \int \frac{d^3q}{\sqrt{2\epsilon_q}} \left(e^{-i\epsilon_q t + i\boldsymbol{p}\cdot\boldsymbol{r}}\, b_q + e^{i\epsilon_q t - i\boldsymbol{p}\cdot\boldsymbol{r}}\, b_q^\dagger\right) , \tag{B.4}$$

and expressing the nuclear matrix element in Eq. (B.3) in Heisenberg representation

$$\begin{aligned} \langle\Psi_f|\, \mathcal{J}^k(\boldsymbol{r},t)\, |\Psi_i\rangle &= \langle\Psi_f|\, e^{iHt}\mathcal{J}^k(\boldsymbol{r},0)e^{-iHt}\, |\Psi_i\rangle \\ &= e^{i(E_f-E_i)t}\, \langle\Psi_f|\, \mathcal{J}^k(\boldsymbol{r})\, |\Psi_i\rangle \ , \end{aligned} \tag{B.5}$$

the transition amplitude can be expressed as

$$\mathcal{M}_{if} = -\frac{g_{aN}}{2m_N}\frac{2\pi\delta(E_f - E_i - \epsilon_p)}{\sqrt{2\epsilon_p}} \int d^3\boldsymbol{r},\, \langle\Psi_f|\, \mathcal{J}^k(\boldsymbol{r},)\, |\Psi_i\rangle\, \partial_k e^{i\boldsymbol{p}\cdot\boldsymbol{r},} . \tag{B.6}$$

Carrying out a multipole expansion of the exponential term, the transition amplitude can be expressed as

$$\mathcal{M}_{if} = -\frac{g_{aN}}{2m_N}\frac{2\pi\delta(\omega - \epsilon_p)}{\sqrt{2\epsilon_p}}\epsilon_p \sum_{l=0}^{\infty} i^{l-1}\sqrt{4\pi(2l+1)}L_{l,0}\,, \tag{B.7}$$

where $\omega = E_f - E_i$ is the nuclear excitation energy. In this expression, $L_{l,0}$ is defined as:

$$L_{l,0} = \frac{i}{p}\int d^3\boldsymbol{r}\ \langle\Psi_f|\, \mathcal{J}^k(\boldsymbol{r})\, |\Psi_i\rangle\, \partial_k \left[j_l(pr)Y_{l,0}(\Omega)\right] . \tag{B.8}$$

in which we introduced the spherical Bessel function j_l and the spherical harmonics $Y_{l,0}$, while where $p \equiv |\boldsymbol{p}|$, $r \equiv |\boldsymbol{r}|$, and j_l and Ω defines the angular polar coordinates. The nuclear states are defined by the total angular momentum J, its third component M and by their parity Π. Even-even nuclei, as the oxygen nucleus, are characterized by ground states with $J = 0$ and $\Pi = +1$. Thus, the transition from the initial to the final nuclear state is then described by

$$\begin{aligned} L_{l,0} &= \frac{i}{p}\, \langle JM;\Pi|\int d^3\boldsymbol{r}\, \mathcal{J}^k(\boldsymbol{r})\partial_k \left[j_l(pr)Y_{l,0}(\Omega)\right] |00;+1\rangle \\ &\equiv \left\langle J^\Pi\right|\, |T_J|\, \left|0^+\right\rangle \ , \end{aligned} \tag{B.9}$$

where we take advantage of the Wigner-Eckart theorem (Edmonds, 1957) to set $l = J$ and $M = 0$, and $\left\langle J^{\Pi}\right| |T_l| \left|0^+\right\rangle$ stands for a reduced matrix element for the angular part (Edmonds, 1957). Given these definitions, the total matrix element, summed over all the possible final states for axion absorption on the oxygen nucleus, is then given by (Engel et al., 1990)

$$\begin{aligned}\sigma(\epsilon_p) &= \int \frac{d\omega}{\mathcal{T}} \sum_J \left(\frac{d\rho}{d\omega}\right)_J |M_{if}|^2 \\ &= \frac{4\pi^2 g_{aN}^2}{m_N^2} \sum_J \epsilon_p \, (2J+1) \left|\left\langle J^{\Pi}\right| |T_J| \left|0^+\right\rangle\right|^2 \delta(\epsilon_p - E_J) \,,\end{aligned} \tag{B.10}$$

where $\mathcal{T}$ is the observation time and $\delta^2(E) = \mathcal{T}/2\pi \, \delta(E)$ in the limit $\mathcal{T} \to \infty$, while $(d\rho/d\omega)_J = 4\,\delta(\omega - E_J)$ is the density of nuclear states for the excitation level J^{Π} with energy E_J.

Appendix C

The interplay between ALPs coupled to QCD and the QCD axions

In Section 5.1 we discussed the UV origin of nuclear interactions for generic axion-like-particle (ALP), arguing that they might descend from axion couplings to the QCD sector in the high-energy theory. Nevertheless, the solution of the strong-CP problem would remain an open issue. In principle, one can wonder how the picture changes when a solution of this problem, in the form of a QCD axion, is introduced in addition to the ALP. In this scenario, the Lagrangian in Eq. (5.2) would acquire an extra term

$$\mathcal{L} = \frac{g^2}{32\pi^2 f_a} \left(a_{\rm QCD} + c_g a\right) G^a_{\mu\nu} \tilde{G}^{a\mu\nu} + \frac{(m_{a,0})^2}{2} (a - a_0)^2 \,, \tag{C.1}$$

where we neglect the quark couplings for simplicity and have absorbed any possible difference between the two decay constants of $a_{\rm QCD}$ and a into c_g. We highlight that $a_{\rm QCD}$ does not have a bare mass term, as it would either be negligible or spoil the solution to the strong CP problem. However, after confinement, both axion and ALP gain a mass through non-perturbative QCD dynamics, leading to a non-diagonal mass matrix (Gavela et al., 2024)

$$\mathbf{M}^2 = m^2_{\rm QCD} \begin{pmatrix} 1 & c_g \\ c_g & c_g^2 + \frac{m^2_{a,0}}{m^2_{\rm QCD}} \end{pmatrix} \,, \tag{C.2}$$

where $m^2_{\rm QCD}$ is the QCD-induced mass. Therefore, the mass eigenvalues read

$$m^2_{1,2} = \frac{1}{2}\left(m^2_{a,0} + C_G^2\, m^2_{\rm QCD} \pm \Delta m^2\right)\,, \tag{C.3}$$

where we have defined

$$\begin{aligned} \Delta m^2 &= \sqrt{(m^2_{a,0} + C_G^2\, m^2_{\rm QCD})^2 - 4 m^2_{a,0}\, m^2_{\rm QCD}} \\ C_G^2 &= 1 + c_g^2\,. \end{aligned} \tag{C.4}$$

Remarkably, in the limit $m_{a,0} \gg m_{\rm QCD}$, which is the physical case considered in Section 5.1, the mass eigenvalues reduce to $m_1 \simeq m_{a,0}$ and $m_2 \simeq c_g^2 m_{\rm QCD}$. In the same way, the corresponding eigenstates

$$\begin{aligned} |a_1\rangle &= \begin{pmatrix} -\frac{m^2_{a,0}+(c_g^2-1)m^2_{\rm QCD}-\Delta m^2}{2c_g m^2_{\rm QCD}} \\ 1 \end{pmatrix} \to |a_{\rm QCD}\rangle = \begin{pmatrix} 1 \\ 0 \end{pmatrix} \\ |a_2\rangle &= \begin{pmatrix} -\frac{m^2_{a,0}+(c_g^2-1)m^2_{\rm QCD}+\Delta m^2}{2c_g m^2_{\rm QCD}} \\ 1 \end{pmatrix} \to |a\rangle = \begin{pmatrix} 0 \\ 1 \end{pmatrix}\,, \end{aligned} \tag{C.5}$$

where we have employed a proper normalization.
These results suggest that the large mass splitting, $m_{a,0} \gg m_{\rm QCD}$, leads to a negligible mixing between the two mass eigenstates, which are actually the eigenstates propagating in vacuum. Therefore, we can always look at the phenomenology of the ALP without referring to the QCD axion. Its existence might only strengthen the SN cooling bound, where the QCD axion is produced and escapes the SN core without giving observational signatures. Otherwise, it might be that the QCD axion is just weakly produced in the SN and, in this case, the cooling bound is unaffected.

The axion-ALP Lagrangian in Eq. (C.1) can be also written in terms of terms of

$$\begin{aligned} a_{G\tilde{G}} &= C_G^{-1}\,(a_{\rm QCD} + c_g\, a) \\ a_\perp &= C_G^{-1}\,(c_g\, a_{\rm QCD} - \, a)\,. \end{aligned} \tag{C.6}$$

It is worthy to highlight that, by employing this orthonormal basis, the only field coupling to the gluon field is $a_{G\tilde{G}}$. Thus, in this formalism, $a_{G\tilde{G}}$ plays the role of a "QCD ALP" as interaction eigenstate [1], while its orthogonal

[1] But only its $a_{\rm QCD}$ component solves the strong CP problem.

counterpart $a_\perp$ is decoupled from $G\tilde{G}$ and appears just in the mass term

$$\mathcal{L} = C_G \frac{g^2}{32\pi^2 f_a} a_{G\tilde{G}} G^a_{\mu\nu} \tilde{G}^{a\mu\nu} - \frac{1}{2} \frac{(m_{a,0})^2}{C_G^2} \left(c_g\, a_{G\tilde{G}} - a_\perp\right)^2 . \tag{C.7}$$

In terms of this basis, the mass matrix after the QCD phase transition reads

$$\mathbf{M}'^2 = \begin{pmatrix} C_G^2\, m_{\rm QCD}^2 + \frac{c_g^2\, m_{a,O}^2}{C_G^2} & -\frac{c_g\, m_{a,O}^2}{C_G^2} \\ -\frac{c_g\, m_{a,O}^2}{C_G^2} & -\frac{m_{a,O}^2}{C_G^2} \, . \end{pmatrix} , \tag{C.8}$$

showing, as expected, the same eigenvalues as in Eq. (C.3). The corresponding eigenstates in the $m_{a,0} \gg m_{\rm QCD}$ limit can be written as

$$\begin{aligned} |a_1'\rangle &= \begin{pmatrix} -\frac{(c_g^2-1)m_{a,0}^2 + C_G^2(C_G^2 m_{\rm QCD}^2 - \Delta m^2)}{2c_g m_{\rm QCD}^2} \\ 1 \end{pmatrix} \to |a_{\rm QCD}\rangle = C_G^{-1} \begin{pmatrix} 1 \\ c_g \end{pmatrix} \\ |a_2'\rangle &= \begin{pmatrix} -\frac{(c_g^2-1)m_{a,0}^2 + C_G^2(C_G^2 m_{\rm QCD}^2 + \Delta m^2)}{2c_g m_{\rm QCD}^2} \\ 1 \end{pmatrix} \to |a\rangle = C_G^{-1} \begin{pmatrix} c_g \\ -1 \end{pmatrix} , \end{aligned} \tag{C.9}$$

and the associated phenomenology reduces to the physics previously discussed. However, this formalism is useful, since it shows that a "QCD ALP" coupled to QCD only, with a non-diagonal mass term, has the same physical effects of a mixture of two axions: a massive ALP and a massless QCD axion.

The picture described by Eq. (C.7) is convenient to recast known results on the QCD axion, to our QCD ALP. Namely, the low-energy interactions between the ALP and hadrons will be described in terms of Eq. (5.2), with the replacement $c_g\, a \to C_G\, a_{G\tilde{G}}$. Similarly for the ALP-photon interaction.

Appendix D

Fitting parameters for axion emission spectra from CC SNe

In this Appendix we show the values of the fitting parameters employed to compute the ALP production spectra for the different SN models we used, computed for $g_{ap} = 5 \times 10^{-10}$ and $g_{an} = 0$ in the time interval $t_{\rm pb} \in [1,\, 8]$ s.

D.1 SFHo-s18.8

In Tab. D.1 we provide the values of the fitting parameters employed in Eq. (5.31) and Eq. (5.32) for our benchmark SN model SFHo-s18.8, described in Sec. 5.3.1. To extract the time-dependence of the ALP spectrum, the parameters in Tab. D.1 can be well interpolated by means of the following functional forms

$$\begin{aligned} E^0_{NN} &= \tilde{E}^0_{NN}\, t_{\rm s}^{0.755}\, e^{-0.413\, t_{\rm s}}\,, \\ \beta_{NN} &= \tilde{\beta}_{NN}\, t_{\rm s}^{0.0410}\, e^{-0.0542\, t_{\rm s}}\,, \\ A_{NN} &= \tilde{A}_{NN}\, t_{\rm s}^{1.865}\, e^{-1.345\, t_{\rm s}}\,, \end{aligned} \tag{D.1}$$

$$\begin{aligned} E^0_{\pi N} &= \tilde{E}^0_{\pi N}\, t_{\rm s}^{0.304}\, e^{-0.542\, t_{\rm s}}\,, \\ \beta_{\pi N} &= \tilde{\beta}_{\pi N}\, t_{\rm s}^{-0.503}\, e^{-0.019\, t_{\rm s}}\,, \\ A_{\pi N} &= \tilde{A}_{\pi N}\, t_{\rm s}^{5.975}\, e^{-4.944\, t_{\rm s}}\,, \\ \omega_{\pi N} &= \tilde{\omega}_{\pi N}\, (1 + 1.537\, t_{\rm s}^{0.050})\,, \end{aligned} \tag{D.2}$$

where $t_{\rm s} = t_{\rm pb}/1$ s. In particular, for NN bremsstrahlung $\tilde{E}^0_{NN} = 102.10$ MeV, $\tilde{\beta}_{NN} = 1.53$, $\tilde{A}_{NN} = 1.75 \times 10^{55}$ MeV^{-1} s^{-1}, while for pion conversion $\tilde{E}^0_{\pi N} = 218.59$ MeV, $\tilde{\beta}_{\pi N} = 1.27$, $\tilde{A}_{\pi N} = 3.88{\times}10^{56}$ MeV^{-1} s^{-1} and $\tilde{\omega}_c = 40.07$ MeV.

D.2 SFHo-s20

In Tab. D.2 we provide the values of the fitting parameters employed in Eq. (5.31) for the SN model SFHo-s20, described in Sec. 5.3.1. The time dependence for fitting parameters for this SN model can be extracted as

$$\begin{aligned} E^0_{NN} &= \tilde{E}^0_{NN}\, t_{\rm s}^{0.368}\, e^{-0.192\, t_{\rm s}}\,, \\ \beta_{NN} &= \tilde{\beta}_{NN}\, t_{\rm s}^{0.0531}\, e^{-0.0420\, t_{\rm s}}\,, \\ A_{NN} &= \tilde{A}_{NN}\, t_{\rm s}^{1.22}\, e^{-0.768\, t_{\rm s}}\,, \end{aligned} \tag{D.3}$$

where $\tilde{E}^0_{NN} = 101.29$ MeV, $\tilde{\beta}_{NN} = 1.53$, $\tilde{A}_{NN} = 4.13 \times 10^{55}$ MeV^{-1} s^{-1}.

D.3 LS220-s20

In Tab. D.3 we provide the values of the fitting parameters in Eq. (5.31) for the SN model LS220-s20, employed in Sec. 5.3.1. Analogously to the previous cases, the analytic formulas interpolating the time-behavior of the fitting parameters are

$$\begin{aligned} E^0_{NN} &= \tilde{E}^0_{NN}\, t_{\rm s}^{-0.089}\, e^{-0.068\, t_{\rm s}}\,, \\ \beta_{NN} &= \tilde{\beta}_{NN}\, t_{\rm s}^{0.073}\, e^{-0.037\, t_{\rm s}}\,, \\ A_{NN} &= \tilde{A}_{NN}\, t_{\rm s}^{0.596}\, e^{-0.693\, t_{\rm s}}\,, \end{aligned} \tag{D.4}$$

in which $\tilde{E}^0_{NN} = 83.55$ MeV, $\tilde{\beta}_{NN} = 1.55$, $\tilde{A}_{NN} = 4.46 \times 10^{55}$ MeV^{-1} s^{-1}.

$t_{\rm pb}$ [s]	E^0_{NN} [MeV]	β_{NN}	A_{NN} [MeV^{-1} s^{-1}]
1	70.19	1.44	4.56×10^{54}
2	70.39	1.42	4.31×10^{54}
3	56.91	1.36	2.41×10^{54}
4	58.36	1.31	1.10×10^{54}
5	47.41	1.24	3.95×10^{53}
6	35.02	1.17	1.04×10^{53}
7	23.98	1.12	2.20×10^{52}
8	16.10	1.10	4.01×10^{51}

$t_{\rm pb}$ [s]	$E^0_{\pi N}$ [MeV]	$\beta_{\pi N}$	$A_{\pi N}$ [MeV^{-1} s^{-1}]	ω_c [MeV]
1	126.43	1.20	2.77×10^{54}	103.27
2	94.47	1.03	1.24×10^{54}	98.87
3	56.14	0.54	9.78×10^{52}	107.00
4	37.20	0.65	2.20×10^{52}	107.06
5	25.02	0.47	3.63×10^{51}	108.59
6	15.62	0.40	2.53×10^{50}	108.04
7	9.18	0.37	3.10×10^{48}	108.33
8	5.64	0.37	6.64×10^{45}	108.37

Table D.1: Fitting parameters for NN bremsstrahlung and pion conversion emission spectra in Eq. (5.31) and Eq. (5.32). These values refer to our benchmark SN model SFHo-s18.8. The time interval considered is $t_{\rm pb} \in [1, 8]$ s with time steps of 1 s. For the considered case, we have set the ALP-proton coupling to $g_{ap} = 5 \times 10^{-10}$.

$t_{\rm pb}$ [s]	E^0_{NN} [MeV]	β_{NN}	A_{NN} [MeV^{-1} s^{-1}]
1	86.42	1.46	1.93×10^{55}
2	85.28	1.45	2.03×10^{55}
3	82.22	1.43	1.58×10^{55}
4	78.10	1.39	1.06×10^{55}
5	72.56	1.35	6.53×10^{54}
6	65.74	1.31	3.59×10^{54}
7	57.54	1.26	1.74×10^{54}
8	48.14	1.22	7.22×10^{53}

Table D.2: Fitting parameters for NN bremsstrahlung spectrum in Eq. (5.31). These values refer to the SFHo-s20 SN model. The considered time interval is $t_{\rm pb} \in [1, 8]$ s with time steps of 1 s. For the considered case, we have set the ALP-proton coupling to $g_{ap} = 5 \times 10^{-10}$.

$t_{\rm pb}$ [s]	E^0_{NN} [MeV]	β_{NN}	A_{NN} [MeV^{-1} s^{-1}]
1	77.46	1.5	2.22×10^{55}
2	69.52	1.51	1.71×10^{55}
3	62.60	1.51	1.07×10^{55}
4	55.89	1.49	5.97×10^{54}
5	50.39	1.47	3.45×10^{54}
6	46.43	1.42	2.21×10^{54}
7	43.34	1.39	1.47×10^{54}
8	40.37	1.35	9.64×10^{53}

Table D.3: Fitting parameters for NN bremsstrahlung spectrum in Eq. (5.31). These values refer to the LS220-s20 SN model. The considered time interval is $t_{\rm pb} \in [1, 8]$ s with time steps of 1 s. For the considered case, we have set the ALP-proton coupling to $g_{ap} = 5 \times 10^{-10}$.

Bibliography

't Hooft, Gerard (1976a). "Computation of the Quantum Effects Due to a Four-Dimensional Pseudoparticle". In: *Phys. Rev. D* 14. Ed. by Mikhail A. Shifman. [Erratum: Phys.Rev.D 18, 2199 (1978)], pp. 3432–3450. DOI: 10.1103/PhysRevD.14.3432.

— (1976b). "Symmetry Breaking Through Bell-Jackiw Anomalies". In: *Phys. Rev. Lett.* 37. Ed. by Mikhail A. Shifman, pp. 8–11. DOI: 10.1103/PhysRevLett.37.8.

Aaboud, Morad et al. (2016). "Search for resonances in diphoton events at $\sqrt{s}$=13 TeV with the ATLAS detector". In: *JHEP* 09, p. 001. DOI: 10.1007/JHEP09(2016)001. arXiv: 1606.03833 [hep-ex].

Aad, Georges et al. (2016). "Search for new phenomena in events with at least three photons collected in pp collisions at $\sqrt{s} = 8$ TeV with the ATLAS detector". In: *Eur. Phys. J. C* 76.4, p. 210. DOI: 10.1140/epjc/s10052-016-4034-8. arXiv: 1509.05051 [hep-ex].

— (2021). "Measurement of light-by-light scattering and search for axion-like particles with 2.2 nb^{-1} of Pb+Pb data with the ATLAS detector". In: *JHEP* 03. [Erratum: JHEP 11, 050 (2021)], p. 243. DOI: 10.1007/JHEP11(2021)050. arXiv: 2008.05355 [hep-ex].

Aartsen, M. G. et al. (2017). "The IceCube Neutrino Observatory: Instrumentation and Online Systems". In: *JINST* 12.03. [Erratum: JINST 19, E05001 (2024)], P03012. DOI: 10.1088/1748-0221/12/03/P03012. arXiv: 1612.05093 [astro-ph.IM].

Aasi, J. et al. (2015). "Advanced LIGO". In: *Class. Quant. Grav.* 32, p. 074001. DOI: 10.1088/0264-9381/32/7/074001. arXiv: 1411.4547 [gr-qc].

Abbott, B. P. et al. (2016). "Observation of Gravitational Waves from a Binary Black Hole Merger". In: *Phys. Rev. Lett.* 116.6, p. 061102. DOI: 10.1103/PhysRevLett.116.061102. arXiv: 1602.03837 [gr-qc].

Abbott, B. P. et al. (2017a). "GW170817: Observation of Gravitational Waves from a Binary Neutron Star Inspiral". In: *Phys. Rev. Lett.* 119.16, p. 161101. DOI: 10.1103/PhysRevLett.119.161101. arXiv: 1710.05832 [gr-qc].

Abbott, Benjamin P et al. (2017b). "Exploring the Sensitivity of Next Generation Gravitational Wave Detectors". In: *Class. Quant. Grav.* 34.4, p. 044001. DOI: 10.1088/1361-6382/aa51f4. arXiv: 1607.08697 [astro-ph.IM].

Abbott, L. F. and P. Sikivie (1983). "A Cosmological Bound on the Invisible Axion". In: *Phys. Lett. B* 120. Ed. by M. A. Srednicki, pp. 133–136. DOI: 10.1016/0370-2693(83)90638-X.

Abdikamalov, Ernazar, Giulia Pagliaroli, and David Radice (Oct. 2020). "Gravitational Waves from Core-Collapse Supernovae". In: DOI: 10.1007/978-981-15-4702-7_21-1. arXiv: 2010.04356 [astro-ph.SR].

— (2022). "Gravitational waves from core-collapse supernovae". In: *Handbook of gravitational wave astronomy*. Springer, pp. 909–945.

Abe, K. et al. (May 2018). "Hyper-Kamiokande Design Report". In: arXiv: 1805.04163 [physics.ins-det].

Abe, Seisho et al. (2024). "Combined Pre-supernova Alert System with KamLAND and Super-Kamiokande". In: *Astrophys. J.* 973.2, p. 140. DOI: 10.3847/1538-4357/ad5fee. arXiv: 2404.09920 [hep-ex].

Abel, C. et al. (2020). "Measurement of the Permanent Electric Dipole Moment of the Neutron". In: *Phys. Rev. Lett.* 124.8, p. 081803. DOI: 10.1103/PhysRevLett.124.081803. arXiv: 2001.11966 [hep-ex].

Abeln, A. et al. (2021). "Conceptual design of BabyIAXO, the intermediate stage towards the International Axion Observatory". In: *JHEP* 05, p. 137. DOI: 10.1007/JHEP05(2021)137. arXiv: 2010.12076 [physics.ins-det].

Abudinén, F. et al. (2020). "Search for Axion-Like Particles produced in e^+e^- collisions at Belle II". In: *Phys. Rev. Lett.* 125.16, p. 161806. DOI: 10.1103/PhysRevLett.125.161806. arXiv: 2007.13071 [hep-ex].

Adam, R. et al. (2016). "Planck intermediate results.: XLII. Large-scale Galactic magnetic fields". In: *Astron. Astrophys.* 596, A103. DOI: 10.1051/0004-6361/201528033. arXiv: 1601.00546 [astro-ph.GA].

Adams, Scott M. et al. (2013). "Observing the Next Galactic Supernova". In: *Astrophys. J.* 778, p. 164. DOI: 10.1088/0004-637X/778/2/164. arXiv: 1306.0559 [astro-ph.HE].

Adelberger, E. G., Blayne R. Heckel, and A. E. Nelson (2003). "Tests of the gravitational inverse square law". In: *Ann. Rev. Nucl. Part. Sci.* 53,

pp. 77–121. DOI: 10.1146/annurev.nucl.53.041002.110503. arXiv: hep-ph/0307284.

Adler, Stephen L. (1969). "Axial vector vertex in spinor electrodynamics". In: *Phys. Rev.* 177, pp. 2426–2438. DOI: 10.1103/PhysRev.177.2426.

Afle, Chaitanya et al. (2023). "Measuring the properties of f-mode oscillations of a protoneutron star by third-generation gravitational-wave detectors". In: *Phys. Rev. D* 107.12, p. 123005. DOI: 10.1103/PhysRevD.107.123005. arXiv: 2304.04283 [astro-ph.IM].

Al Kharusi, S. et al. (2021). "SNEWS 2.0: a next-generation supernova early warning system for multi-messenger astronomy". In: *New J. Phys.* 23.3, p. 031201. DOI: 10.1088/1367-2630/abde33. arXiv: 2011.00035 [astro-ph.HE].

Alekseev, E. N. et al. (1987). "Possible Detection of a Neutrino Signal on 23 February 1987 at the Baksan Underground Scintillation Telescope of the Institute of Nuclear Research". In: *JETP Lett.* 45. Ed. by J. Tran Thanh Van, pp. 589–592.

Altenmüller, K. et al. (2024). "New Upper Limit on the Axion-Photon Coupling with an Extended CAST Run with a Xe-Based Micromegas Detector". In: *Phys. Rev. Lett.* 133.22, p. 221005. DOI: 10.1103/PhysRevLett.133.221005. arXiv: 2406.16840 [hep-ex].

Altmann, M. et al. (1995). "Search for the electron positron decay of axions and axion - like particles at a nuclear power reactor at Bugey". In: *Z. Phys. C* 68, pp. 221–227. DOI: 10.1007/BF01566670.

Anastassopoulos, V. et al. (2017). "New CAST Limit on the Axion-Photon Interaction". In: *Nature Phys.* 13, pp. 584–590. DOI: 10.1038/nphys4109. arXiv: 1705.02290 [hep-ex].

Andersen, Oliver Eggenberger et al. (2021). "Equation-of-state Dependence of Gravitational Waves in Core-collapse Supernovae". In: *Astrophys. J.* 923.2, p. 201. DOI: 10.3847/1538-4357/ac294c. arXiv: 2106.09734 [astro-ph.HE].

Andresen, H., R. Glas, and H. Th. Janka (2021). "Gravitational-wave signals from 3D supernova simulations with different neutrino-transport methods". In: *Mon. Not. Roy. Astron. Soc.* 503.3, pp. 3552–3567. DOI: 10.1093/mnras/stab675. arXiv: 2011.10499 [astro-ph.HE].

Andresen, H., Bernhard Müller, Ewald Müller, et al. (2017). "Gravitational Wave Signals from 3D Neutrino Hydrodynamics Simulations of Core-

Collapse Supernovae". In: *Mon. Not. Roy. Astron. Soc.* 468.2, pp. 2032–2051. DOI: 10.1093/mnras/stx618. arXiv: 1607.05199 [astro-ph.HE].

Andresen, H., E. Müller, H. Th. Janka, et al. (2019). "Gravitational waves from 3D core-collapse supernova models: The impact of moderate progenitor rotation". In: *Mon. Not. Roy. Astron. Soc.* 486.2, pp. 2238–2253. DOI: 10.1093/mnras/stz990. arXiv: 1810.07638 [astro-ph.HE].

Anselm, A. A. (1985). "Arion $\leftrightarrow$ Photon Oscillations in a Steady Magnetic Field. (In Russian)". In: *Yad. Fiz.* 42, pp. 1480–1483.

Anselm, Alexei A. (1988). "Experimental Test for Arion <—> Photon Oscillations in a Homogeneous Constant Magnetic Field". In: *Phys. Rev. D* 37, p. 2001. DOI: 10.1103/PhysRevD.37.2001.

Antypas, D. et al. (Mar. 2022). "New Horizons: Scalar and Vector Ultralight Dark Matter". In: arXiv: 2203.14915 [hep-ex].

Archidiacono, Maria et al. (2015). "Future cosmological sensitivity for hot dark matter axions". In: *JCAP* 05, p. 050. DOI: 10.1088/1475-7516/2015/05/050. arXiv: 1502.03325 [astro-ph.CO].

Arias, Paola et al. (2012). "WISPy Cold Dark Matter". In: *JCAP* 06, p. 013. DOI: 10.1088/1475-7516/2012/06/013. arXiv: 1201.5902 [hep-ph].

Arik, M. et al. (2014). "Search for Solar Axions by the CERN Axion Solar Telescope with ^{3}He Buffer Gas: Closing the Hot Dark Matter Gap". In: *Phys. Rev. Lett.* 112.9, p. 091302. DOI: 10.1103/PhysRevLett.112.091302. arXiv: 1307.1985 [hep-ex].

Arkani-Hamed, Nima et al. (2000). "Solving the hierarchy problem with exponentially large dimensions". In: *Phys. Rev. D* 62, p. 105002. DOI: 10.1103/PhysRevD.62.105002. arXiv: hep-ph/9912453.

Armengaud, E. et al. (2019). "Physics potential of the International Axion Observatory (IAXO)". In: *JCAP* 06, p. 047. DOI: 10.1088/1475-7516/2019/06/047. arXiv: 1904.09155 [hep-ph].

Arvanitaki, Asimina, Savas Dimopoulos, Sergei Dubovsky, et al. (2010). "String Axiverse". In: *Phys. Rev. D* 81, p. 123530. DOI: 10.1103/PhysRevD.81.123530. arXiv: 0905.4720 [hep-th].

Arvanitaki, Asimina, Savas Dimopoulos, and Ken Van Tilburg (2018). "Resonant absorption of bosonic dark matter in molecules". In: *Phys. Rev. X* 8.4, p. 041001. DOI: 10.1103/PhysRevX.8.041001. arXiv: 1709.05354 [hep-ph].

Asakura, K. et al. (2016). "KamLAND Sensitivity to Neutrinos from Pre-Supernova Stars". In: *Astrophys. J.* 818.1, p. 91. DOI: 10.3847/0004-637X/818/1/91. arXiv: 1506.01175 [astro-ph.HE].

Ashenfelter, J. et al. (2019). "The PROSPECT Reactor Antineutrino Experiment". In: *Nucl. Instrum. Meth. A* 922, pp. 287–309. DOI: 10.1016/j.nima.2018.12.079. arXiv: 1808.00097 [physics.ins-det].

Asztalos, S. J. et al. (2004). "An Improved RF cavity search for halo axions". In: *Phys. Rev. D* 69, p. 011101. DOI: 10.1103/PhysRevD.69.011101. arXiv: astro-ph/0310042.

Ayala, Adrian et al. (2014). "Revisiting the bound on axion-photon coupling from Globular Clusters". In: *Phys. Rev. Lett.* 113.19, p. 191302. DOI: 10.1103/PhysRevLett.113.191302. arXiv: 1406.6053 [astro-ph.SR].

Balaji, Shyam et al. (2025). "In-flight positron annihilation as a probe of feebly interacting particles". In: *Phys. Rev. D* 111.8, p. 083053. DOI: 10.1103/PhysRevD.111.083053. arXiv: 2501.07725 [hep-ph].

Ballou, Rafik et al. (2014). "Latest Results of the OSQAR Photon Regeneration Experiment for Axion-Like Particle Search". In: *10th Patras Workshop on Axions, WIMPs and WISPs*, pp. 125–130. DOI: 10.3204/DESY-PROC-2014-03/pugnat_pierre. arXiv: 1410.2566 [hep-ex].

Banerjee, D. et al. (2020). "Search for Axionlike and Scalar Particles with the NA64 Experiment". In: *Phys. Rev. Lett.* 125.8, p. 081801. DOI: 10.1103/PhysRevLett.125.081801. arXiv: 2005.02710 [hep-ex].

Banishev, A. A. et al. (2013). "Demonstration of Angle Dependent Casimir Force Between Corrugations". In: *Phys. Rev. Lett.* 110.25, p. 250403. DOI: 10.1103/PhysRevLett.110.250403. arXiv: 1212.6271 [quant-ph].

— (2014). "Experimental and theoretical investigation of the angular dependence of the Casimir force between sinusoidally corrugated surfaces". In: *Phys. Rev. B* 89.23, p. 235436. DOI: 10.1103/PhysRevB.89.235436. arXiv: 1402.2716 [quant-ph].

Bardeen, William A. (1969). "Anomalous Ward identities in spinor field theories". In: *Phys. Rev.* 184, pp. 1848–1857. DOI: 10.1103/PhysRev.184.1848.

Barr, Stephen M. (1984). "Solving the Strong CP Problem Without the Peccei-Quinn Symmetry". In: *Phys. Rev. Lett.* 53, p. 329. DOI: 10.1103/PhysRevLett.53.329.

Bartram, C. et al. (2021a). "Axion dark matter experiment: Run 1B analysis details". In: *Phys. Rev. D* 103.3, p. 032002. DOI: 10.1103/PhysRevD.103.032002. arXiv: 2010.06183 [astro-ph.CO].

— (2021b). "Search for Invisible Axion Dark Matter in the 3.3–4.2 μeV Mass Range". In: *Phys. Rev. Lett.* 127.26, p. 261803. DOI: 10.1103/PhysRevLett.127.261803. arXiv: 2110.06096 [hep-ex].

Baryakhtar, Masha, Junwu Huang, and Robert Lasenby (2018). "Axion and hidden photon dark matter detection with multilayer optical haloscopes". In: *Phys. Rev. D* 98.3, p. 035006. DOI: 10.1103/PhysRevD.98.035006. arXiv: 1803.11455 [hep-ph].

Basak, S. et al. (2015). "Electromagnetic effects on the light hadron spectrum". In: *J. Phys. Conf. Ser.* 640.1. Ed. by Anders Sandvik et al., p. 012052. DOI: 10.1088/1742-6596/640/1/012052. arXiv: 1510.04997 [hep-lat].

Bauer, Martin, Matthias Neubert, Sophie Renner, et al. (2021). "The Low-Energy Effective Theory of Axions and ALPs". In: *JHEP* 04, p. 063. DOI: 10.1007/JHEP04(2021)063. arXiv: 2012.12272 [hep-ph].

— (2022). "Flavor probes of axion-like particles". In: *JHEP* 09, p. 056. DOI: 10.1007/JHEP09(2022)056. arXiv: 2110.10698 [hep-ph].

Bauer, Martin, Matthias Neubert, and Andrea Thamm (2017). "Collider Probes of Axion-Like Particles". In: *JHEP* 12, p. 044. DOI: 10.1007/JHEP12(2017)044. arXiv: 1708.00443 [hep-ph].

Baumann, Daniel, Daniel Green, and Benjamin Wallisch (2016). "New Target for Cosmic Axion Searches". In: *Phys. Rev. Lett.* 117.17, p. 171301. DOI: 10.1103/PhysRevLett.117.171301. arXiv: 1604.08614 [astro-ph.CO].

Beacom, John F. (2010). "The Diffuse Supernova Neutrino Background". In: *Ann. Rev. Nucl. Part. Sci.* 60, pp. 439–462. DOI: 10.1146/annurev.nucl.010909.083331. arXiv: 1004.3311 [astro-ph.HE].

Beacom, John F. and Hasan Yuksel (2006). "Stringent constraint on galactic positron production". In: *Phys. Rev. Lett.* 97, p. 071102. DOI: 10.1103/PhysRevLett.97.071102. arXiv: astro-ph/0512411.

Beg, M. A. B. and H. -S. Tsao (1978). "Strong P, T Noninvariances in a Superweak Theory". In: *Phys. Rev. Lett.* 41, p. 278. DOI: 10.1103/PhysRevLett.41.278.

Bell, J. S. and R. Jackiw (1969). "A PCAC puzzle: $\pi^0 \to \gamma\gamma$ in the σ model". In: *Nuovo Cim. A* 60, pp. 47–61. DOI: 10.1007/BF02823296.

Bellazzini, Brando et al. (2017). "R-axion at colliders". In: *Phys. Rev. Lett.* 119.14, p. 141804. DOI: 10.1103/PhysRevLett.119.141804. arXiv: 1702.02152 [hep-ph].

Benabou, Joshua N., Quentin Bonnefoy, et al. (2024). "Cosmological dynamics of string theory axion strings". In: *Phys. Rev. D* 110.3, p. 035021. DOI: 10.1103/PhysRevD.110.035021. arXiv: 2312.08425 [hep-ph].

Benabou, Joshua N., Claudio Andrea Manzari, et al. (2025). "Time-delayed gamma-ray signatures of heavy axions from core-collapse supernovae". In: *Phys. Rev. D* 111.9, p. 095029. DOI: 10.1103/PhysRevD.111.095029. arXiv: 2412.13247 [hep-ph].

Benz, Willy and Friedrich-Karl Thielemann (1990). "Convective instabilities in SN 1987A". In: *Astrophysical Journal, Part 2-Letters (ISSN 0004-637X), vol. 348, Jan. 1, 1990, p. L17-L20. Research supported by NSF, SNSF, and William F. Milton Fund.* 348, pp. L17–L20.

Bergé, Joel, Philippe Brax, et al. (2018). "MICROSCOPE Mission: First Constraints on the Violation of the Weak Equivalence Principle by a Light Scalar Dilaton". In: *Phys. Rev. Lett.* 120.14, p. 141101. DOI: 10.1103/PhysRevLett.120.141101. arXiv: 1712.00483 [gr-qc].

Bergé, Joel, Martin Pernot-Borràs, et al. (2022). "MICROSCOPE's constraint on a short-range fifth force". In: *Class. Quant. Grav.* 39.20, p. 204010. DOI: 10.1088/1361-6382/abe142. arXiv: 2102.00022 [gr-qc].

Berger, J. F., M. Girod, and D. Gogny (1991). "Time-dependent quantum collective dynamics applied to nuclear fission". In: *Comp. Phys. Commun.* 63, p. 365.

Bertolini, Stefano, Luca Di Luzio, and Fabrizio Nesti (June 2020). "Axion-mediated forces and CP violation in left-right models". In: arXiv: 2006.12508 [hep-ph].

Bethe, H. A. (1990). "Supernova mechanisms". In: *Rev. Mod. Phys.* 62, pp. 801–866. DOI: 10.1103/RevModPhys.62.801.

Bethe, H. A., G. E. Brown, J. Applegate, et al. (1979). "Equation of state in the gravitational collapse of stars". In: *Nucl. Phys. A* 324, pp. 487–533. DOI: 10.1016/0375-9474(79)90596-7.

Bethe, H. A., G. E. Brown, J. Cooperstein, et al. (1983). "A simplified equation of state near nuclear density". In: *Nucl. Phys. A* 403, pp. 625–648. DOI: 10.1016/0375-9474(83)90626-7.

Bethe, Hans A. and James R. Wilson (1985). "Revival of a stalled supernova shock by neutrino heating". In: *Astrophys. J.* 295, pp. 14–23. DOI: 10.1086/163343.

Bezerra, V. B. et al. (2010). "Advance and prospects in constraining the Yukawa-type corrections to Newtonian gravity from the Casimir effect". In: *Phys. Rev. D* 81, p. 055003. DOI: 10.1103/PhysRevD.81.055003. arXiv: 1002.2141 [hep-th].

Beznogov, Mikhail V. et al. (2018). "Constraints on Axion-like Particles and Nucleon Pairing in Dense Matter from the Hot Neutron Star in HESS J1731-347". In: *Phys. Rev. C* 98.3, p. 035802. DOI: 10.1103/PhysRevC.98.035802. arXiv: 1806.07991 [astro-ph.HE].

Bhusal, Aagaman, Nick Houston, and Tianjun Li (2021). "Searching for Solar Axions Using Data from the Sudbury Neutrino Observatory". In: *Phys. Rev. Lett.* 126.9, p. 091601. DOI: 10.1103/PhysRevLett.126.091601. arXiv: 2004.02733 [hep-ph].

Bibber, K van et al. (Apr. 1989). "Design for a practical laboratory detector for solar axions". In: *Physical Review D* 39.8, pp. 2089–2099. ISSN: 0556-2821. DOI: 10.1103/PhysRevD.39.2089.

Bigazzi, Francesco et al. (2020). "Non-derivative Axionic Couplings to Nucleons at large and small N". In: *JHEP* 01, p. 100. DOI: 10.1007/JHEP01(2020)100. arXiv: 1906.12132 [hep-ph].

Bionta, R. M. et al. (1987). "Observation of a Neutrino Burst in Coincidence with Supernova SN 1987a in the Large Magellanic Cloud". In: *Phys. Rev. Lett.* 58, p. 1494. DOI: 10.1103/PhysRevLett.58.1494.

Bjorken, J. D., S. Ecklund, et al. (1988). "Search for Neutral Metastable Penetrating Particles Produced in the SLAC Beam Dump". In: *Phys. Rev. D* 38, p. 3375. DOI: 10.1103/PhysRevD.38.3375.

Bjorken, J.D. and S.D. Drell (1965). *Relativistic Quantum Fields*. International series in pure and applied physics. McGraw-Hill. ISBN: 9780700549405. URL: https://books.google.it/books?id=ZczvAAAAMAAJ.

Blakemore, Charles P. et al. (2021). "Search for non-Newtonian interactions at micrometer scale with a levitated test mass". In: *Phys. Rev. D* 104.6, p. L061101. DOI: 10.1103/PhysRevD.104.L061101. arXiv: 2102.06848 [hep-ex].

Bloch, Itay M., Yonit Hochberg, et al. (2020). "Axion-like Relics: New Constraints from Old Comagnetometer Data". In: *JHEP* 01, p. 167. DOI: 10.1007/JHEP01(2020)167. arXiv: 1907.03767 [hep-ph].

Bloch, Itay M., Gil Ronen, et al. (2022). "New constraints on axion-like dark matter using a Floquet quantum detector". In: *Sci. Adv.* 8.5, abl8919. DOI: 10.1126/sciadv.abl8919. arXiv: 2105.04603 [hep-ph].

Blondin, John M., Anthony Mezzacappa, and Christine DeMarino (2003). "Stability of standing accretion shocks, with an eye toward core collapse supernovae". In: *Astrophys. J.* 584, pp. 971–980. DOI: 10.1086/345812. arXiv: astro-ph/0210634.

Blondin, John M. and Samantha Shaw (2007). "Linear growth of spiral SASI modes in core-collapse supernovae". In: *Astrophys. J.* 656, pp. 366–371. DOI: 10.1086/510614. arXiv: astro-ph/0611698.

Blumlein, J. et al. (1992). "Limits on the mass of light (pseudo)scalar particles from Bethe-Heitler e+ e- and mu+ mu- pair production in a proton - iron beam dump experiment". In: *Int. J. Mod. Phys. A* 7, pp. 3835–3850. DOI: 10.1142/S0217751X9200171X.

Bogorad, Zachary, Peter W. Graham, and Giorgio Gratta (2023). "Detecting nanometer-scale new forces with coherent neutron scattering". In: *Phys. Rev. D* 108.5, p. 055005. DOI: 10.1103/PhysRevD.108.055005. arXiv: 2303.17744 [hep-ph].

Bollig, R., H. -T. Janka, et al. (Dec. 2017). "Muon Creation in Supernova Matter Facilitates Neutrino-Driven Explosions". In: *Phys. Rev. Lett.* 119.24, 242702, p. 242702. DOI: 10.1103/PhysRevLett.119.242702. arXiv: 1706.04630 [astro-ph.HE].

Bollig, Robert, William DeRocco, et al. (2020). "Muons in Supernovae: Implications for the Axion-Muon Coupling". In: *Phys. Rev. Lett.* 125.5. [Erratum: Phys.Rev.Lett. 126, 189901 (2021)], p. 051104. DOI: 10.1103/PhysRevLett.125.051104. arXiv: 2005.07141 [hep-ph].

Bollig, Robert, Naveen Yadav, et al. (2021). "Self-consistent 3D Supernova Models From −7 Minutes to +7 s: A 1-bethe Explosion of a ∼19 $M_\odot$ Progenitor". In: *Astrophys. J.* 915.1, p. 28. DOI: 10.3847/1538-4357/abf82e. arXiv: 2010.10506 [astro-ph.HE].

Borsanyi, Sz. et al. (2016). "Calculation of the axion mass based on high-temperature lattice quantum chromodynamics". In: *Nature* 539.7627, pp. 69–71. DOI: 10.1038/nature20115. arXiv: 1606.07494 [hep-lat].

Bottaro, Salvatore, Andrea Caputo, and Damiano F. G. Fiorillo (2024). "Neutrino emission in cold neutron stars: Bremsstrahlung and modified urca rates reexamined". In: *JCAP* 11, p. 015. DOI: 10.1088/1475-7516/2024/11/015. arXiv: 2406.18640 [hep-ph].

Bottaro, Salvatore, Andrea Caputo, Georg Raffelt, et al. (2023). "Stellar limits on scalars from electron-nucleus bremsstrahlung". In: *JCAP* 07, p. 071. DOI: 10.1088/1475-7516/2023/07/071. arXiv: 2303.00778 [hep-ph].

Bouchet, Laurent et al. (2010). "On the morphology of the electron-positron annihilation emission as seen by SPI/INTEGRAL". In: *Astrophys. J.* 720, pp. 1772–1780. DOI: 10.1088/0004-637X/720/2/1772. arXiv: 1007.4753 [astro-ph.HE].

Bradley, R. et al. (2003). "Microwave cavity searches for dark-matter axions". In: *Rev. Mod. Phys.* 75, pp. 777–817. DOI: 10.1103/RevModPhys.75.777.

Braginsky, Vladimir B. and Kip S. Thorne (1987a). "Gravitational-wave bursts with memory and experimental prospects". In: *Nature* 327, pp. 123–125. DOI: 10.1038/327123a0.

— (1987b). "Gravitational-wave bursts with memory and experimental prospects". In: *Nature* 327.6118, pp. 123–125. DOI: 10.1038/327123a0. URL: https://doi.org/10.1038/327123a0.

Braine, T. et al. (2020). "Extended Search for the Invisible Axion with the Axion Dark Matter Experiment". In: *Phys. Rev. Lett.* 124.10, p. 101303. DOI: 10.1103/PhysRevLett.124.101303. arXiv: 1910.08638 [hep-ex].

Branco, G. C. et al. (2012). "Theory and phenomenology of two-Higgs-doublet models". In: *Phys. Rept.* 516, pp. 1–102. DOI: 10.1016/j.physrep.2012.02.002. arXiv: 1106.0034 [hep-ph].

Bratton, C. B. et al. (1988). "Angular Distribution of Events From Sn1987a". In: *Phys. Rev. D* 37, p. 3361. DOI: 10.1103/PhysRevD.37.3361.

Brinkmann, Ralf Peter and Michael S. Turner (1988). "Numerical Rates for Nucleon-Nucleon Axion Bremsstrahlung". In: *Phys. Rev. D* 38, p. 2338. DOI: 10.1103/PhysRevD.38.2338.

Brockway, Jack W. et al. (1996). "SN1987A gamma-ray limits on the conversion of pseudoscalars". In: *Phys. Lett. B* 383, pp. 439–443. DOI: 10.1016/0370-2693(96)00778-2. arXiv: astro-ph/9605197.

Brouwer, L. et al. (2022a). "Projected sensitivity of DMRadio-m3: A search for the QCD axion below 1 μeV". In: *Phys. Rev. D* 106.10, p. 103008. DOI: 10.1103/PhysRevD.106.103008. arXiv: 2204.13781 [hep-ex].

Brouwer, L. et al. (2022b). "Proposal for a definitive search for GUT-scale QCD axions". In: *Phys. Rev. D* 106.11, p. 112003. DOI: 10.1103/PhysRevD.106.112003. arXiv: 2203.11246 [hep-ex].

Bruel, Tristan et al. (2023). "Inference of protoneutron star properties in core-collapse supernovae from a gravitational-wave detector network". In: *Phys. Rev. D* 107.8, p. 083029. DOI: 10.1103/PhysRevD.107.083029. arXiv: 2301.10019 [astro-ph.HE].

Brun, P. et al. (2019). "A new experimental approach to probe QCD axion dark matter in the mass range above 40 μeV". In: *Eur. Phys. J. C* 79.3, p. 186. DOI: 10.1140/epjc/s10052-019-6683-x. arXiv: 1901.07401 [physics.ins-det].

Budker, Dmitry et al. (2014). "Proposal for a Cosmic Axion Spin Precession Experiment (CASPEr)". In: *Phys. Rev. X* 4.2, p. 021030. DOI: 10.1103/PhysRevX.4.021030. arXiv: 1306.6089 [hep-ph].

Buras, Robert et al. (2006). "Two-dimensional hydrodynamic core-collapse supernova simulations with spectral neutrino transport. 1. Numerical method and results for a 15 solar mass star". In: *Astron. Astrophys.* 447, pp. 1049–1092. DOI: 10.1051/0004-6361:20053783. arXiv: astro-ph/0507135.

Burrows, A. (1990). "Neutrinos From Supernova Explosions". In: *Ann. Rev. Nucl. Part. Sci.* 40, pp. 181–212. DOI: 10.1146/annurev.ns.40.120190.001145.

Burrows, Adam et al. (1989). "Axions and SN 1987a". In: *Phys. Rev. D* 39, p. 1020. DOI: 10.1103/PhysRevD.39.1020.

— (1990). "Axions and SN1987A: Axion trapping". In: *Phys. Rev. D* 42, pp. 3297–3309. DOI: 10.1103/PhysRevD.42.3297.

Burrows, Adam and J. Goshy (1993). "A Theory of supernova explosions". In: *Astrophys. J. Lett.* 416, pp. L75–L78. DOI: 10.1086/187074.

Burrows, Adam and John Hayes (1996). "Pulsar recoil and gravitational radiation due to asymmetrical stellar collapse and explosion". In: *Phys. Rev. Lett.* 76, pp. 352–355. DOI: 10.1103/PhysRevLett.76.352. arXiv: astro-ph/9511106.

Burrows, Adam, John Hayes, and Bruce A. Fryxell (1995). "On the nature of core collapse supernova explosions". In: *Astrophys. J.* 450, p. 830. DOI: 10.1086/176188. arXiv: astro-ph/9506061.

Burrows, Adam and David Vartanyan (2021). "Core-Collapse Supernova Explosion Theory". In: *Nature* 589.7840, pp. 29–39. DOI: 10.1038/s41586-020-03059-w. arXiv: 2009.14157 [astro-ph.SR].

Buschmann, Malte et al. (2022). "Upper Limit on the QCD Axion Mass from Isolated Neutron Star Cooling". In: *Phys. Rev. Lett.* 128.9, p. 091102. DOI: 10.1103/PhysRevLett.128.091102. arXiv: 2111.09892 [hep-ph].

Cadamuro, Davide et al. (2011). "Cosmological bounds on sub-MeV mass axions". In: *JCAP* 02, p. 003. DOI: 10.1088/1475-7516/2011/02/003. arXiv: 1011.3694 [hep-ph].

Cadamuro, Davide and Javier Redondo (2012). "Cosmological bounds on pseudo Nambu-Goldstone bosons". In: *JCAP* 02, p. 032. DOI: 10.1088/1475-7516/2012/02/032. arXiv: 1110.2895 [hep-ph].

Caldwell, Allen et al. (2017). "Dielectric Haloscopes: A New Way to Detect Axion Dark Matter". In: *Phys. Rev. Lett.* 118.9, p. 091801. DOI: 10.1103/PhysRevLett.118.091801. arXiv: 1611.05865 [physics.ins-det].

Calore, Francesca et al. (2020). "Bounds on axionlike particles from the diffuse supernova flux". In: *Phys. Rev. D* 102.12, p. 123005. DOI: 10.1103/PhysRevD.102.123005. arXiv: 2008.11741 [hep-ph].

— (2022a). "3D template-based Fermi-LAT constraints on the diffuse supernova axion-like particle background". In: *Phys. Rev. D* 105.6, p. 063028. DOI: 10.1103/PhysRevD.105.063028. arXiv: 2110.03679 [astro-ph.HE].

— (2022b). "511 keV line constraints on feebly interacting particles from supernovae". In: *Phys. Rev. D* 105.6, p. 063026. DOI: 10.1103/PhysRevD.105.063026. arXiv: 2112.08382 [hep-ph].

Calore, Francesca, Pierluca Carenza, Christopher Eckner, et al. (2024). "Uncovering axionlike particles in supernova gamma-ray spectra". In: *Phys. Rev. D* 109.4, p. 043010. DOI: 10.1103/PhysRevD.109.043010. arXiv: 2306.03925 [astro-ph.HE].

Calore, Francesca, Pierluca Carenza, Maurizio Giannotti, et al. (2021). "Supernova bounds on axionlike particles coupled with nucleons and electrons". In: *Phys. Rev. D* 104.4, p. 043016. DOI: 10.1103/PhysRevD.104.043016. arXiv: 2107.02186 [hep-ph].

Cameron, R. et al. (1993). "Search for nearly massless, weakly coupled particles by optical techniques". In: *Phys. Rev. D* 47, pp. 3707–3725. DOI: 10.1103/PhysRevD.47.3707.

Capozzi, Francesco and Georg Raffelt (2020). "Axion and neutrino bounds improved with new calibrations of the tip of the red-giant branch using geometric distance determinations". In: *Phys. Rev. D* 102.8, p. 083007. DOI: 10.1103/PhysRevD.102.083007. arXiv: 2007.03694 [astro-ph.SR].

Caputo, Andrea et al. (2022a). "Muonic boson limits: Supernova redux". In: *Phys. Rev. D* 105.3, p. 035022. DOI: 10.1103/PhysRevD.105.035022. arXiv: 2109.03244 [hep-ph].

— (2022b). "Radiative transfer in stars by feebly interacting bosons". In: *JCAP* 08.08, p. 045. DOI: 10.1088/1475-7516/2022/08/045. arXiv: 2204.11862 [astro-ph.SR].

Caputo, Andrea, Hans-Thomas Janka, et al. (2022). "Low-Energy Supernovae Severely Constrain Radiative Particle Decays". In: *Phys. Rev. Lett.* 128.22, p. 221103. DOI: 10.1103/PhysRevLett.128.221103. arXiv: 2201.09890 [astro-ph.HE].

Caputo, Andrea and Georg Raffelt (2024). "Astrophysical Axion Bounds: The 2024 Edition". In: *PoS* COSMICWISPers, p. 041. DOI: 10.22323/1.454.0041. arXiv: 2401.13728 [hep-ph].

Carena, Marcela and R. D. Peccei (1989). "The Effective Lagrangian for Axion Emission From SN1987A". In: *Phys. Rev. D* 40, p. 652. DOI: 10.1103/PhysRevD.40.652.

Carenza, P., J. A. García Pascual, et al. (Feb. 2025). "Detecting Supernova Axions with IAXO". In: arXiv: 2502.19476 [hep-ph].

Carenza, Pierluca et al. (2019). "Improved axion emissivity from a supernova via nucleon-nucleon bremsstrahlung". In: *JCAP* 10.10. [Erratum: JCAP 05, E01 (2020)], p. 016. DOI: 10.1088/1475-7516/2019/10/016. arXiv: 1906.11844 [hep-ph].

— (2020). "Constraints on the coupling with photons of heavy axion-like-particles from Globular Clusters". In: *Phys. Lett. B* 809, p. 135709. DOI: 10.1016/j.physletb.2020.135709. arXiv: 2004.08399 [hep-ph].

— (2021). "Enhanced Supernova Axion Emission and its Implications". In: *Phys. Rev. Lett.* 126.7, p. 071102. DOI: 10.1103/PhysRevLett.126.071102. arXiv: 2010.02943 [hep-ph].

Carenza, Pierluca (2023). "Axion emission from supernovae: a cheatsheet". In: *Eur. Phys. J. Plus* 138.9, p. 836. DOI: 10.1140/epjp/s13360-023-04484-2. arXiv: 2309.14798 [hep-ph].

Carenza, Pierluca, Giampaolo Co, et al. (2024). "Cross section for supernova axion observation in neutrino water Čherenkov detectors". In: *Phys. Rev. C* 109.1, p. 015501. DOI: 10.1103/PhysRevC.109.015501. arXiv: 2306.17055 [hep-ph].

Carenza, Pierluca, Maurizio Giannotti, et al. (2025). "Axion astrophysics". In: *Phys. Rept.* 1117, pp. 1–102. DOI: 10.1016/j.physrep.2025.02.002. arXiv: 2411.02492 [hep-ph].

Carenza, Pierluca, Giuseppe Lucente, et al. (2024). "Comprehensive constraints on heavy sterile neutrinos from core-collapse supernovae". In: *Phys. Rev. D* 109.6, p. 063010. DOI: 10.1103/PhysRevD.109.063010. arXiv: 2311.00033 [hep-ph].

Castillo-Felisola, Oscar et al. (2015). "Axions in gravity with torsion". In: *Phys. Rev. D* 91.8, p. 085017. DOI: 10.1103/PhysRevD.91.085017. arXiv: 1502.03694 [hep-ph].

Cembranos, J. A. R., A. L. Maroto, and H. Villarrubia-Rojo (2017). "Constraints on hidden gravitons from fifth-force experiments and stellar energy loss". In: *JHEP* 09, p. 104. DOI: 10.1007/JHEP09(2017)104. arXiv: 1706.07818 [hep-ph].

Chabrier, Gilles, Alexander Y. Potekhin, and Dmitry G. Yakovlev (Mar. 1997). "Cooling Neutron Stars with Accreted Envelopes". In: *The Astrophysical Journal* 477.2, p. L99. DOI: 10.1086/310535. URL: https://dx.doi.org/10.1086/310535.

Chadha-Day, Francesca, John Ellis, and David J. E. Marsh (2022). "Axion dark matter: What is it and why now?" In: *Sci. Adv.* 8.8, abj3618. DOI: 10.1126/sciadv.abj3618. arXiv: 2105.01406 [hep-ph].

Chang, Jae Hyeok et al. (2017). "Revisiting Supernova 1987A Constraints on Dark Photons". In: *JHEP* 01, p. 107. DOI: 10.1007/JHEP01(2017)107. arXiv: 1611.03864 [hep-ph].

— (2018). "Supernova 1987A Constraints on Sub-GeV Dark Sectors, Millicharged Particles, the QCD Axion, and an Axion-like Particle". In: *JHEP* 09, p. 051. DOI: 10.1007/JHEP09(2018)051. arXiv: 1803.00993 [hep-ph].

Chang, Sanghyeon and Kiwoon Choi (1993). "Hadronic axion window and the big bang nucleosynthesis". In: *Phys. Lett. B* 316, pp. 51–56. DOI: 10.1016/0370-2693(93)90656-3. arXiv: hep-ph/9306216.

Chen, Y. -J. et al. (2016). "Stronger Limits on Hypothetical Yukawa Interactions in the 30–8000 nm Range". In: *Phys. Rev. Lett.* 116.22, p. 221102. DOI: 10.1103/PhysRevLett.116.221102. arXiv: 1410.7267 [hep-ex].

Chevalier, Roger A and Richard I Klein (1978). "On the Rayleigh-Taylor instability in stellar explosions". In: *Astrophysical Journal, Part 1, vol. 219, Feb. 1, 1978, p. 994-1007.* 219, pp. 994–1007.

Chiu, H. -C. et al. (2009). "Demonstration of the asymmetric lateral Casimir force between corrugated surfaces in the nonadditive regime". In: *Phys. Rev. B* 80.12, p. 121402. DOI: 10.1103/PhysRevB.80.121402. arXiv: 0909.2161 [quant-ph].

Choi, Kang-Sin, Ian-Woo Kim, and Jihn E. Kim (2007). "String compactification, QCD axion and axion-photon-photon coupling". In: *JHEP* 03, p. 116. DOI: 10.1088/1126-6708/2007/03/116. arXiv: hep-ph/0612107.

Choi, Kang-Sin, Hans Peter Nilles, et al. (2009). "Accions". In: *Phys. Lett. B* 675, pp. 381–386. DOI: 10.1016/j.physletb.2009.04.028. arXiv: 0902.3070 [hep-th].

Choi, Kiwoon et al. (2022). "Axion emission from supernova with axion-pion-nucleon contact interaction". In: *JHEP* 02, p. 143. DOI: 10.1007/JHEP02(2022)143. arXiv: 2110.01972 [hep-ph].

Choi, Kiwoon and Jihn E. Kim (1985). "Harmful Axions in Superstring Models". In: *Phys. Lett. B* 154. [Erratum: Phys.Lett.B 156, 452 (1985)], p. 393. DOI: 10.1016/0370-2693(85)90416-2.

Choi, Lyla, Adam Burrows, and David Vartanyan (2024). "Gravitational-wave and Gravitational-wave Memory Signatures of Core-collapse Supernovae". In: *Astrophys. J.* 975.1, p. 12. DOI: 10.3847/1538-4357/ad74f8. arXiv: 2408.01525 [astro-ph.HE].

Christodoulou, D. (1991). "Nonlinear nature of gravitation and gravitational wave experiments". In: *Phys. Rev. Lett.* 67, pp. 1486–1489. DOI: 10.1103/PhysRevLett.67.1486.

Cicoli, Michele et al. (2012). "The type IIB string axiverse and its low-energy phenomenology". In: *JHEP* 10, p. 146. DOI: 10.1007/JHEP10(2012)146. arXiv: 1206.0819 [hep-th].

Colgate, S. A., M. Herant, and W. Benz (1993). "Neutron star accretion and the neutrino fireball". In: *Phys. Rept.* 227, pp. 157–174. DOI: 10.1016/0370-1573(93)90064-K.

Colgate, Stirling A. (1989). "Hot bubbles drive explosions". In: *Nature* 341.6242, pp. 489–490. DOI: 10.1038/341489a0. URL: https://doi.org/10.1038/341489a0.

Colgate, Stirling A. and Montgomery H. Johnson (1960). "Hydrodynamic Origin of Cosmic Rays". In: *Phys. Rev. Lett.* 5, pp. 235–238. DOI: 10.1103/PhysRevLett.5.235.

Conlon, Joseph P. (2006a). "Seeing the Invisible Axion in the Sparticle Spectrum". In: *Phys. Rev. Lett.* 97, p. 261802. DOI: 10.1103/PhysRevLett.97.261802. arXiv: hep-ph/0607138.

— (2006b). "The QCD axion and moduli stabilisation". In: *JHEP* 05, p. 078. DOI: 10.1088/1126-6708/2006/05/078. arXiv: hep-th/0602233.

Cowan, Glen et al. (2011). "Asymptotic formulae for likelihood-based tests of new physics". In: *Eur. Phys. J. C* 71. [Erratum: Eur.Phys.J.C 73, 2501 (2013)], p. 1554. DOI: 10.1140/epjc/s10052-011-1554-0. arXiv: 1007.1727 [physics.data-an].

Cowling, T. G. (1941). "The Non-radial Oscillations of Polytropic Stars". In: *Mon. Not. Roy. Astron. Soc.* 101.8, pp. 367–375. DOI: 10.1093/mnras/101.8.367.

Cyncynates, David and Olivier Simon (Aug. 2024a). "Minimal targets for dilaton direct detection". In: arXiv: 2408.16816 [hep-ph].

— (Oct. 2024b). "Scalar relics from the hot Big Bang". In: arXiv: 2410.22409 [hep-ph].

D'Eramo, Francesco et al. (2022). "Cosmological bound on the QCD axion mass, redux". In: *JCAP* 09, p. 022. DOI: 10.1088/1475-7516/2022/09/022. arXiv: 2205.07849 [astro-ph.CO].

Dadykin, V. L. et al. (1987). "Detection of a Rare Event on 23 February 1987 by the Neutrino Radiation Detector Under Mont Blanc". In: *JETP Lett.* 45, pp. 593–595.

Damour, T. and Alexander M. Polyakov (1994). "The String dilaton and a least coupling principle". In: *Nucl. Phys. B* 423, pp. 532–558. DOI: 10.1016/0550-3213(94)90143-0. arXiv: hep-th/9401069.

De Angelis, Alessandro, Giorgio Galanti, and Marco Roncadelli (2011). "Relevance of axion-like particles for very-high-energy astrophysics". In: *Phys. Rev. D* 84. [Erratum: Phys.Rev.D 87, 109903 (2013)], p. 105030. DOI: 10.1103/PhysRevD.84.105030. arXiv: 1106.1132 [astro-ph.HE].

De Donno, V. et al. (2011). "Self-consistent continuum random-phase approximation calculations with finite-range interactions". In: *Phys. Rev. C* 83, p. 044324.

De la Torre Luque, Pedro, Shyam Balaji, et al. (2025). "γ rays from in-flight positron annihilation as a probe of new physics". In: *Phys. Rev. D* 111.6, p. L061303. DOI: 10.1103/PhysRevD.111.L061303. arXiv: 2405.08482 [hep-ph].

De la Torre Luque, Pedro, Francesco Loparco, and Mario Nicola Mazziotta (2023). "The FLUKA cross sections for cosmic-ray leptons and uncertainties on current positron predictions". In: *JCAP* 10, p. 011. DOI: 10.1088/1475-7516/2023/10/011. arXiv: 2305.02958 [astro-ph.HE].

Dekens, Wouter, Jordy de Vries, and Sachin Shain (2022). "CP-violating axion interactions in effective field theory". In: *JHEP* 07, p. 014. DOI: 10.1007/JHEP07(2022)014. arXiv: 2203.11230 [hep-ph].

DeRocco, William et al. (2019). "Observable signatures of dark photons from supernovae". In: *JHEP* 02, p. 171. DOI: 10.1007/JHEP02(2019)171. arXiv: 1901.08596 [hep-ph].

Dev, P. S. Bhupal, Rabindra N. Mohapatra, and Yongchao Zhang (2017). "Long Lived Light Scalars as Probe of Low Scale Seesaw Models". In: *Nucl. Phys. B* 923, pp. 179–221. DOI: 10.1016/j.nuclphysb.2017.07.021. arXiv: 1703.02471 [hep-ph].

Di Luzio, Luca et al. (2020). "The landscape of QCD axion models". In: *Phys. Rept.* 870, pp. 1–117. DOI: 10.1016/j.physrep.2020.06.002. arXiv: 2003.01100 [hep-ph].

Di Luzio, Luca, Hector Gisbert, Gabriele Levati, et al. (Dec. 2023). "CP-Violating Axions: A Theory Review". In: arXiv: 2312.17310 [hep-ph].

Di Luzio, Luca, Hector Gisbert, Fabrizio Nesti, et al. (2024). "Axion window on new macroscopic forces". In: *Phys. Rev. D* 110.11, p. 115034. DOI: 10.1103/PhysRevD.110.115034. arXiv: 2407.15928 [hep-ph].

Di Luzio, Luca, Alfredo Walter Mario Guerrera, et al. (2024). "Axion-like particles in radiative quarkonia decays". In: *JHEP* 06, p. 217. DOI: 10.1007/JHEP06(2024)217. arXiv: 2402.12454 [hep-ph].

Di Luzio, Luca, Gabriele Levati, and Paride Paradisi (2024). "The chiral Lagrangian of CP-violating axion-like particles". In: *JHEP* 02, p. 020. DOI: 10.1007/JHEP02(2024)020. arXiv: 2311.12158 [hep-ph].

Diamond, Melissa, Damiano F. G. Fiorillo, Gustavo Marques-Tavares, Irene Tamborra, et al. (2024). "Multimessenger Constraints on Radiatively Decaying Axions from GW170817". In: *Phys. Rev. Lett.* 132.10, p. 101004. DOI: 10.1103/PhysRevLett.132.101004. arXiv: 2305.10327 [hep-ph].

Diamond, Melissa, Damiano F. G. Fiorillo, Gustavo Marques-Tavares, and Edoardo Vitagliano (2023). "Axion-sourced fireballs from supernovae". In: *Phys. Rev. D* 107.10. [Erratum: Phys.Rev.D 108, 049902 (2023)], p. 103029. DOI: 10.1103/PhysRevD.107.103029. arXiv: 2303.11395 [hep-ph].

Dicus, Duane A. et al. (1978). "Astrophysical Bounds on the Masses of Axions and Higgs Particles". In: *Phys. Rev. D* 18, p. 1829. DOI: 10.1103/PhysRevD.18.1829.

Dine, Michael and Patrick Draper (2015). "Challenges for the Nelson-Barr Mechanism". In: *JHEP* 08, p. 132. DOI: 10.1007/JHEP08(2015)132. arXiv: 1506.05433 [hep-ph].

Dine, Michael and Willy Fischler (1983). "The Not So Harmless Axion". In: *Phys. Lett. B* 120. Ed. by M. A. Srednicki, pp. 137–141. DOI: 10.1016/0370-2693(83)90639-1.

Dine, Michael, Willy Fischler, and Mark Srednicki (1981). "A Simple Solution to the Strong CP Problem with a Harmless Axion". In: *Phys. Lett. B* 104, pp. 199–202. DOI: 10.1016/0370-2693(81)90590-6.

Divitiis, G. M. de et al. (2013). "Leading isospin breaking effects on the lattice". In: *Phys. Rev. D* 87.11, p. 114505. DOI: 10.1103/PhysRevD.87.114505. arXiv: 1303.4896 [hep-lat].

Döbrich, Babette (2018). "Axion-like Particles from Primakov production in beam-dumps". In: *CERN Proc.* 1. Ed. by David d'Enterria, Albert de Roeck, and Michelangelo Mangano, p. 253. DOI: 10.23727/CERN-Proceedings-2018-001.253. arXiv: 1708.05776 [hep-ph].

Dolan, Matthew J. et al. (2017). "Revised constraints and Belle II sensitivity for visible and invisible axion-like particles". In: *JHEP* 12. [Erratum: JHEP 03, 190 (2021)], p. 094. DOI: 10.1007/JHEP12(2017)094. arXiv: 1709.00009 [hep-ph].

Dolan, Matthew J. et al. (2015). "A taste of dark matter: Flavour constraints on pseudoscalar mediators". In: *JHEP* 03. [Erratum: JHEP 07, 103 (2015)], p. 171. DOI: 10.1007/JHEP03(2015)171. arXiv: 1412.5174 [hep-ph].

Dolgov, A. D. et al. (2000). "Heavy sterile neutrinos: Bounds from big bang nucleosynthesis and SN1987A". In: *Nucl. Phys. B* 590, pp. 562–574. DOI: 10.1016/S0550-3213(00)00566-6. arXiv: hep-ph/0008138.

Donnelly, T. W. et al. (1978). "Do Axions Exist?" In: *Phys. Rev. D* 18, p. 1607. DOI: 10.1103/PhysRevD.18.1607.

Dragos, Jack et al. (2021). "Confirming the Existence of the strong CP Problem in Lattice QCD with the Gradient Flow". In: *Phys. Rev. C* 103.1, p. 015202. DOI: 10.1103/PhysRevC.103.015202. arXiv: 1902.03254 [hep-lat].

Du, N. et al. (2018). "A Search for Invisible Axion Dark Matter with the Axion Dark Matter Experiment". In: *Phys. Rev. Lett.* 120.15, p. 151301. DOI: 10.1103/PhysRevLett.120.151301. arXiv: 1804.05750 [hep-ex].

Duncan, Malcolm J., N. Kaloper, and Keith A. Olive (1992). "Axion hair and dynamical torsion from anomalies". In: *Nucl. Phys. B* 387, pp. 215–235. DOI: 10.1016/0550-3213(92)90052-D.

Ebisuzaki, Toshikazu, Toshikazu Shigeyama, and Ken'ichi Nomoto (1989). "Rayleigh-Taylor instability and mixing in SN 1987A". In: *Astrophysical Journal, Part 2-Letters (ISSN 0004-637X), vol. 344, Sept. 15, 1989, p. L65-L68. Research supported by the Institute of Space and Aeronautical Sciences and Japan-US Cooperative Science Program.* 344, pp. L65–L68.

Eckner, Christopher et al. (2021). "Constraining the diffuse supernova axion-like-particle background with high-latitude Fermi-LAT data". In: *PoS* ICRC2021, p. 543. DOI: 10.22323/1.395.0543.

Edmonds, A. R. (1957). *Angular momentum in quantum mechanics*. Princeton University Press, Princeton.

Ehret, Klaus et al. (2010). "New ALPS Results on Hidden-Sector Lightweights". In: *Phys. Lett. B* 689, pp. 149–155. DOI: 10.1016/j.physletb.2010.04.066. arXiv: 1004.1313 [hep-ex].

Ellis, John R. and Mary K. Gaillard (1979). "Strong and Weak CP Violation". In: *Nucl. Phys. B* 150, pp. 141–162. DOI: 10.1016/0550-3213(79)90297-9.

Ellis, John R. and Keith A. Olive (1987). "Constraints on Light Particles From Supernova Sn1987a". In: *Phys. Lett. B* 193, p. 525. DOI: 10.1016/0370-2693(87)91710-2.

Engel, J., D. Seckel, and A. C. Hayes (1990). "Emission and detectability of hadronic axions from SN1987A". In: *Phys. Rev. Lett.* 65, pp. 960–963. DOI: 10.1103/PhysRevLett.65.960.

Epstein, R. (1978). "The Generation of Gravitational Radiation by Escaping Supernova Neutrinos". In: *Astrophys. J.* 223, pp. 1037–1045. DOI: 10.1086/156337.

Ericson, Torleif Erik Oskar and J. F. Mathiot (1989). "Axion Emission from SN 1987a: Nuclear Physics Constraints". In: *Phys. Lett. B* 219, pp. 507–514. DOI: 10.1016/0370-2693(89)91103-9.

Falk, Sydney W. and David N. Schramm (1978). "Limits From Supernovae on Neutrino Radiative Lifetimes". In: *Phys. Lett. B* 79, p. 511. DOI: 10.1016/0370-2693(78)90417-3.

Favata, Marc (2010). "The gravitational-wave memory effect". In: *Class. Quant. Grav.* 27. Ed. by Zsuzsa Marka and Szabolcs Marka, p. 084036. DOI: 10.1088/0264-9381/27/8/084036. arXiv: 1003.3486 [gr-qc].

Ferreira, Ricardo Z., M. C. David Marsh, and Eike Müller (2022). "Strong supernovae bounds on ALPs from quantum loops". In: *JCAP* 11, p. 057. DOI: 10.1088/1475-7516/2022/11/057. arXiv: 2205.07896 [hep-ph].

Feruglio, Ferruccio, Alessandro Strumia, and Arsenii Titov (May 2023). "Modular invariance and the QCD angle". In: arXiv: 2305.08908 [hep-ph].

Finn, L. S. and C. R. Evans (1990). "Determining gravitational radiation from Newtonian self-gravitating systems". In: *Astrophys. J.* 351, pp. 588–600. DOI: 10.1086/168497.

Fiorillo, Damiano F. G., Malte Heinlein, et al. (Aug. 2023). "Supernova Simulations Confront SN 1987A Neutrinos". In: arXiv: 2308.01403 [astro-ph.HE].

Fiorillo, Damiano F. G., Alessandro Lella, et al. (June 2025). "Leading bounds on micro- to picometer fifth forces from neutron star cooling". In: arXiv: 2506.19906 [hep-ph].

Fiorillo, Damiano F. G., Tetyana Pitik, and Edoardo Vitagliano (Mar. 2025a). "Energy transfer by feebly interacting particles in supernovae: the trapping regime". In: arXiv: 2503.13653 [hep-ph].

— (Mar. 2025b). "Supernova production of axion-like particles coupling to electrons, reloaded". In: arXiv: 2503.15630 [hep-ph].

Fischbach, E. and C. Talmadge (1992). "Six years of the fifth force". In: *Nature* 356, pp. 207–214. DOI: 10.1038/356207a0.

Fischer, T. et al. (2010). "Protoneutron star evolution and the neutrino driven wind in general relativistic neutrino radiation hydrodynamics simulations". In: *Astron. Astrophys.* 517, A80. DOI: 10.1051/0004-6361/200913106. arXiv: 0908.1871 [astro-ph.HE].

Fischer, T., S. C. Whitehouse, et al. (2009). "The neutrino signal from protoneutron star accretion and black hole formation". In: *Astron. Astrophys.* 499, p. 1. DOI: 10.1051/0004-6361/200811055. arXiv: 0809.5129 [astro-ph].

Fischer, Tobias et al. (2021). "Observable signatures of enhanced axion emission from protoneutron stars". In: *Phys. Rev. D* 104.10, p. 103012. DOI: 10.1103/PhysRevD.104.103012. arXiv: 2108.13726 [hep-ph].

Fischer, Tobias, Sovan Chakraborty, et al. (2016). "Probing axions with the neutrino signal from the next galactic supernova". In: *Phys. Rev. D* 94.8, p. 085012. DOI: 10.1103/PhysRevD.94.085012. arXiv: 1605.08780 [astro-ph.HE].

Flacke, Thomas et al. (2017). "Phenomenology of relaxion-Higgs mixing". In: *JHEP* 06, p. 050. DOI: 10.1007/JHEP06(2017)050. arXiv: 1610.02025 [hep-ph].

Fogli, G. L. et al. (2005). "Probing supernova shock waves and neutrino flavor transitions in next-generation water-Cerenkov detectors". In: *JCAP* 04, p. 002. DOI: 10.1088/1475-7516/2005/04/002. arXiv: hep-ph/0412046.

Foglizzo, T. (2002). "Non-radial instabilities of isothermal Bondi accretion with a shock: Vortical-acoustic cycle versus post-shock acceleration". In: *Astron. Astrophys.* 392, p. 353. DOI: 10.1051/0004-6361:20020912. arXiv: astro-ph/0206274.

Foglizzo, T., L. Scheck, and H. -Th. Janka (2006). "Neutrino-driven convection versus advection in core collapse supernovae". In: *Astrophys. J.* 652, pp. 1436–1450. DOI: 10.1086/508443. arXiv: astro-ph/0507636.

Foglizzo, Thierry, P Galletti, et al. (2007a). "Instability of a stalled accretion shock: evidence for the advective-acoustic cycle". In: *The Astrophysical Journal* 654.2, p. 1006.

— (2007b). "Instability of a stalled accretion shock: evidence for the advective-acoustic cycle". In: *Astrophys. J.* 654, pp. 1006–1021. DOI: 10.1086/509612. arXiv: astro-ph/0606640.

Foglizzo, Thierry, Frederic Masset, et al. (2012). "A Shallow Water Analogue of the Standing Accretion Shock Instability: Experimental Demonstration

and Two-Dimensional Model". In: *Phys. Rev. Lett.* 108, p. 051103. DOI: 10.1103/PhysRevLett.108.051103. arXiv: 1112.3448 [astro-ph.HE].

Fore, Bryce, Norbert Kaiser, et al. (2024). "Mass of charged pions in neutron-star matter". In: *Phys. Rev. C* 110.2, p. 025803. DOI: 10.1103/PhysRevC.110.025803. arXiv: 2301.07226 [nucl-th].

Fore, Bryce and Sanjay Reddy (2020). "Pions in hot dense matter and their astrophysical implications". In: *Phys. Rev. C* 101.3, p. 035809. DOI: 10.1103/PhysRevC.101.035809. arXiv: 1911.02632 [astro-ph.HE].

Friman, B. L. and O. V. Maxwell (1979). "Neutron Star Neutrino Emissivities". In: *Astrophys. J.* 232, pp. 541–557. DOI: 10.1086/157313.

Fryxell, B., E. Müller, and D. Arnett (Apr. 1989). "Computation of multi-dimensional flows with non-uniform composition." In: *Nuclear Astrophysics*. Ed. by M. Lozano, M. I. Gallardo, and J. M. Arias, p. 100.

Fryxell, Bruce, Ewald Mueller, and David Arnett (1991). "Instabilities and clumping in SN 1987A. I-Early evolution in two dimensions". In: *Astrophysical Journal, Part 1 (ISSN 0004-637X), vol. 367, Feb. 1, 1991, p. 619-634.* 367, pp. 619–634.

Gallo Rosso, Andrea, Francesco Vissani, and Maria Cristina Volpe (2017). "Measuring the neutron star compactness and binding energy with supernova neutrinos". In: *JCAP* 11, p. 036. DOI: 10.1088/1475-7516/2017/11/036. arXiv: 1708.00760 [hep-ph].

— (2018). "What can we learn on supernova neutrino spectra with water Cherenkov detectors?" In: *JCAP* 04, p. 040. DOI: 10.1088/1475-7516/2018/04/040. arXiv: 1712.05584 [hep-ph].

Garching core-collapse supernova research archive (n.d.). https://wwwmpa.mpa-garching.mpg.de/ccsnarchive//.

Gavela, Belén, Pablo Quílez, and Maria Ramos (2024). "The QCD axion sum rule". In: *JHEP* 04, p. 056. DOI: 10.1007/JHEP04(2024)056. arXiv: 2305.15465 [hep-ph].

Ge, Shao-Feng et al. (2020). "Supernova-scope for the Direct Search of Supernova Axions". In: *JCAP* 11, p. 059. DOI: 10.1088/1475-7516/2020/11/059. arXiv: 2008.03924 [hep-ph].

Georgi, Howard (1978). "A Model of Soft CP Violation". In: *Hadronic J.* 1, p. 155.

Georgi, Howard and Lisa Randall (1986). "Flavor Conserving CP Violation in Invisible Axion Models". In: *Nucl. Phys. B* 276, pp. 241–252. DOI: 10.1016/0550-3213(86)90022-2.

Gérard, Jean-Marc and Philippe Mertens (2012). "Weakly-induced strong CP-violation". In: *Phys. Lett. B* 716, pp. 316–321. DOI: 10.1016/j.physletb.2012.08.036. arXiv: 1206.0914 [hep-ph].

Giannotti, M. and F. Nesti (2005). "Nucleon-nucleon Bremsstrahlung emission of massive axions". In: *Phys. Rev. D* 72, p. 063005. DOI: 10.1103/PhysRevD.72.063005. arXiv: hep-ph/0505090.

Gninenko, S. N. (2012). "Constraints on sub-GeV hidden sector gauge bosons from a search for heavy neutrino decays". In: *Phys. Lett. B* 713, pp. 244–248. DOI: 10.1016/j.physletb.2012.06.002. arXiv: 1204.3583 [hep-ph].

Goldberg, Jared A. and Lars Bildsten (2020). "The Value of Progenitor Radius Measurements for Explosion Modeling of Type II-Plateau Supernovae". In: *Astrophys. J. Lett.* 895.2, p. L45. DOI: 10.3847/2041-8213/ab9300. arXiv: 2005.07290 [astro-ph.SR].

Goldreich, P. and S. V. Weber (June 1980). "Homologously collapsing stellar cores". In: *Astrophys. J.* 238, pp. 991–997. DOI: 10.1086/158065.

Gómez-Bañón, Antonio et al. (2024). "Constraining Light QCD Axions with Isolated Neutron Star Cooling". In: *Phys. Rev. Lett.* 133.25, p. 251002. DOI: 10.1103/PhysRevLett.133.251002. arXiv: 2408.07740 [hep-ph].

Gorghetto, Marco et al. (2021). "More axions from strings". In: *SciPost Phys.* 10.2, p. 050. DOI: 10.21468/SciPostPhys.10.2.050. arXiv: 2007.04990 [hep-ph].

Gorghetto, Marco and Giovanni Villadoro (2019). "Topological Susceptibility and QCD Axion Mass: QED and NNLO corrections". In: *JHEP* 03, p. 033. DOI: 10.1007/JHEP03(2019)033. arXiv: 1812.01008 [hep-ph].

Goriely, S. et al. (2009). "First Gogny-Hartree-Fock-Bogoliubov Nuclear Mass Model". In: *Phys. Rev. Lett.* 102, p. 242501.

Gottlieb, Steven A. et al. (1997). "Thermodynamics of lattice QCD with two light quark flavors on a 16**3 x 8 lattice. 2." In: *Phys. Rev. D* 55, pp. 6852–6860. DOI: 10.1103/PhysRevD.55.6852. arXiv: hep-lat/9612020.

Graham, Peter W. et al. (2015). "Cosmological Relaxation of the Electroweak Scale". In: *Phys. Rev. Lett.* 115.22, p. 221801. DOI: 10.1103/PhysRevLett.115.221801. arXiv: 1504.07551 [hep-ph].

Graham, Peter W., Igor G. Irastorza, et al. (2015). "Experimental Searches for the Axion and Axion-Like Particles". In: *Ann. Rev. Nucl. Part. Sci.* 65, pp. 485–514. DOI: 10.1146/annurev-nucl-102014-022120. arXiv: 1602.00039 [hep-ex].

Graham, Peter W. and Surjeet Rajendran (2013). "New Observables for Direct Detection of Axion Dark Matter". In: *Phys. Rev. D* 88, p. 035023. DOI: 10.1103/PhysRevD.88.035023. arXiv: 1306.6088 [hep-ph].

Greco, Emanuele et al. (2021). "Indication of a Pulsar Wind Nebula in the hard X-ray emission from SN 1987A". In: *Astrophys. J. Lett.* 908.2, p. L45. DOI: 10.3847/2041-8213/abdf5a. arXiv: 2101.09029 [astro-ph.HE].

Griffiths, David (2008). *Introduction to elementary particles*. ISBN: 978-3-527-40601-2.

Grifols, J. A. and E. Masso (1986). "Constraints on Finite Range Baryonic and Leptonic Forces From Stellar Evolution". In: *Phys. Lett. B* 173, pp. 237–240. DOI: 10.1016/0370-2693(86)90509-5.

Grifols, J. A., E. Masso, and S. Peris (1989). "Energy Loss From the Sun and RED Giants: Bounds on Short Range Baryonic and Leptonic Forces". In: *Mod. Phys. Lett. A* 4, p. 311. DOI: 10.1142/S0217732389000381.

Grifols, J. A., E. Masso, and R. Toldra (1996). "Gamma-rays from SN1987A due to pseudoscalar conversion". In: *Phys. Rev. Lett.* 77, pp. 2372–2375. DOI: 10.1103/PhysRevLett.77.2372. arXiv: astro-ph/9606028.

Grilli di Cortona, Giovanni et al. (2016). "The QCD axion, precisely". In: *JHEP* 01, p. 034. DOI: 10.1007/JHEP01(2016)034. arXiv: 1511.02867 [hep-ph].

Haddock, Christopher C. et al. (2018). "Search for deviations from the inverse square law of gravity at nm range using a pulsed neutron beam". In: *Phys. Rev. D* 97.6, p. 062002. DOI: 10.1103/PhysRevD.97.062002. arXiv: 1712.02984 [nucl-ex].

Hall, Lawrence J. and Mark B. Wise (1981). "FLAVOR CHANGING HIGGS - BOSON COUPLINGS". In: *Nucl. Phys. B* 187, pp. 397–408. DOI: 10.1016/0550-3213(81)90469-7.

Halverson, James, Cody Long, and Pran Nath (2017). "Ultralight axion in supersymmetry and strings and cosmology at small scales". In: *Phys. Rev. D* 96.5, p. 056025. DOI: 10.1103/PhysRevD.96.056025. arXiv: 1703.07779 [hep-ph].

Hamaguchi, Koichi et al. (2018). "Limit on the Axion Decay Constant from the Cooling Neutron Star in Cassiopeia A". In: *Phys. Rev. D* 98.10, p. 103015. DOI: 10.1103/PhysRevD.98.103015. arXiv: 1806.07151 [hep-ph].

Hambaryan, V., V. Suleimanov, F. Haberl, et al. (2017). "The compactness of the isolated neutron star RX J0720.4−3125". In: *Astron. Astrophys.* 601, A108. DOI: 10.1051/0004-6361/201630368. arXiv: 1702.07635 [astro-ph.HE].

Hambaryan, V., V. Suleimanov, A. D. Schwope, et al. (2011). "Phase resolved spectroscopic study of the isolated neutron star RBS 1223 (1RXS J130848.6+212708)". In: *AIP Conf. Proc.* 1379.1. Ed. by Ersin Gögüs, Ünal Ertan, and Tomaso Belloni, pp. 195–196. DOI: 10.1063/1.3629512. arXiv: 1108.3897 [astro-ph.SR].

Hanhart, Christoph, Daniel R. Phillips, and Sanjay Reddy (2001). "Neutrino and axion emissivities of neutron stars from nucleon-nucleon scattering data". In: *Phys. Lett. B* 499, pp. 9–15. DOI: 10.1016/S0370-2693(00)01382-4. arXiv: astro-ph/0003445.

Hannestad, Steen et al. (2007). "Unparticle constraints from SN 1987A". In: *Phys. Rev. D* 76, p. 121701. DOI: 10.1103/PhysRevD.76.121701. arXiv: 0708.1404 [hep-ph].

Hannestad, Steen and Georg Raffelt (2001). "New supernova limit on large extra dimensions". In: *Phys. Rev. Lett.* 87, p. 051301. DOI: 10.1103/PhysRevLett.87.051301. arXiv: hep-ph/0103201.

Hardy, Edward and Robert Lasenby (2017). "Stellar cooling bounds on new light particles: plasma mixing effects". In: *JHEP* 02, p. 033. DOI: 10.1007/JHEP02(2017)033. arXiv: 1611.05852 [hep-ph].

Hardy, Edward, Anton Sokolov, and Henry Stubbs (2025). "Supernova bounds on new scalars from resonant and soft emission". In: *JHEP* 04, p. 013. DOI: 10.1007/JHEP04(2025)013. arXiv: 2410.17347 [hep-ph].

Heacock, Benjamin et al. (2021). "Pendellösung interferometry probes the neutron charge radius, lattice dynamics, and fifth forces". In: *Science* 373.6560, abc2794. DOI: 10.1126/science.abc2794. arXiv: 2103.05428 [nucl-ex].

Healy, Sarah et al. (2024). "Red Supergiant Candidates for Multimessenger Monitoring of the Next Galactic Supernova". In: *Mon. Not. Roy. Astron.*

Soc. 529, p. 3630. DOI: 10.1093/mnras/stae738. arXiv: 2307.08785 [astro-ph.SR].

Hempel, Matthias (2015). "Nucleon self-energies for supernova equations of state". In: *Phys. Rev. C* 91, p. 055807. DOI: 10.1103/PhysRevC.91.055807. arXiv: 1410.6337 [nucl-th].

Hempel, Matthias, Tobias Fischer, et al. (2012). "New Equations of State in Simulations of Core-Collapse Supernovae". In: *Astrophys. J.* 748, p. 70. DOI: 10.1088/0004-637X/748/1/70. arXiv: 1108.0848 [astro-ph.HE].

Hempel, Matthias and Jurgen Schaffner-Bielich (2010). "Statistical Model for a Complete Supernova Equation of State". In: *Nucl. Phys. A* 837, pp. 210–254. DOI: 10.1016/j.nuclphysa.2010.02.010. arXiv: 0911.4073 [nucl-th].

Herant, Marc and Willy Benz (1991). "Hydrodynamical instabilities and mixing in SN 1987A-Two-dimensional simulations of the first 3 months". In: *Astrophysical Journal, Part 2-Letters (ISSN 0004-637X), vol. 370, April 1, 1991, p. L81-L84. SNSF-supported research.* 370, pp. L81–L84.

— (1992). "Postexplosion hydrodynamics of SN 1987A". In: *Astrophysical Journal, Part 1 (ISSN 0004-637X), vol. 387, March 1, 1992, p. 294-308. Research supported by SNSF.* 387, pp. 294–308.

Hilaire, S. and M. Girod (2007). "Large-scale mean-field calculations from proton to neutron drip lines using the D1S Gogny force". In: *Eur. Phys. J. A* 33, p. 237.

— (n.d.). *Hartree-Fock-Bogoliubov results based on the Gogny force. AMEDEE database.* http://www-phynu.cea.fr/HFB-Gogny_eng.htm.

Hild, S. et al. (2011). "Sensitivity Studies for Third-Generation Gravitational Wave Observatories". In: *Class. Quant. Grav.* 28, p. 094013. DOI: 10.1088/0264-9381/28/9/094013. arXiv: 1012.0908 [gr-qc].

Hirata, K. et al. (1987). "Observation of a Neutrino Burst from the Supernova SN 1987a". In: *Phys. Rev. Lett.* 58. Ed. by K. C. Wali, pp. 1490–1493. DOI: 10.1103/PhysRevLett.58.1490.

Hirata, K. S. et al. (1988). "Observation in the Kamiokande-II Detector of the Neutrino Burst from Supernova SN 1987a". In: *Phys. Rev. D* 38, pp. 448–458. DOI: 10.1103/PhysRevD.38.448.

Ho, Shu-Yu et al. (2023). "Supernova axion emissivity with $\Delta(1232)$ resonance in heavy baryon chiral perturbation theory". In: *Phys. Rev. D* 107.7,

p. 075002. DOI: 10.1103/PhysRevD.107.075002. arXiv: 2212.01155 [hep-ph].

Ho, Wynn C. G. et al. (2007). "Magnetic Hydrogen Atmosphere Models and the Neutron Star RX J1856.5-3754". In: *Mon. Not. Roy. Astron. Soc.* 375, pp. 821–830. DOI: 10.1111/j.1365-2966.2006.11376.x. arXiv: astro-ph/0612145.

Hoof, Sebastian and Lena Schulz (2023). "Updated constraints on axion-like particles from temporal information in supernova SN1987A gamma-ray data". In: *JCAP* 03, p. 054. DOI: 10.1088/1475-7516/2023/03/054. arXiv: 2212.09764 [hep-ph].

Horsley, R. et al. (2016). "Isospin splittings of meson and baryon masses from three-flavor lattice QCD + QED". In: *J. Phys. G* 43.10, 10LT02. DOI: 10.1088/0954-3899/43/10/10LT02. arXiv: 1508.06401 [hep-lat].

Hoskins, J. K. et al. (1985). "Experimental tests of the gravitational inverse square law for mass separations from 2-cm to 105-cm". In: *Phys. Rev. D* 32, pp. 3084–3095. DOI: 10.1103/PhysRevD.32.3084.

Hudepohl, L. et al. (2010). "Neutrino Signal of Electron-Capture Supernovae from Core Collapse to Cooling". In: *Phys. Rev. Lett.* 104. [Erratum: Phys.Rev.Lett. 105, 249901 (2010)], p. 251101. DOI: 10.1103/PhysRevLett.104.251101. arXiv: 0912.0260 [astro-ph.SR].

Hui, Lam et al. (2017). "Ultralight scalars as cosmological dark matter". In: *Phys. Rev. D* 95.4, p. 043541. DOI: 10.1103/PhysRevD.95.043541. arXiv: 1610.08297 [astro-ph.CO].

Ianni, A. et al. (2009). "The Likelihood for supernova neutrino analyses". In: *Phys. Rev. D* 80, p. 043007. DOI: 10.1103/PhysRevD.80.043007. arXiv: 0907.1891 [hep-ph].

Inoue, Yoshizumi et al. (2002). "Search for sub-electronvolt solar axions using coherent conversion of axions into photons in magnetic field and gas helium". In: *Phys. Lett. B* 536, pp. 18–23. DOI: 10.1016/S0370-2693(02)01822-1. arXiv: astro-ph/0204388.

Irastorza, Igor G. and Javier Redondo (2018). "New experimental approaches in the search for axion-like particles". In: *Prog. Part. Nucl. Phys.* 102, pp. 89–159. DOI: 10.1016/j.ppnp.2018.05.003. arXiv: 1801.08127 [hep-ph].

Isern, J. et al. (2008). "Axions and the cooling of white dwarf stars". In: *Astrophys. J. Lett.* 682, p. L109. DOI: 10.1086/591042. arXiv: 0806.2807 [astro-ph].

— (2009). "Axions and the white dwarf luminosity function". In: *J. Phys. Conf. Ser.* 172. Ed. by Enrique Garcia-Berro et al., p. 012005. DOI: 10.1088/1742-6596/172/1/012005. arXiv: 0812.3043 [astro-ph].

Ishizuka, N. and M. Yoshimura (1990). "Axion and Dilaton Emissivity From Nascent Neutron Stars". In: *Prog. Theor. Phys.* 84, pp. 233–250. DOI: 10.1143/PTP.84.233.

Iwamoto, N. (1984). "Axion Emission from Neutron Stars". In: *Phys. Rev. Lett.* 53, pp. 1198–1201. DOI: 10.1103/PhysRevLett.53.1198.

Jacobsen, E. and R. Lyons (2003). "The sliding DFT". In: *IEEE Signal Processing Magazine* 20.2, pp. 74–80. DOI: 10.1109/MSP.2003.1184347.

Jaeckel, J. et al. (2018). "Decay photons from the axionlike particles burst of type II supernovae". In: *Phys. Rev. D* 98.5, p. 055032. DOI: 10.1103/PhysRevD.98.055032. arXiv: 1702.02964 [hep-ph].

Jaeckel, Joerg and Andreas Ringwald (2010). "The Low-Energy Frontier of Particle Physics". In: *Ann. Rev. Nucl. Part. Sci.* 60, pp. 405–437. DOI: 10.1146/annurev.nucl.012809.104433. arXiv: 1002.0329 [hep-ph].

Jaeckel, Joerg and Michael Spannowsky (2016). "Probing MeV to 90 GeV axion-like particles with LEP and LHC". In: *Phys. Lett. B* 753, pp. 482–487. DOI: 10.1016/j.physletb.2015.12.037. arXiv: 1509.00476 [hep-ph].

Jaffe, Andrew H. and Michael S. Turner (1997). "Gamma-rays and the decay of neutrinos from SN1987A". In: *Phys. Rev. D* 55, pp. 7951–7959. DOI: 10.1103/PhysRevD.55.7951. arXiv: astro-ph/9601104.

Janka, H. -Thomas (Feb. 2025). "Long-Term Multidimensional Models of Core-Collapse Supernovae: Progress and Challenges". In: arXiv: 2502.14836 [astro-ph.HE].

Janka, Hans-Thomas et al. (2007). "Theory of Core-Collapse Supernovae". In: *Phys. Rept.* 442, pp. 38–74. DOI: 10.1016/j.physrep.2007.02.002. arXiv: astro-ph/0612072.

Janka, Hans-Thomas (2012). "Explosion Mechanisms of Core-Collapse Supernovae". In: *Ann. Rev. Nucl. Part. Sci.* 62, pp. 407–451. DOI: 10.1146/annurev-nucl-102711-094901. arXiv: 1206.2503 [astro-ph.SR].

Janka, Hans-Thomas, Wolfgang Keil, et al. (1996). "Nucleon spin fluctuations and the supernova emission of neutrinos and axions". In: *Phys. Rev. Lett.* 76, pp. 2621–2624. DOI: 10.1103/PhysRevLett.76.2621. arXiv: astro-ph/9507023.

Janka, Hans-Thomas and Daniel Kresse (2024). "Interplay between neutrino kicks and hydrodynamic kicks of neutron stars and black holes". In: *Astrophys. Space Sci.* 369.8, p. 80. DOI: 10.1007/s10509-024-04343-1. arXiv: 2401.13817 [astro-ph.HE].

Jansson, Ronnie and Glennys R. Farrar (2012). "A New Model of the Galactic Magnetic Field". In: *Astrophys. J.* 757, p. 14. DOI: 10.1088/0004-637X/757/1/14. arXiv: 1204.3662 [astro-ph.GA].

Jean, P. et al. (2009). "Positron transport in the interstellar medium". In: *Astron. Astrophys.* 508, p. 1099. DOI: 10.1051/0004-6361/200809830. arXiv: 0909.4022 [astro-ph.HE].

Jean, Pierre et al. (2006). "Spectral analysis of the galactic e+ e- annihilation emission". In: *Astron. Astrophys.* 445, pp. 579–589. DOI: 10.1051/0004-6361:20053765. arXiv: astro-ph/0509298.

Jegerlehner, Beat, Frank Neubig, and Georg Raffelt (1996). "Neutrino oscillations and the supernova SN1987A signal". In: *Phys. Rev. D* 54, pp. 1194–1203. DOI: 10.1103/PhysRevD.54.1194. arXiv: astro-ph/9601111.

Jenkins, Elizabeth Ellen and Aneesh V. Manohar (1991). "Baryon chiral perturbation theory using a heavy fermion Lagrangian". In: *Phys. Lett. B* 255, pp. 558–562. DOI: 10.1016/0370-2693(91)90266-S.

Kachru, Shamit et al. (2003). "De Sitter vacua in string theory". In: *Phys. Rev. D* 68, p. 046005. DOI: 10.1103/PhysRevD.68.046005. arXiv: hep-th/0301240.

Kahn, Yonatan et al. (2016). "Broadband and Resonant Approaches to Axion Dark Matter Detection". In: *Phys. Rev. Lett.* 117.14, p. 141801. DOI: 10.1103/PhysRevLett.117.141801. arXiv: 1602.01086 [hep-ph].

Kalemci, Emrah et al. (2006). "Searching for annihilation radiation from sn 1006 with spi on integral". In: *Astrophys. J. Lett.* 640, pp. L55–L58. DOI: 10.1086/503289. arXiv: astro-ph/0602233.

Kalogera, Vicky et al. (Nov. 2021). "The Next Generation Global Gravitational Wave Observatory: The Science Book". In: arXiv: 2111.06990 [gr-qc].

Kamiya, Y. et al. (2015). "Constraints on New Gravitylike Forces in the Nanometer Range". In: *Phys. Rev. Lett.* 114, p. 161101. DOI: 10.1103/PhysRevLett.114.161101. arXiv: 1504.02181 [hep-ex].

Kane, J et al. (1997). "Supernova-relevant hydrodynamic instability experiments on the Nova laser". In: *The Astrophysical Journal* 478.2, p. L75.

Kapner, D. J. et al. (2007). "Tests of the gravitational inverse-square law below the dark-energy length scale". In: *Phys. Rev. Lett.* 98, p. 021101. DOI: 10.1103/PhysRevLett.98.021101. arXiv: hep-ph/0611184.

Kappadath, Srinivas Cheenu (Jan. 1998). "Measurement of ..." PhD thesis. University of New Hampshire.

Kawamura, Seiji et al. (2008). "The Japanese space gravitational wave antenna: DECIGO". In: *J. Phys. Conf. Ser.* 120. Ed. by Kunio Inoue, Atsuto Suzuki, and Tadao Mitsui, p. 032004. DOI: 10.1088/1742-6596/120/3/032004.

Ke, Jun et al. (2021). "Combined Test of the Gravitational Inverse-Square Law at the Centimeter Range". In: *Phys. Rev. Lett.* 126.21, p. 211101. DOI: 10.1103/PhysRevLett.126.211101.

Keil, Wolfgang, H. Thomas Janka, and Georg Raffelt (1995). "Reduced neutrino opacities and the SN1987A signal". In: *Phys. Rev. D* 51, pp. 6635–6646. DOI: 10.1103/PhysRevD.51.6635. arXiv: hep-ph/9410229.

Keil, Wolfgang, Hans-Thomas Janka, David N. Schramm, et al. (1997). "A Fresh look at axions and SN-1987A". In: *Phys. Rev. D* 56, pp. 2419–2432. DOI: 10.1103/PhysRevD.56.2419. arXiv: astro-ph/9612222.

Khlebnikov, S. Yu. and M. E. Shaposhnikov (1988). "Extra Space-time Dimensions: Towards a Solution to the Strong CP Problem". In: *Phys. Lett. B* 203, pp. 121–124. DOI: 10.1016/0370-2693(88)91582-1.

Khriplovich, I. B. (1986). "Quark Electric Dipole Moment and Induced θ Term in the Kobayashi-Maskawa Model". In: *Phys. Lett. B* 173, pp. 193–196. DOI: 10.1016/0370-2693(86)90245-5.

Kifonidis, Konstantinos et al. (2003). "Non-spherical core collapse supernovae. 1. Neutrino - driven convection, Rayleigh-Taylor instabilities, and the formation and propagation of metal clumps". In: *Astron. Astrophys.* 408, pp. 621–650. DOI: 10.1051/0004-6361:20030863. arXiv: astro-ph/0302239.

Kim, Jihn E. (1979). "Weak Interaction Singlet and Strong CP Invariance". In: *Phys. Rev. Lett.* 43, p. 103. DOI: 10.1103/PhysRevLett.43.103.

Kim, Jihn E. and Gianpaolo Carosi (2010). "Axions and the Strong CP Problem". In: *Rev. Mod. Phys.* 82. [Erratum: Rev.Mod.Phys. 91, 049902 (2019)], pp. 557–602. DOI: 10.1103/RevModPhys.82.557. arXiv: 0807.3125 [hep-ph].

Klaer, Vincent B. . and Guy D. Moore (2017). "The dark-matter axion mass". In: *JCAP* 11, p. 049. DOI: 10.1088/1475-7516/2017/11/049. arXiv: 1708.07521 [hep-ph].

Klimchitskaya, G. L., U. Mohideen, and V. M. Mostepanenko (2013). "Constraints on corrections to Newtonian gravity from two recent measurements of the Casimir interaction between metallic surfaces". In: *Phys. Rev. D* 87.12, p. 125031. DOI: 10.1103/PhysRevD.87.125031. arXiv: 1306.4979 [gr-qc].

Klimchitskaya, Galina L. and Vladimir M. Mostepanenko (2023). "How to Strengthen Constraints on Non-Newtonian Gravity from Measuring the Lateral Casimir Force". In: *Universe* 9.1, p. 34. DOI: 10.3390/universe9010034. arXiv: 2305.07884 [quant-ph].

Knapen, Simon et al. (2017a). "Searching for Axionlike Particles with Ultraperipheral Heavy-Ion Collisions". In: *Phys. Rev. Lett.* 118.17, p. 171801. DOI: 10.1103/PhysRevLett.118.171801. arXiv: 1607.06083 [hep-ph].

Knapen, Simon, Tongyan Lin, and Kathryn M. Zurek (2017b). "Light Dark Matter: Models and Constraints". In: *Phys. Rev. D* 96.11, p. 115021. DOI: 10.1103/PhysRevD.96.115021. arXiv: 1709.07882 [hep-ph].

Kotake, Kei (2013). "Multiple physical elements to determine the gravitational-wave signatures of core-collapse supernovae". In: *Comptes Rendus Physique* 14.4, pp. 318–351.

Kotake, Kei, Wakana Iwakami, et al. (2009). "Ray-Tracing Analysis of Anisotropic Neutrino Radiation for Estimating Gravitational Waves in Core-Collapse Supernovae". In: *Astrophys. J.* 704, pp. 951–963. DOI: 10.1088/0004-637X/704/2/951. arXiv: 0909.3622 [astro-ph.HE].

Kotake, Kei and Takami Kuroda (2017). "Gravitational waves from core-collapse supernovae". In: *Handbook of Supernovae*, p. 1671.

Krnjaic, Gordan (2016). "Probing Light Thermal Dark-Matter With a Higgs Portal Mediator". In: *Phys. Rev. D* 94.7, p. 073009. DOI: 10.1103/PhysRevD.94.073009. arXiv: 1512.04119 [hep-ph].

Kuroda, Takami, Tobias Fischer, et al. (2022). "Core-collapse Supernova Simulations and the Formation of Neutron Stars, Hybrid Stars, and Black

Holes". In: *Astrophys. J.* 924.1, p. 38. DOI: 10.3847/1538-4357/ac31a8. arXiv: 2109.01508 [astro-ph.HE].

Kuroda, Takami, Kei Kotake, et al. (2017). "Correlated Signatures of Gravitational-Wave and Neutrino Emission in Three-Dimensional General-Relativistic Core-Collapse Supernova Simulations". In: *Astrophys. J.* 851.1, p. 62. DOI: 10.3847/1538-4357/aa988d. arXiv: 1708.05252 [astro-ph.HE].

Langhoff, Kevin, Nadav Joseph Outmezguine, and Nicholas L. Rodd (2022). "Irreducible Axion Background". In: *Phys. Rev. Lett.* 129.24, p. 241101. DOI: 10.1103/PhysRevLett.129.241101. arXiv: 2209.06216 [hep-ph].

Lattimer, James M. and F. Douglas Swesty (1991). "A Generalized equation of state for hot, dense matter". In: *Nucl. Phys. A* 535, pp. 331–376. DOI: 10.1016/0375-9474(91)90452-C.

Lawson, Matthew et al. (2019). "Tunable axion plasma haloscopes". In: *Phys. Rev. Lett.* 123.14, p. 141802. DOI: 10.1103/PhysRevLett.123.141802. arXiv: 1904.11872 [hep-ph].

Lazarus, D. M. et al. (1992). "A Search for solar axions". In: *Phys. Rev. Lett.* 69, pp. 2333–2336. DOI: 10.1103/PhysRevLett.69.2333.

Lecce, Francesca et al. (2025). "Probing axionlike particles with multimessenger observations of neutron star mergers". In: *Phys. Rev. D* 112.2, p. 023001. DOI: 10.1103/krf3-lm4s. arXiv: 2504.02032 [hep-ph].

Lee, J. G. et al. (2020). "New Test of the Gravitational $1/r^2$ Law at Separations down to 52 μm". In: *Phys. Rev. Lett.* 124.10, p. 101101. DOI: 10.1103/PhysRevLett.124.101101. arXiv: 2002.11761 [hep-ex].

Leeuwen, F. van (2007). "Validation of the new Hipparcos reduction". In: *Astron. Astrophys.* 474, pp. 653–664. DOI: 10.1051/0004-6361:20078357. arXiv: 0708.1752 [astro-ph].

Leinson, L. B. (2014). "Axion mass limit from observations of the neutron star in Cassiopeia A". In: *JCAP* 08, p. 031. DOI: 10.1088/1475-7516/2014/08/031. arXiv: 1405.6873 [hep-ph].

Lella, Alessandro et al. (June 2023). "Getting the most on supernova axions". In: arXiv: 2306.01048 [hep-ph].

Lella, Alessandro, Francesca Calore, Pierluca Carenza, Christopher Eckner, et al. (2024). "Probing protoneutron stars with gamma-ray axionscopes". In: *JCAP* 11, p. 009. DOI: 10.1088/1475-7516/2024/11/009. arXiv: 2405.02395 [hep-ph].

Lella, Alessandro, Francesca Calore, Pierluca Carenza, and Alessandro Mirizzi (2024). "Constraining gravitational-wave backgrounds from conversions into photons in the Galactic magnetic field". In: *Phys. Rev. D* 110.8, p. 083042. DOI: 10.1103/PhysRevD.110.083042. arXiv: 2406.17853 [hep-ph].

Lella, Alessandro, Pierluca Carenza, et al. (2023). "Protoneutron stars as cosmic factories for massive axionlike particles". In: *Phys. Rev. D* 107.10, p. 103017. DOI: 10.1103/PhysRevD.107.103017. arXiv: 2211.13760 [hep-ph].

Lella, Alessandro, Eike Ravensburg, et al. (2024). "Supernova limits on QCD axionlike particles". In: *Phys. Rev. D* 110.4, p. 043019. DOI: 10.1103/PhysRevD.110.043019. arXiv: 2405.00153 [hep-ph].

Li, Hui-Ling et al. (2018). "Towards a complete reconstruction of supernova neutrino spectra in future large liquid-scintillator detectors". In: *Phys. Rev. D* 97.6, p. 063014. DOI: 10.1103/PhysRevD.97.063014. arXiv: 1712.06985 [hep-ph].

Li, Shirley Weishi et al. (June 2023). "Old Data, New Forensics: The First Second of SN 1987A Neutrino Emission". In: arXiv: 2306.08024 [astro-ph.HE].

Li, Weidong et al. (2011). "Nearby Supernova Rates from the Lick Observatory Supernova Search. III. The Rate-Size Relation, and the Rates as a Function of Galaxy Hubble Type and Colour". In: *Mon. Not. Roy. Astron. Soc.* 412, p. 1473. DOI: 10.1111/j.1365-2966.2011.18162.x. arXiv: 1006.4613 [astro-ph.SR].

Liebendoerfer, M. et al. (2004). "A Finite difference representation of neutrino radiation hydrodynamics for spherically symmetric general relativistic supernova simulations". In: *Astrophys. J. Suppl.* 150, pp. 263–316. DOI: 10.1086/380191. arXiv: astro-ph/0207036.

Loredo, Thomas J. and Don Q. Lamb (Dec. 1989). "Neutrinos from SN 1987A - Implications for cooling of the nascent neutron star and the mass of the electron antineutrino". In: *Annals of the New York Academy of Sciences* 571, pp. 601–630. DOI: 10.1111/j.1749-6632.1989.tb50547.x.

— (2002). "Bayesian analysis of neutrinos observed from supernova SN-1987A". In: *Phys. Rev. D* 65, p. 063002. DOI: 10.1103/PhysRevD.65.063002. arXiv: astro-ph/0107260.

Lorimer, Dunc R. (2004). "The galactic population and birth rate of radio pulsars". In: *IAU Symp.* 218, p. 105. arXiv: astro-ph/0308501.

Lucente, Giuseppe et al. (2020). "Heavy axion-like particles and core-collapse supernovae: constraints and impact on the explosion mechanism". In: *JCAP* 12, p. 008. DOI: 10.1088/1475-7516/2020/12/008. arXiv: 2008.04918 [hep-ph].

— (2022). "Axion signatures from supernova explosions through the nucleon electric-dipole portal". In: *Phys. Rev. D* 105.12, p. 123020. DOI: 10.1103/PhysRevD.105.123020. arXiv: 2203.15812 [hep-ph].

Lucente, Giuseppe and Pierluca Carenza (2021). "Supernova bound on axion-like particles coupled with electrons". In: *Phys. Rev. D* 104.10, p. 103007. DOI: 10.1103/PhysRevD.104.103007. arXiv: 2107.12393 [hep-ph].

Lucente, Giuseppe, Malte Heinlein, et al. (2024). "Simple fits for the neutrino luminosities from protoneutron star cooling". In: *Phys. Rev. D* 110.6, p. 063023. DOI: 10.1103/PhysRevD.110.063023. arXiv: 2405.00769 [astro-ph.HE].

Lucente, Giuseppe, Newton Nath, et al. (2022). "Probing high-energy solar axion flux with a large scintillation neutrino detector". In: *Phys. Rev. D* 106.12, p. 123007. DOI: 10.1103/PhysRevD.106.123007. arXiv: 2209.11780 [hep-ph].

Lujan-Peschard, C., G. Pagliaroli, and F. Vissani (2014). "Spectrum of Supernova Neutrinos in Ultra-pure Scintillators". In: *JCAP* 07, p. 051. DOI: 10.1088/1475-7516/2014/07/051. arXiv: 1402.6953 [astro-ph.SR].

Lunardini, Cecilia and Alexei Yu. Smirnov (2004). "Neutrinos from SN1987A: Flavor conversion and interpretation of results". In: *Astropart. Phys.* 21, pp. 703–720. DOI: 10.1016/j.astropartphys.2004.05.005. arXiv: hep-ph/0402128.

Lund, Tina, Andreas Marek, et al. (2010). "Fast time variations of supernova neutrino fluxes and their detectability". In: *Phys. Rev. D* 82, p. 063007. DOI: 10.1103/PhysRevD.82.063007. arXiv: 1006.1889 [astro-ph.HE].

Lund, Tina, Annop Wongwathanarat, et al. (2012). "Fast time variations of supernova neutrino signals from 3-dimensional models". In: *Phys. Rev. D* 86, p. 105031. DOI: 10.1103/PhysRevD.86.105031. arXiv: 1208.0043 [astro-ph.HE].

Maggiore, Michele (2007). *Gravitational Waves. Vol. 1: Theory and Experiments*. Oxford University Press. ISBN: 978-0-19-171766-6, 978-0-19-852074-0. DOI: 10.1093/acprof:oso/9780198570745.001.0001.

Maiani, L., R. Petronzio, and E. Zavattini (1986). "Effects of Nearly Massless, Spin Zero Particles on Light Propagation in a Magnetic Field". In: *Phys. Lett. B* 175, pp. 359–363. DOI: 10.1016/0370-2693(86)90869-5.

Marek, A., H. -Th. Janka, and E. Mueller (2009). "Equation-of-State Dependent Features in Shock-Oscillation Modulated Neutrino and Gravitational-Wave Signals from Supernovae". In: *Astron. Astrophys.* 496, p. 475. DOI: 10.1051/0004-6361/200810883. arXiv: 0808.4136 [astro-ph].

Martin, P. et al. (2012). "Galactic annihilation emission from nucleosynthesis positrons". In: *Astron. Astrophys.* 543, A3. DOI: 10.1051/0004-6361/201118721. arXiv: 1205.1194 [astro-ph.HE].

Martinez-Pinedo, G. et al. (2012). "Charged-current weak interaction processes in hot and dense matter and its impact on the spectra of neutrinos emitted from proto-neutron star cooling". In: *Phys. Rev. Lett.* 109, p. 251104. DOI: 10.1103/PhysRevLett.109.251104. arXiv: 1205.2793 [astro-ph.HE].

Masso, Eduard (2008). "Axions and their relatives". In: *Lect. Notes Phys.* 741. Ed. by Markus Kuster, Georg Raffelt, and Berta Beltran, pp. 83–94. DOI: 10.1007/978-3-540-73518-2_5. arXiv: hep-ph/0607215.

Masso, Eduard, Francesc Rota, and Gabriel Zsembinszki (2002). "On axion thermalization in the early universe". In: *Phys. Rev. D* 66, p. 023004. DOI: 10.1103/PhysRevD.66.023004. arXiv: hep-ph/0203221.

Mastrototaro, Leonardo et al. (2020). "Heavy sterile neutrino emission in core-collapse supernovae: Constraints and signatures". In: *JCAP* 01, p. 010. DOI: 10.1088/1475-7516/2020/01/010. arXiv: 1910.10249 [hep-ph].

Mayle, Ron, James R. Wilson, John R. Ellis, et al. (1988). "Constraints on Axions from SN 1987a". In: *Phys. Lett. B* 203, pp. 188–196. DOI: 10.1016/0370-2693(88)91595-X.

Mayle, Ron, James R. Wilson, and David N. Schramm (1986). "Neutrinos from Gravitational Collapse". In: *Nuovo Cim. C* 9, p. 443. DOI: 10.1007/BF02514862.

Mercuri, Simone (2009). "Peccei-Quinn mechanism in gravity and the nature of the Barbero-Immirzi parameter". In: *Phys. Rev. Lett.* 103, p. 081302. DOI: 10.1103/PhysRevLett.103.081302. arXiv: 0902.2764 [gr-qc].

Meyer, M. et al. (2017). "Fermi Large Area Telescope as a Galactic Supernovae Axionscope". In: *Phys. Rev. Lett.* 118.1, p. 011103. DOI: 10.1103/PhysRevLett.118.011103. arXiv: 1609.02350 [astro-ph.HE].

Mezzacappa, A. and S. W. Bruenn (1993). "A numerical method for solving the neutrino Boltzmann equation coupled to spherically symmetric stellar core collapse". In: *Astrophys. J.* 405, pp. 669–684. DOI: 10.1086/172395.

Mezzacappa, Anthony and Michele Zanolin (Jan. 2024). "Gravitational Waves from Neutrino-Driven Core Collapse Supernovae: Predictions, Detection, and Parameter Estimation". In: arXiv: 2401.11635 [astro-ph.HE].

Mignani, R. P. et al. (2013). "The birthplace and age of the isolated neutron star RX J1856.5-3754". In: *Mon. Not. Roy. Astron. Soc.* 429, p. 3517. DOI: 10.1093/mnras/sts627. arXiv: 1212.3141 [astro-ph.HE].

Mirizzi, Alessandro et al. (2006). "Earth matter effects in supernova neutrinos: Optimal detector locations". In: *JCAP* 05, p. 012. DOI: 10.1088/1475-7516/2006/05/012. arXiv: astro-ph/0604300.

— (2016). "Supernova Neutrinos: Production, Oscillations and Detection". In: *Riv. Nuovo Cim.* 39.1-2, pp. 1–112. DOI: 10.1393/ncr/i2016-10120-8. arXiv: 1508.00785 [astro-ph.HE].

Misner, Charles W., K. S. Thorne, and J. A. Wheeler (1973). *Gravitation*. San Francisco: W. H. Freeman. ISBN: 978-0-7167-0344-0, 978-0-691-17779-3.

Mohapatra, Rabindra N. et al. (1983). "Automatic Solution to the Strong CP Problem in $N = 1$ Supergravity Models". In: *Phys. Lett. B* 126, pp. 329–333. DOI: 10.1016/0370-2693(83)90174-0.

Moody, J. E. and Frank Wilczek (1984). "New Macroscopic Forces?" In: *Phys. Rev. D* 30, p. 130. DOI: 10.1103/PhysRevD.30.130.

Moriyama, Shigetaka et al. (1998). "Direct search for solar axions by using strong magnetic field and x-ray detectors". In: *Phys. Lett. B* 434, p. 147. DOI: 10.1016/S0370-2693(98)00766-7. arXiv: hep-ex/9805026.

Moroi, Takeo and Hitoshi Murayama (1998). "Axionic hot dark matter in the hadronic axion window". In: *Phys. Lett. B* 440, pp. 69–76. DOI: 10.1016/S0370-2693(98)01091-0. arXiv: hep-ph/9804291.

Morozova, Viktoriya et al. (2018). "The gravitational wave signal from core-collapse supernovae". In: *Astrophys. J.* 861.1, p. 10. DOI: 10.3847/1538-4357/aac5f1. arXiv: 1801.01914 [astro-ph.HE].

Mostepanenko, Vladimir M. and Galina L. Klimchitskaya (2020). "The State of the Art in Constraining Axion-to-Nucleon Coupling and Non-Newtonian Gravity from Laboratory Experiments". In: *Universe* 6.9. Ed. by Vladimir M. Mostepanenko, Alexei A. Starobinsky, and Elena N. Velichko, p. 147. DOI: 10.3390/universe6090147. arXiv: 2009.04517 [hep-ph].

Motch, C. et al. (2009). "Proper motions of thermally emitting isolated neutron stars measured with Chandra". In: *Astron. Astrophys.* 497, p. 423. DOI: 10.1051/0004-6361/200811052. arXiv: 0901.1006 [astro-ph.HE].

Mueller, Bernhard, Hans-Thomas Janka, and Andreas Marek (2013). "A New Multi-Dimensional General Relativistic Neutrino Hydrodynamics Code of Core-Collapse Supernovae III. Gravitational Wave Signals from Supernova Explosion Models". In: *Astrophys. J.* 766, p. 43. DOI: 10.1088/0004-637X/766/1/43. arXiv: 1210.6984 [astro-ph.SR].

Mueller, Ewald and Hans-Thomas Janka (1997). "Gravitational radiation from convective instabilities in Type II supernova explosions". In: *Astron. Astrophys.* 317, pp. 140–163.

Mukhopadhyay, Mainak, Carlos Cardona, and Cecilia Lunardini (2021). "The neutrino gravitational memory from a core collapse supernova: phenomenology and physics potential". In: *JCAP* 07, p. 055. DOI: 10.1088/1475-7516/2021/07/055. arXiv: 2105.05862 [astro-ph.HE].

Mukhopadhyay, Mainak, Zidu Lin, and Cecilia Lunardini (2022). "Memory-triggered supernova neutrino detection". In: *Phys. Rev. D* 106.4, p. 043020. DOI: 10.1103/PhysRevD.106.043020. arXiv: 2110.14657 [astro-ph.HE].

Mukhopadhyay, Mainak, Cecilia Lunardini, et al. (2020). "Presupernova neutrinos: directional sensitivity and prospects for progenitor identification". In: *Astrophys. J.* 899.2, p. 153. DOI: 10.3847/1538-4357/ab99a6. arXiv: 2004.02045 [astro-ph.HE].

Muller, E., H. -Th. Janka, and A. Wongwathanarat (2012). "Parametrized 3D models of neutrino-driven supernova explosions: Neutrino emission asymmetries and gravitational-wave signals". In: *Astron. Astrophys.* 537, A63. DOI: 10.1051/0004-6361/201117611. arXiv: 1106.6301 [astro-ph.SR].

Müller, Bernhard (Mar. 2017). "Gravitational Waves from Core-Collapse Supernovae". In: arXiv: 1703.04633 [astro-ph.HE].

Müller, Bernhard, Hans-Thomas Janka, et al. (Dec. 2011). "Core-Collapse Supernovae: Explosion Dynamics, Neutrinos and Gravitational Waves". In: *Hamburg Neutrinos From Supernova Explosions*, pp. 14–21. DOI: 10.3204/DESY-PROC-2011-03/mueller. arXiv: 1112.1913 [astro-ph.SR].

Müller, Eike et al. (June 2023a). "Constraining MeV-scale axion-like particles with Fermi-LAT observations of SN 2023ixf". In: arXiv: 2306.16397 [astro-ph.HE].

Müller, Eike et al. (Apr. 2023b). "Investigating the gamma-ray burst from decaying MeV-scale axion-like particles produced in supernova explosions". In: arXiv: 2304.01060 [astro-ph.HE].

Müller, Ewald, Bruce Fryxell, and David Arnett (1991). "Instability and clumping in SN 1987A". In: *Astronomy and Astrophysics (ISSN 0004-6361), vol. 251, no. 2, Nov. 1991, p. 505-514.* 251, pp. 505–514.

Murphy, Jeremiah W., Christian D. Ott, and Adam Burrows (2009). "A Model for Gravitational Wave Emission from Neutrino-Driven Core-Collapse Supernovae". In: *Astrophys. J.* 707, pp. 1173–1190. DOI: 10.1088/0004-637X/707/2/1173. arXiv: 0907.4762 [astro-ph.SR].

Navas, S. et al. (2024). "Review of particle physics". In: *Phys. Rev. D* 110.3, p. 030001. DOI: 10.1103/PhysRevD.110.030001.

Nelson, Ann E. (1984). "Naturally Weak CP Violation". In: *Phys. Lett. B* 136, pp. 387–391. DOI: 10.1016/0370-2693(84)92025-2.

Ning, Orion and Benjamin R. Safdi (2025a). "Leading Axion-Photon Sensitivity with NuSTAR Observations of M82 and M87". In: *Phys. Rev. Lett.* 134.17, p. 171003. DOI: 10.1103/PhysRevLett.134.171003. arXiv: 2404.14476 [hep-ph].

— (Mar. 2025b). "Probing the Axion-Electron Coupling with NuSTAR Observations of Galaxies". In: arXiv: 2503.09682 [hep-ph].

Noordhuis, Dion et al. (Sept. 2022). "Novel Constraints on Axions Produced in Pulsar Polar Cap Cascades". In: arXiv: 2209.09917 [hep-ph].

O'Connor, Evan and Christian D. Ott (2011). "Black Hole Formation in Failing Core-Collapse Supernovae". In: *Astrophys. J.* 730, p. 70. DOI: 10.1088/0004-637X/730/2/70. arXiv: 1010.5550 [astro-ph.HE].

O'Hare, Ciaran (July 2020). *cajohare/AxionLimits: AxionLimits*. https://cajohare.github.io/AxionLimits/. Version v1.0. DOI: 10.5281/zenodo.3932430.

O'Hare, Ciaran A. J. et al. (2020). "Axion helioscopes as solar magnetometers". In: *Phys. Rev. D* 102.4, p. 043019. DOI: 10.1103/PhysRevD.102.043019. arXiv: 2006.10415 [astro-ph.CO].

Oberauer, L. et al. (1993). "Supernova bounds on neutrino radiative decays". In: *Astropart. Phys.* 1, pp. 377–386. DOI: 10.1016/0927-6505(93)90004-W.

Okawa, Shohei, Maxim Pospelov, and Adam Ritz (2022). "Long-range axion forces and hadronic CP violation". In: *Phys. Rev. D* 105.7, p. 075003. DOI: 10.1103/PhysRevD.105.075003. arXiv: 2111.08040 [hep-ph].

Ott, Christian D (2009a). "The gravitational-wave signature of core-collapse supernovae". In: *Classical and Quantum Gravity* 26.6, p. 063001.

— (2009b). "The Gravitational Wave Signature of Core-Collapse Supernovae". In: *Class. Quant. Grav.* 26, p. 063001. DOI: 10.1088/0264-9381/26/6/063001. arXiv: 0809.0695 [astro-ph].

Ouchi, Ryoma and Keiichi Maeda (2017). "Radii and Mass-loss Rates of Type IIb Supernova Progenitors". In: *Astrophys. J.* 840.2, p. 90. DOI: 10.3847/1538-4357/aa6ea9. arXiv: 1705.02430 [astro-ph.HE].

Page, Dany (Sept. 2016). *NSCool: Neutron star cooling code*. Astrophysics Source Code Library, record ascl:1609.009.

Page, Dany, Mikhail V. Beznogov, et al. (2020). "NS 1987A in SN 1987A". In: *Astrophys. J.* 898.2, p. 125. DOI: 10.3847/1538-4357/ab93c2. arXiv: 2004.06078 [astro-ph.HE].

Page, Dany, Madappa Prakash, et al. (2011). "Rapid Cooling of the Neutron Star in Cassiopeia A Triggered by Neutron Superfluidity in Dense Matter". In: *Phys. Rev. Lett.* 106, p. 081101. DOI: 10.1103/PhysRevLett.106.081101. arXiv: 1011.6142 [astro-ph.HE].

Pagliaroli, G. et al. (2009). "Improved analysis of SN1987A antineutrino events". In: *Astropart. Phys.* 31, pp. 163–176. DOI: 10.1016/j.astropartphys.2008.12.010. arXiv: 0810.0466 [astro-ph].

Pajkos, Michael A. et al. (2019). "Features of Accretion Phase Gravitational Wave Emission from Two-dimensional Rotating Core-Collapse Supernovae". In: *Astrophys. J.* 878.1, p. 13. DOI: 10.3847/1538-4357/ab1de2. arXiv: 1901.09055 [astro-ph.HE].

Pan, Kuo-Chuan et al. (2018). "Equation of State Dependent Dynamics and Multi-messenger Signals from Stellar-mass Black Hole Formation". In: *Astrophys. J.* 857.1, p. 13. DOI: 10.3847/1538-4357/aab71d. arXiv: 1710.01690 [astro-ph.HE].

Payez, Alexandre et al. (2015). "Revisiting the SN1987A gamma-ray limit on ultralight axion-like particles". In: *JCAP* 02, p. 006. DOI: 10.1088/1475-7516/2015/02/006. arXiv: 1410.3747 [astro-ph.HE].

Peccei, R. D. (2008). "The Strong CP problem and axions". In: *Lect. Notes Phys.* 741. Ed. by Markus Kuster, Georg Raffelt, and Berta Beltran,

pp. 3–17. DOI: 10.1007/978-3-540-73518-2_1. arXiv: hep-ph/0607268.

Peccei, R. D. and Helen R. Quinn (1977a). "Constraints Imposed by CP Conservation in the Presence of Instantons". In: *Phys. Rev. D* 16, pp. 1791–1797. DOI: 10.1103/PhysRevD.16.1791.

— (1977b). "CP Conservation in the Presence of Instantons". In: *Phys. Rev. Lett.* 38, pp. 1440–1443. DOI: 10.1103/PhysRevLett.38.1440.

Pires, A. M. et al. (2019). "A deep XMM-Newton look on the thermally emitting isolated neutron star RX J1605.3+3249". In: *Astron. Astrophys.* 623, A73. DOI: 10.1051/0004-6361/201834801. arXiv: 1901.08533 [astro-ph.HE].

Plakkot, V. et al. (2023). "CP-violating axion interactions II: axions as dark matter". In: *JHEP* 11, p. 012. DOI: 10.1007/JHEP11(2023)012. arXiv: 2306.07065 [hep-ph].

Pokotilovski, Yu. N. (2006). "Constraints on new interactions from neutron scattering experiments". In: *Phys. Atom. Nucl.* 69, pp. 924–931. DOI: 10.1134/S1063778806060020. arXiv: hep-ph/0601157.

Pospelov, M. (1998). "CP odd interaction of axion with matter". In: *Phys. Rev. D* 58, p. 097703. DOI: 10.1103/PhysRevD.58.097703. arXiv: hep-ph/9707431 [hep-ph].

Pospelov, Maxim and Adam Ritz (2005). "Electric dipole moments as probes of new physics". In: *Annals Phys.* 318, pp. 119–169. DOI: 10.1016/j.aop.2005.04.002. arXiv: hep-ph/0504231 [hep-ph].

Potekhin, A. Y. et al. (2020). "Thermal luminosities of cooling neutron stars". In: *Mon. Not. Roy. Astron. Soc.* 496.4, pp. 5052–5071. DOI: 10.1093/mnras/staa1871. arXiv: 2006.15004 [astro-ph.HE].

Powell, Jade and Bernhard Müller (2019). "Gravitational Wave Emission from 3D Explosion Models of Core-Collapse Supernovae with Low and Normal Explosion Energies". In: *Mon. Not. Roy. Astron. Soc.* 487.1, pp. 1178–1190. DOI: 10.1093/mnras/stz1304. arXiv: 1812.05738 [astro-ph.HE].

— (2020). "Three-dimensional core-collapse supernova simulations of massive and rotating progenitors". In: *Mon. Not. Roy. Astron. Soc.* 494.4, pp. 4665–4675. DOI: 10.1093/mnras/staa1048. arXiv: 2002.10115 [astro-ph.HE].

— (2024). "The gravitational-wave emission from the explosion of a 15 solar mass star with rotation and magnetic fields". In: *Mon. Not. Roy. Astron.*

Soc. 532.4, pp. 4326–4339. DOI: 10.1093/mnras/stae1731. arXiv: 2406.09691 [astro-ph.HE].

Preskill, John, Mark B. Wise, and Frank Wilczek (1983). "Cosmology of the Invisible Axion". In: *Phys. Lett. B* 120. Ed. by M. A. Srednicki, pp. 127–132. DOI: 10.1016/0370-2693(83)90637-8.

Priya, Alankrita and Cecilia Lunardini (2017). "Diffuse neutrinos from luminous and dark supernovae: prospects for upcoming detectors at the $O(10)$ kt scale". In: *JCAP* 11, p. 031. DOI: 10.1088/1475-7516/2017/11/031. arXiv: 1705.02122 [astro-ph.HE].

Punturo, M. et al. (2010). "The Einstein Telescope: A third-generation gravitational wave observatory". In: *Class. Quant. Grav.* 27. Ed. by Fulvio Ricci, p. 194002. DOI: 10.1088/0264-9381/27/19/194002.

Radice, David et al. (2019). "Characterizing the Gravitational Wave Signal from Core-Collapse Supernovae". In: *Astrophys. J. Lett.* 876.1, p. L9. DOI: 10.3847/2041-8213/ab191a. arXiv: 1812.07703 [astro-ph.HE].

Raffelt, G. G. (May 1996). *Stars as laboratories for fundamental physics: The astrophysics of neutrinos, axions, and other weakly interacting particles.* ISBN: 978-0-226-70272-8.

Raffelt, Georg and David Seckel (1988). "Bounds on Exotic Particle Interactions from SN 1987a". In: *Phys. Rev. Lett.* 60, p. 1793. DOI: 10.1103/PhysRevLett.60.1793.

— (1991). "Multiple scattering suppression of the bremsstrahlung emission of neutrinos and axions in supernovae". In: *Phys. Rev. Lett.* 67, pp. 2605–2608. DOI: 10.1103/PhysRevLett.67.2605.

— (1995). "A selfconsistent approach to neutral current processes in supernova cores". In: *Phys. Rev. D* 52, pp. 1780–1799. DOI: 10.1103/PhysRevD.52.1780. arXiv: astro-ph/9312019.

Raffelt, Georg and Leo Stodolsky (1988). "Mixing of the Photon with Low Mass Particles". In: *Phys. Rev. D* 37, p. 1237. DOI: 10.1103/PhysRevD.37.1237.

Raffelt, Georg G. (1990a). "Astrophysical methods to constrain axions and other novel particle phenomena". In: *Phys. Rept.* 198, pp. 1–113. DOI: 10.1016/0370-1573(90)90054-6.

— (1990b). "What Have We Learned From SN 1987A?" In: *Mod. Phys. Lett. A* 5. Ed. by H. Miettinen, pp. 2581–2592. DOI: 10.1142/S0217732390003000.

Raffelt, Georg G. (2008). "Astrophysical axion bounds". In: *Lect. Notes Phys.* 741. Ed. by Markus Kuster, Georg Raffelt, and Berta Beltran, pp. 51–71. DOI: 10.1007/978-3-540-73518-2_3. arXiv: hep-ph/0611350.

Raffelt, Georg G. and David S. P. Dearborn (1988). "Bounds on Weakly Interacting Particles From Observational Lifetimes of Helium Burning Stars". In: *Phys. Rev. D* 37, pp. 549–551. DOI: 10.1103/PhysRevD.37.549.

Raffelt, Georg G. and otheres (2011). "The meV mass frontier of axion physics". In: *Phys. Rev. D* 84, p. 103008. DOI: 10.1103/PhysRevD.84.103008. arXiv: 1110.6397 [hep-ph].

Raffelt, Georg G. and Shun Zhou (2011). "Supernova bound on keV-mass sterile neutrinos reexamined". In: *Phys. Rev. D* 83, p. 093014. DOI: 10.1103/PhysRevD.83.093014. arXiv: 1102.5124 [hep-ph].

Rampp, Markus and H. Thomas Janka (2002). "Radiation hydrodynamics with neutrinos: Variable Eddington factor method for core collapse supernova simulations". In: *Astron. Astrophys.* 396, p. 361. DOI: 10.1051/0004-6361:20021398. arXiv: astro-ph/0203101.

Rauscher, T. (2011). "The Path to Improved Reaction Rates for Astrophysics". In: *Int. J. Mod. Phys. E* 20, p. 1071.

— (2018). "computer code SPECTRUM, unpublished".

— (2010 - 2022). "computer code SMARAGD, version 0.9.3s, unpublished".

Reynolds, Christopher S. et al. (2020). "Astrophysical limits on very light axion-like particles from Chandra grating spectroscopy of NGC 1275". In: *Astrophys. J.* 890, p. 59. DOI: 10.3847/1538-4357/ab6a0c. arXiv: 1907.05475 [hep-ph].

Richardson, Colter J. et al. (2022). "Modeling core-collapse supernovae gravitational-wave memory in laser interferometric data". In: *Phys. Rev. D* 105.10, p. 103008. DOI: 10.1103/PhysRevD.105.103008. arXiv: 2109.01582 [astro-ph.HE].

Richers, Sherwood et al. (2017). "Equation of State Effects on Gravitational Waves from Rotating Core Collapse". In: *Phys. Rev. D* 95.6, p. 063019. DOI: 10.1103/PhysRevD.95.063019. arXiv: 1701.02752 [astro-ph.HE].

Roberts, L. F. et al. (2012). "Proto-Neutron Star Cooling with Convection: The Effect of the Symmetry Energy". In: *Phys. Rev. Lett.* 108, p. 061103. DOI: 10.1103/PhysRevLett.108.061103. arXiv: 1112.0335 [astro-ph.HE].

Rodriguez, M. C. et al. (2023). "Three approaches for the classification of protoneutron star oscillation modes". In: *Mon. Not. Roy. Astron. Soc.* 523.2, pp. 2236–2246. DOI: 10.1093/mnras/stad1459. arXiv: 2304.00033 [astro-ph.HE].

Rozwadowska, Karolina, Francesco Vissani, and Enrico Cappellaro (2021). "On the rate of core collapse supernovae in the milky way". In: *New Astron.* 83, p. 101498. DOI: 10.1016/j.newast.2020.101498. arXiv: 2009.03438 [astro-ph.HE].

Ruoso, G. et al. (1992). "Limits on light scalar and pseudoscalar particles from a photon regeneration experiment". In: *Z. Phys. C* 56, pp. 505–508. DOI: 10.1007/BF01474722.

Saikawa, Ken'ichi et al. (2024). "Spectrum of global string networks and the axion dark matter mass". In: *JCAP* 10, p. 043. DOI: 10.1088/1475-7516/2024/10/043. arXiv: 2401.17253 [hep-ph].

Sartore, N. et al. (2012). "Spectral monitoring of RX J1856.5-3754 with XMM-Newton. Analysis of EPIC-pn data". In: *Astron. Astrophys.* 541, A66. DOI: 10.1051/0004-6361/201118489. arXiv: 1202.2121 [astro-ph.HE].

Schierholz, G. (1994). "Towards a dynamical solution of the strong CP problem". In: *Nucl. Phys. B Proc. Suppl.* 37.1. Ed. by Y. Kuno and Y. Okada, pp. 203–210. DOI: 10.1016/0920-5632(94)90751-X. arXiv: hep-lat/9403012.

Scholberg, Kate (2012). "Supernova Neutrino Detection". In: *Ann. Rev. Nucl. Part. Sci.* 62, pp. 81–103. DOI: 10.1146/annurev-nucl-102711-095006. arXiv: 1205.6003 [astro-ph.IM].

Sedrakian, Armen (2016). "Axion cooling of neutron stars". In: *Phys. Rev. D* 93.6, p. 065044. DOI: 10.1103/PhysRevD.93.065044. arXiv: 1512.07828 [astro-ph.HE].

Shi, X. and G. Sigl (1994). "A Type II supernovae constraint on electron-neutrino - sterile-neutrino mixing". In: *Phys. Lett. B* 323. [Erratum: Phys.Lett.B 324, 516–516 (1994)], pp. 360–366. DOI: 10.1016/0370-2693(94)91232-7. arXiv: hep-ph/9312247.

Shifman, Mikhail A., A. I. Vainshtein, and Valentin I. Zakharov (1980). "Can Confinement Ensure Natural CP Invariance of Strong Interactions?" In: *Nucl. Phys. B* 166, pp. 493–506. DOI: 10.1016/0550-3213(80)90209-6.

Siegert, Thomas et al. (2016). "Gamma-ray spectroscopy of Positron Annihilation in the Milky Way". In: *Astron. Astrophys.* 586, A84. DOI: 10.1051/0004-6361/201527510. arXiv: 1512.00325 [astro-ph.HE].

— (2019). "Constraints on positron annihilation kinematics in the inner Galaxy". In: *Astron. Astrophys.* 627, A126. DOI: 10.1051/0004-6361/201833856. arXiv: 1906.00498 [astro-ph.HE].

Sikivie, P. (1983). "Experimental Tests of the Invisible Axion". In: *Phys. Rev. Lett.* 51. Ed. by M. A. Srednicki. [Erratum: Phys.Rev.Lett. 52, 695 (1984)], pp. 1415–1417. DOI: 10.1103/PhysRevLett.51.1415.

Sikivie, P., N. Sullivan, and D. B. Tanner (2014). "Proposal for Axion Dark Matter Detection Using an LC Circuit". In: *Phys. Rev. Lett.* 112.13, p. 131301. DOI: 10.1103/PhysRevLett.112.131301. arXiv: 1310.8545 [hep-ph].

Sikivie, Pierre (1985). "Detection Rates for 'Invisible' Axion Searches". In: *Phys. Rev. D* 32. [Erratum: Phys.Rev.D 36, 974 (1987)], p. 2988. DOI: 10.1103/PhysRevD.36.974.

— (2008). "Axion Cosmology". In: *Lect. Notes Phys.* 741. Ed. by Markus Kuster, Georg Raffelt, and Berta Beltran, pp. 19–50. DOI: 10.1007/978-3-540-73518-2_2. arXiv: astro-ph/0610440.

— (2021). "Invisible Axion Search Methods". In: *Rev. Mod. Phys.* 93.1, p. 015004. DOI: 10.1103/RevModPhys.93.015004. arXiv: 2003.02206 [hep-ph].

Sirunyan, Albert M et al. (2019). "Evidence for light-by-light scattering and searches for axion-like particles in ultraperipheral PbPb collisions at $\sqrt{s_{\mathrm{NN}}} = 5.02$ TeV". In: *Phys. Lett. B* 797, p. 134826. DOI: 10.1016/j.physletb.2019.134826. arXiv: 1810.04602 [hep-ex].

Smith, G. L. et al. (2000). "Short range tests of the equivalence principle". In: *Phys. Rev. D* 61, p. 022001. DOI: 10.1103/PhysRevD.61.022001. arXiv: 2405.10982 [gr-qc].

Springmann, Konstantin et al. (2025). "From supernovae to neutron stars: a systematic approach to axion production at finite density". In: *JHEP* 02, p. 138. DOI: 10.1007/JHEP02(2025)138. arXiv: 2410.10945 [hep-ph].

Srednicki, Mark (1985). "Axion Couplings to Matter. 1. CP Conserving Parts". In: *Nucl. Phys. B* 260, pp. 689–700. DOI: 10.1016/0550-3213(85)90054-9.

Stacy, J. G. et al. (Jan. 2008). "Limits on MeV Gamma-Ray Emission from Active Galaxies and Other Unidentified High-Latitude Gamma-Ray Sources

Observed with COMPTEL". In: *International Cosmic Ray Conference*. Vol. 3. International Cosmic Ray Conference, pp. 1085–1088.

Steiner, Andrew W., Matthias Hempel, and Tobias Fischer (2013). "Core-collapse supernova equations of state based on neutron star observations". In: *Astrophys. J.* 774, p. 17. DOI: 10.1088/0004-637X/774/1/17. arXiv: 1207.2184 [astro-ph.SR].

Stern, I. (2016). "ADMX Status". In: *PoS* ICHEP2016, p. 198. DOI: 10.22323/1.282.0198. arXiv: 1612.08296 [physics.ins-det].

Stockinger, G. et al. (2020). "Three-dimensional Models of Core-collapse Supernovae From Low-mass Progenitors With Implications for Crab". In: *Mon. Not. Roy. Astron. Soc.* 496.2, pp. 2039–2084. DOI: 10.1093/mnras/staa1691. arXiv: 2005.02420 [astro-ph.HE].

Stoica, S. et al. (2009). "Pion mass effects on axion emission from neutron stars through NN bremsstrahlung processes". In: *Nucl. Phys. A* 828. [Erratum: Nucl.Phys.A 832, 148 (2010)], pp. 439–449. DOI: 10.1016/j.nuclphysa.2009.07.007. arXiv: 0906.3134 [nucl-th].

Straniero, O. et al. (2020). "The RGB tip of galactic globular clusters and the revision of the axion-electron coupling bound". In: *Astron. Astrophys.* 644, A166. DOI: 10.1051/0004-6361/202038775. arXiv: 2010.03833 [astro-ph.SR].

Strong, A. W., K. Bennett, et al. (Dec. 1994a). "Diffuse continuum gamma rays from the Galaxy observed by COMPTEL." In: *Astronomy & Astrophysics* 292, pp. 82–91.

— (Dec. 1994b). "Diffuse continuum gamma rays from the Galaxy observed by COMPTEL." In: *A&A* 292, pp. 82–91.

Strong, Andrew W. et al. (2005). "Gamma-ray continuum emission from the inner galactic region as observed with integral/spi". In: *Astron. Astrophys.* 444, p. 495. DOI: 10.1051/0004-6361:20053798. arXiv: astro-ph/0509290.

Strong, Andrew W., Igor V. Moskalenko, and Olaf Reimer (Oct. 2004). "Diffuse Galactic Continuum Gamma Rays: A Model Compatible with EGRET Data and Cosmic-Ray Measurements". In: *The Astrophysical Journal* 613.2, p. 962. DOI: 10.1086/423193. URL: https://dx.doi.org/10.1086/423193.

Sukhbold, Tuguldur, Stan Woosley, and Alexander Heger (2018). "A High-resolution Study of Presupernova Core Structure". In: *Astrophys. J.* 860.2, p. 93. DOI: 10.3847/1538-4357/aac2da. arXiv: 1710.03243 [astro-ph.HE].

Sumiyoshi, Kohsuke et al. (2005). "Postbounce evolution of core-collapse supernovae: Long-term effects of equation of state". In: *Astrophys. J.* 629, pp. 922–932. DOI: 10.1086/431788. arXiv: astro-ph/0506620.

Sung, Allan et al. (2019). "New constraint from supernova explosions on light particles beyond the Standard Model". In: *Phys. Rev. D* 99.12, p. 121305. DOI: 10.1103/PhysRevD.99.121305. arXiv: 1903.07923 [hep-ph].

Sushkov, A. O. et al. (2011). "New Experimental Limits on Non-Newtonian Forces in the Micrometer Range". In: *Phys. Rev. Lett.* 107, p. 171101. DOI: 10.1103/PhysRevLett.107.171101. arXiv: 1108.2547 [quant-ph].

Suzuki, Hiromasa, Aya Bamba, and Shinpei Shibata (2021). "Quantitative Age Estimation of Supernova Remnants and Associated Pulsars". In: *Astrophys. J.* 914.2, p. 103. DOI: 10.3847/1538-4357/abfb02. arXiv: 2104.10052 [astro-ph.HE].

Takami, Kentaro, Luciano Rezzolla, and Luca Baiotti (2015). "Spectral properties of the post-merger gravitational-wave signal from binary neutron stars". In: *Phys. Rev. D* 91.6, p. 064001. DOI: 10.1103/PhysRevD.91.064001. arXiv: 1412.3240 [gr-qc].

Takiwaki, Tomoya, Kei Kotake, and Thierry Foglizzo (2021). "Insights into non-axisymmetric instabilities in three-dimensional rotating supernova models with neutrino and gravitational-wave signatures". In: *Mon. Not. Roy. Astron. Soc.* 508.1, pp. 966–985. DOI: 10.1093/mnras/stab2607. arXiv: 2107.02933 [astro-ph.HE].

Tamborra, Irene, Florian Hanke, et al. (2013). "Neutrino signature of supernova hydrodynamical instabilities in three dimensions". In: *Phys. Rev. Lett.* 111.12, p. 121104. DOI: 10.1103/PhysRevLett.111.121104. arXiv: 1307.7936 [astro-ph.SR].

Tamborra, Irene, Georg Raffelt, et al. (2014). "Neutrino emission characteristics and detection opportunities based on three-dimensional supernova simulations". In: *Phys. Rev. D* 90.4, p. 045032. DOI: 10.1103/PhysRevD.90.045032. arXiv: 1406.0006 [astro-ph.SR].

Tan, Wen-Hai et al. (2020). "Improvement for Testing the Gravitational Inverse-Square Law at the Submillimeter Range". In: *Phys. Rev. Lett.* 124.5, p. 051301. DOI: 10.1103/PhysRevLett.124.051301.

Tan, Wen-Hai et al. (2016). "New Test of the Gravitational Inverse-Square Law at the Submillimeter Range with Dual Modulation and Compensation". In: *Phys. Rev. Lett.* 116.13, p. 131101. DOI: 10.1103/PhysRevLett.116.131101.

Taylor, T. R. and G. Veneziano (1988). "Dilaton Couplings at Large Distances". In: *Phys. Lett. B* 213, pp. 450–454. DOI: 10.1016/0370-2693(88)91290-7.

Tetzlaff, Nina, Thomas Eisenbeiss, et al. (2011). "The origin of RXJ1856.5-3754 and RXJ0720.4-3125 – updated using new parallax measurements". In: *Mon. Not. Roy. Astron. Soc.* 417, p. 617. DOI: 10.1111/j.1365-2966.2011.19302.x. arXiv: 1107.1673 [astro-ph.GA].

Tetzlaff, Nina, Janos G. Schmidt, et al. (2012). "Neutron stars from young nearby associations the origin of RXJ1605.3+3249". In: *Publ. Astron. Soc. Austral.* 29, p. 98. DOI: 10.1071/AS11057. arXiv: 1202.1388 [astro-ph.GA].

Thorsett, S. E. et al. (2003). "Pulsar psr b0656+14, the monogem ring, and the origin of the 'knee' in the primary cosmic ray spectrum". In: *Astrophys. J. Lett.* 592, pp. L71–L74. DOI: 10.1086/377682. arXiv: astro-ph/0306462.

Tino, G. M. et al. (2020). "Precision Gravity Tests and the Einstein Equivalence Principle". In: *Prog. Part. Nucl. Phys.* 112, p. 103772. DOI: 10.1016/j.ppnp.2020.103772. arXiv: 2002.02907 [gr-qc].

Torre Luque, Pedro de la et al. (2022). "FLUKA cross sections for cosmic-ray interactions with the DRAGON2 code". In: *JCAP* 07.07, p. 008. DOI: 10.1088/1475-7516/2022/07/008. arXiv: 2202.03559 [astro-ph.HE].

Torres-Forné, Alejandro et al. (2019). "Universal Relations for Gravitational-Wave Asteroseismology of Protoneutron Stars". In: *Phys. Rev. Lett.* 123.5. [Erratum: Phys.Rev.Lett. 127, 239901 (2021)], p. 051102. DOI: 10.1103/PhysRevLett.127.239901. arXiv: 1902.10048 [gr-qc].

Totani, T. et al. (1998). "Future detection of supernova neutrino burst and explosion mechanism". In: *Astrophys. J.* 496, pp. 216–225. DOI: 10.1086/305364. arXiv: astro-ph/9710203.

Touboul, Pierre et al. (2022). "MICROSCOPE Mission: Final Results of the Test of the Equivalence Principle". In: *Phys. Rev. Lett.* 129.12, p. 121102. DOI: 10.1103/PhysRevLett.129.121102. arXiv: 2209.15487 [gr-qc].

Tu, Liang-Cheng et al. (2007). "Null Test of Newtonian Inverse-Square Law at Submillimeter Range with a Dual-Modulation Torsion Pendulum". In: *Phys. Rev. Lett.* 98, p. 201101. DOI: 10.1103/PhysRevLett.98.201101.

Tubbs, David L. et al. (Dec. 1979). "NEUTRINO ENERGY EQUILIBRATION MODELS". In.

Turner, Michael S. (1978). "Gravitational Radiation from Supernova Neutrino Bursts". In: *Nature* 274, pp. 565–566. DOI: 10.1038/274565a0.

— (1988). "Axions from SN 1987a". In: *Phys. Rev. Lett.* 60, p. 1797. DOI: 10.1103/PhysRevLett.60.1797.

— (1992). "Dirac neutrinos and SN1987A". In: *Phys. Rev. D* 45, pp. 1066–1075. DOI: 10.1103/PhysRevD.45.1066.

Van Bibber, K. et al. (1987). "Proposed experiment to produce and detect light pseudoscalars". In: *Phys. Rev. Lett.* 59, pp. 759–762. DOI: 10.1103/PhysRevLett.59.759.

Vartanyan, David and Adam Burrows (2020). "Gravitational Waves from Neutrino Emission Asymmetries in Core-collapse Supernovae". In: *Astrophys. J.* 901.2, p. 108. DOI: 10.3847/1538-4357/abafac. arXiv: 2007.07261 [astro-ph.HE].

Vartanyan, David, Adam Burrows, et al. (2023). "Gravitational-wave signature of core-collapse supernovae". In: *Phys. Rev. D* 107.10, p. 103015. DOI: 10.1103/PhysRevD.107.103015. arXiv: 2302.07092 [astro-ph.HE].

Vasilakis, G. et al. (2009). "Limits on new long range nuclear spin-dependent forces set with a K - He-3 co-magnetometer". In: *Phys. Rev. Lett.* 103, p. 261801. DOI: 10.1103/PhysRevLett.103.261801. arXiv: 0809.4700 [physics.atom-ph].

Vecchi, Luca (2017). "Spontaneous CP violation and the strong CP problem". In: *JHEP* 04, p. 149. DOI: 10.1007/JHEP04(2017)149. arXiv: 1412.3805 [hep-ph].

Venugopalan, Gautam et al. (Dec. 2024). "Search for new interactions at the micron scale with a vector force sensor". In: arXiv: 2412.13167 [hep-ex].

Wang, Wei et al. (2006). "Could electron-positron annihilation lines in the galactic center result from pulsar winds?" In: *Astron. Astrophys.* 446, pp. 943–948. DOI: 10.1051/0004-6361:20053559. arXiv: astro-ph/0509760.

Wei, Li-Wei (2024). "Towards the first axion search results of the Any Light Particle Search II experiment". In: *PoS* TAUP2023, p. 049. DOI: 10.22323/1.441.0049. arXiv: 2401.14773 [hep-ex].

Weinberg, Steven (1975). "The U(1) Problem". In: *Phys. Rev. D* 11, pp. 3583–3593. DOI: 10.1103/PhysRevD.11.3583.

— (1978). "A New Light Boson?" In: *Phys. Rev. Lett.* 40, pp. 223–226. DOI: 10.1103/PhysRevLett.40.223.

Wenger, Marc et al. (2000). "The simbad astronomical database". In: *Astron. Astrophys. Suppl. Ser.* 143, p. 9. DOI: 10.1051/aas:2000332. arXiv: astro-ph/0002110.

Wheeler, J. A. (1966). "Superdense stars". In: *Ann. Rev. Astron. Astrophys.* 4, pp. 393–432. DOI: 10.1146/annurev.aa.04.090166.002141.

Wilczek, Frank (1977). "Decays of Heavy Vector Mesons Into Higgs Particles". In: *Phys. Rev. Lett.* 39, p. 1304. DOI: 10.1103/PhysRevLett.39.1304.

— (1978). "Problem of Strong P and T Invariance in the Presence of Instantons". In: *Phys. Rev. Lett.* 40, pp. 279–282. DOI: 10.1103/PhysRevLett.40.279.

Wilks, S. S. (1938). "The Large-Sample Distribution of the Likelihood Ratio for Testing Composite Hypotheses". In: *Annals Math. Statist.* 9.1, pp. 60–62. DOI: 10.1214/aoms/1177732360.

Will, Clifford M. (2014). "The Confrontation between General Relativity and Experiment". In: *Living Rev. Rel.* 17, p. 4. DOI: 10.12942/lrr-2014-4. arXiv: 1403.7377 [gr-qc].

Willoughby, Ralph A. (1977). "Fourier Analysis of Time Series: An Introduction (Peter Bloomfield)". In: *SIAM Review* 19.4, pp. 745–746. DOI: 10.1137/1019120. eprint: https://doi.org/10.1137/1019120. URL: https://doi.org/10.1137/1019120.

Wilson, J. R. et al. (1986). "Stellar core collapse and supernova". In: *Annals N. Y. Acad. Sci.* 470, pp. 267–293. DOI: 10.1111/j.1749-6632.1986.tb47980.x.

Wilson, James R. (1974). "Coherent Neutrino Scattering and Stellar Collapse". In: *Phys. Rev. Lett.* 32, pp. 849–852. DOI: 10.1103/PhysRevLett.32.849.

Witten, Edward (1984). "Some Properties of O(32) Superstrings". In: *Phys. Lett. B* 149, pp. 351–356. DOI: 10.1016/0370-2693(84)90422-2.

Woosley, S. E., A. Heger, and T. A. Weaver (2002). "The evolution and explosion of massive stars". In: *Rev. Mod. Phys.* 74, pp. 1015–1071. DOI: 10.1103/RevModPhys.74.1015.

Woosley, S. E. and Alexander Heger (2007). "Nucleosynthesis and Remnants in Massive Stars of Solar Metallicity". In: *Phys. Rept.* 442, pp. 269–283. DOI: 10.1016/j.physrep.2007.02.009. arXiv: astro-ph/0702176.

Yadav, N. (2023). *Private communication*.

Yadav, Naveen et al. (May 2019). "Large-Scale Mixing in a Violent Oxygen-Neon Shell Merger Prior to a Core-Collapse Supernova". In: DOI: 10.3847/1538-4357/ab66bb. arXiv: 1905.04378 [astro-ph.HE].

Yang, Haifeng and Roger A. Chevalier (2015). "Evolution of the Crab nebula in a low energy supernova". In: *Astrophys. J.* 806.2, p. 153. DOI: 10.1088/0004-637X/806/2/153. arXiv: 1505.03211 [astro-ph.HE].

Yang, Shan-Qing, Bi-Fu Zhan, et al. (2012). "Test of the Gravitational Inverse Square Law at Millimeter Ranges". In: *Phys. Rev. Lett.* 108, p. 081101. DOI: 10.1103/PhysRevLett.108.081101.

Yuksel, Hasan and John F. Beacom (2007). "Neutrino Spectrum from SN 1987A and from Cosmic Supernovae". In: *Phys. Rev. D* 76, p. 083007. DOI: 10.1103/PhysRevD.76.083007. arXiv: astro-ph/0702613.

Yusifov, I. and I. Kucuk (2004). "Revisiting the radial distribution of pulsars in the galaxy". In: *Astron. Astrophys.* 422, pp. 545–553. DOI: 10.1051/0004-6361:20040152. arXiv: astro-ph/0405559.

Zel'dovich, Y. B. and A. G. Polnarev (1974). "Radiation of gravitational waves by a cluster of superdense stars". In: *Sov. Astron.* 18, p. 17.

Zharikov, S. et al. (2021). "PSR B0656+14: the unified outlook from the infrared to X-rays". In: *Mon. Not. Roy. Astron. Soc.* 502.2, pp. 2005–2022. DOI: 10.1093/mnras/stab157. arXiv: 2101.07459 [astro-ph.HE].

Zhitnitsky, A. R. (1980). "On Possible Suppression of the Axion Hadron Interactions. (In Russian)". In: *Sov. J. Nucl. Phys.* 31, p. 260.

Acronyms

Here we list the acronyms used in this Thesis, without including names of experiments such as JUNO or IMB, nor names of laboratories such as CERN or SLAC.

1D	One-Dimensional
3D	Three-Dimensional
AGB	Asymptotic-Giant Branch
AGN	Active Galactic Nuclei
ASD	Amplitude Spectral Density
BNS	Binary Nuetron Star
CC	Core-Collapse
CDM	Cold Dark Matter
CO	Carbon-Oxygen
CP	Charge conjugation - Parity
CRPA	Continuum Random Phase Approximation
DFSZ	Dine-Fischler-Srednicki-Zhitnistsky
DM	Dark Matter
EoS	Equation of State
FIP	Feebly-Interacting Particle
GC	Globular Cluster
GR	General Relativity
GRS	Gamma-Ray Spectrometer
GUT	Grand Unified Theories
GW	Gravitational Waves
HB	Horizontal branch
HDM	Hot Dark Matter
HFGW	High-Frequency Gravitational Waves
IBD	Inverse-Beta Decay

IA	In-flight Annihilation
KSVZ	Kim-Shifman-Vainshtein-Zakharov
LSW	Light-Shining-through-Walls
MFP	Mean Free Path
MS	Main sequence
multi-D	Multidimensional
nEDM	neutron elctric dipole moment
NS	Neutron Star
OPE	One-Pion-Exchange
PNS	Proto-Neutron Star
PQ	Peccei-Quinn
PQWW	Peccei-Quinn-Weinberg-Wilczek
QCD	Quantum ChromoDynamics
RG	Red Giant
RGB	Red Giant Branch
RSG	Red SuperGiant
SGB	Sub-Giant Branch
SM	Standard Model
SN	Supernova
TO	main-sequence Turnoff
UV	Ultraviolet
WD	White Dwarf